

# Suitability of binary oxides for molecular-beam epitaxy source materials: A comprehensive thermodynamic analysis <sup>F</sup>

Cite as: APL Mater. **8**, 081110 (2020); <https://doi.org/10.1063/5.0013159>

Submitted: 08 May 2020 • Accepted: 06 August 2020 • Published Online: 24 August 2020

Kate M. Adkison,  Shun-Li Shang,  Brandon J. Bocklund, et al.

## COLLECTIONS

 This paper was selected as Featured



View Online



Export Citation



CrossMark

## ARTICLES YOU MAY BE INTERESTED IN

[Adsorption-controlled growth of Ga<sub>2</sub>O<sub>3</sub> by suboxide molecular-beam epitaxy](#)

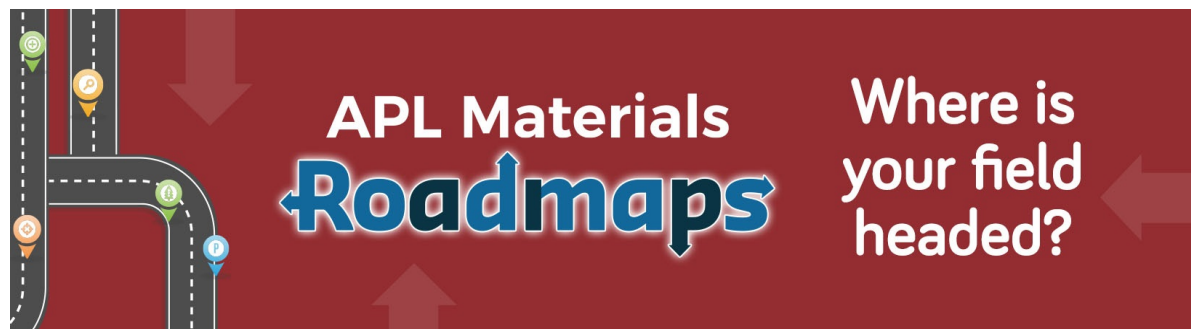
APL Materials **9**, 031101 (2021); <https://doi.org/10.1063/5.0035469>

[Efficient suboxide sources in oxide molecular beam epitaxy using mixed metal + oxide charges: The examples of SnO and Ga<sub>2</sub>O](#)

APL Materials **8**, 031110 (2020); <https://doi.org/10.1063/1.5134444>

[New approaches for achieving more perfect transition metal oxide thin films](#)

APL Materials **8**, 040904 (2020); <https://doi.org/10.1063/5.0003268>



APL Materials  
**Roadmaps**

Where is your field headed?

# Suitability of binary oxides for molecular-beam epitaxy source materials: A comprehensive thermodynamic analysis

Cite as: APL Mater. 8, 081110 (2020); doi: 10.1063/5.0013159

Submitted: 8 May 2020 • Accepted: 6 August 2020 •

Published Online: 24 August 2020



View Online



Export Citation



CrossMark

Kate M. Adkison,<sup>1</sup> Shun-Li Shang,<sup>1,a)</sup>  Brandon J. Bocklund,<sup>1</sup>  Detlef Klimm,<sup>2</sup>  Darrell C. Schlom,<sup>2,3,4</sup>   
and Zi-Kui Liu<sup>1</sup> 

## AFFILIATIONS

<sup>1</sup>Department of Materials Science and Engineering, The Pennsylvania State University, University Park, Pennsylvania 16802, USA

<sup>2</sup>Leibniz-Institut für Kristallzüchtung, Max-Born-Str. 2, 12489 Berlin, Germany

<sup>3</sup>Department of Materials Science and Engineering, Cornell University, Ithaca, New York 14853, USA

<sup>4</sup>Kavli Institute at Cornell for Nanoscale Science, Ithaca, New York 14853, USA

<sup>a)</sup>Author to whom correspondence should be addressed: [sus26@psu.edu](mailto:sus26@psu.edu)

## ABSTRACT

We have conducted a comprehensive thermodynamic analysis of the volatility of 128 binary oxides to evaluate their suitability as source materials for oxide molecular-beam epitaxy (MBE). 16 solid or liquid oxides are identified that evaporate nearly congruently from stable oxide sources to gas species:  $\text{As}_2\text{O}_3$ ,  $\text{B}_2\text{O}_3$ ,  $\text{BaO}$ ,  $\text{MoO}_3$ ,  $\text{OsO}_4$ ,  $\text{P}_2\text{O}_5$ ,  $\text{PbO}$ ,  $\text{PuO}_2$ ,  $\text{Rb}_2\text{O}$ ,  $\text{Re}_2\text{O}_7$ ,  $\text{Sb}_2\text{O}_3$ ,  $\text{SeO}_2$ ,  $\text{SnO}$ ,  $\text{ThO}_2$ ,  $\text{Tl}_2\text{O}$ , and  $\text{WO}_3$ . An additional 24 oxides could provide molecular beams with dominant gas species of  $\text{CeO}$ ,  $\text{Cs}_2\text{O}$ ,  $\text{DyO}$ ,  $\text{ErO}$ ,  $\text{Ga}_2\text{O}$ ,  $\text{GdO}$ ,  $\text{GeO}$ ,  $\text{HfO}$ ,  $\text{HoO}$ ,  $\text{In}_2\text{O}$ ,  $\text{LaO}$ ,  $\text{LuO}$ ,  $\text{NdO}$ ,  $\text{PmO}$ ,  $\text{PrO}$ ,  $\text{PuO}$ ,  $\text{ScO}$ ,  $\text{SiO}$ ,  $\text{SmO}$ ,  $\text{TbO}$ ,  $\text{Te}_2\text{O}_2$ ,  $\text{U}_2\text{O}_6$ ,  $\text{VO}_2$ , and  $\text{YO}_2$ . The present findings are in close accord with available experimental results in the literature. For example,  $\text{As}_2\text{O}_3$ ,  $\text{B}_2\text{O}_3$ ,  $\text{BaO}$ ,  $\text{MoO}_3$ ,  $\text{PbO}$ ,  $\text{Sb}_2\text{O}_3$ , and  $\text{WO}_3$  are the only oxides in the ideal category that have been used in MBE. The remaining oxides deemed ideal for MBE awaiting experimental verification. We also consider two-phase mixtures as a route to achieve the desired congruent evaporation characteristic of an ideal MBE source. These include  $(\text{Ga}_2\text{O}_3 + \text{Ga})$  to produce a molecular beam of  $\text{Ga}_2\text{O}(\text{g})$ ,  $(\text{GeO}_2 + \text{Ge})$  to produce  $\text{GeO}(\text{g})$ ,  $(\text{SiO}_2 + \text{Si})$  to produce  $\text{SiO}(\text{g})$ ,  $(\text{SnO}_2 + \text{Sn})$  to produce  $\text{SnO}(\text{g})$ , etc.; these suboxide sources enable suboxide MBE. Our analysis provides the vapor pressures of the gas species over the condensed phases of 128 binary oxides, which may be either solid or liquid depending on the melting temperature.

© 2020 Author(s). All article content, except where otherwise noted, is licensed under a Creative Commons Attribution (CC BY) license (<http://creativecommons.org/licenses/by/4.0/>). <https://doi.org/10.1063/5.0013159>

## I. INTRODUCTION

Oxides are of enormous interest for a wide range of applications due to the useful behaviors they exhibit, often with property coefficients or figures of merit at or near the very highest. These include magnetoelectrics (e.g.,  $\text{Cr}_2\text{O}_3$ ),<sup>1</sup> ferroelectrics (e.g.,  $\text{PbZr}_{0.2}\text{Ti}_{0.8}\text{O}_3$ ),<sup>2</sup> ferromagnets (e.g.,  $\text{La}_{0.7}\text{Sr}_{0.3}\text{MnO}_3$ ),<sup>3</sup> ferrimagnets (e.g.,  $\text{Sr}_2\text{FeMoO}_6$  and  $\text{BaFe}_{12}\text{O}_{19}$ ),<sup>4,5</sup> piezoelectrics (e.g.,  $\text{PbZn}_{1/3}\text{Nb}_{2/3}\text{O}_3\text{-PbTiO}_3$ ),<sup>6</sup> multiferroics (e.g.,  $\text{BiFeO}_3$ ),<sup>7</sup> superconductors (e.g.,  $\text{HgBa}_2\text{Ca}_2\text{Cu}_3\text{O}_{8+x}$ ),<sup>8</sup> metal-to-insulator transition

materials (e.g.,  $\text{EuO}$ ),<sup>9</sup> and semiconductors (e.g.,  $\text{BaSnO}_3$ <sup>10,11</sup> and  $\text{CdO}$ <sup>12</sup> with their high mobilities and  $\text{Ga}_2\text{O}_3$ <sup>13,14</sup> with its high figure of merit for power electronics).

To go from properties to technology, it is often desired to combine oxides with other materials to build and investigate the performance of proof-of-principle devices. One technique for producing high-quality oxides in thin film form is molecular-beam epitaxy (MBE). The resulting thin films can be used to establish the intrinsic properties of a material or assess its performance in prototype devices. MBE is widely employed for making high-quality thin films

because of its clean, ultra-high vacuum environment allowing film synthesis to be monitored by a variety of techniques during growth as well as its notable absence of highly energetic species. These characteristics allow for the precise customization of thin films with very few impurities and minimal disorder.<sup>15</sup> When it comes to preparing materials that are highly sensitive to crystalline perfection, MBE achieves electrical transport characteristics surpassing all other thin film growth methods, making it the gold-standard technique for preparing oxide heterostructures.<sup>16–19</sup>

MBE traditionally utilizes elemental molecular beams—one for each element in the compound being formed—that all impinge on the substrate to form the desired compound.<sup>15</sup> Challenges arise when this approach is applied to oxides. Consider trying to grow a layer of an oxide containing harder-to-oxidize elements on top of a layer that oxidizes easily and one does not want to overoxidize, as in the case for SrTiO<sub>3</sub>/Si or SrTiO<sub>3</sub>/GdTiO<sub>3</sub>.<sup>20,21</sup> Having an increased variety of molecular beams to choose from, for example, ones that deliver species already oxidized, could enhance the ability to make well-controlled heterostructures involving oxides by MBE.

For multicomponent materials such as oxides, one might be tempted to just evaporate the desired oxide directly. In general, such an approach does not work because when most oxides are heated, they do not simply evaporate as molecules with the same composition as the starting material, i.e., congruently. Instead, some of the constituents have higher vapor pressures and evaporate first; they evaporate incongruently. This leads to the composition of what is left behind changing, resulting in the partial pressures of the species that evaporate from a multicomponent source to change over time, making it useless for the controlled deposition of thin films. There are, however, some well-known exceptions to this rule. For example, SiO is known to evaporate congruently in vacuum as SiO molecules.<sup>22–24</sup> However, how many other exceptions are there among oxides? Answering this question is important for experimentalists seeking suitable source materials for the growth of oxides by MBE.

Stolyarova and Semenov<sup>22</sup> summarized the gas species emanating from Knudsen cells containing many different binary oxides. Complete data, however, showing the partial pressure of each gas species as a function of temperature are not available for many of these oxides,<sup>22</sup> limiting the usefulness of the information for MBE experimentalists. Lamoreaux *et al.*<sup>25,26</sup> conducted thermodynamic analyses on the evaporation behavior of the oxides of elements in groups 1, 2, and 12–14 under reducing conditions ( $P_{O_2} = 10^{-10}$  Pa), oxidizing conditions ( $P_{O_2} = 2 \times 10^4$  Pa), and congruent evaporation conditions. By providing the partial pressures of the vapor species over the condensed oxides as a function of temperature, their results<sup>25,26</sup> are widely used to determine if an oxide will make a good MBE source material. Nonetheless, much of the periodic table remains to be filled in as data for many of the oxides of transition metals and rare-earth (RE) metals are missing from their studies.<sup>25,26</sup> This lack of knowledge motivates the present thermodynamic analyses in which we analyze the evaporation behavior of 128 binary oxides; see Table S1 in the [supplementary material](#) for a complete list.

In the present work, we perform thermodynamic calculations to comprehensively consider the suitability of binary oxides and two-phase mixtures as potential sources for oxide MBE. Most binary

oxides are found to be unsuitable because upon heating, they decompose and evaporate a dominant species that contains either pure oxygen, which pollutes the vacuum environment, or the pure metal, which provides no benefit over using the pure metal directly. A few binary oxides are found that evaporate a metal oxide molecule in the vapor phase and are thus suitable for oxide MBE. Some of these are well appreciated and utilized, while others are new and await experimental verification. Several two-phase mixtures are also found to be suitable for oxide MBE.

## II. METHODOLOGY

### A. Thermodynamic analysis of evaporation for oxides

Equilibrium calculations were performed using the SGTE substance database (SSUB5)<sup>27</sup> within the Thermo-Calc software<sup>28</sup> to assess the evaporation behavior of binary oxides, i.e., the gaseous species and their vapor pressures. For amorphous SiO(am), which is well-known to evaporate congruently,<sup>22–24</sup> its close chemical relative GeO(am), and compounds including PtO<sub>2</sub>, Pt<sub>3</sub>O<sub>4</sub>, and PtO, which are missing in the SSUB5 database, thermodynamic descriptions were added using the reported enthalpies (and entropies when available) of formation at 298.15 K for GeO(am),<sup>29</sup> SiO(am),<sup>30</sup> and the Pt–O compounds.<sup>31</sup> In calculating the evaporation behavior of oxides, the gas species with the highest partial pressure—which with the increasing temperature is the first to reach a vapor pressure of  $10^{-1}$  Pa—is described as the “dominant” species. The relevance of  $10^{-1}$  Pa for MBE is that this partial pressure at the source is typically used for thin film growth.<sup>32–34</sup> If two gas-phase species have the same concentration within a factor of 10, they are both considered dominant; this is the case for the binary oxides of CsO<sub>2</sub>, PbO, Rb<sub>2</sub>O, Sc<sub>2</sub>O<sub>3</sub>, TeO<sub>2</sub>, U<sub>4</sub>O<sub>9</sub>, and ZrO<sub>2</sub>.

In thermodynamic calculations, the components of the system are defined as the element of interest and O<sub>2</sub> with the number of moles of the non-oxygen element fixed to one, i.e.,  $n(M) = 1$  mol. It is worth mentioning that there are many oxygen-containing species in the gas phase such as O, O<sub>2</sub>, and O<sub>3</sub>. At equilibrium, there is only one independent partial pressure for the independent component O, which can be represented by  $P_{O_2}$ , or  $P_O$ , or  $P_{O_3}$ , or the partial pressure of any O-containing species, and the partial pressures of other O-containing species are dependent variables and can be calculated. In other words, the number of independent partial pressures (or activity or chemical potential) equals the number of independent components in the system, and the partial pressures of other components (species) can be calculated, but they are not independent.

The partial pressure of O<sub>2</sub> is fixed at  $10^{-4}$  Pa, a typical oxygen background pressure in the growth of oxides by MBE, because at higher background pressures, hot filaments and other MBE components are damaged from oxidation and the fluxes from many elemental sources become unstable due to surface oxidation.<sup>35,36</sup> Calculations are made with the gas phase fixed at zero amount as this is considered to represent equilibrium evaporation from an MBE source; when the material evaporates from an MBE source into the open system of MBE, it does not return. It is worth noting that the total pressure in the system equals the vapor pressure of the condensed phases, which varies with temperature in equilibrium with

the fixed gas phase and should not be set as a fixed equilibrium condition in thermodynamic calculations. Furthermore, another benefit in using the partial pressure of  $O_2$  as a fixed equilibrium condition is that the oxygen content in the system is self-regulated by the phase stability of the system. This is an open system with respect to  $O_2$ , and the amount of  $O_2$  not only is different in different systems but also varies in the same system as the temperature is changed. An example of the macro file (i.e., the tcm file used by the Thermo-Calc software) to calculate the evaporation of a stable oxide source is provided in Table S3 in the [supplementary material](#).

For metastable oxides in equilibrium with gas, the gas compositions are calculated under the same conditions (temperature,  $O_2$  activity, and moles of the element) as those used for the stable oxide sources, but with all condensed phases removed except for the metastable oxide of interest. Two scenarios are possible when the oxide decomposes; these depend on the kinetics of the compound. If the solid oxide decomposes faster into a metal-oxygen containing gas phase than into another oxide or metal condensed phase, the metastable oxide is potentially useful as an oxide MBE source. If, on the other hand, the solid oxide decomposes faster into another condensed phase (oxide or pure element),  $O_2$  gas will be produced and pollute the vacuum. An example of the macro file to calculate the evaporation of a metastable oxide source is provided in Table S3 in the [supplementary material](#).

For the cases of gas species evaporated from a two-phase mixture of  $M_mO_n + M$  with an overall composition  $M_xO_y$ , the conditions for thermodynamic calculations are  $n(M) = 1$  mol,  $n(O_2) = 0.5y/x$  mol, and the amount of gas phase is fixed at zero, while the partial pressure of  $O_2$  is determined by the three-phase equilibrium of the two condensed phases and the gas phase. The pressure of the gas phase is much lower than the  $10^{-4}$  Pa typical oxygen background pressure used in the growth of oxides by MBE that is mentioned above due to the presence of the pure metal in equilibrium at low temperatures. Nevertheless, when the pure metal becomes metastable at high temperatures, the partial pressure of  $O_2$  can increase significantly as shown in the discussion of  $Ga_2O_3$  and relevant to suboxide-MBE (S-MBE). An example of the macro file to calculate the evaporation of a two-phase mixture case is provided in Table S3 in the [supplementary material](#).

These two types of calculations, i.e., the cases with the fixed partial pressure of  $O_2$  vs the two-phase mixture, represent the two different thermodynamic constraints on the system, viz., an open system vs a closed system. Even though the MBE chamber is an open system, in practice because gas is exchanged between the MBE chamber and the surroundings via the input of gases and its departure through several vacuum pumps, it can behave like either an open or a closed system depending on the fluxes of metallic elements, the partial pressure of  $O_2$ , and temperature as demonstrated in the discussion of the thermodynamics of MBE (TOMBE) diagram for ternary systems.<sup>19</sup> In the TOMBE diagram,  $O_2$  partial pressure is plotted against temperature and the diagram is labeled with the stable phases with the gas phase always present. For a binary system, in the closed-system regions of the TOMBE diagram, two condensed phases and the gas phase are in equilibrium with one degree of freedom (independent number of potentials) based on the Gibbs phase rule.<sup>37</sup> This is the same situation as typical Ellingham diagrams, such as the two-phase mixture in the present work of two components, with the temperature being the independent potential and

the chemical potentials being dependent potentials. Meanwhile in the open-system regions, one condensed phase and the gas phase are in equilibrium with two degrees of freedom. This is the case for a fixed partial pressure of the non-oxygen element with both the temperature and the chemical potential of  $O_2$  being independent potentials in maintaining the two-phase equilibrium. For evaporation, both scenarios are useful as demonstrated in the present work, while for MBE growth of thin films, the open-system scenario with one condensed phase is ideal as demonstrated in the MBE growth of  $Sr_2RuO_4$ ,  $SrRuO_3$ , and  $CaRuO_3$  epitaxial films.<sup>17,19</sup>

## B. Five scenarios of oxide source evaporation

Four possible scenarios for the evaporation of oxide sources are shown in Fig. 1. These are each described in detail below, together with one additional possibility (scenario 5) consisting of the evaporation of mixtures of two condensed phases. Note that we ignore the complex reaction products in scenarios 2–4 for the sake of simplicity; for example, we ignore the possible products of new oxide +  $O_2$ , or new oxide +  $M$ , or new oxide + additional oxide, or any combination of them other than the mentioned product  $M_mO_n$ .

**Scenario 1: Nearly congruent evaporation of metal-oxygen gas species** [ $M_xO_y(s \text{ or } \ell) \rightarrow M_xO_y(g)$ ; see S1 of Fig. 1]. Here, the letters s,  $\ell$ , and g in the parentheses indicate solid, liquid, and gas phases, respectively. In congruent evaporation, the species that evaporates into the gas phase has the same stoichiometric ratio as the solid or liquid source from which it comes; see additional details in Sec. II C. Two attributes make congruent evaporation the best scenario for MBE sources: (i) when the oxide is heated in the crucible and evaporates, metal-oxygen containing gas species of known composition will traverse the MBE chamber and deposit onto the substrate, and (ii) the metal-oxygen gas species  $M_xO_y(g)$  has the same stoichiometric ratio as the source material  $M_xO_y(s \text{ or } \ell)$ , so the composition of the source material will remain constant over time, making it easier to provide a stable flux of this molecular beam of known composition.

**Scenario 2: Incongruent evaporation of metal-oxygen gas species** [ $M_xO_y(s \text{ or } \ell) \rightarrow M_mO_n(g)$ ; see S2 of Fig. 1]. In incongruent evaporation, the species that evaporate have a different

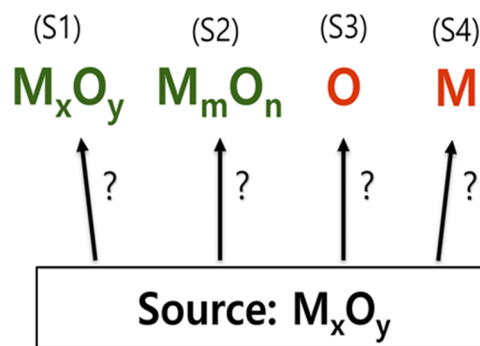


**FIG. 1.** Four scenarios (S1–S4) possible during evaporation plus an additional scenario (S5) examined in the present work with a two-phase mixture of  $M_xO_y + M$  as a source. Note that this plot ignores the possibility of complex reaction products that form from the oxide source for the sake of simplicity.

overall stoichiometric ratio than the solid or liquid source from which they emanate. Like congruent evaporation, incongruent evaporation can work for the MBE process, but it is less ideal. Although metal-oxygen containing gas species will be deposited onto the substrate, the gas species coming off of the oxide source  $[M_mO_n(g)]$  has a different stoichiometric ratio than the source  $[M_xO_y(s \text{ or } \ell)]$ . This difference in chemistry will cause the source material composition to change over time, making it more difficult to control the flux and composition of the molecular beam.

**Scenario 3: Evaporation of oxygen species  $[M_xO_y(s \text{ or } \ell) \rightarrow O_2(g)]$ ; see S3 of Fig. 1.** For some oxides, oxygen species  $[O_2(g)]$  will be the dominant species in the vapor. The dominant evaporation of oxygen species from the metal-oxide source is undesirable for an MBE process. In oxide MBE, it is desired to control the oxidant species (often an activated species such as ozone or those emitted from an oxygen plasma) and its flux directly. Oxygen species  $[O_2(g)]$  coming from the metal-oxide sources effectively pollute the ultra-high vacuum and cause a loss of the independent control of growth parameters that is desired in MBE.

**Scenario 4: Evaporation of elemental metal species  $[M_xO_y(s \text{ or } \ell) \rightarrow M_z(g)]$ ; see S4 of Fig. 1.** An elemental metal  $[M_z(g)]$  can also be the dominant species given off by the oxide source. Oxides that evaporate elemental metal species are also undesirable for MBE. Evaporation of the elemental metal causes the oxide source composition to become oxygen rich over time. In addition, using such an oxide source to generate a flux of metal species generally offers no advantage over the use of a pure metal source.

**Scenario 5: Two-phase mixture of  $M_mO_n + M$  as sources.** In addition to the above four scenarios, we also examine one more scenario to produce gas species  $M_xO_y$  from a two-phase mixture  $M_mO_n + M$  with an overall composition  $M_xO_y$ . This scenario builds upon experimental work, showing that this is a viable approach.<sup>38,39</sup>

### C. Three criteria for a nearly ideal MBE source material

Once the gas compositions emanating from the binary oxides are calculated, each binary oxide is evaluated against three criteria based on MBE chamber conditions necessary to produce high-quality thin films. A binary oxide source is identified as the most ideal for oxide MBE if it meets all three of the following criteria:

**Criterion 1. The solid or liquid metal-oxide source is stable under the given conditions.** Stable metal-oxide sources are ideal because they do not decompose and release oxygen, which would pollute the MBE vacuum. Some elements in the SSUB5 database<sup>27</sup> such as actinium, astatine, californium, curium, einsteinium, fermium, francium, radium, and protactinium do not have solid or liquid oxides, so these are disqualified. Oxides of some transition metal are disqualified because the stable phase under the given conditions is a pure metal in solid or liquid form. Examples include Ag(s), Au( $\ell$ ), Co(s), Cu(s), Ir(s), Os(s), Pd(s), Rh(s), and Ru(s). A select few of the elements are stable as liquid oxides under the given conditions such as Bi<sub>2</sub>O<sub>3</sub>( $\ell$ ), FeO( $\ell$ )

(i.e., the liquid Fe-oxide phase or the slag phase), Nb<sub>2</sub>O<sub>5</sub>( $\ell$ ), Rb<sub>2</sub>O( $\ell$ ), Ta<sub>2</sub>O<sub>5</sub>( $\ell$ ), and Ti<sub>4</sub>O<sub>7</sub>( $\ell$ ). If an element is able to form a metastable oxide, the metastable oxide is investigated. For example, Ir(s) is the most stable phase under the given conditions, but iridium also forms IrO<sub>2</sub>. Hence, IrO<sub>2</sub> is investigated as a metastable source. Note that the liquid state of FeO( $\ell$ ) is a slag phase with a mixture of all iron oxides (such as FeO, Fe<sub>3</sub>O<sub>4</sub>, and Fe<sub>2</sub>O<sub>3</sub>) in arbitrary ratios. Usually, melting processes are accompanied by a change in the metal-oxygen stoichiometry to lower the Gibbs energy by mixing, but not in the solid state.

**Criterion 2. The oxygen-metal containing gas species is dominant.** A metal-oxygen gas species  $[M_xO_y(g)]$  is ideal as it provides pre-oxidized metals with the known oxygen content to the growing film when it reaches the substrate. Binary oxides for which the dominant evaporant is the oxygen species or metal species are disqualified as MBE sources for not meeting this second criterion.

**Criterion 3. The oxide source evaporates nearly congruently.** Congruent evaporation ensures that the oxide source provides a constant flux of the desired species at a fixed temperature. This third criterion distinguishes between the most ideal sources for MBE and those that are less ideal because they evaporate incongruently.

Note that for exact congruent evaporation, the composition of the source oxide (solid or liquid phase) and that of the gas phase evaporating from it must be identical. The ideal case is where only one species exists in the gas phase and that species has the same stoichiometric ratio as the solid or liquid MBE source from which it evaporated. This is rarely the case; usually, multiple species evaporate into the gas phase, and congruent evaporation occurs when the overall composition of the gas phase matches that of the solid or liquid MBE source from which it came. As a practical matter, exact congruent evaporation is not needed for a source to perform well in MBE. Sources with evaporation characteristics sufficiently close to exact congruent evaporation can be tolerated. In the present work, we define nearly congruent evaporation as the condition where the mole fraction difference for each component, such as O<sub>2</sub>, in the oxide source and in the gas phase is less than 0.01, i.e.,  $|\Delta x(O_2)| < 0.01$ , with

$$\Delta x(O_2) = x(\text{oxide}, O_2) - x(\text{gas}, O_2), \quad (1)$$

where  $x(\text{oxide}, O_2)$  and  $x(\text{gas}, O_2)$  are the mole fractions of the component O<sub>2</sub> in the oxide source (s or  $\ell$ ) and in the gas phase, respectively. The same condition is also used to define what we mean by the nearly congruent evaporation of metastable oxide sources.

### III. RESULTS AND DISCUSSION

In the SSUB5 database,<sup>27</sup> 58 elements have stable solid oxides and 14 elements have metastable oxides under the given conditions. To make the present study more comprehensive, additional metastable oxides under the given conditions are included. The list of all evaluated 128 stable and metastable oxides and 17 elements under the given conditions is available in Table S1 in the [supplementary material](#). In addition, 27 two-phase mixtures of  $M_mO_n + M$

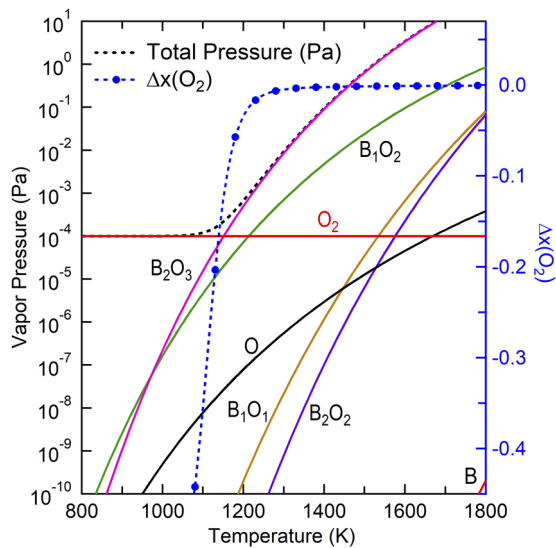


**FIG. 2.** Calculated partial pressures of the species in the gas phase (the solid lines) over the stable solid  $B_2O_3$  (the amorphous/glass phase) source at a fixed oxygen partial pressure,  $P_{O_2} = 10^{-4}$  Pa. The dominant gas species possesses the same composition as the  $B_2O_3(s)$  source at  $T > 1160$  K. Nearly congruent evaporation of  $B_2O_3(s)$  occurs at  $T > 1255$  K [see the definition in Eq. (1)]. If the total pressure is fixed at  $P_{tot} = 0.1$  Pa, instead of  $P_{O_2}$  being fixed at  $10^{-4}$  Pa, then nearly congruent evaporation of  $B_2O_3(s)$  occurs at  $T > 1398$  K; see also the summary in Table I.

are examined, where the elements  $M$  considered are rare-earth elements and other elements of practical interest; see Table S2. Note that we do not plot phase stability as a function of temperature for these oxides. Instead, we note in Figs. 2 and 4 and each supplemental figure caption (Figs. S1–S81) the stable phases as a function of temperature for each system.

## A. Ideal MBE sources

16 solid and liquid oxides meet the criteria to be classified as ideal MBE sources. These are  $As_2O_3$ ,  $B_2O_3$ ,  $BaO$ ,  $MoO_3$ ,  $OsO_4$ ,  $P_2O_5$ ,  $PbO$ ,  $PuO_2$ ,  $Rb_2O$ ,  $Re_2O_7$ ,  $Sb_2O_3$ ,  $SeO_2$ ,  $SnO$ ,  $ThO_2$ ,  $Tl_2O$ , and  $WO_3$ ; see Table I. Some of these oxides have been well studied in Knudsen cell evaporation experiments. Some of the identified oxide sources have been used to make thin films via various deposition methods, but only  $As_2O_3$ ,  $B_2O_3$ ,  $MoO_3$ ,  $PbO$ ,  $Sb_2O_3$ ,  $SeO_2$ , and  $WO_3$  have been used successfully for MBE growth as described in below. We discuss these oxides in Secs. III A 1–III A 13 in alphabetical order except for  $As_2O_3$  and  $SnO$ , which are discussed with  $Sb_2O_3$  in Sec. III A 9, and  $PuO_2$ , which is discussed with  $ThO_2$  in Sec. III A 11.

### 1. $B_2O_3(s)$ (Fig. 2)

Figure 2 shows the calculated evaporation behavior of solid  $B_2O_3$  (the amorphous/glass phase) as a function of temperature under  $P_{O_2} = 10^{-4}$  Pa, where the  $B_2O_3$  gas species is dominant above 1160 K in equilibrium with solid  $B_2O_3(s)$ ; see also Table I.

**TABLE I.** Oxide sources (s or  $\ell$ ) meeting the criteria for an ideal MBE source under the following conditions:  $P_{O_2} = 10^{-4}$  Pa, fixed gas phase at zero amount, fixed  $T$ , and  $n(M) = 1$  mol.

Element	Oxide source	Dominant gas species	$T$ -range <sup>a</sup>	$T$ -range <sup>b</sup>	$T$ -range <sup>c</sup>
As	$As_2O_3(\ell)$	$As_4O_6$	>677	>611	650–1274 <sup>d</sup>
B	$B_2O_3$ -glass(s)	$B_2O_3$	700–1800	1160–1800 ( $O_2$ at $T < 1160$ )	1255–1800
Ba	$BaO(s)$	$BaO$	700–1800	>1330 ( $O_2$ at $T < 1330$ )	>1473
Mo	$MoO_3(s)$	$Mo_3O_9$ ; $Mo_4O_{12}$	700–1800	760–1800 ( $O_2$ at $T < 760$ )	768–1800
Os	$OsO_4(s, \ell)$	$OsO_4$	<314	<314	<314
P	$P_2O_5$ -orth(s, $\ell$ )	$P_4O_{10}$	s at 300–839; $\ell$ at $T > 839$	422–1552 ( $O_2$ at $T < 422$ )	438–1510
Pb	$PbO$ -yellow(s)	$PbO$	700–1162	848–1032 ( $Pb$ at $T > 1032$ )	905–918
Pu	$PuO_2(s)$	$PuO_2$	700–2200	1850–2200 ( $O$ at $T < 1850$ )	1999–2063
Rb	$Rb_2O(s, \ell)$	$Rb_2O$ ; $Rb$	s at 517–778; $\ell$ at $T > 778$	660–795 ( $O_2$ at $T < 660$ )	701–716
Re	$Re_2O_7(s, \ell)$	$Re_2O_7$	s at 300–600; $\ell$ at $T > 600$	320–1286 ( $O_2$ at $T < 320$ )	332–1244
Sb	$Sb_2O_3(\ell)$	$Sb_4O_6$	>997	997–1429	997–1383
Se	$SeO_2(s, \ell)$	$SeO_2$	s at 300–633; $\ell$ at $T > 633$	314–650 ( $O_2$ at $T < 314$ )	337–644
Sn	$SnO(\ell)$	$SnO$	>1498	1498–1800 ( $O_2$ at $T < 863$ )	1498–1756
Th	$ThO_2(s)$	$ThO_2$	700–3000	2440–2970 ( $O$ at $T < 2440$ and $ThO$ at $T > 2970$ )	2631–2720
Tl	$Tl_2O(s, \ell)$	$Tl_2O$	s at 650–852; $\ell$ at $T > 852$	650–1456 ( $Tl$ at $T > 1456$ )	650–1188
W	$WO_3(s)$	$W_3O_9$	700–1800	1150–1800 ( $O_2$ at $T < 1150$ )	1176–1800

<sup>a</sup>Temperature range (in K) where the oxide source (s or  $\ell$ ) is stable.

<sup>b</sup>Temperature range (in K) where the dominant gas species possesses the same composition as the binary oxide source from which it evaporates.

<sup>c</sup>Temperature range (in K) of nearly congruent evaporation as defined by Eq. (1) for an absolute value of  $\Delta x(O_2) < 0.01$ . Note that some high-temperature limits represent the selected temperature limits used in the present work to perform thermodynamic calculations; for example, 1800 K is the limit of our calculations rather than the limit of nearly congruent evaporation.

<sup>d</sup>Liquid  $As_2O_3$  is stable at  $T > 677$  K. The temperature range for nearly congruent evaporation from a stable source is 677 K–1274 K.

Figure 2 shows that nearly congruent evaporation of  $B_2O_3(s)$ , defined by  $|\Delta x(O_2)| < 0.01$  [see Eq. (1)], occurs at  $T > 1255$  K. As an ancillary test, the ideal congruent evaporation of  $B_2O_3(s)$  occurs at  $T > 1398$  K under a fixed total pressure,  $P_{tot} = 0.1$  Pa. The thermodynamics of  $B_2O_3(s)$  volatility was investigated by Lamoreaux *et al.*,<sup>26</sup> and it was shown to evaporate congruently as  $B_2O_3(g)$ . Stolyarova and Semenov<sup>22</sup> also noted that the dominant vapor species of  $B_2O_3(s)$  thermally evaporated by a Knudsen cell is  $B_2O_3(g)$ .  $B_2O_3$  sources in MBE are well known, though they have only been used as doping sources for the MBE growth of silicon.<sup>40,41</sup>

Although  $B_2O_3$  is ideal for oxide MBE (see Fig. 2), and thin films have been successfully fabricated using MBE, the high reactivity of  $B_2O_3$  with water to form  $H_3BO_3$  under ambient conditions precludes it from many practical applications.<sup>42</sup> Putkonen and Niinistö<sup>42</sup> applied a protective  $Al_2O_3$  capping layer using atomic layer deposition (ALD) to prevent the  $B_2O_3$  thin film from reacting. When patterned, however, the film immediately suffered degradation from the exposed  $B_2O_3$  edge. Proposed applications of  $B_2O_3$  thin films include transistors, ultra-wide bandgap amorphous oxide semiconductors, and optoelectronics when combined with other oxides.<sup>43–45</sup> Glassy thin films such as  $B_2O_3$  also have potential as electrolytes used in batteries, as electrochemical sensors, as supercapacitors, and as electrochromic sensors.<sup>45</sup>

## 2. BaO(s) (Fig. S8)

The calculated evaporation behavior of BaO is shown in Fig. S8 along with that of  $BaO_2$ ; see also Table I. It can be seen that the primary species evaporating from  $BaO_2$  is BaO, so a  $BaO_2$  source works the same as BaO. The dominant BaO species in the molecular beam is relevant to making high dielectric constant perovskites such as  $BaTiO_3$  and  $(Ba, Sr)TiO_3$ , which have applications in high- $K$  ( $K$  is the dielectric constant) memory,<sup>46</sup> tunable dielectrics,<sup>47,48</sup> optoelectronics,<sup>49–51</sup> and fuel cells.<sup>52,53</sup> Another important barium-containing oxide is  $BaSnO_3$ —a semiconductor with high mobility at room temperature—which offers tantalizing properties for transparent electronics.<sup>10,11,54,55</sup> Barium hexaferrites including  $BaFe_{12}O_{19}$  are ferrimagnetic insulators with excellent performance at high frequency.<sup>5,56–58</sup>

In addition to complex oxides containing barium, BaO thin films themselves have applications in high current density cathodes, thermionic energy converters, and optical devices.<sup>59</sup> BaO films have been grown by many groups using MBE with separate beams of barium and  $O_2$ .<sup>60–62</sup> Less common, but nonetheless demonstrated, is the growth of BaO films using a  $BaO_2$  source<sup>63</sup> or a BaO source.<sup>64,65</sup> A BaO source could prove particularly advantageous when it is desired to not introduce any excess oxygen, e.g., when growing BaO on silicon and it is ideal to have all of the barium oxidized, yet not to oxidize any of the silicon (which can easily occur if excess oxygen is present).<sup>61,62</sup>

## 3. MoO<sub>3</sub>(s) (Fig. S41)

Several studies have been carried out on the evaporation of  $MoO_3$  from a Knudsen cell. In these studies,  $(MoO_3)_3$ ,  $(MoO_3)_4$ , and  $(MoO_3)_5$  are all observed in the gas phase with  $(MoO_3)_3$  being most abundant at 850 K.<sup>66,67</sup> Our calculations (Fig. S41, see also Table I) indicate congruent evaporation of  $MoO_3$  as well ( $T > 768$  K at  $P_{O_2} = 10^{-4}$  Pa) also with  $Mo_3O_9$  and  $Mo_4O_{12}$  being most dominant followed by  $Mo_5O_{15}$ . Du *et al.*<sup>68</sup> grew  $MoO_3$  thin films by MBE on

$SrTiO_3$  substrates by evaporating  $MoO_3$  powder from an effusion cell onto a substrate held at 673 K–823 K and immersed in activated oxygen species from an oxygen plasma operating at  $P_{O_2} = 4 \times 10^{-4}$  Pa.  $MoO_3$  molecular beams could be used as a route to grow  $SrMoO_3$  thin films, which are being studied for use as transparent conductors because of their very high conductivity.<sup>69,70</sup>  $MoO_3$  thin films are also used as electrochromic sensors and in lithium batteries.<sup>71</sup>

## 4. OsO<sub>4</sub>(s, ℓ) (Fig. S48)

Solid  $OsO_4(s)$  is a stable phase at low temperature,  $T < 304$  K. With the increasing temperature, liquid  $OsO_4(l)$  becomes stable in a narrow temperature range from 304 K to 314 K. Above 314 K,  $OsO_2(s)$  is the stable phase and remains so up to 832 K where solid  $Os(s)$  becomes stable. Figure S48 shows that the dominant gas species is  $OsO_4(g)$  at low temperatures, i.e.,  $T < 1028$  K in the plot of  $OsO_2(s)$  as an oxide source as well as in the plot of  $OsO_4(s)$  as an oxide source. These results indicate that  $OsO_4(s, \ell)$  is an ideal source for MBE oxide when  $T < 314$  K at  $P_{O_2} = 10^{-4}$  Pa; see also Table I.

## 5. P<sub>2</sub>O<sub>5</sub>(s, ℓ) (Fig. S47)

The calculated evaporation behavior of solid  $P_2O_5$  with an orthorhombic structure is shown in Fig. S47; see also the data in Table I.  $P_2O_5$  has exciting uses as a bioactive thin film material to modify surface properties of biomedical devices, to increase corrosion resistance, or for osteogenic applications.<sup>72</sup> The  $P_2O_5$  thin films are commonly fabricated using a sol-gel method instead of physical vapor deposition. Stolyarova and Semenov<sup>22</sup> recorded the congruent evaporation of  $P_4O_{10}$  to  $P_4O_{10}$  gas species from a  $P_2O_5(s)$  source at 500 K. No publication in the literature was found using  $P_2O_5$  in an MBE process.

## 6. PbO(s) (Fig. S50)

$PbO(s)$  was shown by Lamoreaux *et al.*<sup>26</sup> to have dominant species  $Pb(g)$  under reducing conditions and  $PbO(g)$  under oxidizing conditions. Experiments by Lopatin *et al.*<sup>73</sup> found that the dominant gas species in  $PbO(s)$  evaporated at 900 K–1150 K are  $Pb_nO_n(g)$ ,  $Pb(g)$ , and  $O(g)$ . The  $Pb_nO_n(g)$  species comes from the congruent evaporation of  $nPbO(s) \rightarrow Pb_nO_n$  with  $n = 1–6$ ; the  $Pb(g)$  and  $O(g)$  species come from a partial dissociation of  $PbO(s) \rightarrow Pb(g) + \frac{1}{2}O_2$ . The polymeric  $Pb_nO_n$  gas species observed by Lopatin *et al.*<sup>73</sup> were also included in the evaporation analysis by Lamoreaux *et al.*,<sup>26</sup> but these  $Pb_nO_n$  gas species are not included in the SSUB5 database and can thus not be seen in Fig. S50. Although the present work does not take into account the  $Pb_nO_n$  ( $n = 2–6$ ) species, the yellow orthorhombic phase  $PbO\_yellow$  is dominant below 1163 K under the conditions of our thermodynamic calculations (not shown), which agrees with Lopatin's assessment that  $PbO$  is dominant between 900 K and 1150 K.

The evaporation behavior of  $PbO\_yellow$  in Fig. S50 disagrees with the analysis by Lamoreaux *et al.*,<sup>26</sup> which shows  $Pb(g)$  to be dominant from 700 K to 1800 K at  $P_{O_2} = 10^{-10}$  Pa. On the other hand, an experimental attempt at using  $PbO(s)$  as an MBE source in an MBE system with no added oxygen (and a chamber background pressure in the  $10^{-10}$  Pa range) found that  $PbO(s)$  decomposed into mainly  $Pb(g)$  with very little  $PbO(g)$ ,<sup>74</sup> which is consistent with

the expectations of Lamoreaux *et al.*<sup>26</sup> To see if the disagreement between our calculations and those of Lamoreaux *et al.*<sup>26</sup> is due to the difference in  $O_2$  partial pressure conditions, we redid our calculations as a function of oxygen partial pressure for  $P_{O_2}$  from  $10^{-1}$  Pa to  $10^{-10}$  Pa. Figure 3 shows the temperatures at which Pb(g) becomes the dominant species in the gas phase as a function of  $P_{O_2}$ ; the temperature at which Pb(g) becomes dominant over PbO(g) decreases with decreasing  $P_{O_2}$ . At the pressure used by Lamoreaux *et al.*,<sup>26</sup>  $P_{O_2} = 10^{-10}$  Pa, the calculations show that the partial pressure of Pb(g) exceeds that of PbO(g) at 725 K, in good agreement with findings of Lamoreaux *et al.*<sup>26</sup> who found that this crossover occurs around 700 K at  $P_{O_2} = 10^{-10}$  Pa.

A PbO source was used by Rispens and Noheda to grow high-quality PbTiO<sub>3</sub> films by MBE.<sup>75</sup> These authors found the use of PbO(s) advantageous over Pb(*l*), which is consistent with the results from Fig. S50 where the dominant species in the gas phase at MBE-relevant growth conditions is PbO. We note that based on the diagram by Lamoreaux *et al.*,<sup>26</sup> PbO is not a good source to use for the growth of PbTiO<sub>3</sub> or other Pb-containing oxides by MBE. This points to the importance of the current comprehensive analysis at a fixed oxygen pressure ( $10^{-4}$  Pa) that is relevant for oxide MBE and in the case of PbO dramatically changes the dominant species in the gas phase as shown in Fig. 3.

### 7. Rb<sub>2</sub>O(*s, l*) (Fig. S56)

Rb<sub>2</sub>O is a liquid at temperatures at which the dominant species evaporated from it have a vapor pressure of  $10^{-1}$  Pa. At this temperature, there are actually two species with high and comparable vapor pressure in the gas phase: Rb(g) and Rb<sub>2</sub>O(g). From the calculated vapor pressures over liquid Rb<sub>2</sub>O, Rb<sub>2</sub>O is seen to evaporate nearly congruently at higher partial pressures of  $O_2$  (such as  $P_{O_2} = 10^{-4}$  Pa and  $10^{-1}$  Pa); see Fig. S56 as well as Table I.

At lower  $P_{O_2}$  (e.g.,  $<10^{-4}$  Pa), the vapor is Rb-rich compared to the Rb<sub>2</sub>O source. Although at these lower oxygen partial pressures it is not an ideal MBE source, it should still produce a molecular beam containing a significant fraction of pre-oxidized rubidium in the

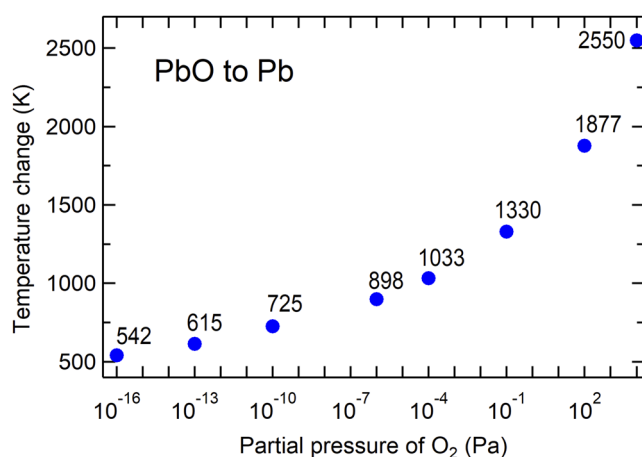


**FIG. 3.** Plot of the temperature (in K) at which the partial pressure of Pb(g) exceeds that of PbO(g) as a function of the partial pressure of  $O_2$ .

form of Rb<sub>2</sub>O. Rb<sub>2</sub>O has been used as an MBE source for the growth of superconducting (Bi, Rb)BaO<sub>3</sub> films by Hellman *et al.*<sup>76</sup> These authors noted that the Rb<sub>2</sub>O source showed signs of decomposition into a Rb-rich molecular beam, consistent with the present calculations at different  $P_{O_2}$  values (Fig. S56). They also mentioned that they did not observe any Rb oxide molecules by mass spectrometry. This is inconsistent with the present calculations with higher partial pressures of  $O_2$ , in which significant Rb<sub>2</sub>O(g) in the gas phase is expected (see  $P_{O_2} = 10^{-4}$  Pa and  $10^{-1}$  Pa in Fig. S56). A possible reason for this is the strong dependence of the Rb<sub>2</sub>O(g) partial pressure on the oxygen partial pressure. Our calculations are done at  $P_{O_2} = 10^{-4}$  Pa (as well as  $10^{-1}$  Pa and  $10^{-7}$  Pa in the present case); at lower oxygen partial pressures, which are likely the conditions under which Hellman *et al.*<sup>76</sup> operated their mass spectrometer, Rb(g) becomes the dominant gas species.

### 8. Re<sub>2</sub>O<sub>7</sub>(*s, l*) (Fig. S57)

Through Knudsen cell studies, Skinner<sup>77</sup> found that Re<sub>2</sub>O<sub>7</sub>(s) evaporates congruently as Re<sub>2</sub>O<sub>7</sub>(g) at  $P_{O_2} = 2 \times 10^{-4}$  Pa and  $T = 404$  K. Due to a small amount of  $O_2$  that simultaneously vaporized, some residual ReO<sub>3</sub>(s) was left in the cell. The ions exhibiting the highest signal in Skinner's mass spectrometry study are in the following order: Re<sub>2</sub>O<sub>7</sub>, ReO<sub>3</sub>, ReO<sub>2</sub>, Re<sub>2</sub>O<sub>6</sub>, and Re<sub>2</sub>O<sub>5</sub>. In the present calculations (Fig. S57 as well as Table I), Re<sub>2</sub>O<sub>7</sub> is the dominant gas species followed by Re<sub>2</sub>O<sub>6</sub>, which shares the stoichiometric ratio of ReO<sub>3</sub>. To the best of our knowledge, Re<sub>2</sub>O<sub>7</sub>(*s, l*) has not yet been used as an oxide source for MBE growth. Like B<sub>2</sub>O<sub>3</sub>, Re<sub>2</sub>O<sub>7</sub> is very hygroscopic, which may limit its applications.<sup>78</sup>

### 9. As<sub>2</sub>O<sub>3</sub>(*l*) (Fig. S5), Sb<sub>2</sub>O<sub>3</sub>(*l*) (Fig. S60), and SnO(*l*) (Fig. S65)

Figure S5 indicates liquid As<sub>2</sub>O<sub>3</sub>(*l*) is a stable phase at higher temperatures ( $T > 677$  K) transformed from solid As<sub>2</sub>O<sub>5</sub>(*s*). In the temperature range 677 K–1274 K, As<sub>2</sub>O<sub>3</sub>(*l*) is a possible ideal MBE source with the dominant gas species of As<sub>4</sub>O<sub>6</sub>(g) at  $P_{O_2} = 10^{-4}$  Pa; see also Table I.

The behavior calculated for Sb<sub>2</sub>O<sub>3</sub> is analogous to that of As<sub>2</sub>O<sub>3</sub>. At higher temperatures ( $T > 997$  K), liquid Sb<sub>2</sub>O<sub>3</sub>(*l*) is a stable phase transformed from solid Sb<sub>2</sub>O<sub>3</sub>(*s*). Figure S60 as well as Table I shows that Sb<sub>2</sub>O<sub>3</sub>(*l*) is also a possible ideal MBE source with the dominant gas species being Sb<sub>4</sub>O<sub>6</sub>(g) in the temperature range of 997 K–1429 K. Nearly congruent evaporation of Sb<sub>2</sub>O<sub>3</sub>(*l*) is calculated to occur over the temperature range 997 K–1398 K at  $P_{O_2} = 10^{-4}$  Pa.

Similar to As<sub>2</sub>O<sub>3</sub>(*l*) and Sb<sub>2</sub>O<sub>3</sub>(*l*), at higher temperatures ( $T > 1498$  K), liquid SnO(*l*) becomes a stable phase. Figure S65 as well as Table I shows that SnO(*l*) is also a possible ideal MBE source with the dominant gas species being Sn<sub>1</sub>O<sub>1</sub>(g) when  $T > 1498$  K. SnO and SnO<sub>2</sub> are discussed further in Sec. III B 1.

Note that the solid phases of As<sub>2</sub>O<sub>3</sub>(*s*), Sb<sub>2</sub>O<sub>3</sub>(*s*), and SnO(*s*) are metastable, but they evaporate nearly congruently based on our calculations; see Figs. S5, S60, and S65 and Table III. Both As<sub>2</sub>O<sub>3</sub>(*s*) and Sb<sub>2</sub>O<sub>3</sub>(*s*) have been used as source materials in oxide MBE and were observed to evaporate congruently by Stall.<sup>74</sup> In his study, Stall noted the much lower vapor pressure of Sb<sub>2</sub>O<sub>3</sub> ( $\sim 10^{-2}$  Torr) compared with As<sub>2</sub>O<sub>3</sub> ( $\sim 10^2$  Torr) at 673 K.<sup>74</sup> To provide the desired flux of Sb<sub>4</sub>O<sub>6</sub>(g), the effusion cell containing Sb<sub>2</sub>O<sub>3</sub>(*s*) was operated at a temperature around 750 K, at which our calculations

indicate that  $\text{SbO}_2(\text{s})$  is the stable phase. Nonetheless,  $\text{Sb}_2\text{O}_3(\text{s})$  was observed to behave as an ideal MBE source by providing a molecular beam with the same stoichiometry as the source material [consistent with our calculation that the dominant species in the gas phase is  $\text{Sb}_4\text{O}_6(\text{g})$ ].

### 10. $\text{SeO}_2(\text{s}, \ell)$ (Fig. S62)

The calculated evaporation behavior of  $\text{SeO}_2(\text{s})$  is shown in Fig. S62 as well as Table I. The results indicate that the gaseous  $\text{SeO}_2$  species is dominant when  $\text{SeO}_2(\text{s})$  is heated and agree well with Knudsen evaporation measurements between 360 K and 660 K.<sup>22,79,80</sup>

Metal oxides including  $\text{SeO}_2$  as well as  $\text{SnO}_2$ ,  $\text{ZnO}$ ,  $\text{TiO}_2$ ,  $\text{VO}$ , and  $\text{WO}_3$  are particularly good gas sensors because the electrical conductivity of the thin film changes with gas adsorption.<sup>81,82</sup> Manno *et al.*<sup>82</sup> studied both  $\text{SeO}_2$ - $\text{SnO}_2$  and  $\text{SeO}_2$ - $\text{In}_2\text{O}_3$  thin films for applications in  $\text{NO}_x$  sensors. The  $\text{SeO}_2$ - $\text{In}_2\text{O}_3$  thin films were made by evaporating an InSe source and post-annealing the film in  $\text{O}_2$ . The  $\text{SeO}_2$ - $\text{SnO}_2$  thin films on the other hand were deposited onto an unheated quartz substrate by vaporizing 99.999% pure  $\text{SeO}_2$  and  $\text{SnO}_2$  with  $P_{\text{O}_2} = 5 \times 10^{-5}$  Pa. After deposition, the films were annealed in flowing oxygen at 400 °C. The specific evaporation behavior of  $\text{SeO}_2$  and  $\text{SnO}_2$  is not discussed by the authors,<sup>82</sup> but it is likely that  $\text{SnO}_x$  species were in the vapor since  $\text{SnO}_x$  species from an  $\text{SnO}_2$  source were noted under similar evaporation conditions.<sup>11</sup>

### 11. $\text{ThO}_2(\text{s})$ (Fig. S71) and $\text{PuO}_2(\text{s})$ (Fig. S55)

In agreement with the present calculations (Fig. S71 as well as Table I), the dominant gas species given off by a  $\text{ThO}_2$  source in a Knudsen cell was shown to be  $\text{ThO}_2(\text{g})$ .<sup>22</sup> The evaporation behavior of  $\text{ThO}_2$  is, however, not well studied in the literature, and the use of  $\text{ThO}_2$  source materials in MBE is not reported. Similar to  $\text{ThO}_2(\text{s})$ ,  $\text{PuO}_2(\text{s})$  has not been reported as an MBE source either. In addition, no Knudsen cell evaporation studies could be found for  $\text{PuO}_2$  in the literature.

### 12. $\text{Tl}_2\text{O}(\text{s}, \ell)$ (Fig. S73)

$\text{Tl}_2\text{O}$  was calculated by Lamoreaux *et al.*<sup>26</sup> to exhibit congruent evaporation behavior under reducing conditions.  $\text{Tl}_2\text{O}$  is more stable than  $\text{Tl}_4\text{O}_3$  and  $\text{Tl}_2\text{O}_3$  at low oxygen partial pressures, which makes it ideal for the MBE vacuum environment.<sup>26,83</sup>  $\text{Tl}_2\text{O}$  powder is widely available from commercial distributors but is quite toxic. One concern with  $\text{Tl}_2\text{O}$  is its high reactivity with  $\text{O}_2$  and many other elements at elevated temperatures.<sup>83</sup> Holstein<sup>83</sup> used an argon atmosphere to mitigate this issue and found the vapor pressure of  $\text{Tl}_2\text{O}(\text{g})$  over the  $\text{Tl}_2\text{O}(\text{s})$  source to be 29 Pa at 820 K, which agrees well with the evaporation behavior calculated in the present work (Fig. S73 and Table I).  $\text{Tl}_2\text{O}$  has been used in the growth of thin films of the high-temperature superconductors  $\text{Tl-Ba-Ca-Cu-O}$  and  $\text{Tl-Pb-Sr-Ca-Cu-O}$ , but no literature was found showing  $\text{Tl}_2\text{O}(\text{s}, \ell)$  used as a source material in MBE.<sup>83</sup>

### 13. $\text{WO}_3(\text{s})$ (Fig. S77)

$\text{WO}_3(\text{s})$  is described to vaporize polymerically like  $\text{MoO}_3(\text{s})$ ;<sup>22</sup> see Fig. S77 vs Fig. S41. A Knudsen cell evaporation study by Blackburn *et al.*<sup>84</sup> showed that  $(\text{WO}_3)_3$  is the dominant vapor species.  $\text{WO}_2$  is also a vapor species but is reported to decompose into

$(\text{WO}_3)_3$  and W species.<sup>84</sup> The latter observation is not reflected in the present calculations (Fig. S77 and Table I), since the partial pressures of  $\text{WO}_2$  and W in the present calculations are many orders of magnitude lower than that of  $\text{W}_3\text{O}_9$  or any of the  $\text{W}_x\text{O}_{3x}$  species. The results shown in Fig. S77 are consistent with a heated charge of  $\text{WO}_3$  that provides a beam of  $\text{W}_3\text{O}_9$  as described in the Knudsen cell study of Blackburn *et al.*<sup>84</sup> Li *et al.*<sup>85</sup> used  $\text{WO}_3$  powder as an MBE source to successfully grow  $\text{WO}_3$  thin films for applications as a photocatalyst. In their experiments,  $\text{WO}_3$  powder was evaporated from a high-temperature effusion cell and deposited as an epitaxial  $\text{WO}_3$  film at a substrate temperature of 773 K in the presence of activated oxygen species from an oxygen plasma operating at  $P_{\text{O}_2} = 4 \times 10^{-4}$  Pa.<sup>85</sup>

## B. Stable solid oxide with incongruent evaporation

Having established which binary oxides evaporate nearly congruently, we next consider the possibility that a metastable binary oxide (if there were some way to produce it and constrain it from not decomposing in the solid state) would evaporate nearly congruently when heated. Table II summarizes the binary oxides that do not meet criterion 3 for nearly congruent evaporation (see Sec. II C) but evaporate incongruently instead. Such oxides are not ideal as the composition of the source will generally change over time as it becomes depleted in some component, but they might still be useful for MBE if they provide a desired gaseous species. In addition to considering the binary oxides in Table II, the species emanating from them with the highest partial pressure, i.e., the dominant gas species, were separately investigated as metastable sources to see if nearly congruent evaporation exists for those species.  $\text{TcO}_2$  was also investigated but is omitted from the present work because it exhibits a decrease in vapor pressure with the increasing temperature in our calculations.

### 1. $\text{SnO}_2$ (Fig. S65)

Figure S65 shows the calculated evaporation behavior of  $\text{SnO}_2$  as a function of temperature, where the gaseous species  $\text{SnO}$  is dominant above 1128 K in equilibrium with solid  $\text{SnO}_2$  (see also Table II). To provide MBE-relevant fluxes, the temperature of the  $\text{SnO}_2$  source is about 1350 K–1400 K, so when an  $\text{SnO}_2$  source is used in oxide MBE,  $\text{SnO}$  is indeed the dominant species in the gas phase.  $\text{SnO}_2$  was first used as a source in oxide MBE to achieve *n*-type doping of  $\text{Ga}_2\text{O}_3$  with  $\text{Sn}^{4+}$ .<sup>86</sup> More recently, it has been used to grow  $\text{BaSnO}_3$ <sup>10,11</sup> and  $\text{SnO}$ .<sup>87</sup> The La-doped  $\text{BaSnO}_3$  films grown by MBE with an  $\text{SnO}_2$  source exhibit the highest mobility<sup>10,11</sup> and the best transistor performance<sup>55</sup> achieved to date, demonstrating  $\text{SnO}_2$  as a viable MBE source.

Because  $\text{SnO}(\text{g})$  is the dominant evaporating species, the use of  $\text{SnO}_2(\text{s})$  as an MBE source also provides a possible route to grow  $\text{Sn}^{2+}$ -containing compounds such as *p*-type semiconductors that are predicted to have high mobility including  $\text{SnO}$ ,<sup>87,88</sup>  $\text{K}_2\text{Sn}_2\text{O}_3$ ,<sup>87</sup>  $\text{Rb}_2\text{Sn}_2\text{O}_3$ ,<sup>87</sup> and  $\text{Ta}_2\text{SnO}_6$ .<sup>88,89</sup> Note that  $\text{Sn}^{2+}$  is a difficult oxidation state to stabilize. Many thermodynamic phase diagrams, e.g., those for  $\text{Sn-O}$ <sup>90</sup> as well as  $\text{Sn-SnO}_2$ ,<sup>91</sup> omit  $\text{SnO}$  considering it to be metastable and to disproportionate into Sn and  $\text{SnO}_2$ ; this agrees with the present thermodynamic analysis shown in Fig. S65. Being able to deliver a molecular beam of  $\text{SnO}$  to the substrate surface greatly simplifies the synthetic challenge to preparing

**TABLE II.** Incongruent evaporation of stable solid oxide sources under the following conditions:  $P_{O_2} = 10^{-4}$  Pa, fixed gas phase at zero amount, fixed  $T$ , and  $n(M) = 1$  mol.

Element	Solid oxide source	$T$ -range (K) <sup>a</sup>	Dominant gas species	$T$ -range (K) <sup>b</sup>
Si	SiO <sub>2</sub> _cristobalite	700–1800	SiO	1570–1800
Sc	Sc <sub>2</sub> O <sub>3</sub>	700–2500	ScO <sub>2</sub> , ScO	2170–2400, 2400–2500
V	V <sub>2</sub> O <sub>3</sub>	1289–1800	VO <sub>2</sub>	1360–1800
Ga	Ga <sub>2</sub> O <sub>3</sub>	700–1800	Ga <sub>2</sub> O	1362–1800
Ge	GeO <sub>2</sub>	700–1389	GeO	1010–1800
As	As <sub>2</sub> O <sub>5</sub>	300–677	As <sub>4</sub> O <sub>6</sub>	612–1312
Rb	Rb <sub>2</sub> O	517–778	Rb <sub>2</sub> O, Rb	660–1800
Y	Y <sub>2</sub> O <sub>3</sub>	700–2500	YO <sub>2</sub>	2000–2500
Zr	ZrO <sub>2</sub>	700–2800	ZrO	2490–2800
In	In <sub>2</sub> O <sub>3</sub>	700–1676	In <sub>2</sub> O	1218–1800
Sn	SnO <sub>2</sub>	700–1498	SnO	1128–1800
Sb	SbO <sub>2</sub>	700–997	Sb <sub>4</sub> O <sub>6</sub>	792–1429
Te	TeO <sub>2</sub>	700–913	Te <sub>2</sub> O <sub>2</sub>	760–892
Cs	CsO <sub>2</sub>	300–754	Cs <sub>2</sub> O <sub>2</sub> , Cs <sub>2</sub> O	546–614, 614–700
La	La <sub>2</sub> O <sub>3</sub>	700–2500	LaO	1960–2500
Ce	Ce <sub>2</sub> O <sub>3</sub>	1988–2500	CeO	1940–2500
Pr	Pr <sub>2</sub> O <sub>3</sub>	1361–2500	PrO	1934–2500
Nd	Nd <sub>2</sub> O <sub>3</sub>	700–2500	NdO	1980–2500
Pm	Pm <sub>2</sub> O <sub>3</sub>	700–2593	PmO	2010–2926
Sm	Sm <sub>2</sub> O <sub>3</sub>	700–2500	SmO	2050–2460
Gd	Gd <sub>2</sub> O <sub>3</sub>	700–2500	GdO	2190–2500
Tb	Tb <sub>2</sub> O <sub>3</sub>	800–2500	TbO	2290–2500
Dy	Dy <sub>2</sub> O <sub>3</sub>	700–2500	DyO	2270–2500
Ho	Ho <sub>2</sub> O <sub>3</sub>	700–2500	HoO	2320–2500
Er	Er <sub>2</sub> O <sub>3</sub>	700–2500	ErO	2350–2500
Lu	Lu <sub>2</sub> O <sub>3</sub>	700–2500	LuO	2450–2500
Hf	HfO <sub>2</sub>	700–3000	HfO, O	2640–3000
U	U <sub>3</sub> O <sub>8</sub>	525–939	U <sub>2</sub> O <sub>6</sub>	518–1800

<sup>a</sup>Temperature range where the oxide source is stable.<sup>b</sup>Temperature range where the oxide gas species is dominant.

Sn<sup>2+</sup>-containing materials. Furthermore, for the synthesis of anti-perovskites such as Sr<sub>3</sub>SnO, it is preferable to have SnO arrive to the growth surface pre-oxidized and without any excess oxygen in order to avoid the undesired reaction of Sr<sub>3</sub>SnO with excess oxygen to form unwanted SrO.<sup>92</sup> Finally, the present work (Fig. S65) also indicates that SnO(s) can be a metastable source that nearly congruently evaporates as SnO.

Following the recent experimental work of Hoffmann *et al.*,<sup>39</sup> we also examined the gas species for evaporation from a two-phase mixture of SnO<sub>2</sub>(s) + Sn(*l*) that has an overall composition SnO. Figure 4 shows that SnO(g) is the dominant gas species, indicating that a mixture of SnO<sub>2</sub>(s) + Sn(*l*) is also an ideal MBE source providing the nearly congruent evaporation of SnO; see a complete list of the two-phase mixtures examined in Table S2. As discussed in Sec. II A, the partial pressure of O<sub>2</sub> in the two-phase mixture is much lower than the typical MBE background value of 10<sup>-4</sup> Pa, e.g., its value for a two-phase mixture of SnO<sub>2</sub>(s) + Sn(*l*) at 1200 K is about 10<sup>-9</sup> Pa. The partial pressures of O<sub>2</sub> and all other species in the gas phase are determined by the two-phase equilibrium and are independent of the relative amounts of SnO<sub>2</sub>(s) and Sn(*l*) in the

system. The use of equal amounts of SnO<sub>2</sub>(s) and Sn(*l*) to give the nominal SnO composition of the source may simplify experimental control if SnO<sub>2</sub>(s) and Sn(*l*) have similar evaporation rates. If the two condensed phases have very different evaporation kinetics, one may adjust the relative amounts of each phase in the two-phase mixture to provide the desired partial pressures in the MBE beam. Additional impacts of the metal-to-oxide ratio will be discussed in a forthcoming paper where the S-MBE method is more systematically examined.<sup>95</sup>

## 2. Ga<sub>2</sub>O<sub>3</sub> (Fig. S27)

The present calculations (Fig. S27) show that Ga<sub>2</sub>O<sub>3</sub>(s) provides a beam of Ga<sub>2</sub>O(g). This is in agreement with the experiments performed by Butt *et al.*<sup>94</sup> demonstrating that Ga<sub>2</sub>O is the dominant gas species over Ga<sub>2</sub>O<sub>3</sub>(s). We did not investigate the nearly congruent evaporation of Ga<sub>2</sub>O because Ga<sub>2</sub>O(s) is not available in the SSUB5 database<sup>27</sup> [note that Ga<sub>2</sub>O(s) is not a stable phase at 0 K according to first-principles calculations in the OQMD database].<sup>95</sup>

Ga<sub>2</sub>O<sub>3</sub> thin films have several applications, including gas sensing. Its large bandgap, ability to be doped with *n*-type carriers,

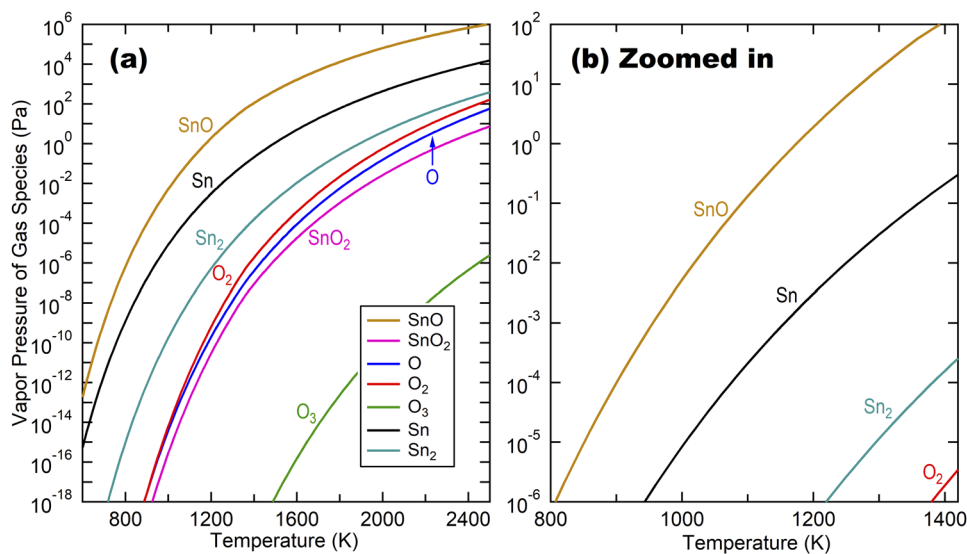


**FIG. 4.** (a) Calculated partial pressures of gas species for the evaporation of a two-phase mixture of  $\text{SnO}_2(\text{s}) + \text{Sn}(\ell)$  with an overall composition of SnO and (b) a zoomed-in view in the pressure range of interest for oxide MBE. The conditions for the calculations are fixed gas phase at zero amount,  $n(\text{Sn}) = 1$  mol, and  $n(\text{O}_2) = 0.5$  mol. Note that liquid  $\text{Sn}(\ell)$  is stable at  $T < 1359$  K, and liquid  $\text{SnO}(\ell)$  is stable at  $T > 1359$  K. Hence, the phase regions are “Gas +  $\text{SnO}_2(\text{s}) + \text{Sn}(\ell)$ ” when  $T < 1359$  and “Gas +  $\text{SnO}(\ell)$ ” when  $T > 1359$  K in this figure, where the mole fraction of gas phase is fixed at zero amount.

relatively high mobility, and high Baliga figure of merit that is second only to diamond also attract tremendous interest for this semiconductor to be used for high-power electronics and ultraviolet (UV) detectors.<sup>13,14</sup> The growth of  $\text{Ga}_2\text{O}_3$  thin films by MBE is a burgeoning area of research. Although most groups use  $\text{Ga}(\ell)$  as the MBE source,<sup>86,96–100</sup> both amorphous<sup>101</sup> and epitaxial<sup>102</sup> films of  $\text{Ga}_2\text{O}_3(\text{s})$  have been grown by MBE from a  $\text{Ga}_2\text{O}_3(\text{s})$  source.

Another route to produce a molecular beam of  $\text{Ga}_2\text{O}(\text{g})$  is to use a mixture of  $\text{Ga}(\ell)$  and  $\text{Ga}_2\text{O}_3(\text{s})$  instead of the incongruent evaporation of  $\text{Ga}_2\text{O}_3(\text{s})$ .<sup>38,39</sup> Such an approach has the advantage that a much lower temperature is needed to provide the same flux of  $\text{Ga}_2\text{O}(\text{g})$  in the molecular beam from a  $\text{Ga}_2\text{O}_3(\text{s}) + \text{Ga}(\ell)$  mixture compared to that from just  $\text{Ga}_2\text{O}_3(\text{s})$ , see Fig. S27 and Table S2 with the partial pressure of  $\text{O}_2$  being  $10^{-22}$  Pa at 1000 K. A prior MBE work used an iridium crucible to contain  $\text{Ga}_2\text{O}_3(\text{s})$  because of the reactivity of  $\text{Ga}_2\text{O}_3$  at high temperatures (in excess of 1900 K) needed to grow  $\text{Ga}_2\text{O}_3$  films by MBE from a pure  $\text{Ga}_2\text{O}_3(\text{s})$  source.<sup>101,102</sup> This temperature is considerably higher than that expected from Fig. S27 to yield a  $\text{Ga}_2\text{O}(\text{g})$  partial pressure of  $10^{-1}$  Pa ( $\sim 1500$  K is expected). Using a 5:1 mixture of Ga: $\text{Ga}_2\text{O}_3$  decreases the temperature of the crucible, i.e., the temperature needed to reach the same vapor pressure of  $\text{Ga}_2\text{O}(\text{g})$ , by about  $500^\circ\text{C}$ .<sup>38</sup> A more recent MBE study shows similar temperature lowering for a 3.8:1 mixture of Ga: $\text{Ga}_2\text{O}_3$ .<sup>39</sup> Exploiting molecular beams of suboxides such as  $\text{Ga}_2\text{O}(\text{g})$  to grow films of compounds such as  $\text{Ga}_2\text{O}_3(\text{s})$  is a powerful alternative to conventional MBE with many advantages; this approach is termed suboxide-MBE (S-MBE).<sup>93</sup>

### 3. $\text{TeO}_2$ (Fig. S70)

$\text{TeO}_2$  thin films have applications as gamma radiation detectors due to their sensitivity to gamma radiation. Sudha *et al.*<sup>103</sup> thermally evaporated  $\text{TeO}_2$  powder onto a glass substrate at  $10^{-3}$  Pa to form  $\text{TeO}_2$  amorphous thin films for gas sensing; these amorphous films could be subsequently annealed to make them crystalline. The congruent evaporation behavior reported in Sudha *et al.*'s work<sup>103</sup>

disagrees with the incongruent evaporation calculated in the present study of  $\text{TeO}_2(\text{s})$  sublimation to  $\text{Te}_2\text{O}_2(\text{s})$  at 760 K–892 K, although  $\text{TeO}_2(\text{s})$  is the dominant gas species below 760 K (Fig. S70). Unfortunately, Sudha *et al.*<sup>103</sup> did not provide a temperature for the thermal evaporation of the  $\text{TeO}_2$  powder to allow for comparison between their work and the present study. Additionally, Fig. S70 shows that the vapor pressures of  $\text{Te}_2\text{O}_2$ ,  $\text{TeO}_2$ , and  $\text{Te}_2\text{O}_4$  gas species decrease at temperatures above 913 K, while the vapor pressures of the other gas species continue to increase based on the present thermodynamic calculations.<sup>27</sup>

### 4. Rare-earth (RE) oxides

The present calculations (see the figures in the [supplementary material](#)) indicate that the majority of the rare-earth oxides share a similar evaporation behavior that is described below. The majority are most stable in sesquioxide form and provide molecular beams of stoichiometric REO ( $RE = \text{rare earth}$ ), making them incongruent evaporation sources for MBE. There are, however, a few exceptions where the gas-phase species with the highest partial pressure is RE or  $\text{REO}_2$ :

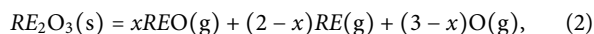
- **Supply REO:**  $\text{Sc}_2\text{O}_3$ ,  $\text{La}_2\text{O}_3$ ,  $\text{Ce}_2\text{O}_3$  (and  $\text{CeO}_2$ ),  $\text{Pr}_2\text{O}_3$ ,  $\text{Nd}_2\text{O}_3$ ,  $\text{Pm}_2\text{O}_3$ ,  $\text{Sm}_2\text{O}_3$ ,  $\text{Gd}_2\text{O}_3$ ,  $\text{Tb}_2\text{O}_3$ ,  $\text{Dy}_2\text{O}_3$ ,  $\text{Er}_2\text{O}_3$ , and  $\text{Lu}_2\text{O}_3$ .
- **Supply RE:**  $\text{Eu}_2\text{O}_3$  (and  $\text{EuO}$ ),  $\text{Tm}_2\text{O}_3$ , and  $\text{Yb}_2\text{O}_3$ .
- **Supply  $\text{REO}_2$ :**  $\text{Y}_2\text{O}_3$ .

*a. Lanthanides with 2+ valence (Fig. S24).*  $\text{EuO}(\text{s})$ ,  $\text{SmO}(\text{s})$ , and  $\text{YbO}(\text{s})$  are known to be stable as  $\text{RE}^{2+}$  ions in addition to their sesquioxide forms.  $\text{EuO}(\text{s})$  is calculated to produce a beam of Eu metal when heated as is its sesquioxide counterpart,  $\text{Eu}_2\text{O}_3(\text{s})$ ; see Fig. S24. Unfortunately, thermodynamic calculations for  $\text{SmO}(\text{s})$  and  $\text{YbO}(\text{s})$  as oxide MBE sources could not be performed because they are not included in the SSUB5 database.<sup>27</sup> Experimentally,  $\text{YbO}$  thin films have been grown by MBE, although using separate beams of ytterbium and  $\text{O}_2$  to deposit  $\text{YbO}$ .<sup>104</sup> The same is true for the

growth of EuO by MBE: from separate beams of europium and O<sub>2</sub>.<sup>105–107</sup>

*b. Rare-earth sesquioxides.* Many of these rare-earth sesquioxides have been investigated as high-*K* gate dielectrics for use in metal–oxide–semiconductor field-effect transistors (MOSFETs) because of their high dielectric constant, large bandgap, and thermodynamic stability in contact with silicon.<sup>108–112</sup> To investigate these rare-earth sesquioxides as a replacement for SiO<sub>2</sub> in MOSFETs, researchers have used MBE to deposit Sc<sub>2</sub>O<sub>3</sub>, Y<sub>2</sub>O<sub>3</sub>, La<sub>2</sub>O<sub>3</sub>, Pr<sub>2</sub>O<sub>3</sub>, Nd<sub>2</sub>O<sub>3</sub>, Gd<sub>2</sub>O<sub>3</sub>, and Lu<sub>2</sub>O<sub>3</sub> films on silicon from solid oxide sources of these same materials, i.e., from Sc<sub>2</sub>O<sub>3</sub>(s),<sup>113</sup> Y<sub>2</sub>O<sub>3</sub>(s),<sup>114</sup> La<sub>2</sub>O<sub>3</sub>(s),<sup>108</sup> Pr<sub>6</sub>O<sub>11</sub>(s),<sup>115,116</sup> Nd<sub>2</sub>O<sub>3</sub>(s),<sup>117</sup> Gd<sub>2</sub>O<sub>3</sub>(s),<sup>108,114,118</sup> to Lu<sub>2</sub>O<sub>3</sub>(s).<sup>108</sup>

The evaporation behavior of the majority of the sesquioxides proceeds as follows based on high-temperature Knudsen effusion mass spectrometry:<sup>119</sup>



where  $0 < x < 2$ . The present calculations show that this evaporation behavior is exhibited by all rare-earth oxides except for Eu<sub>2</sub>O<sub>3</sub> (and EuO), Tm<sub>2</sub>O<sub>3</sub>, Yb<sub>2</sub>O<sub>3</sub>, and Y<sub>2</sub>O<sub>3</sub>.

For Sc<sub>2</sub>O<sub>3</sub> (Fig. S61), Y<sub>2</sub>O<sub>3</sub> (Fig. S78), La<sub>2</sub>O<sub>3</sub> (Fig. S36), Ce<sub>2</sub>O<sub>3</sub> (Fig. S14), Pr<sub>2</sub>O<sub>3</sub> (Fig. S53), Nd<sub>2</sub>O<sub>3</sub> (Fig. S44), Pm<sub>2</sub>O<sub>3</sub> (Fig. S52), Sm<sub>2</sub>O<sub>3</sub> (Fig. S64), Gd<sub>2</sub>O<sub>3</sub> (Fig. S28), Tb<sub>2</sub>O<sub>3</sub> (Fig. S68), Dy<sub>2</sub>O<sub>3</sub> (Fig. S21), Er<sub>2</sub>O<sub>3</sub> (Fig. S22), and Lu<sub>2</sub>O<sub>3</sub> (Fig. S38), our thermodynamic calculations indicate that all of these rare-earth sesquioxides should provide molecular beams of REO(g) when heated to a temperature where the dominant species in the gas phase has a vapor pressure of 10<sup>-1</sup> Pa, i.e., the vapor pressure needed for typical oxide MBE growth. Unfortunately, the temperatures needed according to our vapor pressure calculations are near the limit of effusion cells for many of these RE<sub>2</sub>O<sub>3</sub>(s) sources, making it appropriate to use an e-beam evaporator or laser thermal evaporator to produce REO(g) molecular beams with source longevity.<sup>120</sup>

Stolyarova *et al.*<sup>22,121</sup> listed YO(g) as the dominant vapor constituent of thermally evaporated Y<sub>2</sub>O<sub>3</sub>(s). In the present calculations (Fig. S78), however, YO<sub>2</sub>(g) is shown to be the dominant gas species when a Y<sub>2</sub>O<sub>3</sub> source is heated in the temperature range of 1980 K < *T* < 2680 K, and YO(g) becomes the dominant vapor constituent when *T* > 2680 K. By omitting YO<sub>2</sub>(g), YO(g) will be the dominant vapor constituent when *T* > 2370 K (Fig. S78). From the present study of the Y–O system, we note that calculations that disagree with experiments could be because certain gas species are added or omitted from the oxide systems in the SSUB5 database.<sup>27</sup> This is also seen in other systems such as the Pb–O system where the Pb<sub>*n*</sub>O<sub>*n*</sub> species are omitted from the SSUB5 database but included in the analysis by Lamoreaux *et al.*<sup>26</sup>; see Sec. III A 5.

For Eu<sub>2</sub>O<sub>3</sub> (and EuO), the present calculations (Fig. S24) reveal that Eu<sub>2</sub>O<sub>3</sub>(s) and EuO(s) should evaporate as Eu(g), which offers no advantage in using oxide sources over elemental europium. The advantage of europium metal is that it can be melted into the crucible to provide a dense fill with good thermal contact to the crucible (and surrounding thermocouple). Elemental europium has been used in oxide MBE for the growth of EuTiO<sub>3</sub><sup>122</sup> and EuO.<sup>105–107</sup>

For Tm<sub>2</sub>O<sub>3</sub>, no literature on the evaporation behavior of Tm<sub>2</sub>O<sub>3</sub> could be found to corroborate that Tm<sub>2</sub>O<sub>3</sub> evaporates as a gas of the elemental metal thulium. If this is the case, a Tm<sub>2</sub>O<sub>3</sub> source would offer no advantage over using elemental thulium metal as an MBE source (see Fig. S74).

Following a recent publication by Hoffmann *et al.*,<sup>39</sup> we also examined the gas species as a function of temperature for a two-phase mixture of RE<sub>2</sub>O<sub>3</sub> + RE that has an overall composition of REO. It is shown that the dominant gas species is in general RE(g) and the second dominant gas species is REO(g); see Table S2 and associated figures, including those for the two-phase mixture case with cerium (Fig. S14), dysprosium (Fig. S21), erbium (Fig. S22), europium (Fig. S24), gadolinium (Fig. S28), holmium (Fig. S32), lanthanum (Fig. S36), lutetium (Fig. S38), neodymium (Fig. S44), promethium (Fig. S52), praseodymium (Fig. S53), samarium (Fig. S64), terbium (Fig. S68), thulium (Fig. S74), and ytterbium (Fig. S79). At high temperatures, REO(g) is calculated to be the most dominant gas species, for example, *T* > 1136 K for CeO(g), *T* > 1308 K for LaO(g), and *T* > 2239 K for PrO(g). For other RE elements, however, the temperatures are extremely high (>>3000 K) in order to make the dominant gas species REO(g).

### C. Metastable solid oxide with nearly congruent evaporation

Table III summarizes the metastable oxides that evaporate nearly congruently based on the present calculations. Of these, the oxides IrO<sub>2</sub>, PtO<sub>2</sub>, and RuO<sub>2</sub> would give the most advantage because their stable counterparts are elemental metals (iridium, platinum, and ruthenium) meaning no other solid (or liquid) binary oxide sources are available to create molecular beams of these oxides. Similar to Table I, Table III also lists the temperature range for nearly congruent evaporation defined by  $|\Delta x(O_2)| < 0.01$ ; see Eq. (1).

The concern with using metastable oxides as source materials for MBE is that these compounds could decompose into more stable compounds and in the process pollute the MBE vacuum with O<sub>2</sub> species. For metastable oxides, there are two scenarios that can occur when the oxide is heated, which depend on the kinetics of the compound as discussed in Sec. II A. The kinetics of oxide decomposition is beyond the scope of the present work, but a literature search has been conducted for experimental evidence of the successful use of metastable oxides in MBE; the details are described below. Furthermore, the decomposition of RuO<sub>2</sub> has been studied in the present work by differential thermal analysis with simultaneous thermogravimetry (DTA/TG) to follow the decomposition process under conditions approaching those in the high-vacuum MBE environment.

#### 1. Cs<sub>2</sub>O (Fig. S19)

Figure S19 shows that Cs<sub>2</sub>O(s) is a metastable phase, but it evaporates nearly congruently in the temperature range of 705 K–1059 K due to the value of  $|\Delta x(O_2)| < 0.01$  [see Eq. (1)]; see Table III.

#### 2. SiO (Fig. S63) and GeO (Fig. S29)

From Table II, it can be seen that the evaporation of SiO<sub>2</sub> and GeO<sub>2</sub> is incongruent and provides molecular beams of SiO and GeO,

**TABLE III.** Metastable sources under the following conditions:  $P_{O_2} = 10^{-4}$ , fixed gas phase at zero amount, fixed  $T$ , and  $n(M) = 1$  mol, which evaporate nearly congruently.

Element	Solid oxide source	Dominant gas species	Stable oxide <sup>a</sup>	$T$ -range <sup>b</sup>	$T$ -range <sup>c</sup>
As	As <sub>2</sub> O <sub>3</sub>	As <sub>4</sub> O <sub>6</sub>	As <sub>2</sub> O <sub>5</sub>	611–677 <sup>d</sup>	650–1278
Cs	Cs <sub>2</sub> O	Cs <sub>2</sub> O	CsO <sub>2</sub>	612–1476	705–1059
Ge	GeO	GeO	GeO <sub>2</sub>	>1290	>1595
Ir	IrO <sub>2</sub>	IrO <sub>2</sub>	Ir	1260–1520	1390–1425
Nb	NbO <sub>2</sub>	NbO <sub>2</sub>	Nb <sub>2</sub> O <sub>5</sub> ( $\ell$ )	1550–2590	1768–2283
Os	OsO <sub>4</sub>	OsO <sub>4</sub>	OsO <sub>2</sub>	200–1000	200–1000
Pt	PtO <sub>2</sub>	PtO <sub>2</sub>	Pt	846–1253	915–1156
Re	ReO <sub>3</sub> <sup>e</sup>	Re <sub>2</sub> O <sub>6</sub>	Re <sub>2</sub> O <sub>7</sub>	>848	>around 850
Ru	RuO <sub>2</sub>	RuO <sub>2</sub>	Ru	1220–1480	1326–1368
Sb	Sb <sub>2</sub> O <sub>3</sub>	Sb <sub>2</sub> O <sub>3</sub>	SbO <sub>2</sub>	>528	555–1391
Si	SiO	SiO	SiO <sub>2</sub>	>1320	1556–2983
Sn	SnO	SnO	SnO <sub>2</sub>	>889	983–1750
Ti	TiO <sub>2</sub> anatase	TiO <sub>2</sub>	Ti <sub>4</sub> O <sub>7</sub> ( $\ell$ )	1790–2220	1914–2007
Ti	TiO <sub>2</sub> rutile	TiO <sub>2</sub>	Ti <sub>4</sub> O <sub>7</sub> ( $\ell$ )	1800–2220	1952–2025
U	UO <sub>3</sub>	U <sub>2</sub> O <sub>6</sub>	U <sub>3</sub> O <sub>8</sub>	>517	544–1900
V	V <sub>2</sub> O <sub>5</sub>	V <sub>4</sub> O <sub>10</sub>	V <sub>2</sub> O <sub>4</sub>	804–2116	838–2092

<sup>a</sup>Stable oxide phase under given conditions.<sup>b</sup>Temperature range (in K) where the oxide gas species is dominant.<sup>c</sup>Temperature range (in K) of nearly congruent evaporation as defined by Eq. (1) for an absolute value of  $\Delta x(O_2) < 0.01$ .<sup>d</sup>Liquid As<sub>2</sub>O<sub>3</sub> is stable at  $T > 677$  K and is an ideal MBE source (see Table I).<sup>e</sup>Thermodynamic calculations of ReO<sub>3</sub>(s) were performed at  $P_{O_2} = 10^{-15}$  Pa where its gas phase is metastable, a requirement for our calculations under the constraint that the fixed gas phase has zero amount. This zero amount requirement is not satisfied for ReO<sub>3</sub>(s) at  $P_{O_2} = 10^{-4}$  Pa.

respectively. Unfortunately, these latter monoxides are not in the SSUB5 database.<sup>27</sup> Amorphous SiO(am) is well-known to evaporate nearly congruently,<sup>22–24</sup> its thermodynamic properties<sup>30</sup> were added to the database in the present work. In addition, the enthalpy of formation of the amorphous GeO(am)<sup>29</sup> was also added. The fact that SiO(am) evaporates nearly congruently makes it of interest for synthesizing Si<sup>2+</sup>-based compounds in MBE, and GeO(am) behaves similarly to SiO(am) and could be a route to Ge<sup>2+</sup>-based compounds.

Figure S63 illustrates the evaporation behavior of SiO(am) calculated at  $P_{O_2} = 10^{-4}$  Pa, showing that SiO(am) gives off SiO<sub>2</sub>(g) species at low temperatures (below 1320 K) and SiO(g) species at higher temperatures (above 1320 K). Stoichiometric SiO has been found to evaporate from an SiO(am) source at temperatures in the vicinity of 1520 K in high vacuum ( $\sim 10^{-6}$  Pa),<sup>23,24</sup> which is consistent with the results shown in Fig. S63. When the evaporation behavior of SiO(am) is calculated under a stronger vacuum such as  $P_{O_2} = 10^{-15}$  Pa, the SiO gas species becomes dominant at lower temperatures (above 990 K) than it does in lower vacuum (e.g., 1320 K as mentioned above). Stolyarova and Semenov<sup>22</sup> indicated that SiO(am) evaporates congruently in a Knudsen cell experiment between 1175 K and 1410 K. This is confirmed by the present calculations. Should an interesting Si-containing multicomponent oxide warrant investigation, SiO(am) could be used to provide a molecular beam of SiO(g). One system that might be relevant is the growth of Si-doped Ga<sub>2</sub>O<sub>3</sub>, where the high oxidant pressures involved in the growth of Ga<sub>2</sub>O<sub>3</sub> result in the oxidation of the surface of the traditional Si(s) doping sources used in MBE.<sup>34</sup> This oxidation results in

the flux emanating from a Si(s) source to change rapidly over time, impeding the use of silicon as a dopant in the growth of oxides by MBE.

The calculated evaporation from a two-phase mixture of SiO<sub>2</sub> + Si with an overall composition SiO (Fig. S63) indicates that SiO(g) is the dominant gas species in the temperature range of study (see also Table S2) in agreement with a recent report.<sup>39</sup> Similar to the Si–O case, GeO<sub>2</sub>(s) is the stable phase up to 872 K, beyond which GeO(am) becomes stable based on the SSUB5 database and the enthalpy of formation of GeO(am) from the literature;<sup>29</sup> see also the note in the figure caption of Fig. S29. GeO(g) is the dominant gas species when the solid/liquid source is GeO<sub>2</sub>(s), GeO(am), or a two-phase mixture of GeO<sub>2</sub> + Ge (see also Table S2). Our conclusions for the GeO<sub>2</sub> + Ge mixture are in good agreement with the thermodynamic calculations by Hoffmann *et al.*<sup>39</sup>

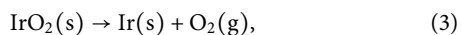
### 3. IrO<sub>2</sub>, PtO<sub>2</sub>, and RuO<sub>2</sub> (Figs. S34, S54, and S59)

IrO<sub>2</sub>(s) and RuO<sub>2</sub>(s) are of particular interest for oxide MBE because in elemental form, Ir(s) and Ru(s) sources have such low vapor pressures that today's MBE effusion cells are unable to evaporate them. Solid iridium and ruthenium can be evaporated by electron-beam evaporation sources, but the stability of the flux from an electron-beam evaporator is inferior to the flux stability provided by effusion cells. IrO<sub>2</sub> and RuO<sub>2</sub> are components of materials with a multitude of interesting properties and electronic structures due to the high spin–orbit coupling and electron correlations present in materials containing these constituents. Examples

include the unconventional superconductor  $\text{Sr}_2\text{RuO}_4$ ,<sup>123</sup> the itinerant metamagnet  $\text{Sr}_3\text{Ru}_2\text{O}_7$ ,<sup>124</sup> features in the electronic structure of doped  $\text{Sr}_2\text{IrO}_4$  that are akin to the cuprate high-temperature superconductors,<sup>125</sup> the magnetically ordered Mott insulator  $\text{Na}_2\text{IrO}_3$ ,<sup>126</sup> Weyl semimetals in the  $\text{RE}_2\text{Ir}_2\text{O}_7$  pyrochlores,<sup>127</sup> and heterostructures containing these materials that could, for example, host a two-dimensional gas of magnetic monopoles.<sup>128</sup> MBE sources that provided stable fluxes of  $\text{IrO}_2$  and  $\text{RuO}_2$  could thus greatly enhance the ability of oxide MBE to create iridates and ruthenates that are customized with atomic-layer precision.

$\text{IrO}_2$  and  $\text{RuO}_2$  are commercially available powders, so it is important to investigate these oxides even though they are metastable under MBE deposition conditions. In the present calculations, metastable  $\text{IrO}_2$  and  $\text{RuO}_2$  are found to evaporate nearly congruently as shown in Figs. S34 and S59, respectively.  $\text{IrO}_2$  and  $\text{RuO}_2$  thin films have been fabricated using MBE; however, they were made using elemental iridium or ruthenium sources heated by an electron-beam evaporator with oxidation provided by a separate molecular beam of ozone.<sup>129,130</sup> No literature was found on the evaporation of  $\text{RuO}_2$  or the use of  $\text{RuO}_2$  as a source in oxide MBE.

The suitability of  $\text{IrO}_2$  and  $\text{RuO}_2$  to create molecular beams depends on the kinetics of their decomposition as discussed in Sec. II A. For example,  $\text{IrO}_2$  could follow two scenarios when heated in the MBE crucible,



The first scenario, Eq. (3), shows  $\text{IrO}_2(\text{s})$  decomposition into  $\text{Ir}(\text{s})$  and  $\text{O}_2(\text{g})$ , which would pollute the MBE chamber with oxygen species. The  $\text{Ir}(\text{s})$  species would then evaporate with the partial pressures of the gas species shown in Fig. S34. If this first pathway is relevant,  $\text{IrO}_2(\text{s})$  as an MBE source offers no advantages (and many disadvantages) over an elemental  $\text{Ir}(\text{s})$  source. In the second scenario, Eq. (4), as  $\text{IrO}_2(\text{s})$  is heated up, it evaporates  $\text{IrO}_2(\text{g})$  as shown in Fig. S34. These  $\text{IrO}_2(\text{g})$  species would be emitted as a molecular beam, which would travel to the substrate in the MBE chamber. In this latter case, the  $\text{IrO}_2(\text{g})$  species would be depleted at the surface of the  $\text{IrO}_2(\text{s})$  source as it evaporates. To restore equilibrium, the  $\text{IrO}_2$  species would produce more  $\text{IrO}_2(\text{g})$ . In this second scenario, the  $\text{IrO}_2(\text{s})$  species evaporates into  $\text{IrO}_2(\text{g})$  much faster than it decomposes; for oxide MBE, this would be the preferred kinetic pathway to make  $\text{IrO}_2(\text{s})$  a viable MBE source material. Another thing to consider is the energy required to break  $\text{IrO}_2(\text{s})$  into  $\text{Ir}(\text{s})$  and  $\text{O}_2(\text{g})$ . If the activation barrier is high, it would be much more likely for  $\text{IrO}_2(\text{s})$  to evaporate as  $\text{IrO}_2$ , where only intermolecular bonds have to be broken. In addition to metastable  $\text{IrO}_2$  and  $\text{RuO}_2$ , the present calculations (Fig. S54 and Table III) also indicate that metastable  $\text{PtO}_2$  evaporates nearly congruently in the temperature range of 915 K–1156 K at  $P_{\text{O}_2} = 10^{-4}$  Pa.

As  $\text{IrO}_2$ ,  $\text{PtO}_2$ , and  $\text{RuO}_2$  share the chemical similarity of all being 4+ oxides of platinumoids, we performed some preliminary experiments on one of these compounds,  $\text{RuO}_2(\text{s})$ , and found that it decomposes before it evaporates. Specifically, our experiments indicate that when heated,  $\text{RuO}_2(\text{s})$  undergoes the reaction  $2\text{RuO}_2(\text{s}) \rightarrow \text{Ru}_2\text{O}_3(\text{s}) + \frac{1}{2}\text{O}_2(\text{g})$ . The predominant species that  $\text{RuO}_2(\text{s})$  gives

off when heated is thus  $\text{O}_2(\text{g})$ , making it not useful as an MBE source. Figure 5 shows two thermogravimetric (TG) measurements where  $\text{RuO}_2(\text{s})$  was heated under ambient pressure in an  $\text{Ar}/\text{O}_2$  mixture or in nominally pure Ar with 99.9999%–99.9999% purity, which results in the stated oxygen partial pressures.<sup>131</sup> Between room temperature and 773 K, the changes in the first TG step occur, corresponding to  $\Delta m/m = -5.7\%$  (oxidizing atmosphere) or  $-6.0\%$  (Ar). These observed mass changes would be consistent with the reaction  $2\text{RuO}_2(\text{s}) \rightarrow \text{Ru}_2\text{O}_3(\text{s}) + \frac{1}{2}\text{O}_2(\text{g})$ , where  $\Delta m/m$  of the condensed phases would be  $-6.0\%$ . The decomposition of the remainder becomes significant above 1273 K–1370 K. Since  $\text{Ru}_2\text{O}_3(\text{s})$  is not in the SSUB5 thermodynamic database, this reaction is not predicted by our thermodynamic calculations. Nonetheless,  $\text{Ru}^{3+}$  is reported in halides, such as  $\text{RuF}_3$  and  $\text{RuCl}_3$ , as well as in the oxide  $\text{LaRuO}_3$ .<sup>132</sup>

#### 4. $\text{NbO}_2$ (Fig. S43)

$\text{NbO}_2$  has been shown to have  $\text{NbO}_2$  species in the gas phase when evaporated from a Knudsen cell at 2050 K.<sup>22</sup> Having  $\text{NbO}_2$  as the dominant species in the gas phase is expected regardless of whether evaporation occurs from metastable  $\text{NbO}_2(\text{s})$  or from the stable phase,  $\text{Nb}_2\text{O}_5(\ell)$ , at 2050 K. The present work (Fig. S43 and Table III) predicts that (metastable)  $\text{NbO}_2$  evaporates nearly congruently between 1768 K and 2283 K at  $P_{\text{O}_2} = 10^{-4}$  Pa.  $\text{NbO}_2$  has useful metal-to-insulator transition electronic properties motivating its growth by MBE.<sup>133</sup>  $\text{NbO}_2(\text{s})$  could be a viable source for the growth of  $\text{NbO}_2$  thin films and is worth trying as an MBE source.

#### 5. $\text{ReO}_3$ (Fig. S57)

$\text{ReO}_3(\text{s})$  is a metastable phase in the Re–O system, and it is expected that it could evaporate nearly congruently. In our thermodynamic calculations using  $P_{\text{O}_2} = 10^{-4}$  Pa, however, the gas phase does not satisfy the requirement of having zero amount. So we performed ancillary thermodynamic calculations of  $\text{ReO}_3(\text{s})$  at a very

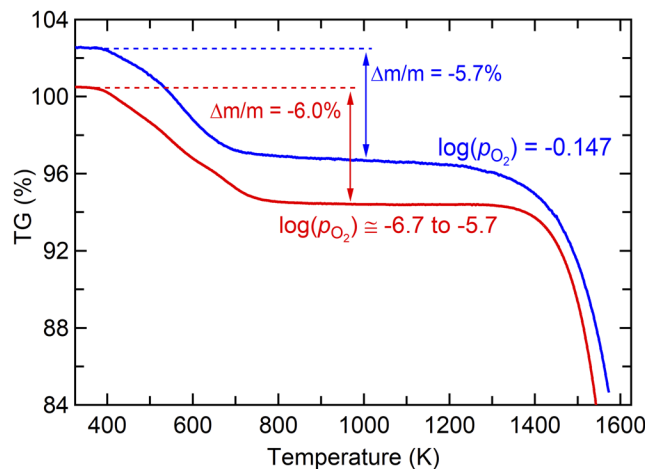


FIG. 5. Thermogravimetric (TG) curves of  $\text{RuO}_2(\text{s})$  heated in 71%  $\text{O}_2 + 29\%$  Ar (blue curve) or in “pure” Ar (red curve). Here,  $P_{\text{O}_2}$  indicates the oxygen partial pressure in atm and  $\Delta m/m$  shows the mass change in the TG curves.

**TABLE IV.** Metastable oxide sources under the following conditions:  $P_{O_2} = 10^{-4}$ , fixed gas phase at zero amount, fixed  $T$ , and  $n(M) = 1$  mol, which evaporate incongruently.

Element	Solid oxide source	Dominant gas species	Stable oxide <sup>a</sup>	$T$ -range (K) <sup>b</sup>
Cs	Cs <sub>2</sub> O <sub>2</sub>	Cs <sub>2</sub> O	CsO <sub>2</sub>	612–1030
Cs	Cs <sub>2</sub> O <sub>3</sub>	Cs <sub>2</sub> O	CsO <sub>2</sub>	612–880
Ce	CeO <sub>2</sub>	CeO	Ce <sub>2</sub> O <sub>3</sub>	1880–2990
Pr	PrO <sub>2</sub>	Pr <sub>2</sub> O	Pr <sub>2</sub> O <sub>3</sub>	1600–2900
Pr	Pr <sub>7</sub> O <sub>12</sub>	Pr <sub>3</sub> O	Pr <sub>2</sub> O <sub>3</sub>	1880–3000
Pr	Pr <sub>6</sub> O <sub>11</sub>	Pr <sub>4</sub> O	Pr <sub>2</sub> O <sub>3</sub>	1650–2920
Tb	TbO <sub>2</sub>	TbO	Tb <sub>2</sub> O <sub>3</sub>	1790–2500
Ta	Ta <sub>2</sub> O <sub>5</sub>	TaO <sub>2</sub>	Ta <sub>2</sub> O <sub>5</sub> liquid	2020–2740
Pb	Pb <sub>2</sub> O <sub>3</sub>	PbO	PbO yellow	700–1034
Pb	Pb <sub>3</sub> O <sub>4</sub>	PbO <sub>2</sub>	PbO yellow	700–1034
Pb	PbO <sub>2</sub>	PbO	PbO yellow	700–950

<sup>a</sup>Stable oxide phase under given conditions.<sup>b</sup>Temperature range where the oxide gas species is dominant.

low oxygen partial pressure of  $P_{O_2} = 10^{-15}$  Pa. The results of these calculations, shown in Fig. S57, indicate that ReO<sub>3</sub>(s) is a metastable oxide that evaporates nearly congruently at  $P_{O_2} = 10^{-15}$  Pa, i.e., the dominant gas species is Re<sub>2</sub>O<sub>6</sub> when  $T > 848$  K; see also Table III. It is expected that ReO<sub>3</sub>(s) could be a viable source for the growth of ReO<sub>3</sub> thin films albeit our calculations were performed at  $P_{O_2} = 10^{-15}$  Pa. ReO<sub>3</sub> is also discussed in Sec. III A 8.

### 6. TiO<sub>2</sub> (Fig. S72)

TiO<sub>2</sub> has been shown to evolve TiO species when evaporated from a Knudsen cell at 1920 K.<sup>22</sup> This result is unexpected from our thermodynamic calculations. If the initial TiO<sub>2</sub> loaded into the Knudsen cell decomposes into the stable phase, on heating to 1920 K, it would be Ti<sub>4</sub>O<sub>7</sub>(s) and the dominant species evaporated at 1920 K would be TiO<sub>2</sub>(g). On the other hand, if TiO<sub>2</sub> loaded into the Knudsen cell remained in the metastable rutile polymorph at 1920 K, then the dominant species evaporated at 1920 K would also be TiO<sub>2</sub>(g). Our calculations only show TiO to be the dominant vapor species at temperatures above 2220 K for both anatase and rutile TiO<sub>2</sub>, which are both metastable at this temperature, at the  $10^{-4}$  Pa O<sub>2</sub> partial pressure of the present work; see Fig. S72 as well as Table III.

### 7. UO<sub>3</sub> (Fig. S75)

Solid UO<sub>3</sub>(s) is a stable phase when  $T < 525$  K; at higher temperatures, the solid U<sub>3</sub>O<sub>8</sub>(s) becomes stable ( $>525$  K). Figure S75 shows that U<sub>2</sub>O<sub>6</sub>(g) is the dominant gas species at temperatures  $T > 517$  K and  $P_{O_2} = 10^{-4}$  Pa [O<sub>2</sub>(g) is dominant at  $T < 517$  K]. Although U<sub>2</sub>O<sub>6</sub>(g) is the dominant species in the gas phase, the value of  $|\Delta x(O_2)| > 0.01$  [see Eq. (1)] in the temperature range of 517 K–525 K due to the nonnegligible concentration of other species in the gas phase. This disqualifies UO<sub>3</sub>(s) as an ideal MBE source from the definition of nearly congruent evaporation that we have used. It is worth mentioning that at an extremely low partial pressure of O<sub>2</sub>(g), such as  $P_{O_2} = 10^{-15}$  Pa, it is possible to make  $|\Delta x(O_2)| < 0.01$  for UO<sub>3</sub>(s).

As a metastable phase, the present calculations show that UO<sub>3</sub>(s) evaporates nearly congruently in the temperature range of 544 K–1900 K at  $P_{O_2} = 10^{-4}$  Pa; see Table III.

### D. Metastable solid oxide with incongruent evaporation

Table IV shows the metastable oxide sources that exhibit incongruent evaporation. Based on the dominant species in the molecular beams from the stable sources that exhibit incongruent evaporation, these metastable oxides are calculated in the present work to see if they would exhibit nearly congruent evaporation. Unfortunately, they all exhibit incongruent evaporation as can be seen in the calculated figures in the supplementary material. Specifically, see Fig. S14 for the binary oxides containing cerium, Fig. S19 for those containing cesium, Fig. S50 for those containing lead, Fig. S53 for those containing praseodymium, Fig. S67 for those containing tantalum, and Fig. S68 for those containing terbium. These metastable incongruent evaporants offer no advantage over their stable incongruent evaporant counterparts and hence are not discussed further.

## IV. SUMMARY

A comprehensive thermodynamic investigation regarding the evaporation behavior of 128 binary oxides has been performed to evaluate their suitability as MBE source materials. Based mainly on the SSUB5 database used in the present work,<sup>27</sup> we conclude that 16 solid or liquid oxides are most ideal for MBE, i.e., As<sub>2</sub>O<sub>3</sub>, B<sub>2</sub>O<sub>3</sub>, BaO, MoO<sub>3</sub>, OsO<sub>4</sub>, P<sub>2</sub>O<sub>5</sub>, PbO, PuO<sub>2</sub>, Rb<sub>2</sub>O, Re<sub>2</sub>O<sub>7</sub>, Sb<sub>2</sub>O<sub>3</sub>, SeO<sub>2</sub>, SnO, ThO<sub>2</sub>, Tl<sub>2</sub>O, and WO<sub>3</sub>. Of these, As<sub>2</sub>O<sub>3</sub>, B<sub>2</sub>O<sub>3</sub>, BaO, MoO<sub>3</sub>, PbO, Sb<sub>2</sub>O<sub>3</sub>, and WO<sub>3</sub> have been utilized to date as MBE source materials. The remaining nine oxides await verification as good oxide source materials in MBE. The use of PbO(s) as a source material may be limited by the allowable O<sub>2</sub> partial pressure in the MBE chamber. Of the solid oxide sources that show incongruent evaporation, SnO<sub>2</sub> has been shown to work experimentally and produces

H																			He
Li	Be											B	C	N	O	F		Ne	
Na	Mg											Al	Si	P	S	Cl		Ar	
K	Ca	Sc	Ti	V	Cr	Mn	Fe	Co	Ni	Cu	Zn	Ga	Ge	As	Se	Br		Kr	
Rb	Sr	Y	Zr	Nb	Mo	Tc	Ru	Rh	Pd	Ag	Cd	In	Sn	Sb	Te	I		Xe	
Cs	Ba		Hf	Ta	W	Re	Os	Ir	Pt	Au	Hg	Tl	Pb	Bi	Po	At		Rn	
Fr	Ra																		
			La	Ce	Pr	Nd	Pm	Sm	Eu	Gd	Tb	Dy	Ho	Er	Tm	Yb		Lu	
			Ac	Th	Pa	U	Np	Pu	Am	Cm	Bk	Cf	Es	Fm	Md	No		Lr	

Congruent evaporation from stable source	Incongruent evaporation from metastable source
Incongruent evaporation from stable source	Mainly metal evaporated from metastable source
Mainly metal evaporated from stable source	No thermodynamic data for oxides in SSUB5
Congruent evaporation from metastable source	Not calculated

**FIG. 6.** Periodic table summarizing the evaporation behavior of binary oxides. Note that congruent evaporation is indicated whenever at least one of the oxides of a particular element evaporates nearly congruently (as defined in the text).

a molecular beam of mainly SnO(g). Although they do not meet the third criterion to be ideal MBE sources (i.e., nearly congruent evaporation; see Sec. II C), some oxides that meet the first criterion (i.e., solid or liquid metal-oxide source that is stable under the given conditions; see Sec. II C) may also work as oxide MBE source materials, like SnO<sub>2</sub> does. The amorphous and metastable phase SiO(s) is known to evaporate before it decomposes, making it suitable as an MBE source. The same may be true for other metastable phases including amorphous GeO(s) and SnO(s). Finally, a likely route to achieve the desired nearly congruent evaporation characteristic of an ideal MBE source—a characteristic that keeps the fluxes of the species in the molecular beams constant, because the composition of the source itself is not changing over the life of the source—is to use a two-phase mixture. Potential MBE sources of this mixture type are, for example, (Al<sub>2</sub>O<sub>3</sub> + Al) to produce a molecular beam of Al<sub>2</sub>O(g), (Ce<sub>2</sub>O<sub>3</sub> + Ce) to produce CeO(g), (Ga<sub>2</sub>O<sub>3</sub> + Ga) to produce Ga<sub>2</sub>O(g), (GeO<sub>2</sub> + Ge) to produce GeO(g), (HfO<sub>2</sub> + Hf) to produce HfO(g), (In<sub>2</sub>O<sub>3</sub> + In) to produce In<sub>2</sub>O(g), (La<sub>2</sub>O<sub>3</sub> + La) to produce LaO(g), (Pr<sub>2</sub>O<sub>3</sub> + Pr) to produce PrO(g), (SiO<sub>2</sub> + Si) to produce SiO(g), (SnO<sub>2</sub> + Sn) to produce SnO(g), (Ta<sub>2</sub>O<sub>5</sub> + Ta) to produce TaO<sub>2</sub>(g), and (ZrO<sub>2</sub> + Zr) to produce ZrO(g); see the 27 cases examined in Table S2. Our conclusions for two-phase mixtures are in agreement with the recent thermodynamic calculations by Hoffmann *et al.*<sup>39</sup> for Al<sub>2</sub>O(g), Ga<sub>2</sub>O(g), GeO(g), In<sub>2</sub>O(g), LaO(g), PrO(g), SiO(g), and SnO(g). Our predictions also identify four additional two-phase sources of interest for producing molecular beams of CeO(g), HfO(g), TaO<sub>2</sub>(g), and ZrO(g).

Several trends are evident in the evaporation behavior of binary metal oxides. These are shown in Fig. 6. Alkali-metal oxides, alkaline-earth metal oxides, and some of the transition-metal oxides evaporate mainly elemental metal gas species and thus are not ideal for MBE. The rare-earth oxides and some of the transition metals

surrounding them as well as the metalloid oxides exhibit incongruent evaporation. Oxides ideal for MBE are the column IVA oxides SiO, GeO, SnO, and PbO, although the first three of these are metastable (amorphous). In addition, there are disruptions to certain trends such as the evaporation of elemental metals from EuO, Tm<sub>2</sub>O<sub>3</sub>, and Yb<sub>2</sub>O<sub>3</sub>, which do not follow the incongruent evaporation trend of the other rare earths.

## SUPPLEMENTARY MATERIAL

See the [supplementary material](#) for an alphabetical list of 128 solid and liquid oxides together with a list of 17 elements of which the most stable phase is not an oxide (Table S1), a list of 27 two-phase mixtures of a solid (or liquid) of pure element *M* in combination with one of its binary oxides yielding an overall composition of *M<sub>x</sub>O<sub>y</sub>* (Table S2), three illustrative examples of macro files to perform some of the Thermo-Calc calculations presented (Table S3), and an alphabetical list of supplemental figures (Figs. S1–S81) showing the calculated partial pressures of gas species over the phase(s) of interest.

## ACKNOWLEDGMENTS

We acknowledge financial support from the National Science Foundation (NSF) through Grant No. CMMI-1825538 and the Platform for the Accelerated Realization, Analysis and Discovery of Interface Materials (PARADIM) under Cooperative Agreement No. DMR-1539918. B.J.B. was supported by a NASA Space Technology Research Fellowship (Grant No. 80NSSC18K1168). This material is based on the work supported by the Air Force Office of Scientific Research under Award No. FA9550-18-1-0529. D.G.S.

acknowledges stimulating interactions with O. Bierwagen, W. Braun, M. Budde, G. Christiani, R. Droopad, G. Hoffmann, J. P. Maria, and P. Vogt regarding oxide MBE utilizing oxide sources.

## DATA AVAILABILITY

The data that support the findings of this study are available from the corresponding author upon reasonable request.

## REFERENCES

- 1 V. J. Folen, G. T. Rado, and E. W. Stalder, *Phys. Rev. Lett.* **6**, 607 (1961).
- 2 I. Vrejoiu, G. Le Rhun, L. Pintilie, D. Hesse, M. Alexe, and U. Gösele, *Adv. Mater.* **18**, 1657 (2006).
- 3 G. H. Jonker and J. H. Van Santen, *Physica* **16**, 337 (1950).
- 4 A. J. Hauser, R. E. A. Williams, R. A. Ricciardo, A. Genc, M. Dixit, J. M. Lucy, P. M. Woodward, H. L. Fraser, and F. Yang, *Phys. Rev. B* **83**, 014407 (2011).
- 5 H. P. J. Wijn, *Nature* **170**, 707 (1952).
- 6 S.-E. Park and T. R. Shrout, *J. Appl. Phys.* **82**, 1804 (1997).
- 7 J. Wang, *Science* **299**, 1719 (2003).
- 8 A. Schilling, M. Cantoni, J. D. Guo, and H. R. Ott, *Nature* **363**, 56 (1993).
- 9 T. Penney, M. W. Shafer, and J. B. Torrance, *Phys. Rev. B* **5**, 3669 (1972).
- 10 S. Raghavan, T. Schumann, H. Kim, J. Y. Zhang, T. A. Cain, and S. Stemmer, *APL Mater.* **4**, 016106 (2016).
- 11 H. Paik, Z. Chen, E. Lochocki, A. Seidner H., A. Verma, N. Tanen, J. Park, M. Uchida, S. Shang, B.-C. Zhou, M. Brützmam, R. Uecker, Z.-K. Liu, D. Jena, K. M. Shen, D. A. Muller, and D. G. Schlom, *APL Mater.* **5**, 116107 (2017).
- 12 E. Sachet, C. T. Shelton, J. S. Harris, B. E. Gaddy, D. L. Irving, S. Curtarolo, B. F. Donovan, P. E. Hopkins, P. A. Sharma, A. L. Sharma, J. Ihlefeld, S. Franzen, and J.-P. Maria, *Nat. Mater.* **14**, 414 (2015).
- 13 M. Higashiwaki, K. Sasaki, H. Murakami, Y. Kumagai, A. Koukitsu, A. Kuramata, T. Masui, and S. Yamakoshi, *Semicond. Sci. Technol.* **31**, 034001 (2016).
- 14 M. Higashiwaki and G. H. Jessen, *Appl. Phys. Lett.* **112**, 060401 (2018).
- 15 M. A. Herman and H. Sitter, *Beam Epitaxy: Fundamentals and Current Status*, 2nd ed. (Springer-Verlag, Berlin, 1996).
- 16 D. G. Schlom, *APL Mater.* **3**, 062403 (2015).
- 17 H. P. Nair, J. P. Ruf, N. J. Schreiber, L. Miao, M. L. Grandon, D. J. Baek, B. H. Goodge, J. P. C. Ruff, L. F. Kourkoutis, K. M. Shen, and D. G. Schlom, *APL Mater.* **6**, 101108 (2018).
- 18 J. L. MacManus-Driscoll, M. P. Wells, C. Yun, J.-W. Lee, C.-B. Eom, and D. G. Schlom, *APL Mater.* **8**, 040904 (2020).
- 19 H. P. Nair, Y. Liu, J. P. Ruf, N. J. Schreiber, S.-L. Shang, D. J. Baek, B. H. Goodge, L. F. Kourkoutis, Z.-K. Liu, K. M. Shen, and D. G. Schlom, *APL Mater.* **6**, 046101 (2018).
- 20 H. Li, X. Hu, Y. Wei, Z. Yu, X. Zhang, R. Droopad, A. A. Demkov, J. Edwards, K. Moore, W. Ooms, J. Kulik, and P. Fejes, *J. Appl. Phys.* **93**, 4521 (2003).
- 21 P. Moetakef, T. A. Cain, D. G. Ouellette, J. Y. Zhang, D. O. Klenov, A. Janotti, C. G. Van de Walle, S. Rajan, S. J. Allen, and S. Stemmer, *Appl. Phys. Lett.* **99**, 232116 (2011).
- 22 V. L. Stolyarova and G. A. Semenov, *Mass Spectrometric Study of the Vaporization of Oxide Systems*, 2nd ed. (John Wiley & Sons, West Sussex, England, 1994).
- 23 G. HASS, *J. Am. Ceram. Soc.* **33**, 353 (1950).
- 24 M. Fernández-Perea, M. Vidal-Dasilva, J. I. Larruquert, J. A. Aznárez, J. A. Méndez, E. Gullikson, A. Aquila, and R. Soufli, *J. Appl. Phys.* **105**, 113505 (2009).
- 25 R. H. Lamoreaux and D. L. Hildenbrand, *J. Phys. Chem. Ref. Data* **13**, 151 (1984).
- 26 R. H. Lamoreaux, D. L. Hildenbrand, and L. Brewer, *J. Phys. Chem. Ref. Data* **16**, 419 (1987).
- 27 Scientific Group Thermodata Europe (SGTE), in *Landolt-Boernstein New Ser. Gr. IV*, edited by Lehrstuhl fuer Theoretische Huetttenkunde (Springer, Verlag Berlin Heidelberg, 1999).
- 28 J.-O. Andersson, T. Helander, L. Höglund, P. Shi, and B. Sundman, *Calphad* **26**, 273 (2002).
- 29 J. Drowart, F. Degève, G. Verhaegen, and R. Colin, *Trans. Faraday Soc.* **61**, 1072 (1965).
- 30 O. Kubaschewski and C. B. Alcock, *Metallurgical Thermochemistry*, 5th ed. (Pergamon, Elmsford, NY, 1979).
- 31 F. Tesfaye, D. Sukhomlinov, D. Lindberg, P. Taskinen, and G. Akdogan, *J. Chem. Thermodyn.* **106**, 47 (2017).
- 32 H. Lüth, *Solid Surfaces, Interfaces and Thin Films*, 6th ed. (Springer-Verlag, Berlin, 2015).
- 33 S. Franchi, in *Molecular Beam Epitaxy*, edited by M. Henini (Elsevier, Amsterdam, 2013), pp. 1–46.
- 34 N. K. Kalarickal, Z. Xia, J. McGlone, S. Krishnamoorthy, W. Moore, M. Brenner, A. R. Arehart, S. A. Ringel, and S. Rajan, *Appl. Phys. Lett.* **115**, 152106 (2019).
- 35 Y. S. Kim, N. Bansal, C. Chaparro, H. Gross, and S. Oh, *J. Vac. Sci. Technol., A* **28**, 271 (2010).
- 36 Y.-S. Kim, N. Bansal, and S. Oh, *J. Vac. Sci. Technol., A* **29**, 041505 (2011).
- 37 Z. K. Liu and Y. Wang, *Computational Thermodynamics of Materials* (Cambridge University Press, Cambridge, UK, 2016).
- 38 C. J. Frosch and C. D. Thurmond, *J. Phys. Chem.* **66**, 877 (1962).
- 39 G. Hoffmann, M. Budde, P. Mazzolini, and O. Bierwagen, *APL Mater.* **8**, 031110 (2020).
- 40 H. Aizaki and T. Tatsumi, in *Extended Abstracts of the 17th Conference on Solid State Devices and Materials* (The Japan Society of Applied Physics, Tokyo, 1985), p. 297.
- 41 R. M. Ostrom and F. G. Allen, *Appl. Phys. Lett.* **48**, 221 (1986).
- 42 M. Putkonen and L. Niinistö, *Thin Solid Films* **514**, 145 (2006).
- 43 K. A. Stewart, V. Gouliouk, D. A. Keszler, and J. F. Wager, *Solid-State Electron.* **137**, 80 (2017).
- 44 O. M. Moon, B.-C. Kang, S.-B. Lee, and J.-H. Boo, *Thin Solid Films* **464-465**, 164 (2004).
- 45 A. Edukondalu, S. Rahman, S. K. Ahmmad, A. Gupta, and K. Siva Kumar, *J. Taibah Univ. Sci.* **10**, 363 (2016).
- 46 A. I. Kingon, S. K. Streiffer, C. Basceri, and S. R. Summerfelt, *MRS Bull.* **21**, 46 (1996).
- 47 C. J. G. Meyers, C. R. Freeze, S. Stemmer, and R. A. York, *Appl. Phys. Lett.* **109**, 112902 (2016).
- 48 N. M. Dawley, E. J. Marksz, A. M. Hagerstrom, G. H. Olsen, M. E. Holtz, V. Goian, C. Kadlec, J. Zhang, X. Lu, J. A. Drisko, R. Uecker, S. Ganschow, C. J. Long, J. C. Booth, S. Kamba, C. J. Fennie, D. A. Muller, N. D. Orloff, and D. G. Schlom, *Nat. Mater.* **19**, 176 (2020).
- 49 S. Abel, T. Stöferle, C. Marchiori, C. Rossel, M. D. Rossel, R. Erni, D. Caimi, M. Sousa, A. Chelnokov, B. J. Offrein, and J. Fompeyrine, *Nat. Commun.* **4**, 1671 (2013).
- 50 L. Mazet, S. M. Yang, S. V. Kalinin, S. Schamm-Chardon, and C. Dubourdieu, *Sci. Technol. Adv. Mater.* **16**, 036005 (2015).
- 51 S. Abel, F. Eltes, J. E. Ortmann, A. Messner, P. Castera, T. Wagner, D. Urbonas, A. Rosa, A. M. Gutierrez, D. Tulli, P. Ma, B. Baeuerle, A. Josten, W. Heni, D. Caimi, L. Czornomaz, A. A. Demkov, J. Leuthold, P. Sanchis, and J. Fompeyrine, *Nat. Mater.* **18**, 42 (2019).
- 52 S. Acharya, J. Torgersen, Y. Kim, J. Park, P. Schindler, A. L. Dadlani, M. Winterkorn, S. Xu, S. P. Walch, T. Usui, C. Schildknecht, and F. B. Prinz, *J. Mater. Chem. C* **4**, 1945 (2016).
- 53 G. Niu, G. Saint-Girons, and B. Vilquin, *Molecular Beam Epitaxy* (Elsevier, 2013), pp. 451–475.
- 54 H. J. Kim, U. Kim, H. M. Kim, T. H. Kim, H. S. Mun, B.-G. Jeon, K. T. Hong, W.-J. Lee, C. Ju, K. H. Kim, and K. Char, *Appl. Phys. Express* **5**, 061102 (2012).
- 55 J. Park, H. Paik, K. Nomoto, K. Lee, B.-E. Park, B. Grisafe, L.-C. Wang, S. Salahuddin, S. Datta, Y. Kim, D. Jena, H. G. Xing, and D. G. Schlom, *APL Mater.* **8**, 011110 (2020).
- 56 G. H. Jonker, H. P. J. Wijn, and P. B. Braun, *Philips Tech. Rev.* **18**, 145 (1956-1957).
- 57 P. B. Braun, *Philips Res. Rep.* **12**, 491–548 (1957).

- <sup>58</sup>Z. Cai, T. L. Goodrich, B. Sun, Z. Chen, V. G. Harris, and K. S. Ziemer, *J. Phys. D.: Appl. Phys.* **43**, 095002 (2010).
- <sup>59</sup>C. Wu, K. Kruska, and M. R. Castell, *Surf. Sci.* **618**, 94 (2013).
- <sup>60</sup>R. A. McKee, F. J. Walker, J. R. Conner, E. D. Specht, and D. E. Zelmon, *Appl. Phys. Lett.* **59**, 782 (1991).
- <sup>61</sup>J. Lettieri, J. H. Haeni, and D. G. Schlom, *J. Vac. Sci. Technol., A* **20**, 1332 (2002).
- <sup>62</sup>Y. Segal, J. W. Reiner, A. M. Kolpak, Z. Zhang, S. Ismail-Beigi, C. H. Ahn, and F. J. Walker, *Phys. Rev. Lett.* **102**, 116101 (2009).
- <sup>63</sup>K. P. Muthe, J. C. Vyas, G. P. Kothiyal, D. P. Gandhi, A. K. Debnath, S. K. Gupta, S. C. Sabharwal, and M. K. Gupta, *J. Cryst. Growth* **118**, 213 (1992).
- <sup>64</sup>Y. Kado and Y. Arita, in *Extended Abstracts of the 20th (1988 International) Conference on Solid State Devices and Materials, August 24–26, 1988, Keio Plaza Hotel, Tokyo* (Publication Office, Business Center for Academic Societies Japan, Tokyo, 1988), pp. 181–184.
- <sup>65</sup>Y. Du, D. J. Kim, T. Varga, Z. Wang, J. Szanyi, and I. Lyubintsev, *Thin Solid Films* **519**, 5335 (2011).
- <sup>66</sup>T. V. Charlu and O. J. Kleppa, *J. Chem. Thermodyn.* **3**, 697 (1971).
- <sup>67</sup>M. Yano, K. Koike, M. Matsuo, T. Murayama, Y. Harada, and K. Inaba, *Appl. Surf. Sci.* **381**, 32 (2016).
- <sup>68</sup>Y. Du, G. Li, E. W. Peterson, J. Zhou, X. Zhang, R. Mu, Z. Dohnálek, M. Bowden, I. Lyubintsev, and S. A. Chambers, *Nanoscale* **8**, 3119 (2016).
- <sup>69</sup>A. Radetinac, J. Zimmermann, K. Hoyer, H. Zhang, P. Komissinskiy, and L. Alff, *J. Appl. Phys.* **119**, 055302 (2016).
- <sup>70</sup>P. Salg, D. Walk, L. Zeinar, A. Radetinac, L. Molina-Luna, A. Zintler, R. Jakoby, H. Maune, P. Komissinskiy, and L. Alff, *APL Mater.* **7**, 051107 (2019).
- <sup>71</sup>T. M. McEvoy, K. J. Stevenson, J. T. Hupp, and X. Dang, *Langmuir* **19**, 4316 (2003).
- <sup>72</sup>L. P. Borilo and E. S. Lyutova, *Inorg. Mater.* **53**, 400 (2017).
- <sup>73</sup>S. I. Lopatin, I. Y. Mittova, F. S. Gerasimov, S. M. Shugurov, V. F. Kostyukov, and S. M. Skorokhodova, *Russ. J. Inorg. Chem.* **51**, 1646 (2006).
- <sup>74</sup>R. A. Stall, *J. Vac. Sci. Technol., B* **1**, 135 (1983).
- <sup>75</sup>G. Rispen and B. Noheda, *Integr. Ferroelectr.* **92**, 30 (2007).
- <sup>76</sup>E. S. Hellman, E. H. Hartford, and R. M. Fleming, *Appl. Phys. Lett.* **55**, 2120 (1989).
- <sup>77</sup>H. B. Skinner, *Mass Spectrometric Studies of Gaseous Oxides of Rhenium and of the Lanthanum Trifluoride Dimer* (U.S. Atomic Energy Commission, 1970).
- <sup>78</sup>I. R. Beattie, T. R. Gilson, and P. J. Jones, *Inorg. Chem.* **35**, 1301 (1996).
- <sup>79</sup>R. G. Behrens, R. S. Lemons, and G. M. Rosenblatt, *J. Chem. Thermodyn.* **6**, 457 (1974).
- <sup>80</sup>R. F. Brebrick, *J. Phase Equilib.* **21**, 235 (2000).
- <sup>81</sup>D. Manno, G. Micocci, A. Serra, and A. Tepore, *J. Appl. Phys.* **83**, 3541 (1998).
- <sup>82</sup>D. Manno, G. Micocci, A. Serra, M. Di Giulio, and A. Tepore, *J. Appl. Phys.* **88**, 6571 (2000).
- <sup>83</sup>W. L. Holstein, *J. Phys. Chem.* **97**, 4224 (1993).
- <sup>84</sup>P. E. Blackburn, M. Hoch, and H. L. Johnston, *J. Phys. Chem.* **62**, 769 (1958).
- <sup>85</sup>G. Li, T. Varga, P. Yan, Z. Wang, C. Wang, S. A. Chambers, and Y. Du, *Phys. Chem. Chem. Phys.* **17**, 15119 (2015).
- <sup>86</sup>K. Sasaki, A. Kuramata, T. Masui, E. G. Villora, K. Shimamura, and S. Yamakoshi, *Appl. Phys. Express* **5**, 035502 (2012).
- <sup>87</sup>A. B. Mei, L. Miao, M. J. Wahila, G. Khalsa, Z. Wang, M. Barone, N. J. Schreiber, L. E. Noskin, H. Paik, T. E. Tiwald, Q. Zheng, R. T. Haasch, D. G. Sangiovanni, L. F. J. Piper, and D. G. Schlom, *Phys. Rev. Mater.* **3**, 105202 (2019).
- <sup>88</sup>Y. Hu, J. Hwang, Y. Lee, P. Conlin, D. G. Schlom, S. Datta, and K. Cho, *J. Appl. Phys.* **126**, 185701 (2019).
- <sup>89</sup>G. Hautier, A. Miglio, G. Ceder, G.-M. Rignanese, and X. Gonze, *Nat. Commun.* **4**, 2292 (2013).
- <sup>90</sup>H. Okamoto, *Desk Handbook: Phase Diagram for Binary Alloys*, 2nd ed. (ASM International, 2010).
- <sup>91</sup>*Phase Diagrams for Ceramists*, edited by R. S. Roth, J. R. Dennis, and H. F. McMurdie (American Ceramic Society, Westerville, 1987), Vol. VI.
- <sup>92</sup>Y. Ma, A. Edgeton, H. Paik, B. D. Faeth, C. T. Parzyck, B. Pamuk, S. L. Shang, Z. K. Liu, K. M. Shen, D. G. Schlom, and C. B. Eom, *Adv. Mater.* **32**, 2000809 (2020).
- <sup>93</sup>P. Vogt, F. V. E. Hensling, K. Azizie, C. S. Chang, D. Turner, J. Park, J. P. McCandless, H. Paik, B. J. Bocklund, G. Hoffman, M. Budde, O. Bierwagen, D. Jena, H. G. Xing, S. Mou, D. A. Muller, S. L. Shang, Z. K. Liu, and D. G. Schlom, “Adsorption-controlled growth of Ga<sub>2</sub>O<sub>3</sub> by suboxide molecular-beam epitaxy” (unpublished).
- <sup>94</sup>D. P. Butt, Y. Park, and T. N. Taylor, *J. Nucl. Mater.* **264**, 71 (1999).
- <sup>95</sup>S. Kirklin, J. E. Saal, B. Meredig, A. Thompson, J. W. Doak, M. Aykol, S. Rühl, and C. Wolverton, *npj Comput. Mater.* **1**, 15010 (2015).
- <sup>96</sup>P. Vogt and O. Bierwagen, *Appl. Phys. Lett.* **108**, 072101 (2016).
- <sup>97</sup>T. Oshima, T. Okuno, and S. Fujita, *Jpn. J. Appl. Phys., Part 1* **46**, 7217 (2007).
- <sup>98</sup>M.-Y. Tsai, O. Bierwagen, M. E. White, and J. S. Speck, *J. Vac. Sci. Technol., A* **28**, 354 (2010).
- <sup>99</sup>P. Vogt and O. Bierwagen, *Appl. Phys. Lett.* **106**, 081910 (2015).
- <sup>100</sup>S. Krishnamoorthy, Z. Xia, S. Bajaj, M. Brenner, and S. Rajan, *Appl. Phys. Express* **10**, 051102 (2017).
- <sup>101</sup>Z. Yu, C. D. Overgaard, R. Droopad, M. Passlack, and J. K. Abrokwha, *Appl. Phys. Lett.* **82**, 2978 (2003).
- <sup>102</sup>S. Ghose, S. Rahman, L. Hong, J. S. Rojas-Ramirez, H. Jin, K. Park, R. Klie, and R. Droopad, *J. Appl. Phys.* **122**, 095302 (2017).
- <sup>103</sup>A. Sudha, T. K. Maity, S. L. Sharma, and A. N. Gupta, *Mater. Sci. Semicond. Process.* **74**, 347 (2018).
- <sup>104</sup>M. D. Losego, *Interfacial Epitaxial Oxides to Gallium Nitride* (North Carolina State University, 2008).
- <sup>105</sup>A. Schmehl, V. Vaithyanathan, A. Herrnberger, S. Thiel, C. Richter, M. Liberati, T. Heeg, M. Röckerath, L. F. Kourkoutis, S. Mühlbauer, P. Böni, D. A. Müller, Y. Barash, J. Schubert, Y. Idzerda, J. Mannhart, and D. G. Schlom, *Nat. Mater.* **6**, 882 (2007).
- <sup>106</sup>R. Sutarto, S. G. Altendorf, B. Coloru, M. Moretti Sala, T. Haupricht, C. F. Chang, Z. Hu, C. Schüsler-Langeheine, N. Hollmann, H. Kierspel, H. H. Hsieh, H.-J. Lin, C. T. Chen, and L. H. Tjeng, *Phys. Rev. B* **79**, 205318 (2009).
- <sup>107</sup>D. V. Averyanov, O. E. Parfenov, A. M. Tokmachev, I. A. Karateev, O. A. Kondratev, A. N. Taldenkov, M. S. Platonov, F. Wilhelm, A. Rogalev, and V. G. Storchak, *Nanotechnology* **29**, 195706 (2018).
- <sup>108</sup>O. Bierwagen, A. Proessdorf, M. Niehle, F. Grosse, A. Trampert, and M. Klingsporn, *Cryst. Growth Des.* **13**, 3645 (2013).
- <sup>109</sup>J. Wang, T. Ji, Y. Zhu, Z. Fang, and W. Ren, *J. Rare Earths* **30**, 233 (2012).
- <sup>110</sup>K. J. Hubbard and D. G. Schlom, *J. Mater. Res.* **11**, 2757 (1996).
- <sup>111</sup>D. G. Schlom and J. H. Haeni, *MRS Bull.* **27**, 198 (2002).
- <sup>112</sup>D. G. Schlom, S. Guha, and S. Datta, *MRS Bull.* **33**, 1017 (2008).
- <sup>113</sup>C. P. Chen, M. Hong, J. Kwo, H. M. Cheng, Y. L. Huang, S. Y. Lin, J. Chi, H. Y. Lee, Y. F. Hsieh, and J. P. Mannaerts, *J. Cryst. Growth* **278**, 638 (2005).
- <sup>114</sup>J. Kwo, M. Hong, A. R. Kortan, K. L. Queeney, Y. J. Chabal, R. L. Opila, D. A. Müller, S. N. G. Chu, B. J. Sapjeta, T. S. Lay, J. P. Mannaerts, T. Boone, H. W. Krautter, J. J. Krajewski, A. M. Sergnt, and J. M. Rosamilia, *J. Appl. Phys.* **89**, 3920 (2001).
- <sup>115</sup>J. P. Liu, P. Zaumseil, E. Bugiel, and H. J. Osten, *Appl. Phys. Lett.* **79**, 671 (2001).
- <sup>116</sup>T. Watahiki, W. Braun, and H. Riechert, *J. Vac. Sci. Technol., B* **27**, 262 (2009).
- <sup>117</sup>A. Fissel, Z. Elassar, O. Kirfel, E. Bugiel, M. Czernohorsky, and H. J. Osten, *J. Appl. Phys.* **99**, 074105 (2006).
- <sup>118</sup>M. Czernohorsky, E. Bugiel, H. J. Osten, A. Fissel, and O. Kirfel, *Appl. Phys. Lett.* **88**, 152905 (2006).
- <sup>119</sup>G.-Y. Adachi and N. Imanaka, *Chem. Rev.* **98**, 1479 (1998).
- <sup>120</sup>W. Braun and J. Mannhart, *AIP Adv.* **9**, 085310 (2019).
- <sup>121</sup>V. L. Stolyarova, A. L. Shilov, G. G. Ivanov, M. M. Shultz, and S. Seetharaman, *Rapid Commun. Mass Spectrom.* **9**, 1244 (1995).
- <sup>122</sup>J. H. Lee, L. Fang, E. Vlahos, X. Ke, Y. W. Jung, L. F. Kourkoutis, J.-W. Kim, P. J. Ryan, T. Heeg, M. Röckerath, V. Goian, M. Bernhagen, R. Uecker, P. C. Hammel, K. M. Rabe, S. Kamba, J. Schubert, J. W. Freeland, D. A. Müller, C. J. Fennie, P. Schiffer, V. Gopalan, E. Johnston-Halperin, and D. G. Schlom, *Nature* **466**, 954 (2010).
- <sup>123</sup>A. P. Mackenzie and Y. Maeno, *Rev. Mod. Phys.* **75**, 657 (2003).

- <sup>124</sup>S. A. Grigera, *Science* **306**, 1154 (2004).
- <sup>125</sup>Y. K. Kim, N. H. Sung, J. D. Denlinger, and B. J. Kim, *Nat. Phys.* **12**, 37 (2016).
- <sup>126</sup>Y. Singh, S. Manni, J. Reuther, T. Berlijn, R. Thomale, W. Ku, S. Trebst, and P. Gegenwart, *Phys. Rev. Lett.* **108**, 127203 (2012).
- <sup>127</sup>X. Wan, A. M. Turner, A. Vishwanath, and S. Y. Savrasov, *Phys. Rev. B* **83**, 205101 (2011).
- <sup>128</sup>L. Miao, Y. Lee, A. B. Mei, M. J. Lawler, and K. M. Shen, *Nat. Commun.* **11**, 1341 (2020).
- <sup>129</sup>D.-Y. Kuo, J. K. Kawasaki, J. N. Nelson, J. Kloppenburg, G. Hautier, K. M. Shen, D. G. Schlom, and J. Suntivich, *J. Am. Chem. Soc.* **139**, 3473 (2017).
- <sup>130</sup>D.-Y. Kuo, H. Paik, J. Kloppenburg, B. Faeth, K. M. Shen, D. G. Schlom, G. Hautier, and J. Suntivich, *J. Am. Chem. Soc.* **140**, 017597 (2018).
- <sup>131</sup>D. Klimm, S. Ganschow, D. Schulz, R. Bertram, R. Uecker, P. Reiche, and R. Fornari, *J. Cryst. Growth* **311**, 534 (2009).
- <sup>132</sup>C. Mallika and O. M. Sreedharan, *J. Less-Common Met.* **162**, 51 (1990).
- <sup>133</sup>L. E. Noskin, A. Seidner H., and D. G. Schlom, *MRS Adv.* **2**, 3031 (2017).

## Supplementary Material

### **Suitability of Binary Oxides for Molecular-Beam Epitaxy Source Materials: A Comprehensive Thermodynamic Analysis**

Kate M. Adkison,<sup>1</sup> Shun-Li Shang,<sup>1,a)</sup> Brandon J. Bocklund,<sup>1</sup> Detlef Klimm,<sup>2</sup> Darrell G. Schlom,<sup>2,3,4</sup> and Zi-Kui Liu<sup>1</sup>

<sup>1</sup> Department of Materials Science and Engineering, The Pennsylvania State University, University Park, Pennsylvania 16802, USA

<sup>2</sup> Leibniz-Institut für Kristallzüchtung, Max-Born-Str. 2, 12489 Berlin, Germany

<sup>3</sup> Department of Materials Science and Engineering, Cornell University, Ithaca, New York 14853, USA

<sup>4</sup> Kavli Institute at Cornell for Nanoscale Science, Ithaca, New York 14853, USA

<sup>a)</sup> Author to whom correspondence should be addressed: sus26@psu.edu (S. L. Shang)

This Supplementary Material includes 3 supplementary tables (Table S 1 to Table S 3) and 81 supplementary figures (Figure S 1 to Figure S 81).

Table S 1. Alphabetical list of 128 solid and liquid oxides (oxides are solid unless otherwise noted; all liquid oxides are marked) together with 17 solid and liquid elements whose most stable phase is not an oxide.

Oxide or element in equilibrium with gas phase	Dominant gas species	* = metastable oxide and note based on SSUB5	Calculated figures
Ac liquid	Ac	no solid or liquid oxide phase	Figure S 1
Ag solid	Ag		Figure S 2
Ag <sub>2</sub> O	Ag	*	Figure S 2
Al <sub>2</sub> O <sub>3</sub> corundum	Al		Figure S 3
Am <sub>2</sub> O <sub>3</sub>	Am		Figure S 4
AmO <sub>2</sub>	Am	*	Figure S 4
As <sub>2</sub> O <sub>3</sub> solid claudetite	As <sub>4</sub> O <sub>6</sub>	*	Figure S 5
As <sub>2</sub> O <sub>3</sub> liquid	As <sub>4</sub> O <sub>6</sub>	* Stable for $T > 677$ K	Figure S 5
As <sub>2</sub> O <sub>5</sub>	As <sub>4</sub> O <sub>6</sub>	Stable for $T < 677$ K	Figure S 5
At	At <sub>2</sub>	no solid or liquid oxide phase	Figure S 6
Au liquid	Au		Figure S 7
Au <sub>2</sub> O <sub>3</sub>	Au <sub>2</sub>	*	Figure S 7
B <sub>2</sub> O <sub>3</sub> glass	B <sub>2</sub> O <sub>3</sub>		Figure 2
BaO	BaO		Figure S 8
BaO <sub>2</sub>	BaO	*	Figure S 8
BeO	Be		Figure S 9
Bi <sub>2</sub> O <sub>3</sub> liquid	Bi	Liquid Bi <sub>2</sub> O <sub>3</sub> is stable for $T > 1075$	Figure S 10
Bi <sub>2</sub> O <sub>3</sub> solid	Bi	* Solid Bi <sub>2</sub> O <sub>3</sub> is stable for $T < 1075$	Figure S 10
CaO	Ca		Figure S 12
CaO <sub>2</sub>	Ca	*	Figure S 12
CdO	Cd		Figure S 13
Ce <sub>2</sub> O <sub>3</sub>	CeO		Figure S 14
CeO <sub>2</sub>	CeO	*	Figure S 14
Cf solid	O	no solid or liquid oxide phase	Figure S 15
Cm liquid	Cm	no solid or liquid oxide phase	Figure S 16
Co solid	Co		Figure S 17
CoO	Co	*	Figure S 17
Cr <sub>2</sub> O <sub>3</sub>	Cr		Figure S 18
Cs <sub>2</sub> O	Cs <sub>2</sub> O	*	Figure S 19
Cs <sub>2</sub> O <sub>2</sub>	Cs <sub>2</sub> O	*	Figure S 19
Cs <sub>2</sub> O <sub>3</sub>	Cs <sub>2</sub> O	*	Figure S 19
CsO <sub>2</sub>	Cs <sub>2</sub> O, Cs <sub>2</sub> O <sub>2</sub>		Figure S 19
Cu liquid	Cu		
Cu <sub>2</sub> O	Cu	*	Figure S 20
CuO	Cu	*	Figure S 20
Dy <sub>2</sub> O <sub>3</sub>	DyO		Figure S 21
Er <sub>2</sub> O <sub>3</sub>	ErO		Figure S 22
Es solid	Es	no solid or liquid oxide phase	Figure S 23
Eu <sub>2</sub> O <sub>3</sub>	Eu		Figure S 24
EuO	Eu	*	Figure S 24
Fe <sub>2</sub> O <sub>3</sub> hematite	Fe	*	Figure S 25
Fe <sub>3</sub> O <sub>4</sub> magnetite	Fe	*	Figure S 25
FeO liquid	Fe	Liquid FeO is stable for $T > 1650$ K	Figure S 25
FeO solid	Fe	* Solid FeO is stable for $1421 < T < 1650$ K	Figure S 25
Fm solid	Fm	no solid or liquid oxide phase	Figure S 26
Fr	Not available	no solid or liquid oxide phase	

Ga <sub>2</sub> O <sub>3</sub>	Ga <sub>2</sub> O		Figure S 27
Gd <sub>2</sub> O <sub>3</sub>	GdO		Figure S 28
GeO amorphous	GeO	*	Figure S 29
GeO <sub>2</sub>	GeO		Figure S 29
HfO <sub>2</sub>	HfO		Figure S 30
HgO	Hg		Figure S 31
Ho <sub>2</sub> O <sub>3</sub>	HoO		Figure S 32
In <sub>2</sub> O <sub>3</sub>	In <sub>2</sub> O		Figure S 33
Ir solid	Ir		Figure S 34
IrO <sub>2</sub>	IrO <sub>2</sub>	*	Figure S 34
K <sub>2</sub> O	K	*	Figure S 35
K <sub>2</sub> O <sub>2</sub>	K	*	Figure S 35
KO <sub>2</sub>	K		Figure S 35
La <sub>2</sub> O <sub>3</sub>	LaO		Figure S 36
Li <sub>2</sub> O	Li, Li <sub>2</sub> O		Figure S 37
Li <sub>2</sub> O <sub>2</sub>	Li <sub>2</sub> O	*	Figure S 37
Lu <sub>2</sub> O <sub>3</sub>	LuO		Figure S 38
MgO	Mg		Figure S 39
MnO	Mn		Figure S 40
MoO <sub>3</sub>	Mo <sub>3</sub> O <sub>9</sub> , Mo <sub>4</sub> O <sub>12</sub>		Figure S 41
Na <sub>2</sub> O	Na		Figure S 42
Na <sub>2</sub> O <sub>2</sub>	Na	*	Figure S 42
NaO <sub>2</sub>	Na, Na <sub>2</sub> O	*	Figure S 42
Nb <sub>2</sub> O <sub>5</sub> liquid	NbO <sub>2</sub>	Liquid Nb <sub>2</sub> O <sub>5</sub> is stable for $T > 1785$ K	Figure S 43
NbO <sub>2</sub>	NbO <sub>2</sub>	*	Figure S 43
Nd <sub>2</sub> O <sub>3</sub>	NdO		Figure S 44
NiO	Ni		Figure S 45
Np <sub>2</sub> O <sub>5</sub>	Np	*	Figure S 46
NpO <sub>2</sub>	Np, O		Figure S 46
P <sub>2</sub> O <sub>5</sub> orthorhombic	P <sub>4</sub> O <sub>10</sub>		Figure S 47
OsO <sub>2</sub>	OsO <sub>4</sub>	Solid OsO <sub>2</sub> is stable for $314 < T < 832$ K	Figure S 48
OsO <sub>4</sub> solid/liquid	OsO <sub>4</sub>	Solid OsO <sub>4</sub> is stable for $< 304$ K, liquid OsO <sub>4</sub> is stable for $T < 314$ K	Figure S 48
Pa liquid	O	no solid or liquid oxide phase	Figure S 49
Pb <sub>2</sub> O <sub>3</sub>	PbO	*	Figure S 50
Pb <sub>3</sub> O <sub>4</sub>	PbO	*	Figure S 50
PbO	Pb, PbO	*	Figure S 50
PbO yellow	Pb, PbO		Figure S 50
PbO <sub>2</sub>	PbO	*	Figure S 50
Pd solid	Pd		Figure S 51
PdO	Pd	*	Figure S 51
Pm <sub>2</sub> O <sub>3</sub>	PmO		Figure S 52
Pr <sub>2</sub> O <sub>3</sub>	PrO		Figure S 53
Pr <sub>6</sub> O <sub>11</sub>	PrO	*	Figure S 53
Pr <sub>7</sub> O <sub>12</sub>	PrO	*	Figure S 53
PrO <sub>2</sub>	PrO	*	Figure S 53
PtO	Pt	*	Figure S 54
PtO <sub>2</sub>	PtO <sub>2</sub>	*	Figure S 54
Pt <sub>3</sub> O <sub>4</sub>	PtO <sub>2</sub> , Pt	*	Figure S 54
Pu <sub>2</sub> O <sub>3</sub>	PuO <sub>2</sub>	*	Figure S 55
PuO <sub>2</sub>	PuO <sub>2</sub>		Figure S 55

Ra	Not available	no solid or liquid oxide phase	
Rb <sub>2</sub> O liquid	Rb, Rb <sub>2</sub> O	Liquid Rb <sub>2</sub> O is stable for $T > 778$ K	Figure S 56
Rb <sub>2</sub> O solid	Rb, Rb <sub>2</sub> O	* Solid Rb <sub>2</sub> O is stable for $T < 778$ K	Figure S 56
Rb <sub>2</sub> O <sub>2</sub>	Rb <sub>2</sub> O <sub>2</sub>	*	Figure S 56
RbO <sub>2</sub>	Rb	*	Figure S 56
ReO <sub>3</sub>	Re <sub>2</sub> O <sub>6</sub>	*	Figure S 57
Re <sub>2</sub> O <sub>7</sub>	Re <sub>2</sub> O <sub>7</sub>		Figure S 57
Rh solid	Rh		Figure S 58
Rh <sub>2</sub> O	Rh	*	Figure S 58
RhO	Rh	*	Figure S 58
Ru solid	Ru		Figure S 59
RuO <sub>2</sub>	RuO <sub>2</sub>	*	Figure S 59
Sb <sub>2</sub> O <sub>3</sub> liquid	Sb <sub>4</sub> O <sub>6</sub>	Liquid Sb <sub>2</sub> O <sub>3</sub> is stable for $T > 997$ K	Figure S 60
Sb <sub>2</sub> O <sub>3</sub> solid	Sb <sub>4</sub> O <sub>6</sub>	*	Figure S 60
SbO <sub>2</sub>	Sb <sub>4</sub> O <sub>6</sub>		Figure S 60
Sc <sub>2</sub> O <sub>3</sub>	ScO, ScO <sub>2</sub>		Figure S 61
SeO <sub>2</sub>	SeO <sub>2</sub>		Figure S 62
SiO amorphous	SiO	*	Figure S 63
SiO <sub>2</sub> cristobalite	SiO		Figure S 63
Sm <sub>2</sub> O <sub>3</sub>	SmO		Figure S 64
SnO liquid	SnO	Liquid SnO is stable for $T > 1498$ K	Figure S 65
SnO solid	SnO	*	Figure S 65
SnO <sub>2</sub>	SnO		Figure S 65
SrO	Sr		Figure S 66
SrO <sub>2</sub>	Sr	*	Figure S 66
Ta <sub>2</sub> O <sub>5</sub> liquid	TaO <sub>2</sub>	Liquid Ta <sub>2</sub> O <sub>5</sub> is stable for $T > 2150$ K	Figure S 67
Ta <sub>2</sub> O <sub>5</sub> solid	TaO <sub>2</sub>	* Solid Ta <sub>2</sub> O <sub>5</sub> is stable for $T < 2150$ K	Figure S 67
Tb <sub>2</sub> O <sub>3</sub>	TbO		Figure S 68
TbO <sub>2</sub>	TbO	*	Figure S 68
TcO <sub>2</sub>	TcO, Tc <sub>2</sub> O <sub>7</sub>		Figure S 69
TeO <sub>2</sub>	Te <sub>2</sub> O <sub>2</sub>		Figure S 70
ThO <sub>2</sub>	ThO <sub>2</sub>		Figure S 71
TiO <sub>2</sub> anatase	TiO <sub>2</sub>	*	Figure S 72
TiO <sub>2</sub> rutile	TiO <sub>2</sub>	*	Figure S 72
Ti <sub>4</sub> O <sub>7</sub> liquid	TiO <sub>2</sub>	Liquid Ti <sub>4</sub> O <sub>7</sub> is stable for $1950 < T < 2148$	Figure S 72
Ti <sub>4</sub> O <sub>7</sub> solid	TiO <sub>2</sub>	Solid Ti <sub>4</sub> O <sub>7</sub> is stable for $1881 < T < 1950$	Figure S 72
Ti <sub>3</sub> O <sub>5</sub> liquid	TiO	Liquid Ti <sub>3</sub> O <sub>5</sub> is stable for $T > 2148$	Figure S 72
Tl <sub>2</sub> O	Tl <sub>2</sub> O		Figure S 73
Tm <sub>2</sub> O <sub>3</sub>	Tm		Figure S 74
U <sub>3</sub> O <sub>8</sub>	U <sub>2</sub> O <sub>6</sub>		Figure S 75
U <sub>4</sub> O <sub>9</sub>	UO <sub>3</sub> , U <sub>2</sub> O <sub>5</sub>	*	Figure S 75
UO <sub>3</sub>	U <sub>2</sub> O <sub>6</sub>	*	Figure S 75
V <sub>2</sub> O <sub>3</sub>	V <sub>1</sub> O <sub>2</sub>		Figure S 76
V <sub>2</sub> O <sub>5</sub>	V <sub>4</sub> O <sub>10</sub>	*	Figure S 76
WO <sub>3</sub>	W <sub>3</sub> O <sub>9</sub>		Figure S 77
Y <sub>2</sub> O <sub>3</sub>	YO <sub>2</sub>		Figure S 78
Yb <sub>2</sub> O <sub>3</sub>	Yb		Figure S 79
ZnO	Zn		Figure S 80
ZrO <sub>2</sub>	ZrO, ZrO <sub>2</sub> , O		Figure S 81

Table S 2. Two-phase mixture of solid (or liquid) oxide source plus solid (or liquid) pure element for an overall composition of  $M_xO_y$  under the conditions: fixed gas phase at zero amount,  $T$  fixed,  $n(M) = 1$  mole, and  $n(O_2) = y/(2x)$  mole; where gas species  $M_xO_y$  evaporates nearly congruently or incongruently. Here (s, $\ell$ ) indicate the solid phase at low temperatures and liquid phase at high temperatures; (first) indicates the dominant gas species, and (second) indicates the second most dominant gas species.

Symbol	Sources of two-phase mixture	Overall/target composition	Dominant gas species	Figures
Al	Al <sub>2</sub> O <sub>3</sub> (s, $\ell$ ) + Al(s, $\ell$ )	Al <sub>2</sub> O	Al ( $T < 962$ K), Al <sub>2</sub> O ( $T > 962$ K)	Figure S 3
Ce	Ce <sub>2</sub> O <sub>3</sub> (s, $\ell$ ) + Ce(s, $\ell$ )	CeO	Ce ( $T < 1136$ K), CeO ( $T > 1136$ K)	Figure S 14
Cr	Cr <sub>2</sub> O <sub>3</sub> (s) + Cr(s, $\ell$ )	CrO	Cr (first), CrO (second)	Figure S 18
Dy	Dy <sub>2</sub> O <sub>3</sub> (s, $\ell$ ) + Dy(s, $\ell$ )	DyO	Dy (first), DyO (second)	Figure S 21
Er	Er <sub>2</sub> O <sub>3</sub> (s, $\ell$ ) + Er(s, $\ell$ )	ErO	Er (first), ErO (second)	Figure S 22
Eu	Eu <sub>2</sub> O <sub>3</sub> (s, $\ell$ ) + Eu(s, $\ell$ )	EuO	Eu (first), Eu <sub>2</sub> O (second)	Figure S 24
Ga	Ga <sub>2</sub> O <sub>3</sub> (s, $\ell$ ) + Ga( $\ell$ )	Ga <sub>2</sub> O	Ga <sub>2</sub> O	Figure S 27
Gd	Gd <sub>2</sub> O <sub>3</sub> (s, $\ell$ ) + Gd(s, $\ell$ )	GdO	Gd (first), Gd <sub>2</sub> O (second)	Figure S 28
Ge	GeO <sub>2</sub> (s, $\ell$ ) + Ge(s, $\ell$ )	GeO	GeO	Figure S 29
Hf	HfO <sub>2</sub> (s) + Hf(s, $\ell$ )	HfO	HfO	Figure S 30
Ho	Ho <sub>2</sub> O <sub>3</sub> (s) + Ho(s, $\ell$ )	HoO	Ho (first), HoO (second)	Figure S 32
In	In <sub>2</sub> O <sub>3</sub> (s, $\ell$ ) + In( $\ell$ )	In <sub>2</sub> O	In <sub>2</sub> O	Figure S 33
La	La <sub>2</sub> O <sub>3</sub> (s, $\ell$ ) + La(s, $\ell$ )	LaO	La ( $T < 1308$ K), LaO ( $T > 1308$ K)	Figure S 36
Lu	Lu <sub>2</sub> O <sub>3</sub> (s, $\ell$ ) + Lu(s, $\ell$ )	LuO	Lu (first), LuO (second)	Figure S 38
Nd	Nd <sub>2</sub> O <sub>3</sub> (s, $\ell$ ) + Nd(s, $\ell$ )	NdO	Nd (first), NdO (second)	Figure S 44
Pm	Pm <sub>2</sub> O <sub>3</sub> (s, $\ell$ ) + Pm(s, $\ell$ )	PmO	Pm (first), PmO (second)	Figure S 52
Pr	Pr <sub>2</sub> O <sub>3</sub> (s, $\ell$ ) + Pr(s, $\ell$ )	PrO	Pr ( $T < 2239$ K), PrO ( $T > 2239$ K)	Figure S 53
Sc	Sc <sub>2</sub> O <sub>3</sub> (s) + Sc(s, $\ell$ )	ScO	Sc (first), ScO (second)	Figure S 61
Si	SiO <sub>2</sub> (s, $\ell$ ) + Si(s, $\ell$ )	SiO	SiO	Figure S 63
Sm	Sm <sub>2</sub> O <sub>3</sub> (s) + Sm(s, $\ell$ )	SmO	Sm (first), SmO (second)	Figure S 64
Sn	SnO <sub>2</sub> (s) + Sn( $\ell$ )	SnO	SnO	Figure 4
Ta	Ta <sub>2</sub> O <sub>5</sub> (s, $\ell$ ) + Ta(s)	TaO <sub>2</sub>	TaO <sub>2</sub>	Figure S 67
Tb	Tb <sub>2</sub> O <sub>3</sub> (s, $\ell$ ) + Tb(s, $\ell$ )	TbO	Tb (first), TbO (second)	Figure S 68
Te	TeO <sub>2</sub> (s, $\ell$ ) + Te(s, $\ell$ )	TeO	Te <sub>2</sub> ( $T < 1013$ K), TeO ( $T > 1013$ K)	Figure S 70
Tm	Tm <sub>2</sub> O <sub>3</sub> (s) + Tm(s, $\ell$ )	TmO	Tm (first), TmO (second)	Figure S 74
Yb	Yb <sub>2</sub> O <sub>3</sub> (s, $\ell$ ) + Yb(s, $\ell$ )	YbO	Yb (first), YbO (second)	Figure S 79
Zr	ZrO <sub>2</sub> (s, $\ell$ ) + Zr(s, $\ell$ )	ZrO	Zr ( $T < 1063$ K), ZrO ( $T > 1063$ K)	Figure S 81

Table S 3. Examples of the macro files (i.e., the tcm files used by the Thermo-Calc software) to calculate evaporation of oxide sources in three typical cases; i.e., (i) the oxide source is a stable phase, (ii) the oxide source is a metastable phase, and (iii) the two-phase mixture with an fixed overall composition.

```

$ Case 1: The oxide source is a stable phase
$ Example of stable B2O3_GLASS source with the dominant gas species of B2O3
$ See Figure 1 after converting the mole fractions of gas species to partial pressures
$
go da
sw ssub5
d-ele B O
get

go p-3
d-com B O2
s-re-st O2 gas,,
s-c t=700 acr(o2)=1e-9 n(B)=1
ch p gas=f 0

s-a-v l t 700 1800,,,
s-a-s
1e5
n
o2
y,,,,,,,,
c-e
c-e
c-e

step,,,
po
s-d-a x t-k
s-s-s x n 500 1500
s-d-a y p
s-a-ty y log,,
s-a-te y n Vapor Pressure, Pa
s-lab e
plot,,

s-p-f 17,,,,,,,,
pl B-O-pressure-all.ps
make B-O-pressure-all.txt y
s-d-a y y(gas,*),,,,
s-a-te y n Mole fraction of species in gas
s-la f
pl B-O-gas-all.ps
make B-O-gas-all.txt y

set-inter

```

```

$ Case 2: The oxide source is a metastable phase
$ The metastable O1Sn1_S source
$ See Figure S 65 after converting the mole fractions of gas species to partial pressures
$
go da
sw ssub5
d-el Sn O
l-sys ,,,,
get

go p-3
d-com Sn o2
s-re-st o2 gas,,,
ch p *=sus
ch p O1Sn1_S=e 1
ch p gas=f 0

s-c t=700 acr(o2)=1e-9 n(Sn)=1
s-a-v 1 t 700 1800,,,,
s-a-s
1e5
n
o2
y,,,,,,,,
c-e
c-e

step,,,,,

po
s-d-a x t-k
s-d-a y p
s-a-ty y log,,,
s-a-te y n Vapor Pressure, Pa
s-lab e
plot,,

s-p-f 17,,,,,
pl Sn-O-pressure-all.ps
make Sn-O-pressure-all.txt y

s-d-a y y(gas,*),,,,
s-a-te y n Mole fraction of species in gas

s-la f
pl Sn-O-gas-all.ps
make Sn-O-gas-all.txt y

set-inter

```

```

$ Case3: Two-phase mixture with a fixed overall composition
$ SnO2(s) + Sn(l) with an overall composition of SnO
$ See Figure 4 after converting mole fractions of gas species to partial pressures
$
go da
sw ssub5
d-ele Sn O
get
go p-3
d-com Sn O2
s-re-st O2 gas,,
s-c n(Sn)=1 n(O2)=0.5
s-c t=1200
l-c
ch p gas=f 0
s-a-v 1 t 500 3000,,
s-a-s
1e9
n
o2
,,,,,,,,,
c-e
c-e

step,,,,,
po
s-d-a x t-k
s-d-a y p
s-a-ty y log,,
s-a-te y n Vapor Pressure, Pa
s-lab e
plot,,

s-p-f 17,,,,,
pl Sn-O-two-pressure.ps
make Sn-O-two-pressure.txt y

s-d-a y y(gas,*),,,,,
s-a-te y n Mole fraction of species in gas
s-l f
pl Sn-O-two-gas.ps
make Sn-O-two-gas.txt y

set-inter

```

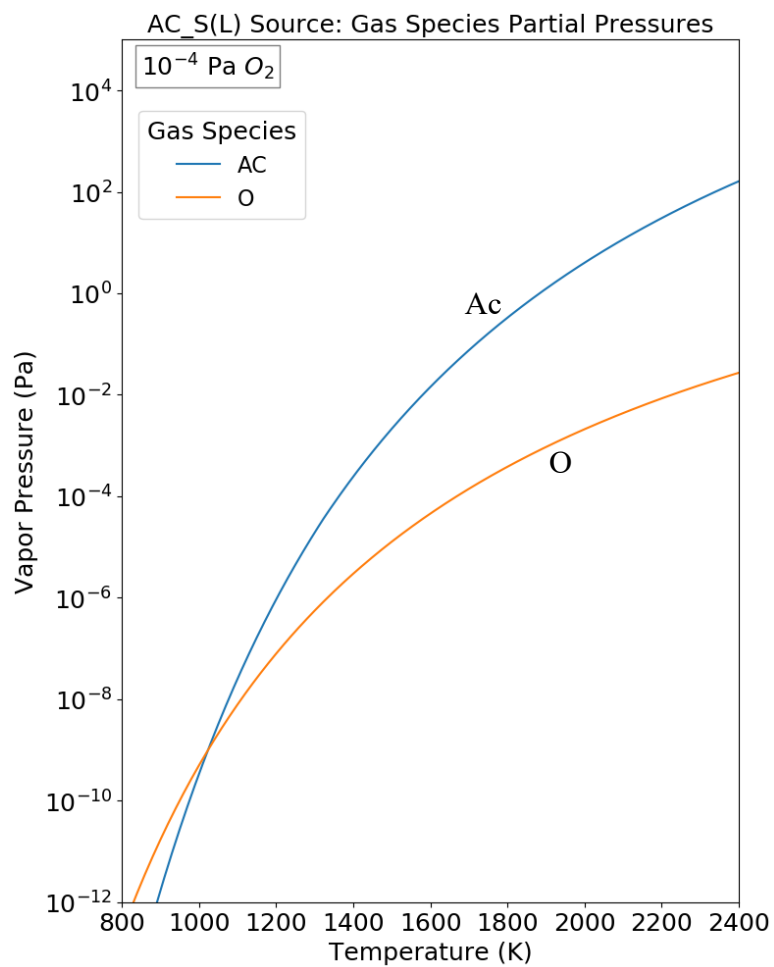


Figure S 1. Solid/liquid Ac (the liquid phase is stable for  $T > 1323$  K). Calculated partial pressures of the gas species over the phase(s) of interest as a function of temperature at  $P_{O_2} = 10^{-4}$  Pa.

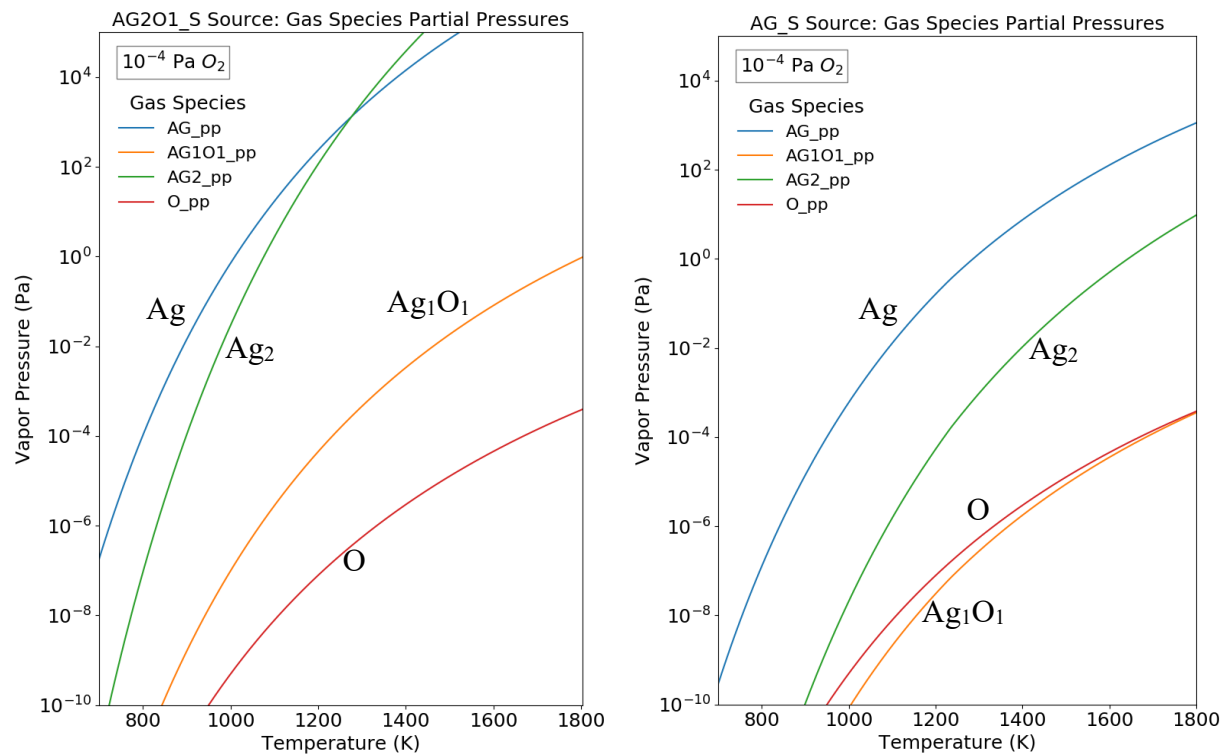


Figure S 2. Solid Ag<sub>2</sub>O (metastable) and solid Ag (the liquid Ag phase is stable for  $T > 1235$  K). Calculated partial pressures of the gas species over the phase(s) of interest as a function of temperature at  $P_{O_2} = 10^{-4}$  Pa. Here, “\_pp” indicates partial pressure when available.

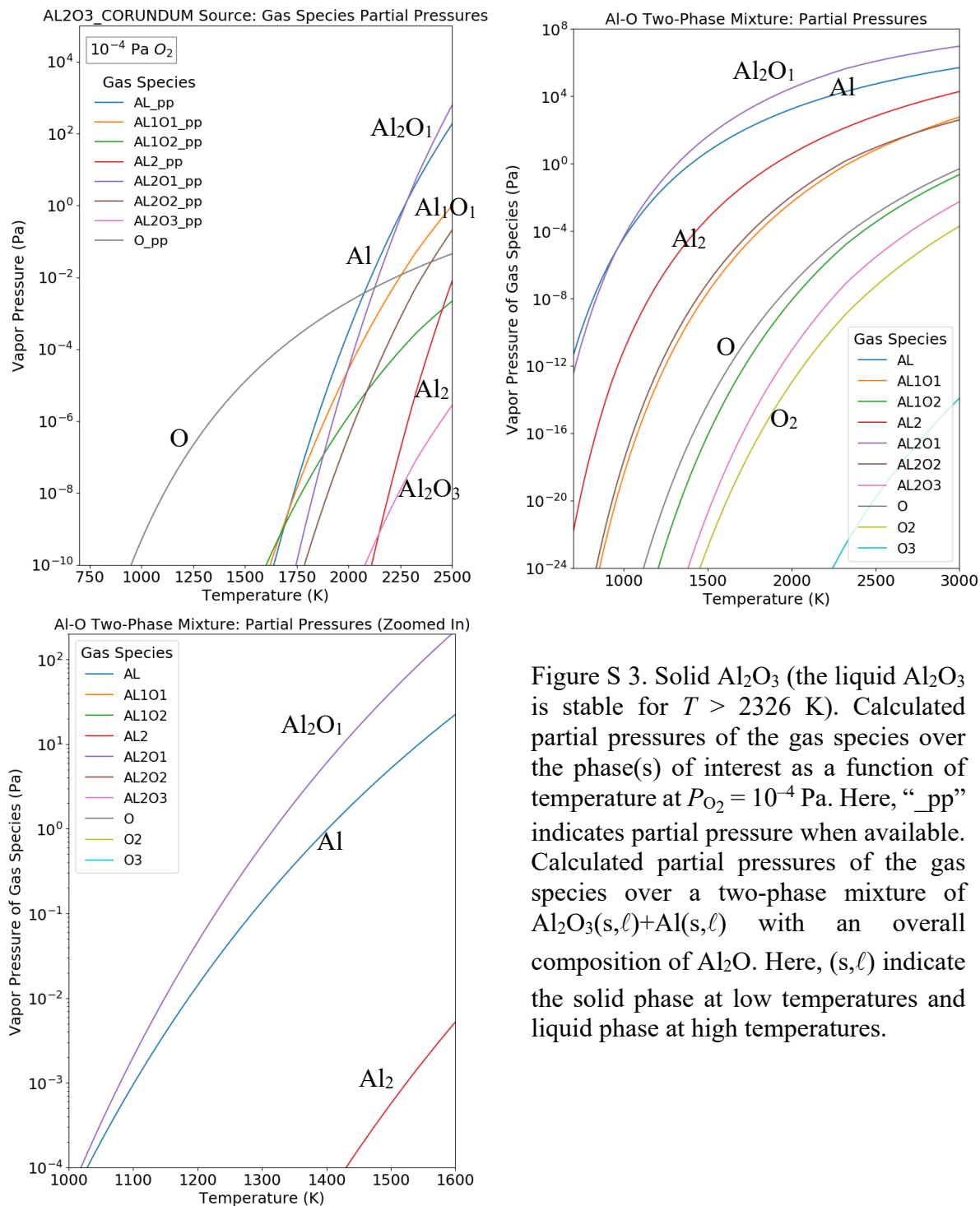


Figure S 3. Solid Al<sub>2</sub>O<sub>3</sub> (the liquid Al<sub>2</sub>O<sub>3</sub> is stable for  $T > 2326$  K). Calculated partial pressures of the gas species over the phase(s) of interest as a function of temperature at  $P_{O_2} = 10^{-4}$  Pa. Here, “\_pp” indicates partial pressure when available. Calculated partial pressures of the gas species over a two-phase mixture of Al<sub>2</sub>O<sub>3</sub>(s, $\ell$ )+Al(s, $\ell$ ) with an overall composition of Al<sub>2</sub>O. Here, (s, $\ell$ ) indicate the solid phase at low temperatures and liquid phase at high temperatures.

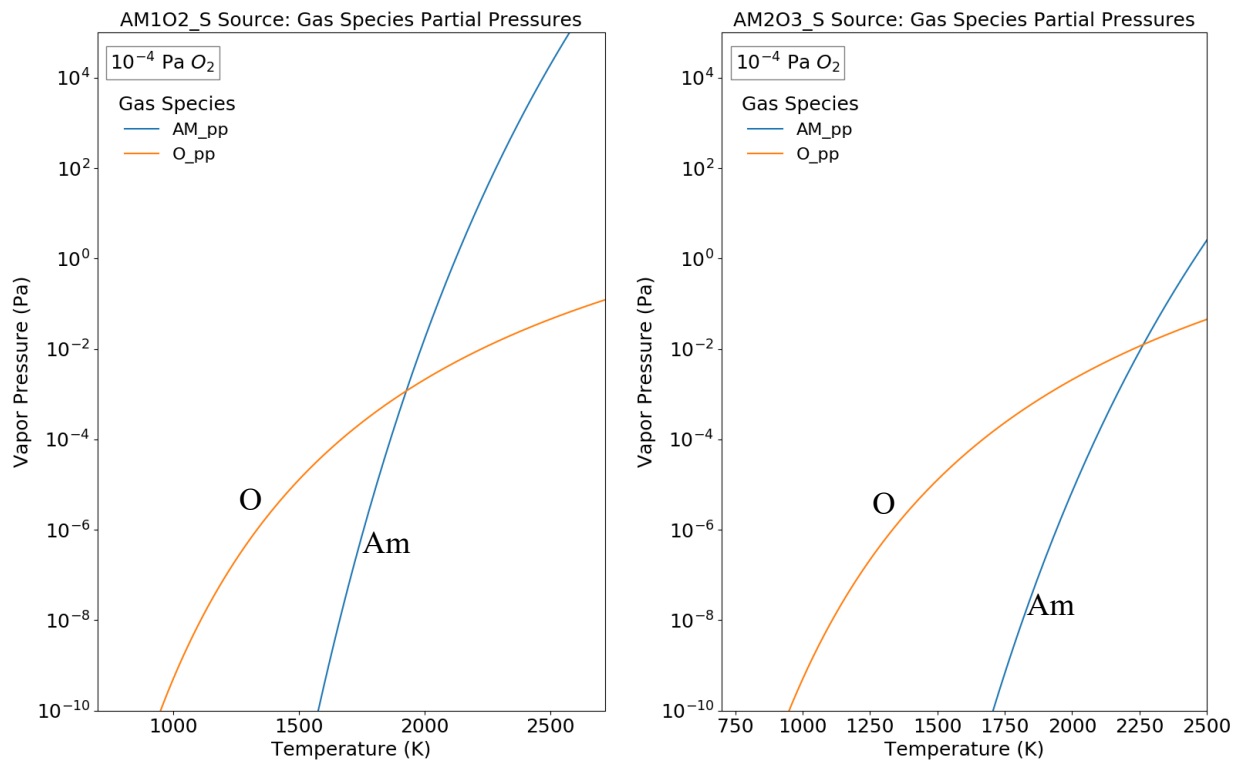


Figure S 4. Solid  $AmO_2$  and solid  $Am_2O_3$  ( $Am_2O_3$  is stable for  $T > 819$  K). Calculated partial pressures of the gas species over the phase(s) of interest as a function of temperature at  $P_{O_2} = 10^{-4}$  Pa. Here, “\_pp” indicates partial pressure when available.

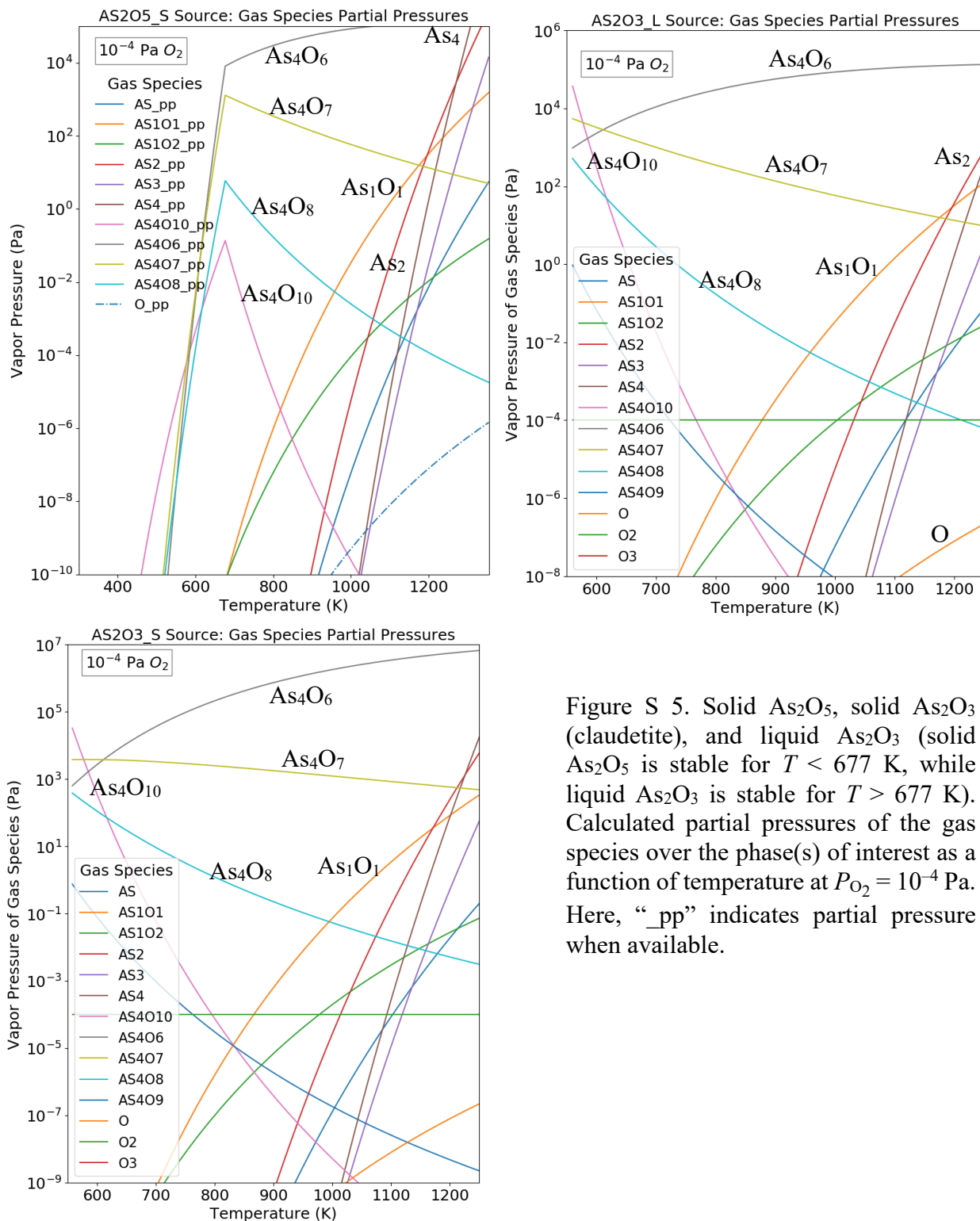


Figure S 5. Solid  $\text{As}_2\text{O}_5$ , solid  $\text{As}_2\text{O}_3$  (claudetite), and liquid  $\text{As}_2\text{O}_3$  (solid  $\text{As}_2\text{O}_5$  is stable for  $T < 677$  K, while liquid  $\text{As}_2\text{O}_3$  is stable for  $T > 677$  K). Calculated partial pressures of the gas species over the phase(s) of interest as a function of temperature at  $P_{\text{O}_2} = 10^{-4}$  Pa. Here, “\_pp” indicates partial pressure when available.

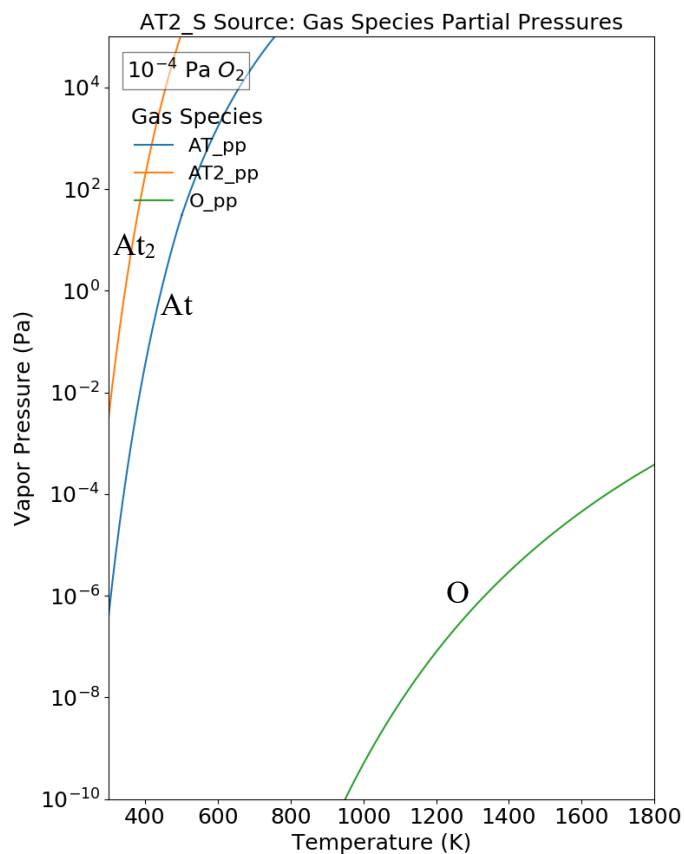


Figure S 6. Solid At (liquid At is stable for  $T > 500$  K). Calculated partial pressures of the gas species over the phase(s) of interest as a function of temperature at  $P_{O_2} = 10^{-4}$  Pa. Here, “\_pp” indicates partial pressure when available.

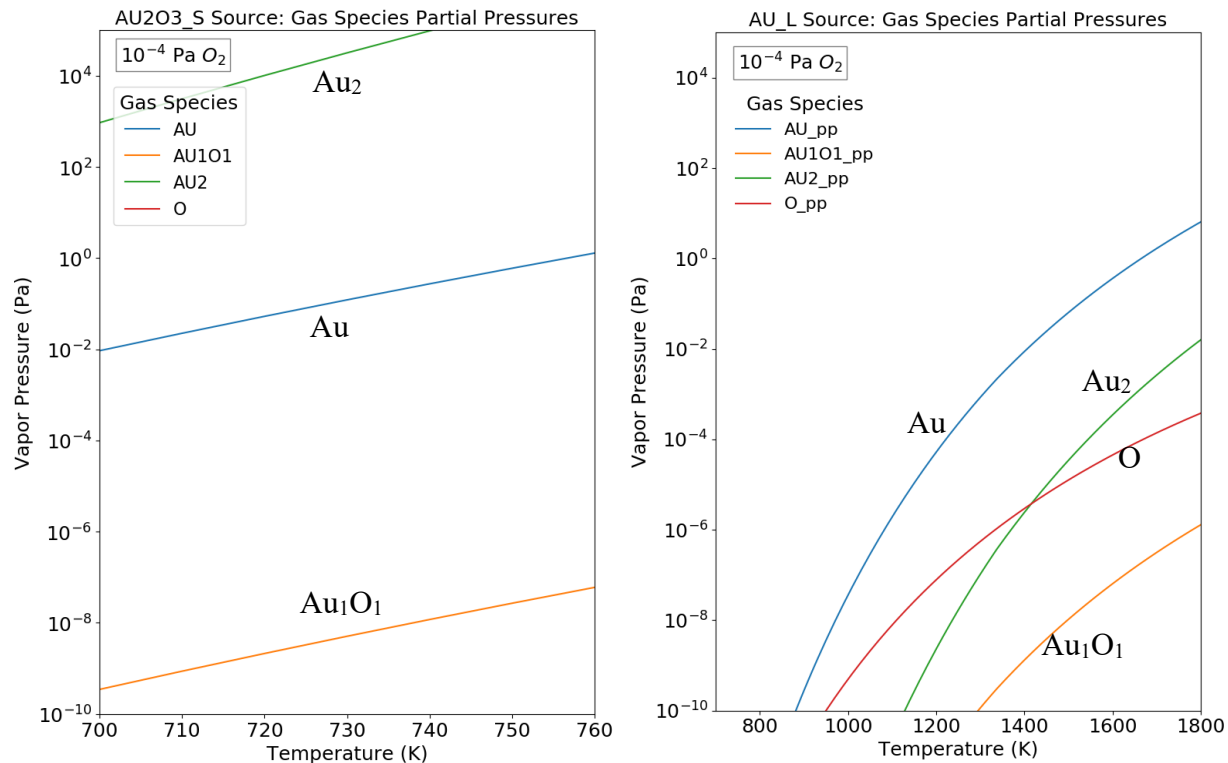


Figure S 7. Solid Au<sub>2</sub>O<sub>3</sub> and liquid Au (solid Au is stable for  $T < 1337$  K). Calculated partial pressures of the gas species over the phase(s) of interest as a function of temperature at  $P_{O_2} = 10^{-4}$  Pa. Here, “\_pp” indicates partial pressure when available.

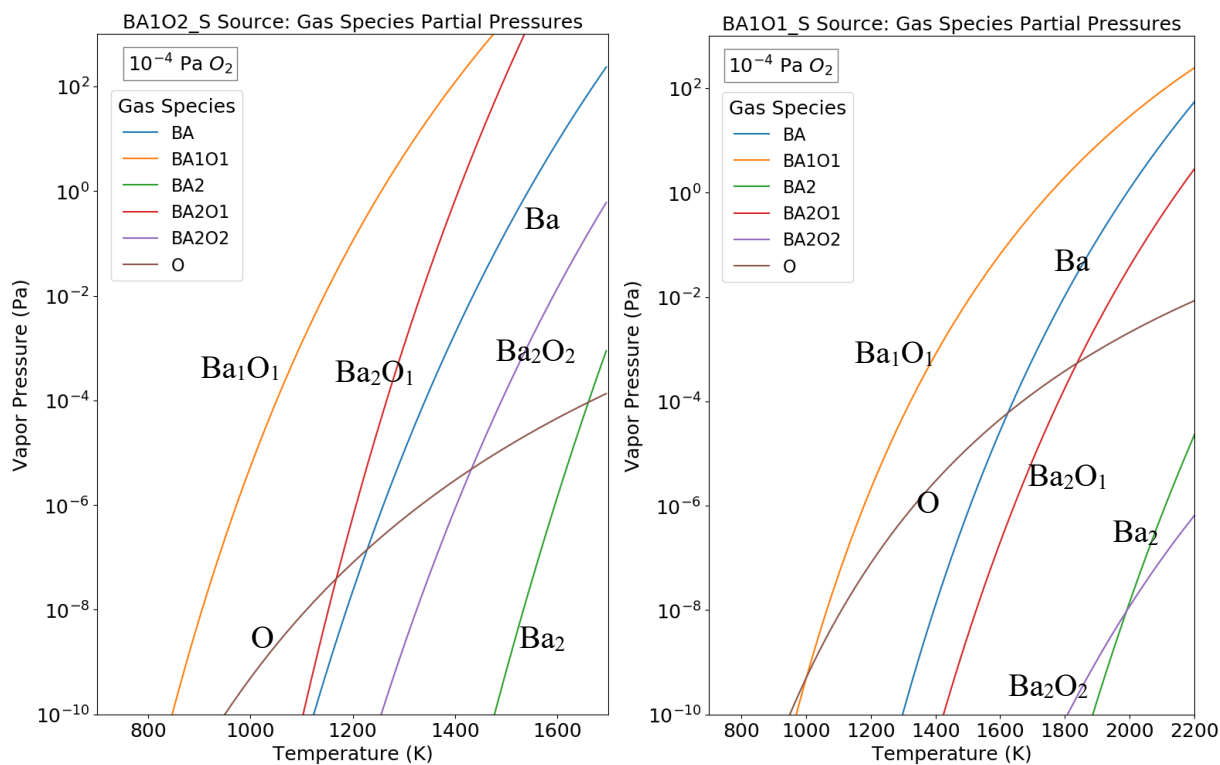


Figure S 8. Solid  $\text{BaO}_2$  and solid  $\text{BaO}$  (solid  $\text{BaO}$  is the stable phase for  $T < 2246$  K, beyond that liquid  $\text{BaO}$  will be stable). Calculated partial pressures of the gas species over the phase(s) of interest as a function of temperature at  $P_{\text{O}_2} = 10^{-4}$  Pa. Here, “\_pp” indicates partial pressure when available.

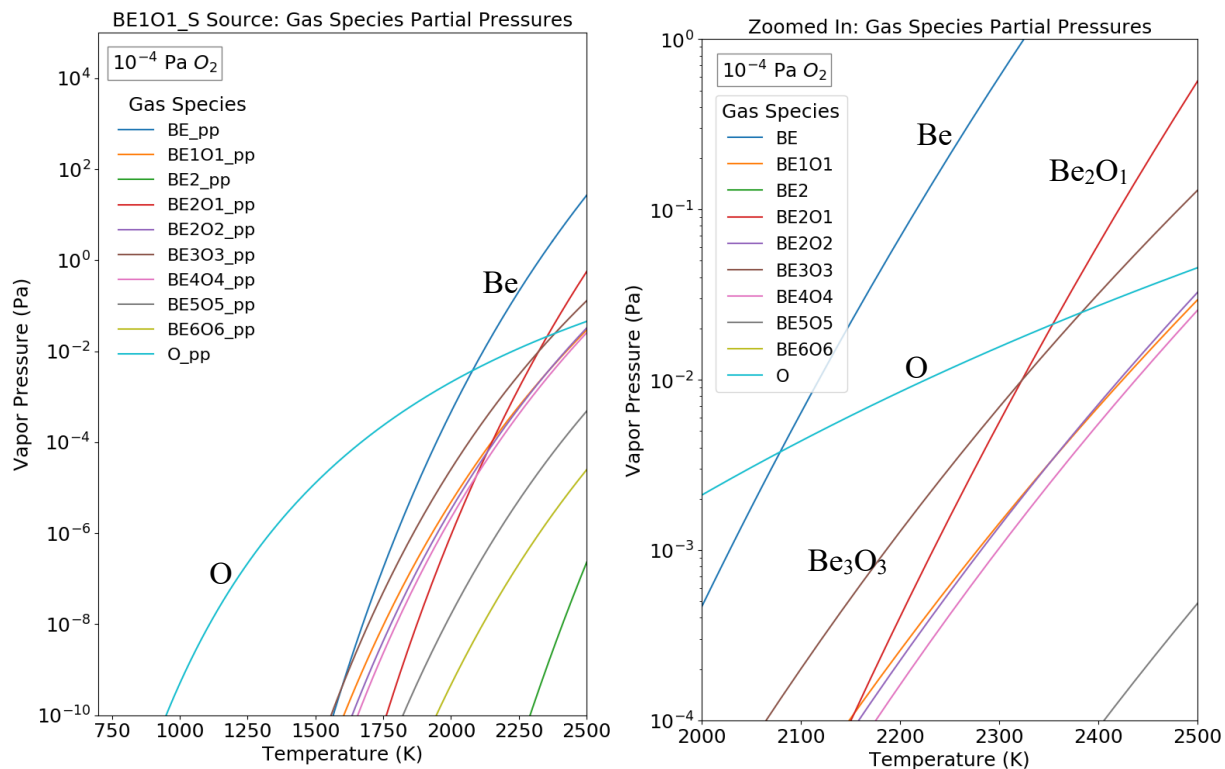


Figure S 9. Solid BeO (with a zoomed in plot on the right). Calculated partial pressures of the gas species over the phase(s) of interest as a function of temperature at  $P_{\text{O}_2} = 10^{-4}$  Pa. Here, “\_pp” indicates partial pressure when available.

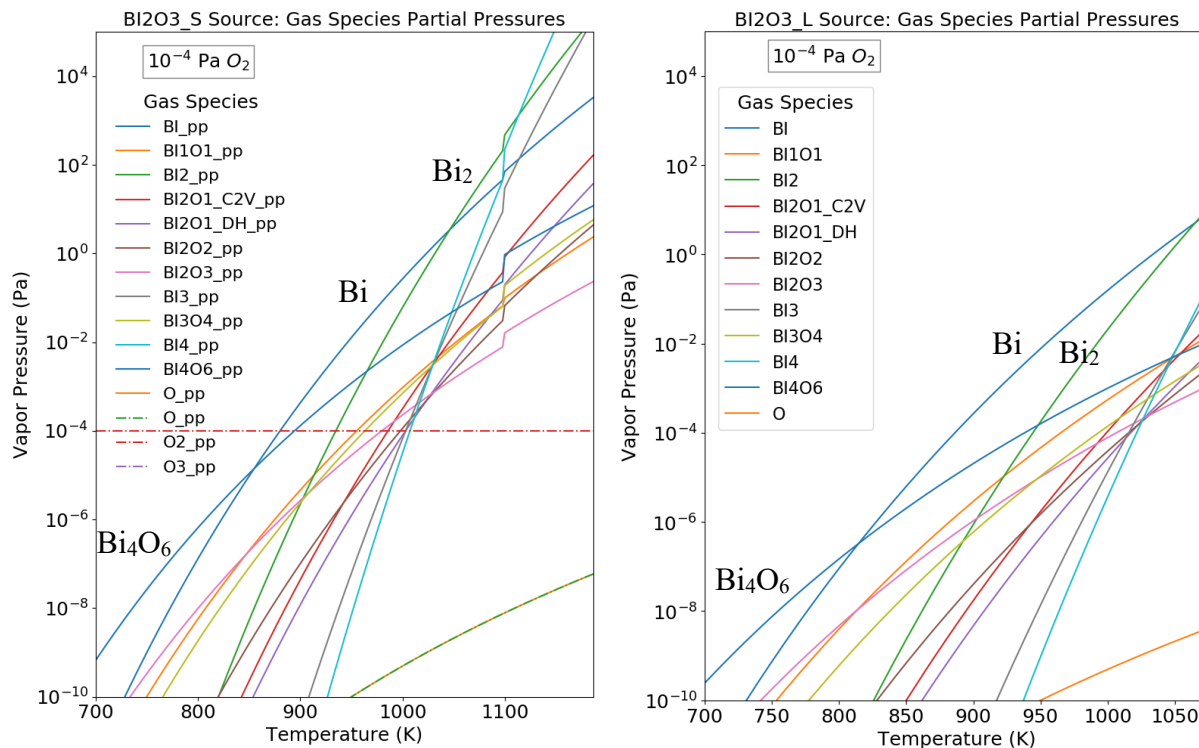


Figure S 10. Solid  $Bi_2O_3$  and liquid  $Bi_2O_3$  (note that liquid  $Bi$  is stable for  $T > 1075$  K). Calculated partial pressures of the gas species over the phase(s) of interest as a function of temperature at  $P_{O_2} = 10^{-4}$  Pa. Here, “\_pp” indicates partial pressure when available.

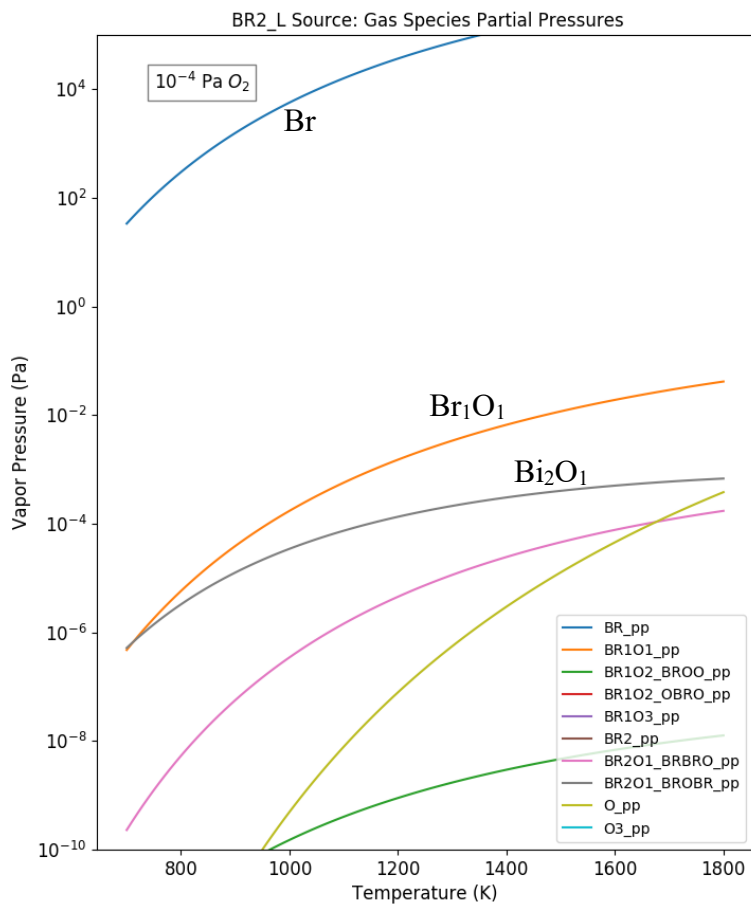


Figure S 11. Liquid Br. Calculated partial pressures of the gas species over the phase(s) of interest as a function of temperature at  $P_{O_2} = 10^{-4} \text{ Pa}$ . Here, “\_pp” indicates partial pressure when available.

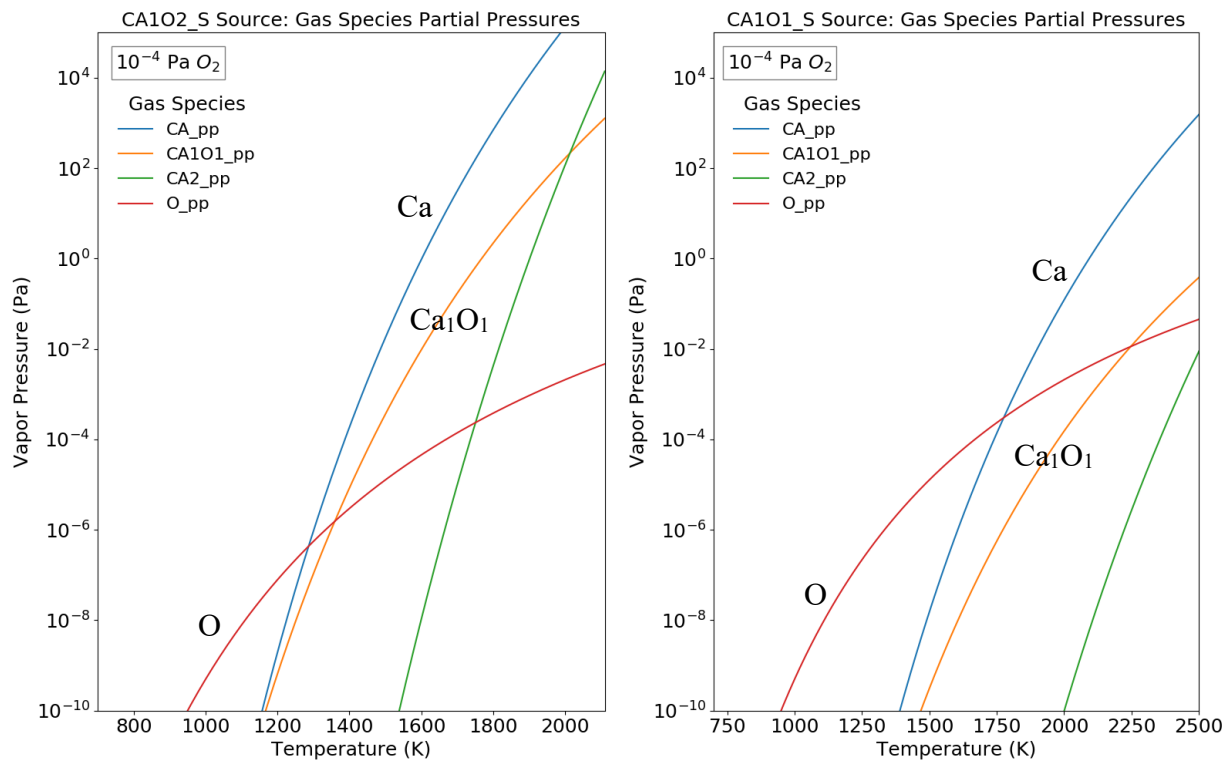


Figure S 12. Solid  $CaO_2$  and solid  $CaO$  (these are the stable phases over the entire temperature range shown). Calculated partial pressures of the gas species over the phase(s) of interest as a function of temperature at  $P_{O_2} = 10^{-4}$  Pa. Here, “\_pp” indicates partial pressure when available.

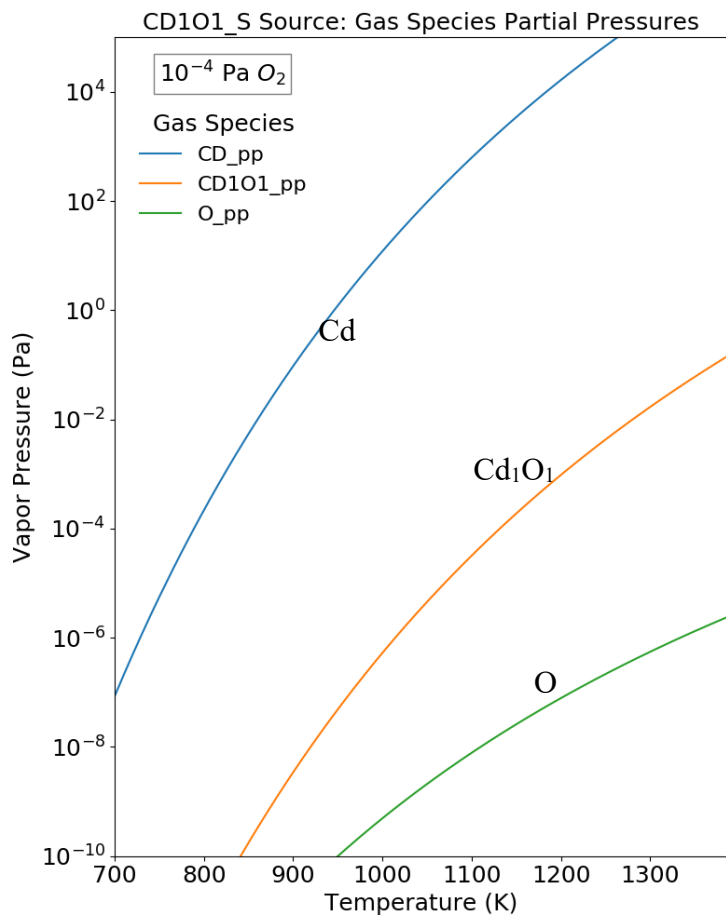
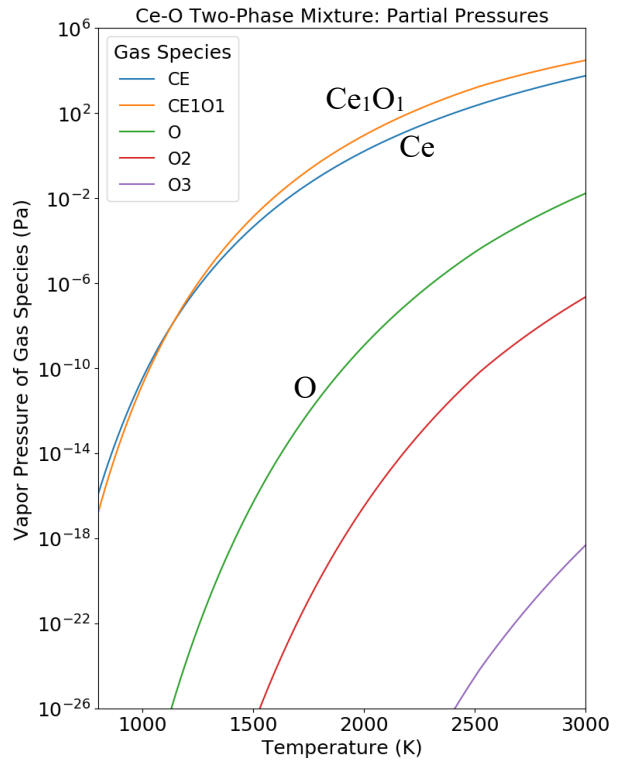
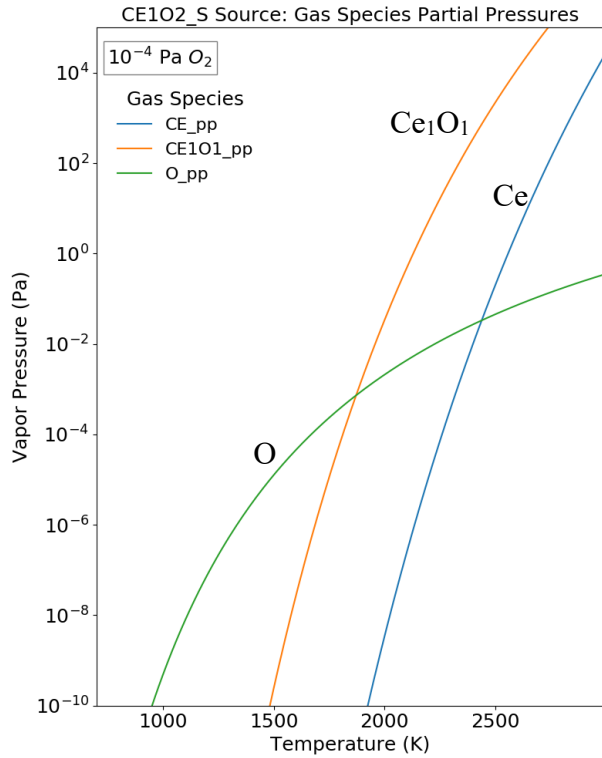
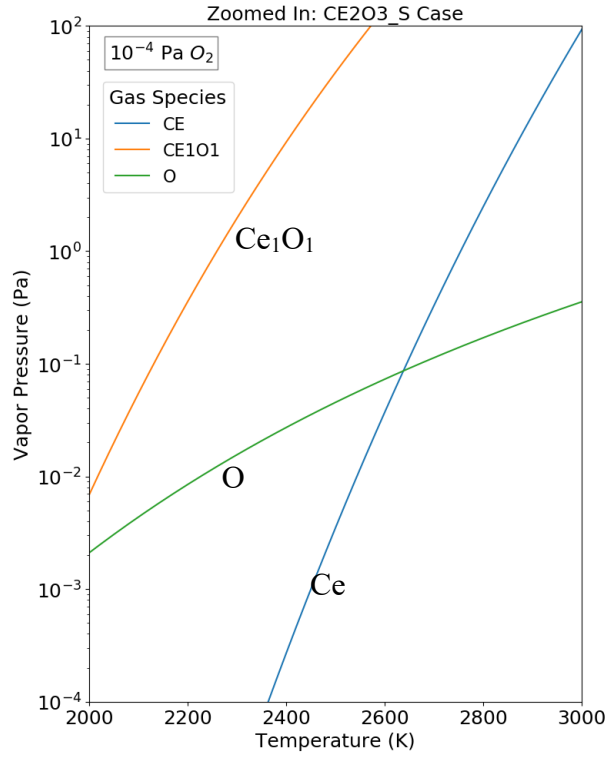
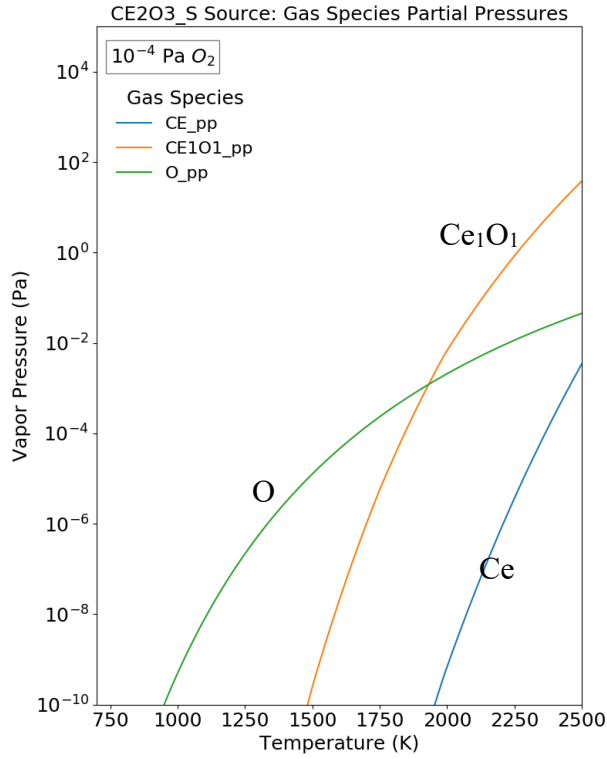


Figure S 13. Solid CdO. Calculated partial pressures of the gas species over the phase(s) of interest as a function of temperature at  $P_{O_2} = 10^{-4}$  Pa. Here, “\_pp” indicates partial pressure when available.



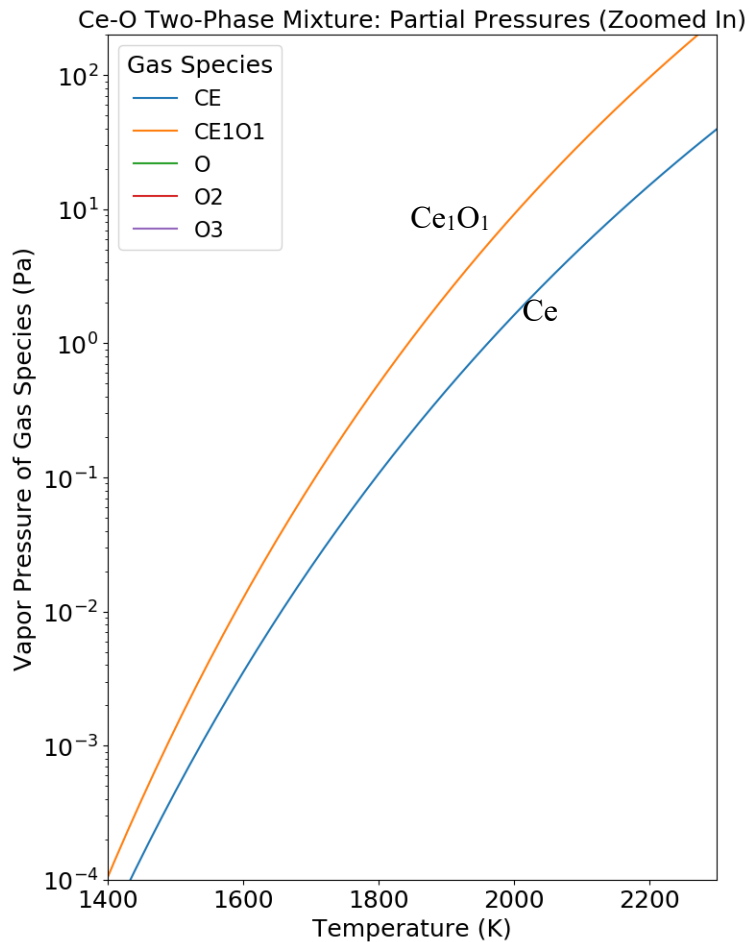


Figure S 14. Solid  $\text{CeO}_2$  (stable for  $T < 1506$  K) and metastable solid  $\text{Ce}_2\text{O}_3$ . Calculated partial pressures of the gas species over the phase(s) of interest as a function of temperature at  $P_{\text{O}_2} = 10^{-4}$  Pa. Here, “\_pp” indicates partial pressure when available. Calculated partial pressures of the gas species over a  $\text{Ce}_2\text{O}_3(\text{s},\ell) + \text{Ce}(\text{s},\ell)$  two-phase mixture with an overall composition of CeO. Here, (s, $\ell$ ) indicate the solid phase at low temperatures and liquid phase at high temperatures.

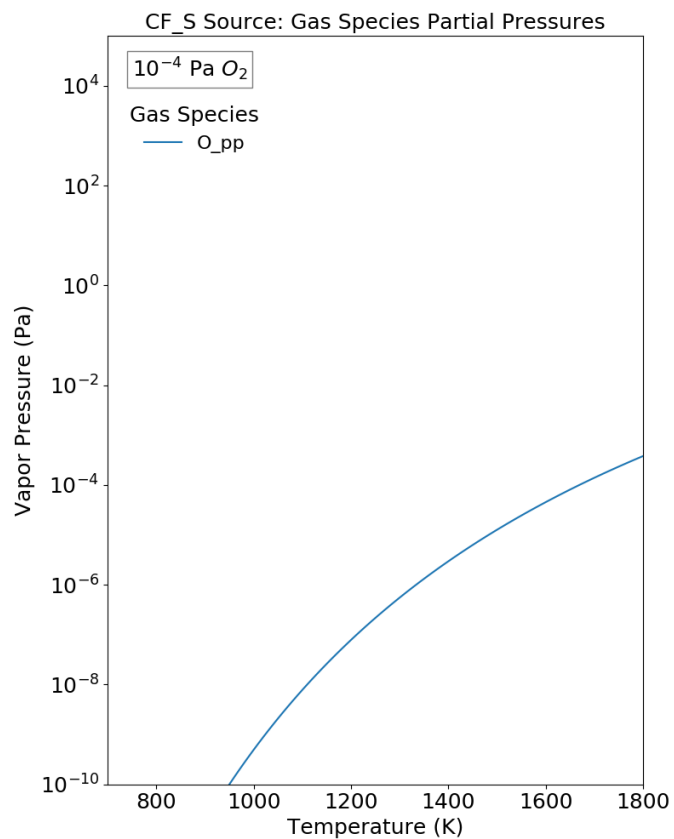


Figure S 15. Solid Cf. Calculated partial pressures of the gas species over the phase(s) of interest as a function of temperature at  $P_{O_2} = 10^{-4}$  Pa. Here, “\_pp” indicates partial pressure when available.

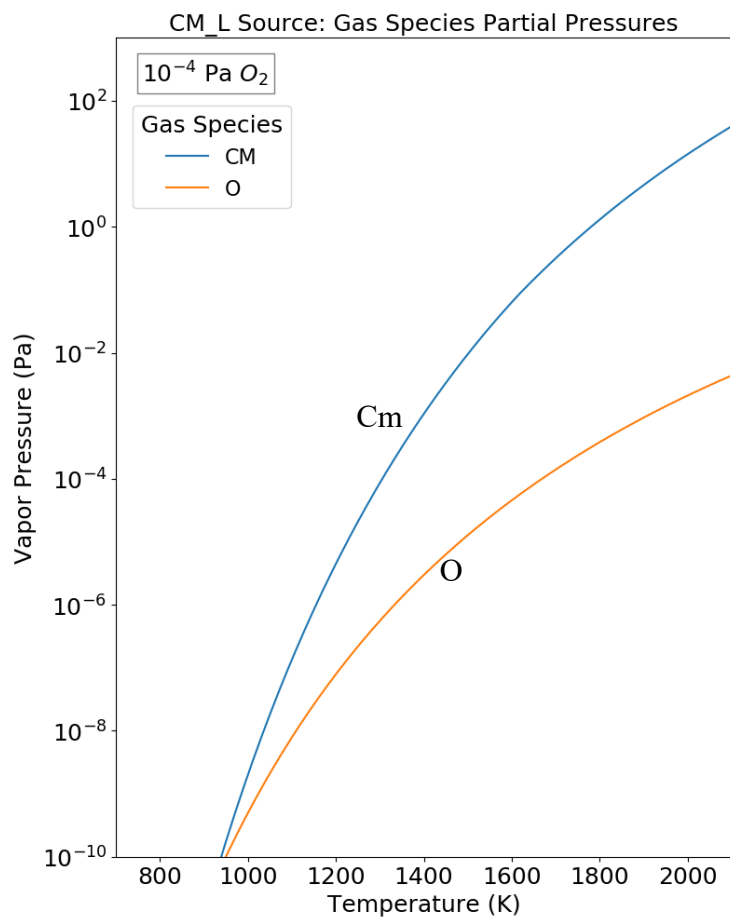


Figure S 16. Liquid Cm (liquid Cm is stable for  $T > 1618$  K). Calculated partial pressures of the gas species over the phase(s) of interest as a function of temperature at  $P_{O_2} = 10^{-4}$  Pa. Here, “\_pp” indicates partial pressure when available.

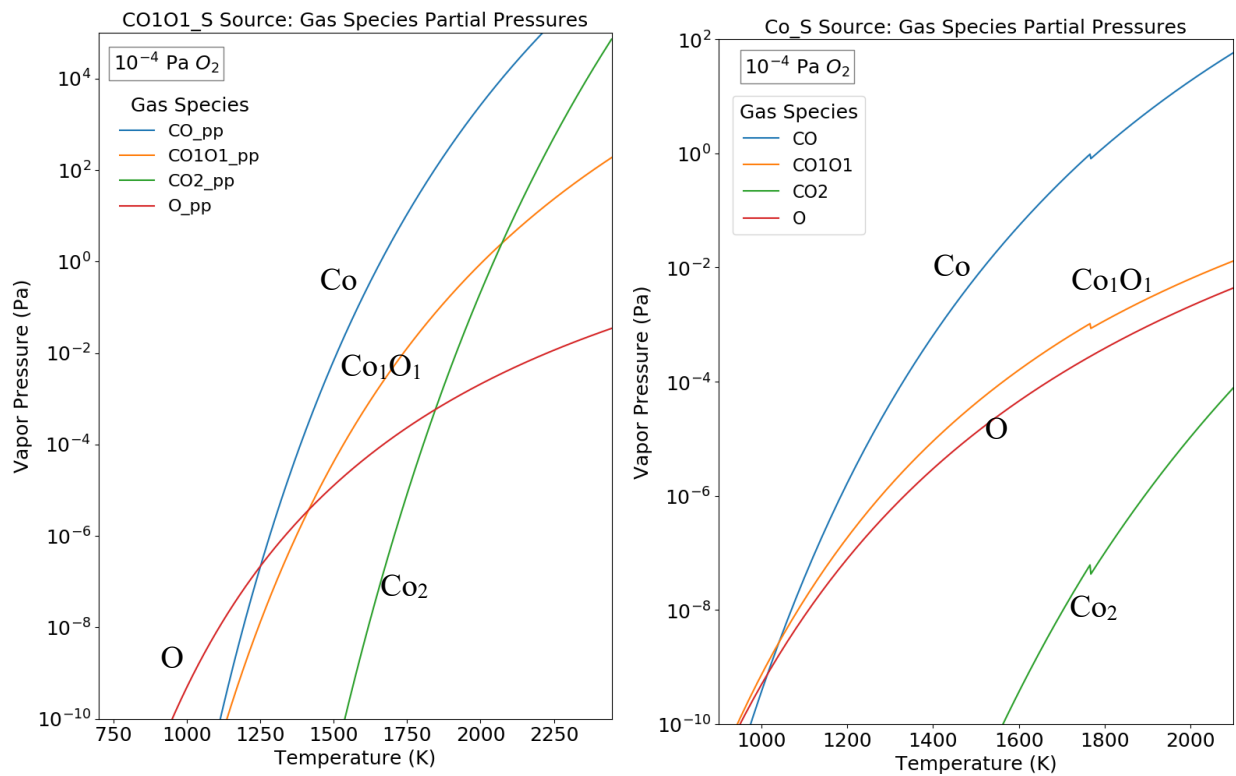


Figure S 17. Solid CoO and solid Co. Calculated partial pressures of the gas species over the phase(s) of interest as a function of temperature at  $P_{O_2} = 10^{-4}$  Pa. Here, “\_pp” indicates partial pressure when available. Note that solid CoO is stable when  $803 < T < 1496$  K, solid Co is stable when  $1496 < T < 1768$  K, and liquid Co is stable when  $T > 1768$  K.

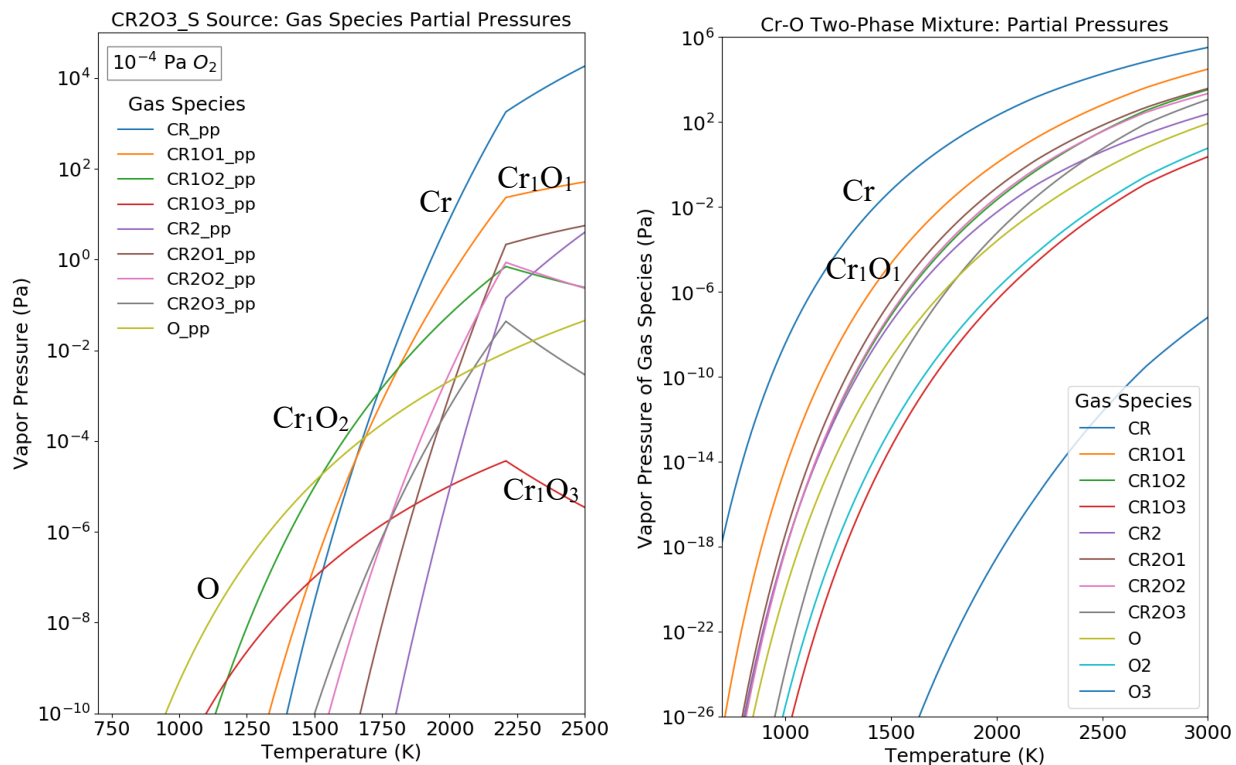


Figure S 18. Solid  $Cr_2O_3$  (solid  $Cr_2O_3$  is stable for  $T < 2208$  K, beyond which liquid Cr is stable). Calculated partial pressures of the gas species over the phase(s) of interest as a function of temperature at  $P_{O_2} = 10^{-4}$  Pa. Here, “\_pp” indicates partial pressure when available. Calculated partial pressures of the gas species over a  $Cr_2O_3(s)+Cr(s,\ell)$  two-phase mixture with an overall composition of CrO. Here, (s, $\ell$ ) indicate the solid phase at low temperatures and liquid phase at high temperatures.

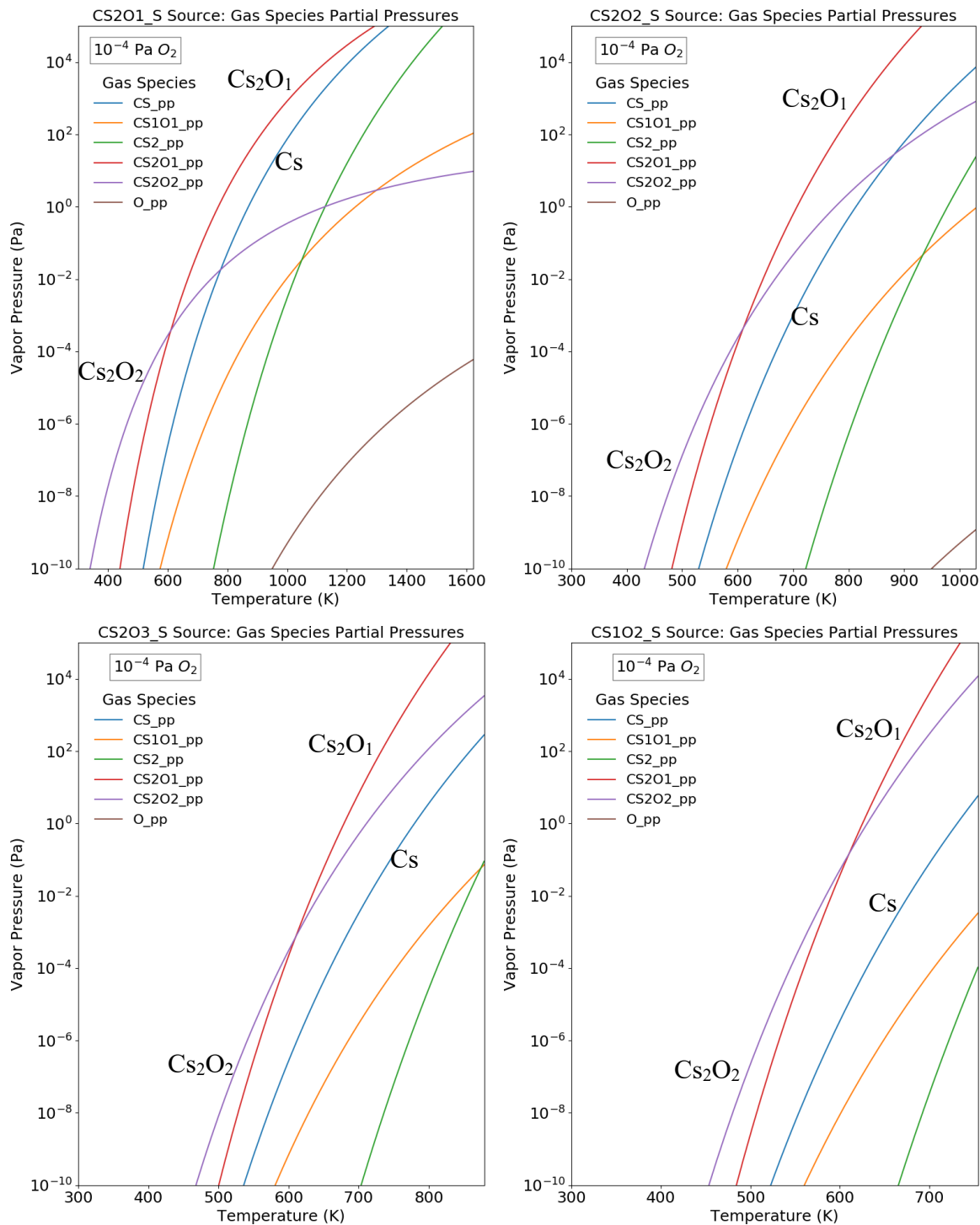


Figure S 19. Solid Cs<sub>2</sub>O, solid Cs<sub>2</sub>O<sub>2</sub>, solid Cs<sub>2</sub>O<sub>3</sub>, and solid CsO<sub>2</sub> (solid CsO<sub>2</sub> is the stable phase). Calculated partial pressures of the gas species over the phase(s) of interest as a function of temperature at  $P_{O_2} = 10^{-4}$  Pa. Here, “\_pp” indicates partial pressure when available.

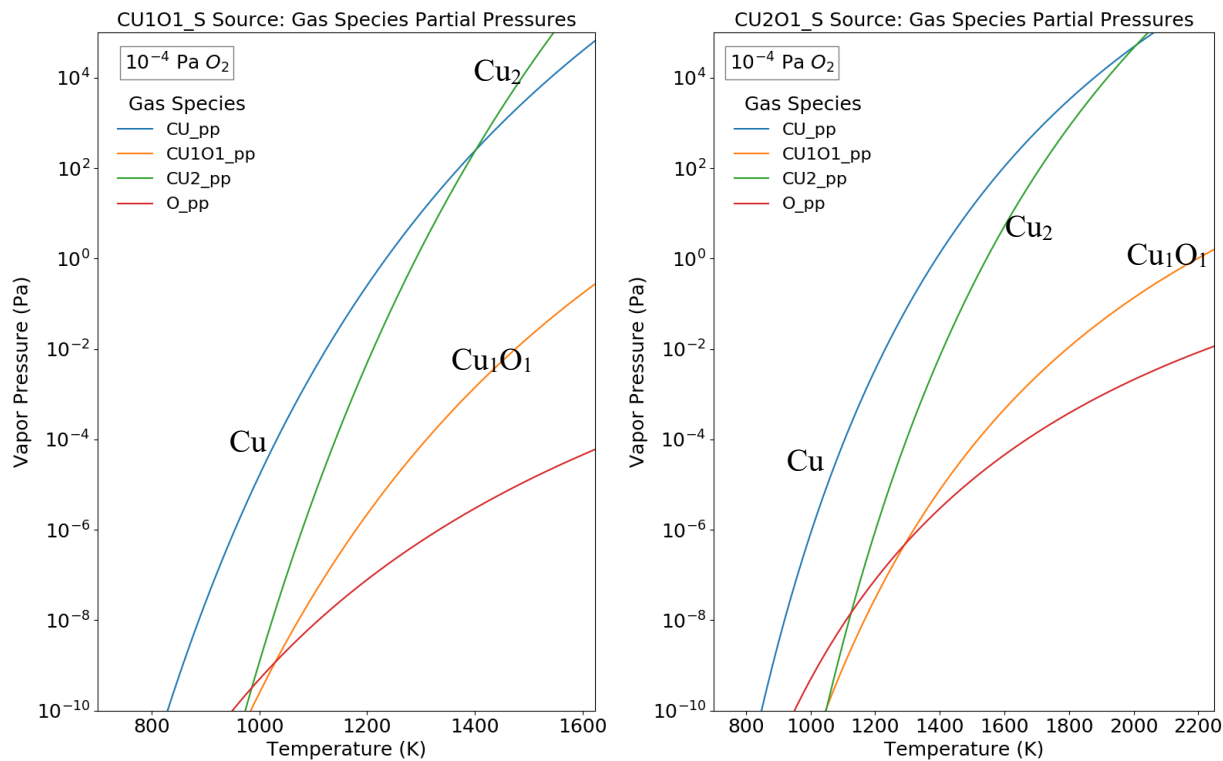


Figure S 20. Solid CuO and solid Cu<sub>2</sub>O (solid Cu<sub>2</sub>O is stable for  $T < 1059$  K, beyond which solid Cu is stable). Calculated partial pressures of the gas species over the phase(s) of interest as a function of temperature at  $P_{O_2} = 10^{-4}$  Pa. Here, “\_pp” indicates partial pressure when available.

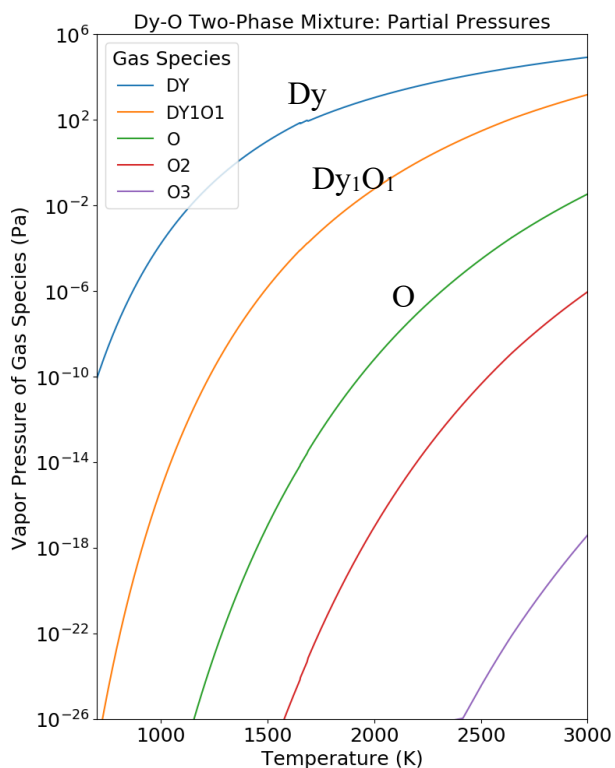
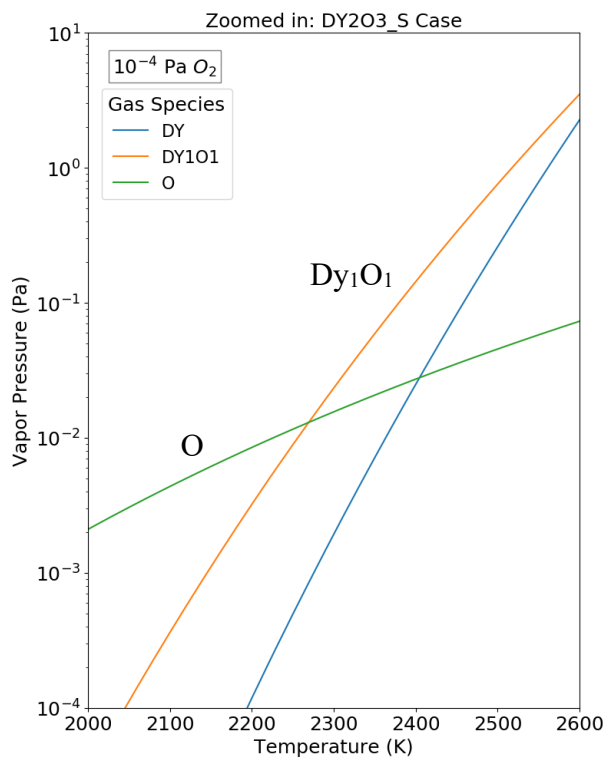
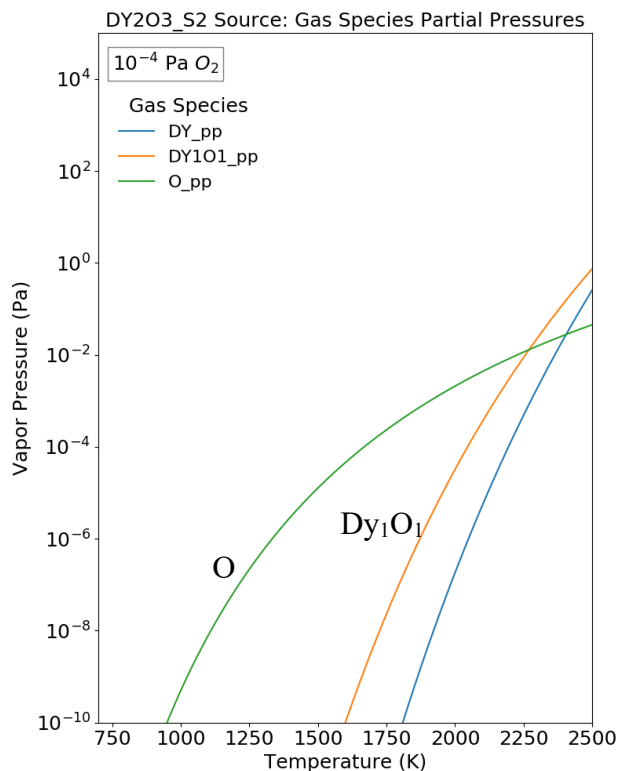


Figure S 21. Solid Dy<sub>2</sub>O<sub>3</sub> (solid Dy<sub>2</sub>O<sub>3</sub> is the stable phase over the temperature range shown). Calculated partial pressures of the gas species over the phase(s) of interest as a function of temperature at  $P_{O_2} = 10^{-4}$  Pa. Here, “\_pp” indicates partial pressure when available. Calculated partial pressures of the gas species over a Dy<sub>2</sub>O<sub>3</sub>(s,*l*)+Dy(s,*l*) two-phase mixture with an overall composition of DyO. Here, (s,*l*) indicate the solid phase at low temperatures and liquid phase at high temperatures.

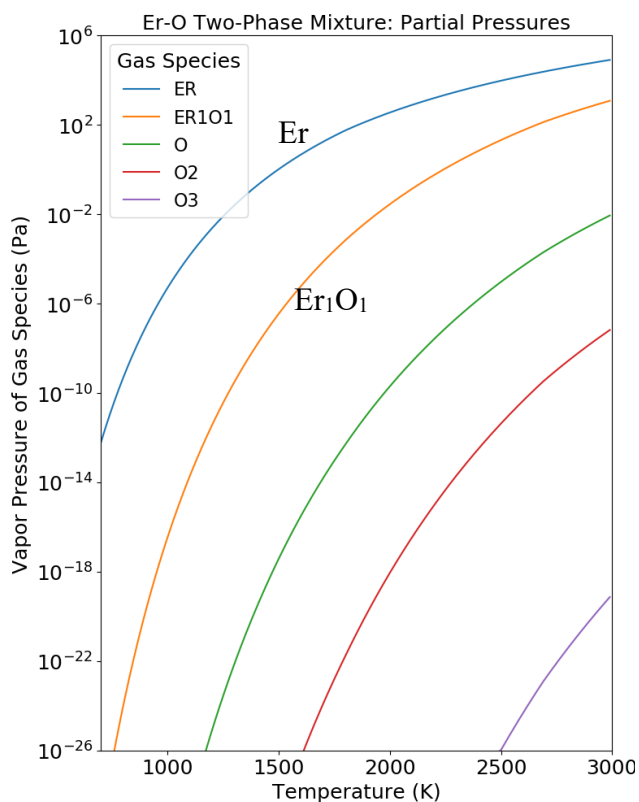
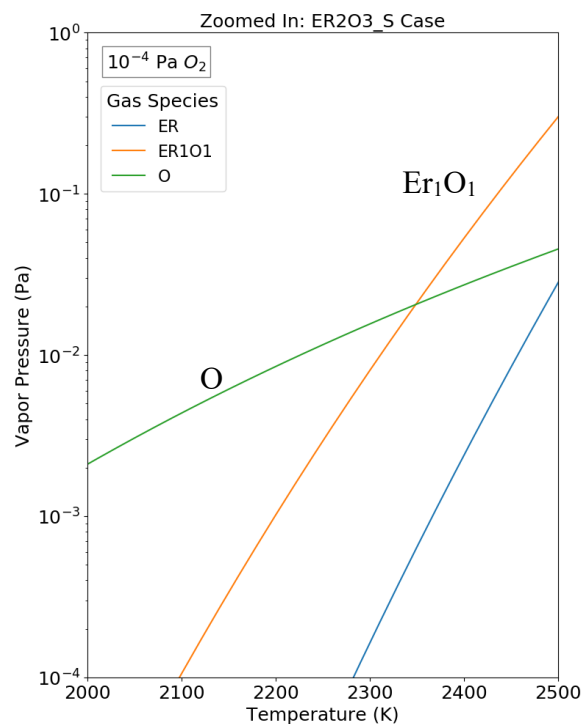
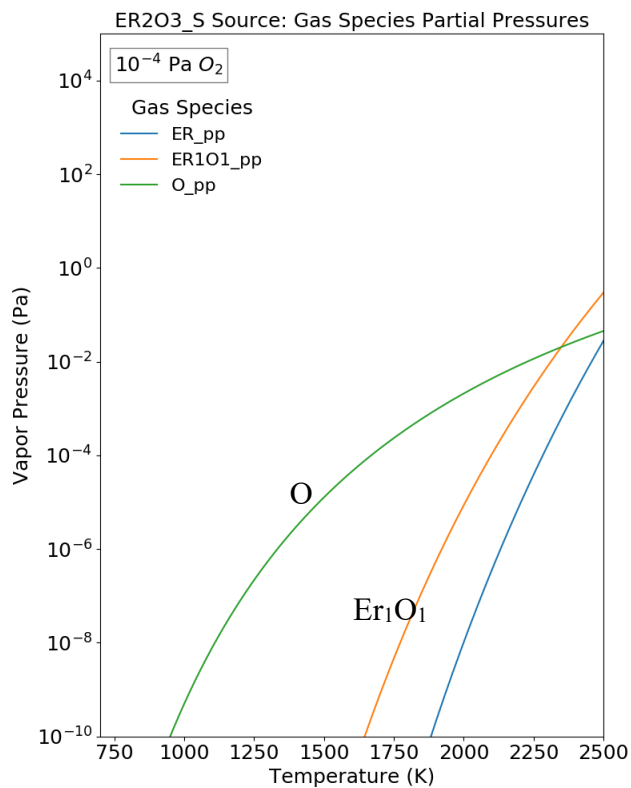


Figure S 22. Solid Er<sub>2</sub>O<sub>3</sub> (with a zoomed-in view in the plot on the right). Calculated partial pressures of the gas species over the phase(s) of interest as a function of temperature at  $P_{O_2} = 10^{-4}$  Pa. Here, “\_pp” indicates partial pressure when available. Calculated partial pressures of the gas species over a Er<sub>2</sub>O<sub>3</sub>(s, $\ell$ ) + Er(s, $\ell$ ) two-phase mixture with an overall composition of ErO. Here, (s, $\ell$ ) indicate the solid phase at low temperatures and liquid phase at high temperatures.

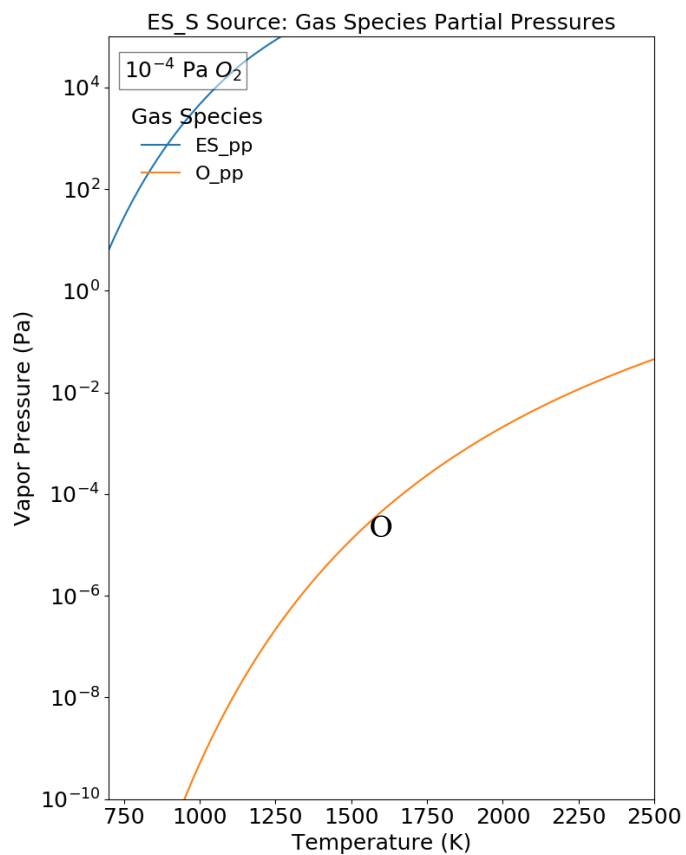


Figure S 23. Solid Es (solid Es stable for  $T < 1133$  K, beyond which the liquid Es is stable). Calculated partial pressures of the gas species over the phase(s) of interest as a function of temperature at  $P_{O_2} = 10^{-4}$  Pa. Here, “\_pp” indicates partial pressure when available.

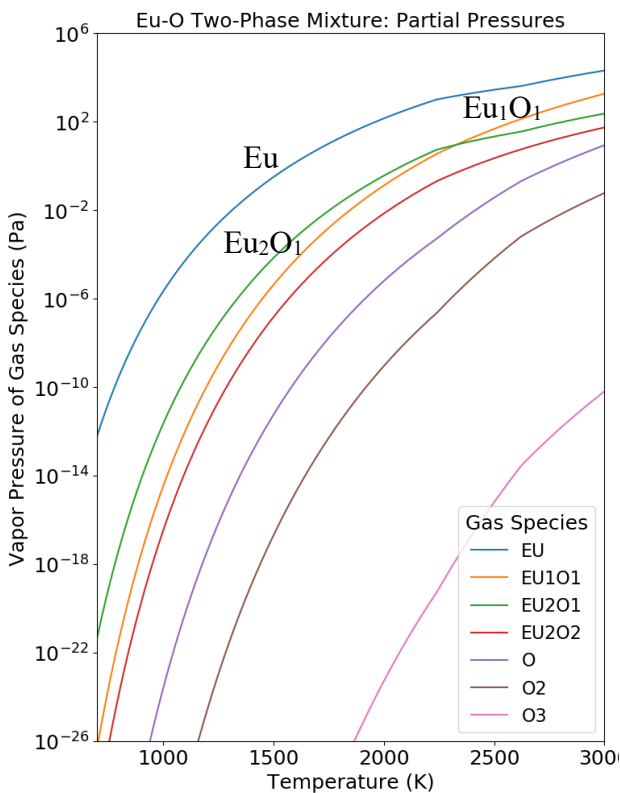
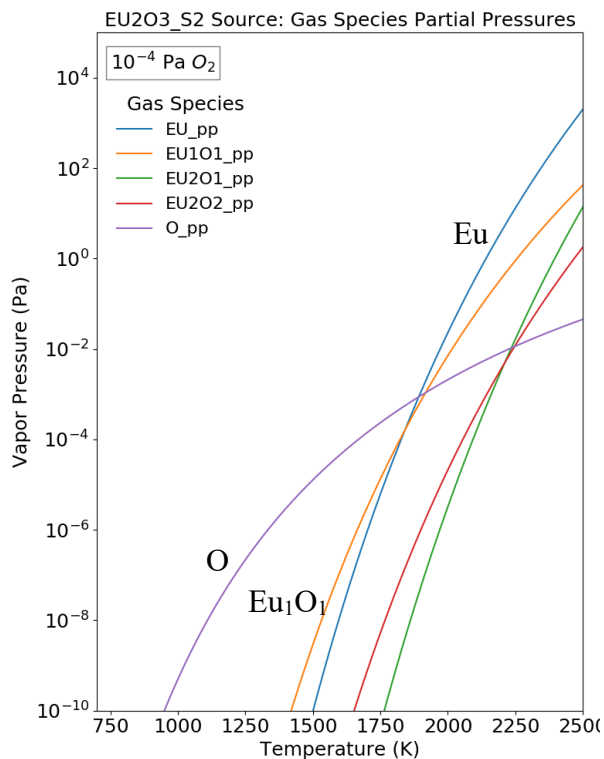
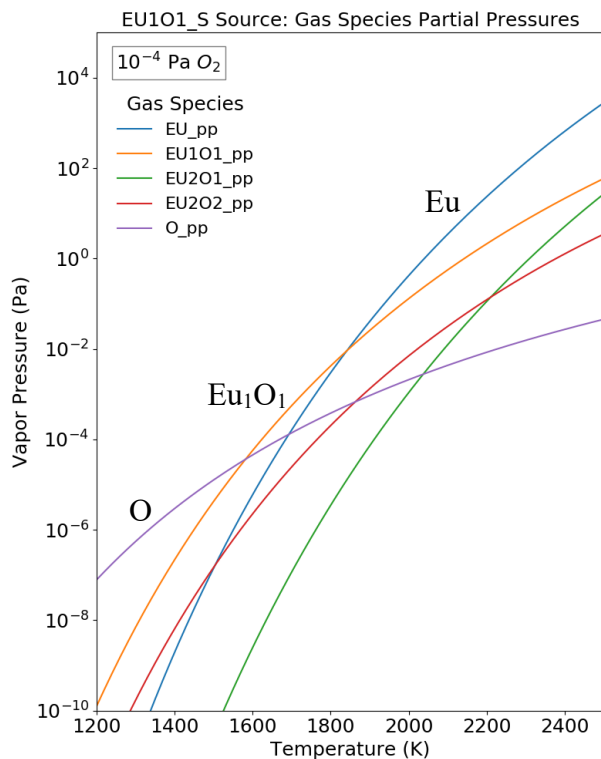


Figure S 24. Solid EuO and solid Eu<sub>2</sub>O<sub>3</sub> (solid Eu<sub>2</sub>O<sub>3</sub> is the stable phase). Calculated partial pressures of the gas species over the phase(s) of interest as a function of temperature at  $P_{O_2} = 10^{-4}$  Pa. Here, “\_pp” indicates partial pressure when available. Calculated partial pressures of the gas species over a Eu<sub>2</sub>O<sub>3</sub>(s,ℓ)+Eu(s,ℓ) two-phase mixture with an overall composition of EuO. Here, (s,ℓ) indicate the solid phase at low temperatures and liquid phase at high temperatures.

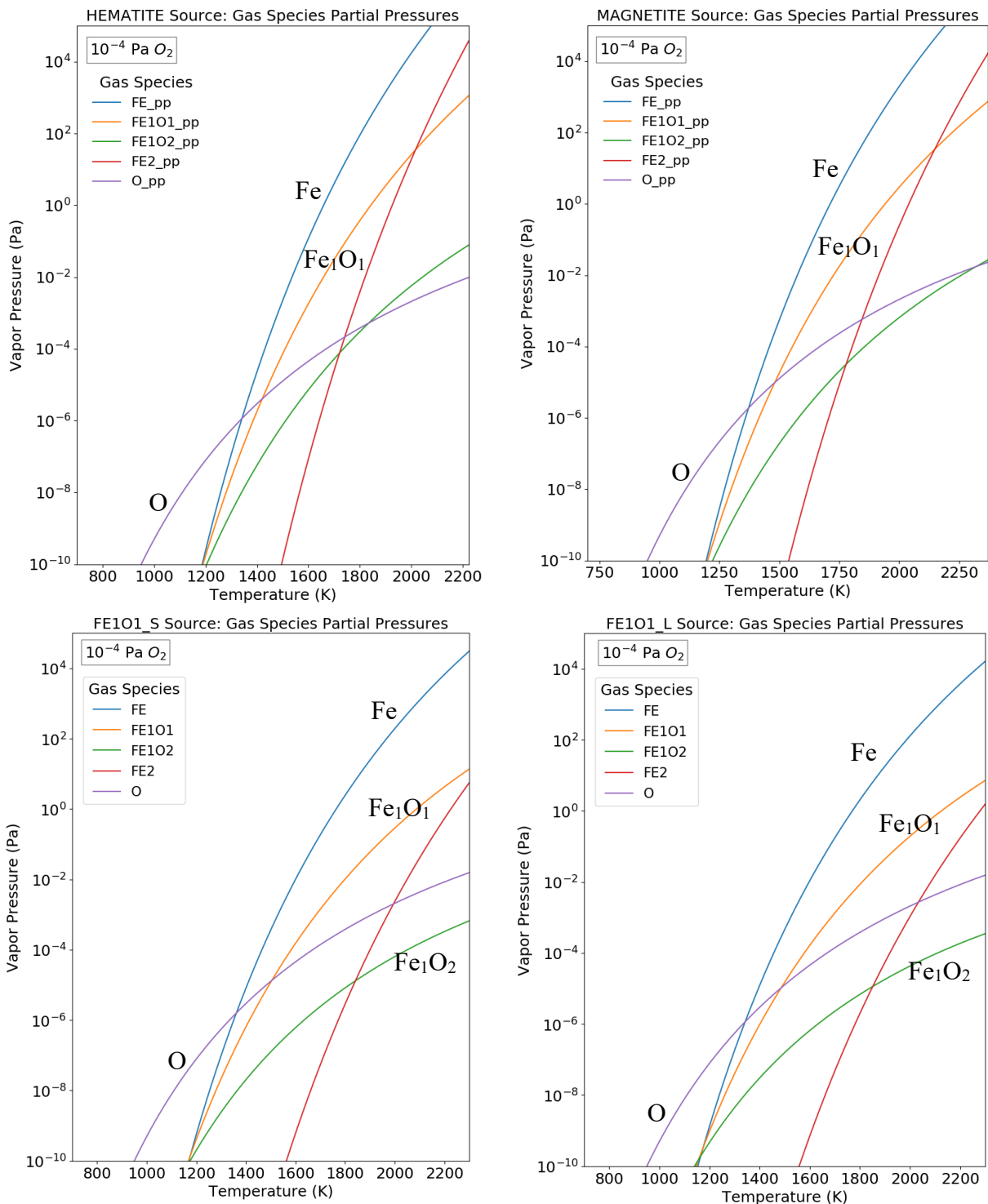


Figure S 25. Solid  $\text{Fe}_2\text{O}_3$  (hematite, stable for  $T < 1051$  K), solid  $\text{Fe}_3\text{O}_4$  (magnetite, stable for  $1051$  K  $< T < 1245$  K), solid  $\text{FeO}$  (stable for  $1421$  K  $< T < 1650$  K), and liquid  $\text{FeO}$  (stable  $T > 1650$  K). Calculated partial pressures of the gas species over the phase(s) of interest as a function of temperature at  $P_{\text{O}_2} = 10^{-4}$  Pa. Here, “\_pp” indicates partial pressure when available. The liquid state of  $\text{FeO}(\ell)$  denotes what in practice should be a slag phase with a mixture of all iron oxides such as  $\text{FeO}$ ,  $\text{Fe}_3\text{O}_4$ , and  $\text{Fe}_2\text{O}_3$ .

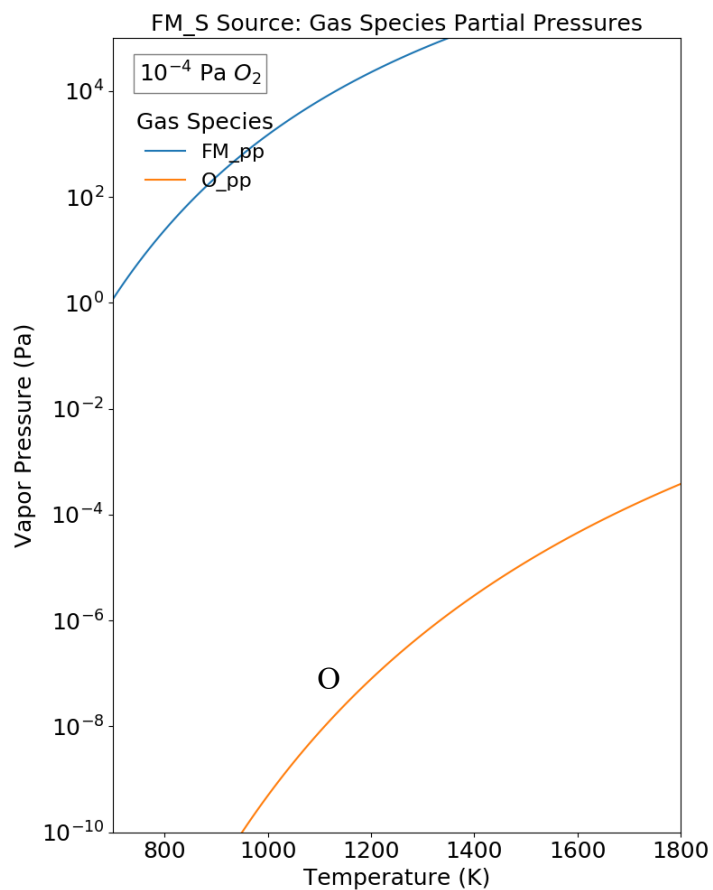


Figure S 26. Solid Fm (the stable phase). Calculated partial pressures of the gas species over the phase(s) of interest as a function of temperature at  $P_{O_2} = 10^{-4}$  Pa. Here, “\_pp” indicates partial pressure when available.

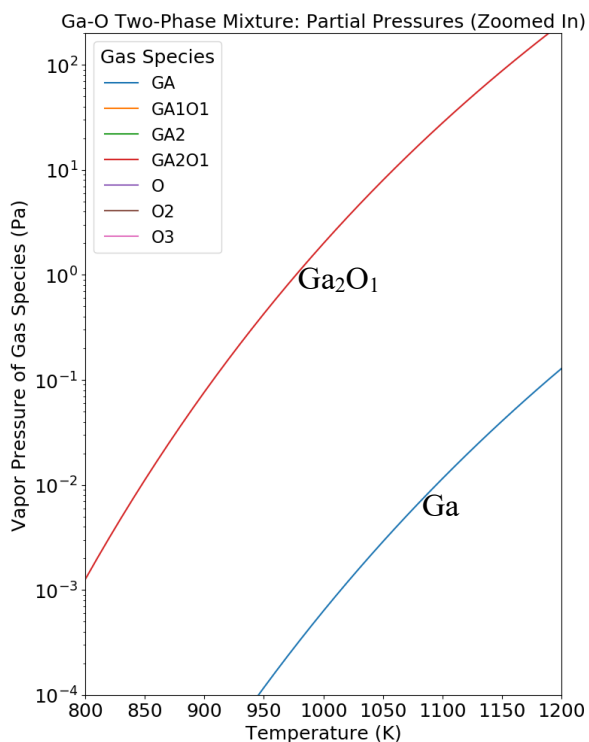
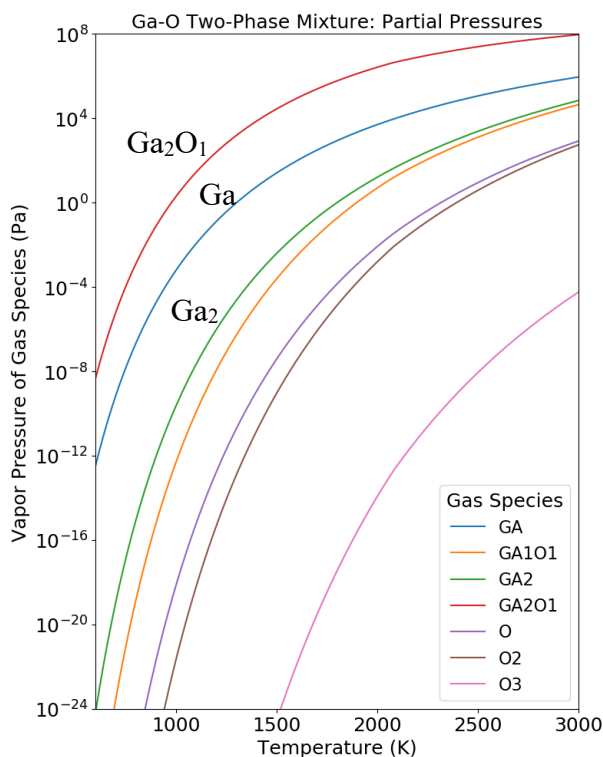
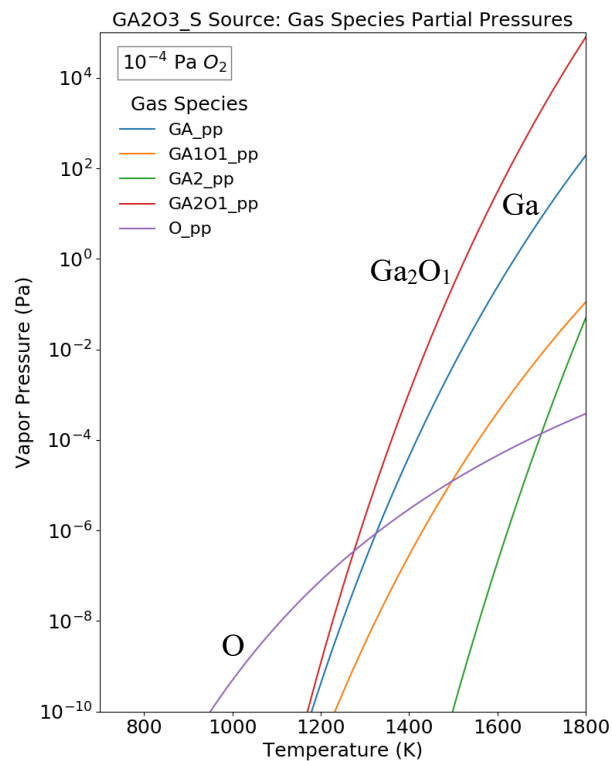


Figure S 27. Solid Ga<sub>2</sub>O<sub>3</sub> (the stable phase). Calculated partial pressures of the gas species over the phase(s) of interest as a function of temperature at  $P_{O_2} = 10^{-4}$  Pa. Here, “\_pp” indicates partial pressure when available. Calculated partial pressures of the gas species over a Ga<sub>2</sub>O<sub>3</sub>(s,ℓ)+Ga(ℓ) two-phase mixture with an overall composition of Ga<sub>2</sub>O. Here, (s,ℓ) indicate the solid phase at low temperatures and liquid phase at high temperatures.

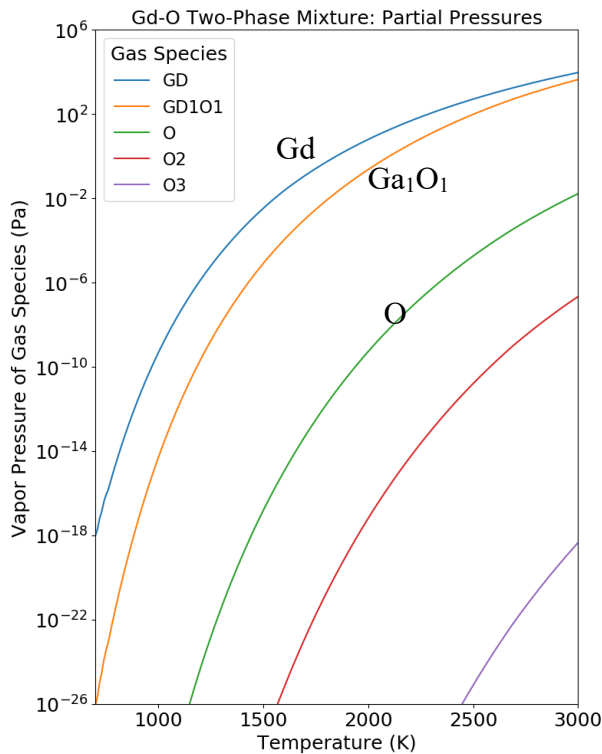
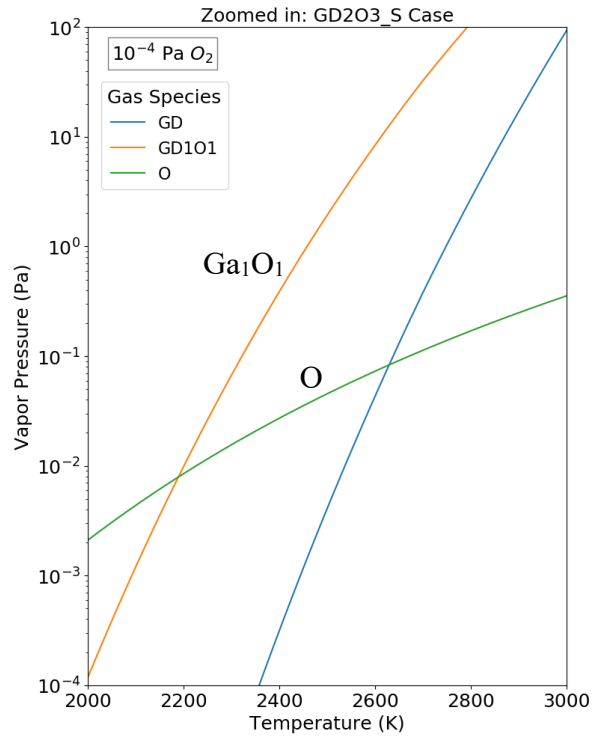
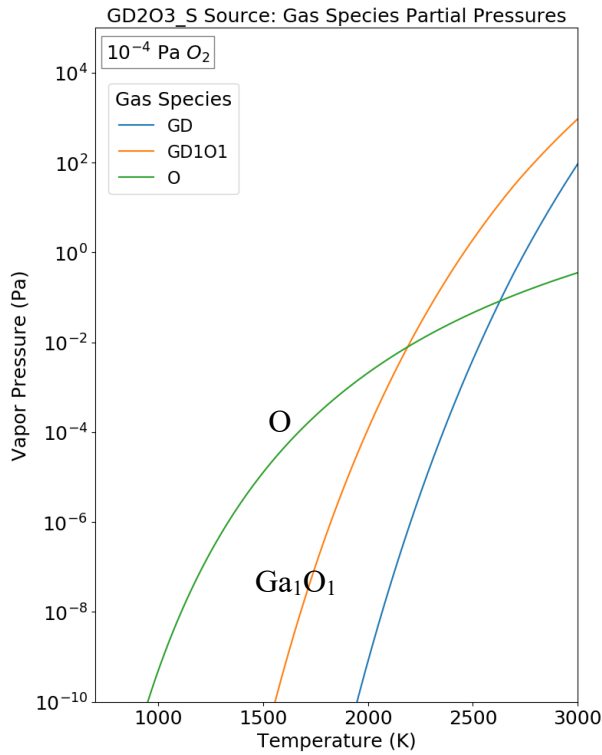
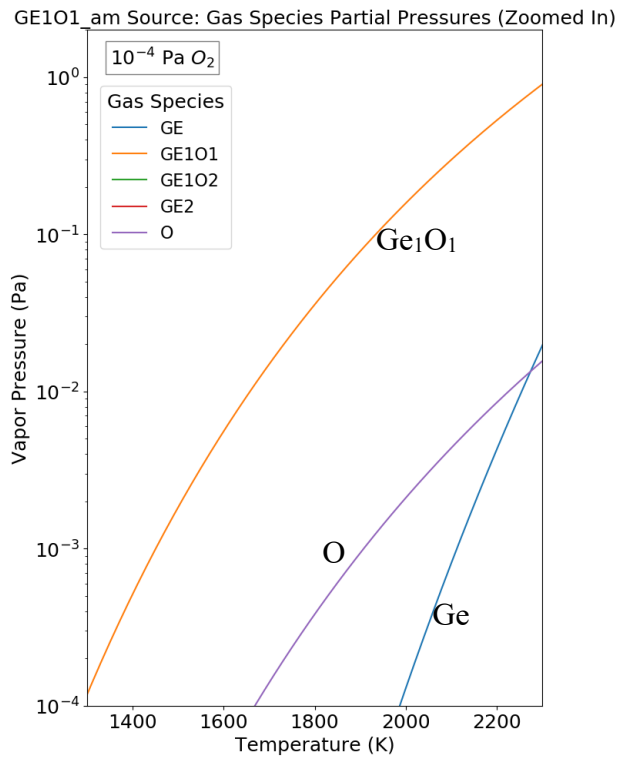
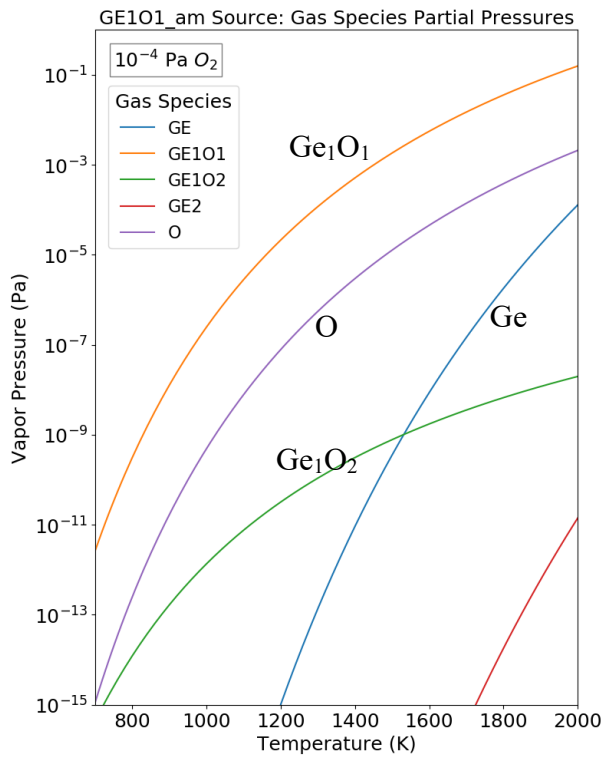
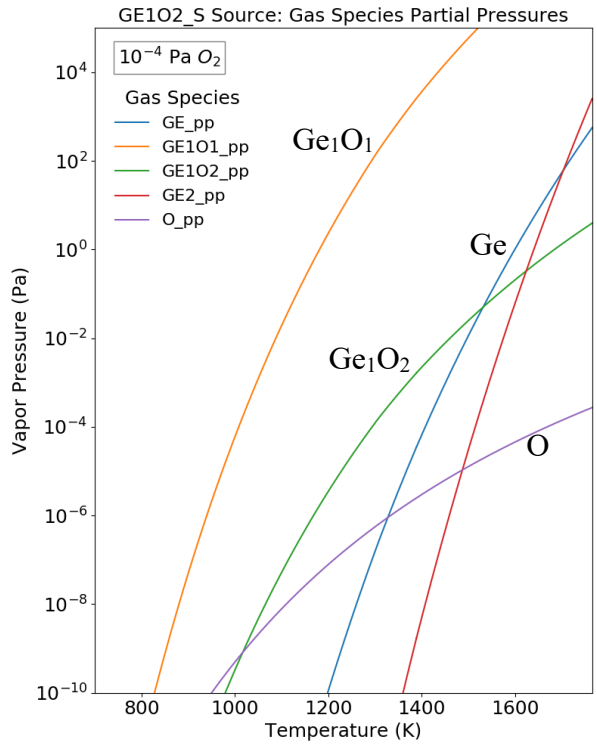


Figure S 28. Solid  $Gd_2O_3$  (stable for  $T < 2698$  K). Calculated partial pressures of the gas species over the phase(s) of interest as a function of temperature at  $P_{O_2} = 10^{-4}$  Pa. Here, “\_pp” indicates partial pressure when available. Calculated partial pressures of the gas species over a  $Gd_2O_3(s,\ell)+Gd(s,\ell)$  two-phase mixture with an overall composition of GdO. Here, (s, $\ell$ ) indicate the solid phase at low temperatures and liquid phase at high temperatures.



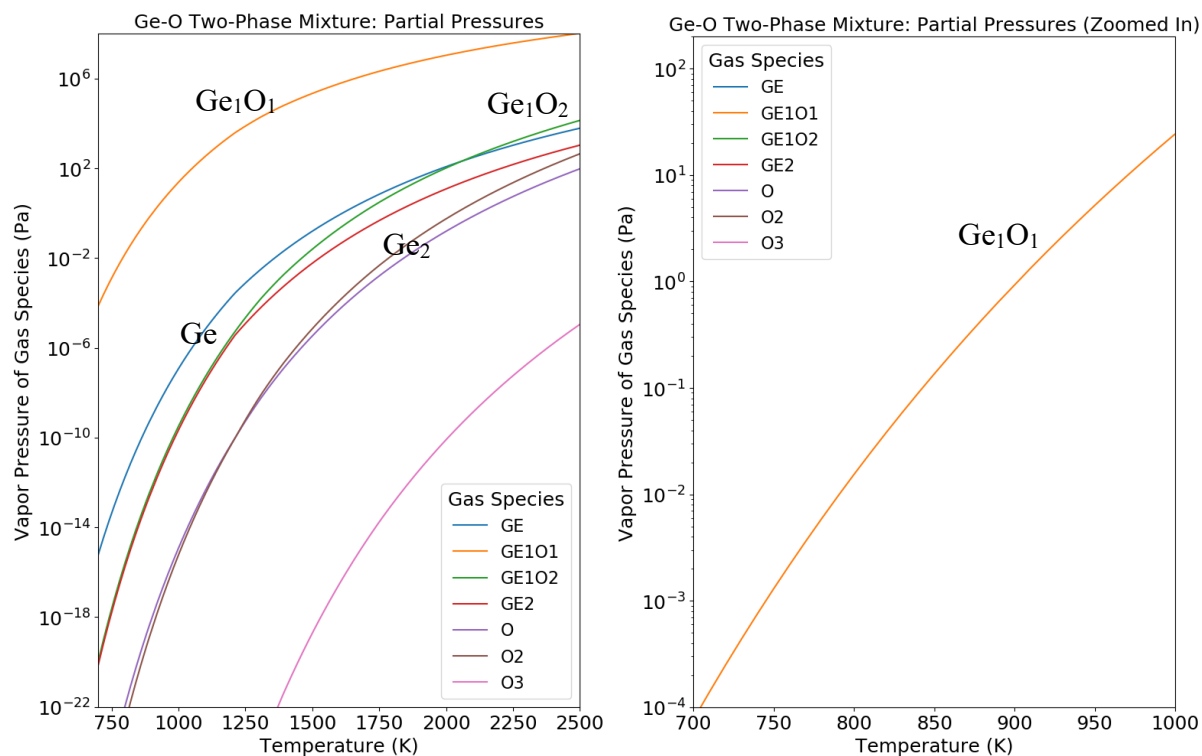


Figure S 29. Solid  $\text{GeO}_2$  (the stable phase for  $T < 872$  K, beyond which solid  $\text{GeO}(\text{am})$  is stable). Calculated partial pressures of the gas species over the phase(s) of interest as a function of temperature at  $P_{\text{O}_2} = 10^{-4}$  Pa. Here, “\_pp” indicates partial pressure when available. Calculated partial pressures of the gas species over a  $\text{GeO}_2(\text{s},\ell)+\text{Ge}(\text{s},\ell)$  two-phase mixture with an overall composition of  $\text{GeO}$ . Here, (s, $\ell$ ) indicate the solid phase at low temperatures and liquid phase at high temperatures.

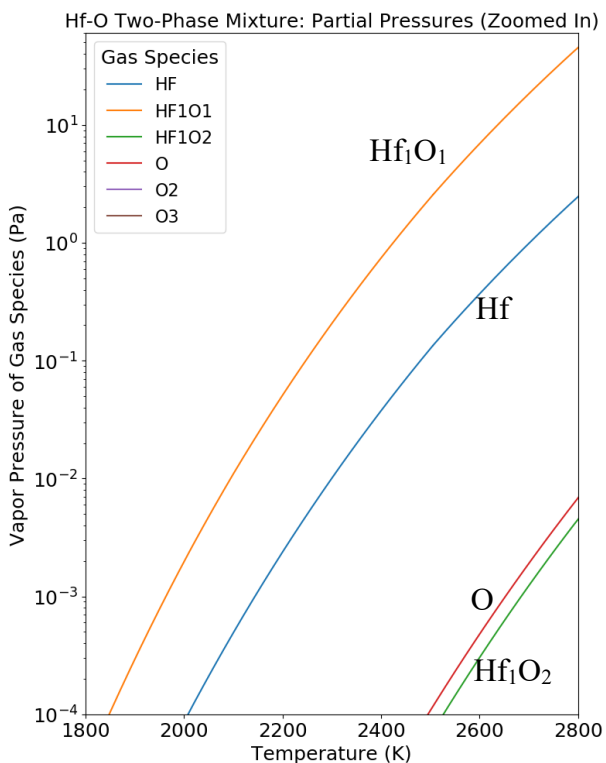
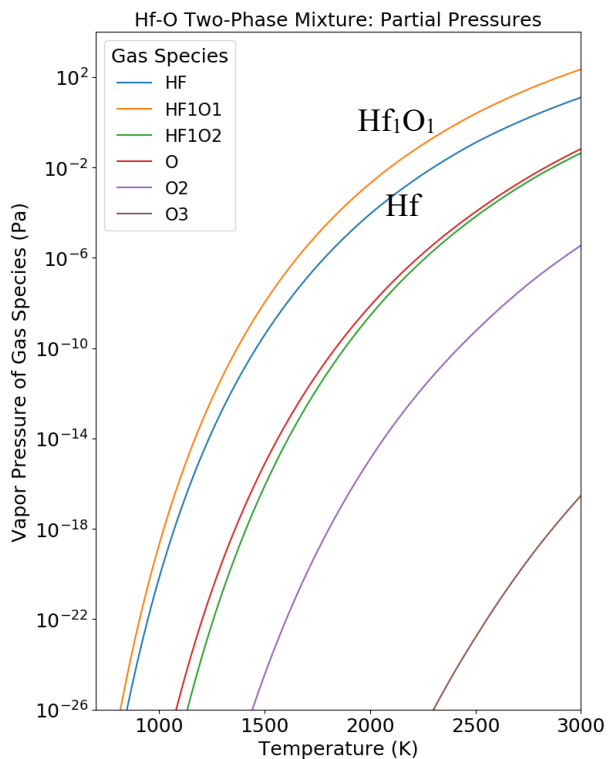
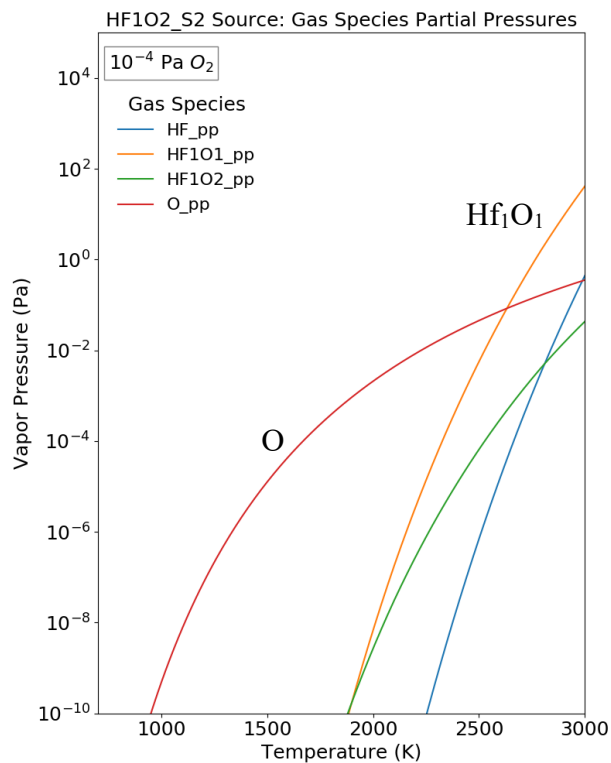


Figure S 30. Solid  $HfO_2$  (the stable phase). Calculated partial pressures of the gas species over the phase(s) of interest as a function of temperature at  $P_{O_2} = 10^{-4}$  Pa. Here, “\_pp” indicates partial pressure when available. Calculated partial pressures of the gas species over a  $HfO_2(s)+Hf(s,\ell)$  two-phase mixture with an overall composition of  $HfO$ . Here, (s, $\ell$ ) indicate the solid phase at low temperatures and liquid phase at high temperatures.

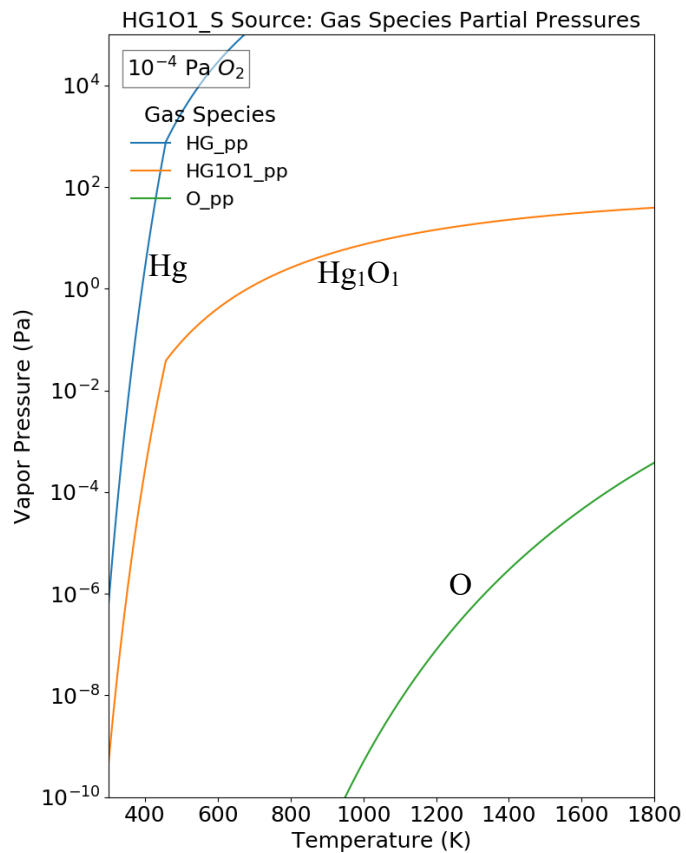


Figure S 31. Solid HgO (solid HgO is stable for  $T < 457$  K, beyond which the liquid HgO phase is stable). Calculated partial pressures of the gas species over the phase(s) of interest as a function of temperature at  $P_{O_2} = 10^{-4}$  Pa. Here, “\_pp” indicates partial pressure when available.

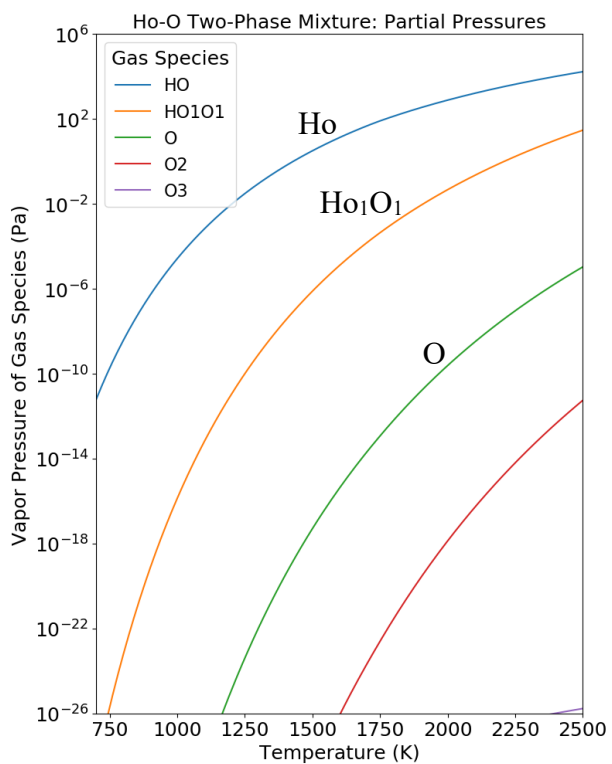
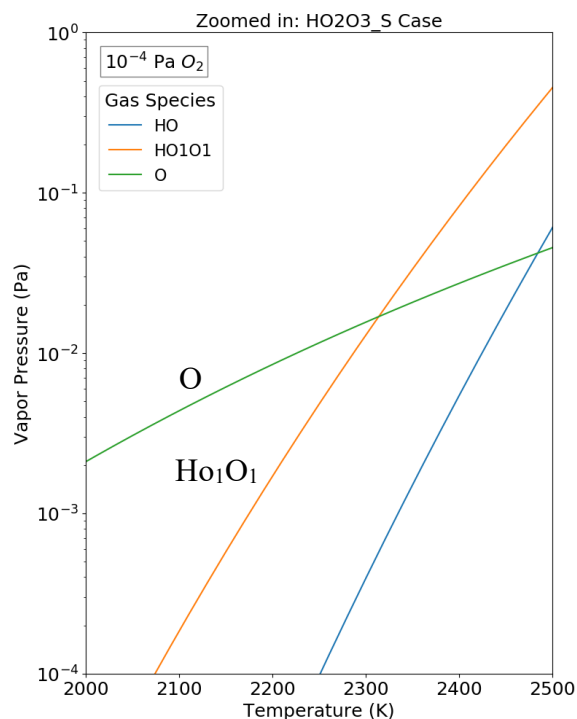
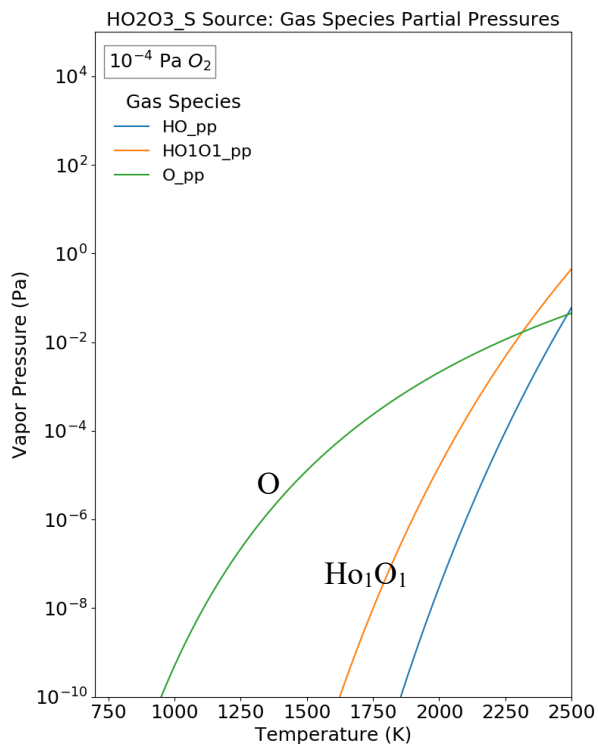


Figure S 32. Solid Ho<sub>2</sub>O<sub>3</sub> (the stable phase) with a zoomed-in view in the plot on the right. Calculated partial pressures of the gas species over the phase(s) of interest as a function of temperature at  $P_{O_2} = 10^{-4}$  Pa. Here, “\_pp” indicates partial pressure when available. Calculated partial pressures of the gas species over a Ho<sub>2</sub>O<sub>3</sub>(s)+Ho(s, $\ell$ ) two-phase mixture with an overall composition of HoO. Here, (s, $\ell$ ) indicate the solid phase at low temperatures and liquid phase at high temperatures.

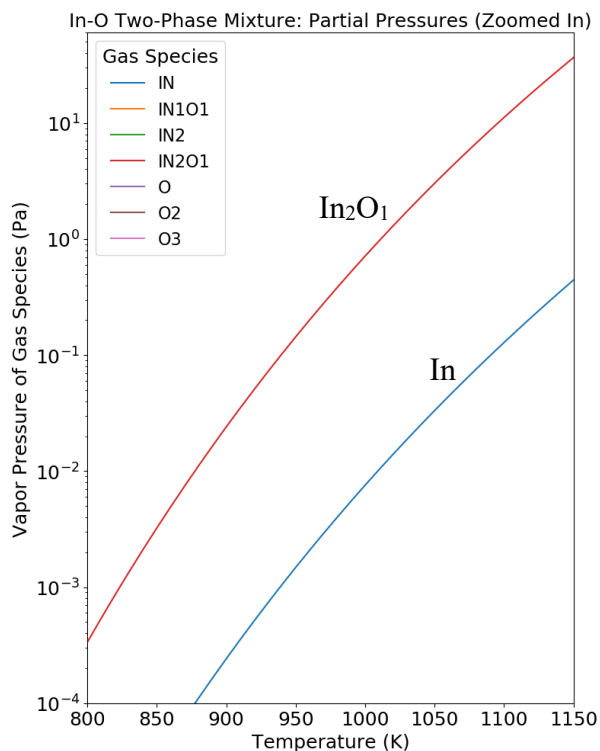
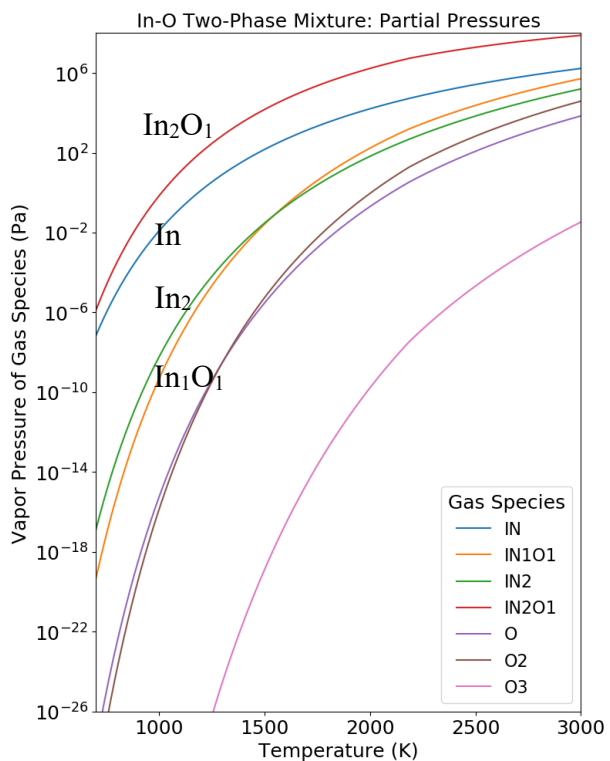
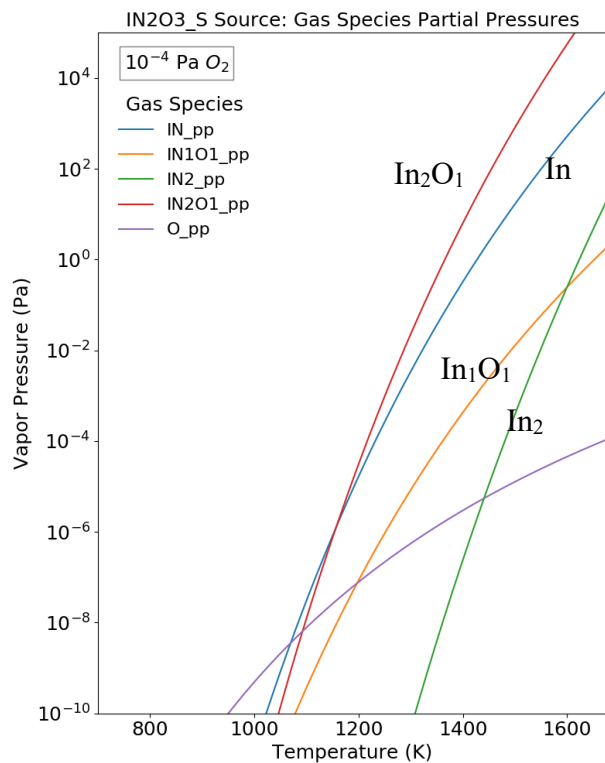


Figure S 33. Solid  $\text{In}_2\text{O}_3$  (the stable phase). Calculated partial pressures of the gas species over the phase(s) of interest as a function of temperature at  $P_{\text{O}_2} = 10^{-4}$  Pa. Here, “\_pp” indicates partial pressure when available. Calculated partial pressures of the gas species over a  $\text{In}_2\text{O}_3(\text{s},\ell) + \text{In}(\ell)$  two-phase mixture with an overall composition of  $\text{In}_2\text{O}$ . Here, (s, $\ell$ ) indicate the solid phase at low temperatures and liquid phase at high temperatures.

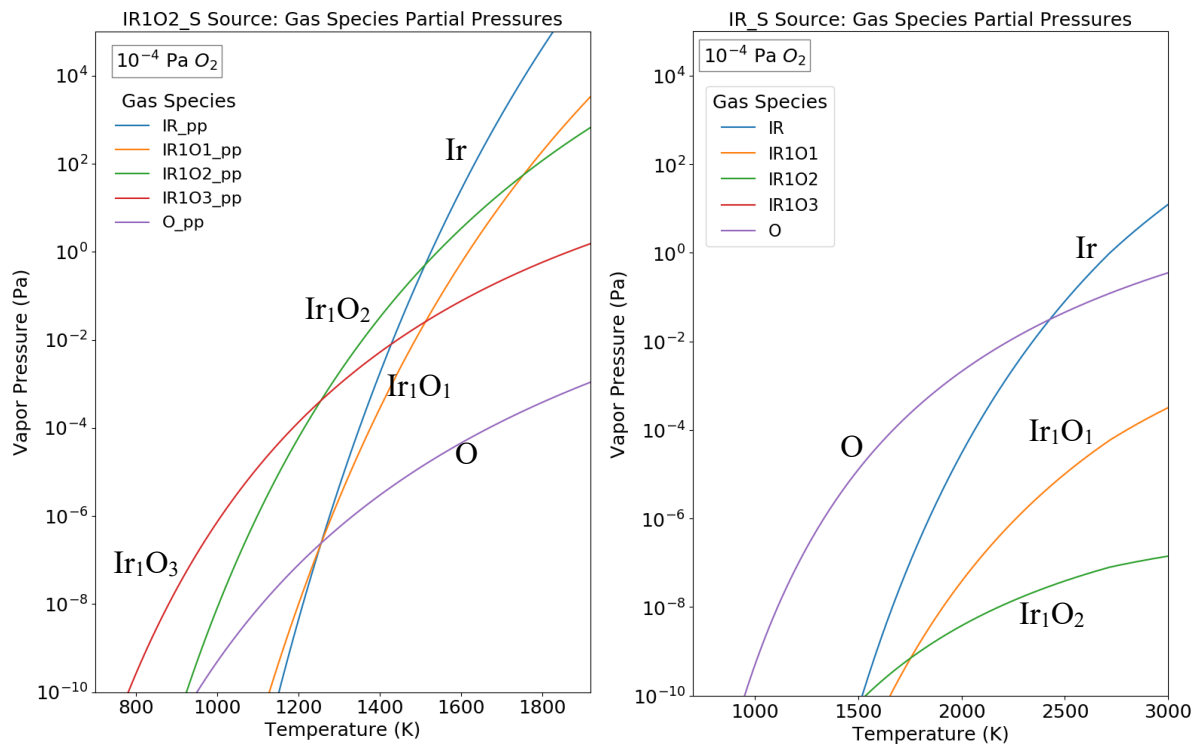


Figure S 34. Solid  $\text{IrO}_2$  and solid Ir (solid Ir is the stable phase). Calculated partial pressures of the gas species over the phase(s) of interest as a function of temperature at  $P_{\text{O}_2} = 10^{-4}$  Pa. Here, “\_pp” indicates partial pressure when available.

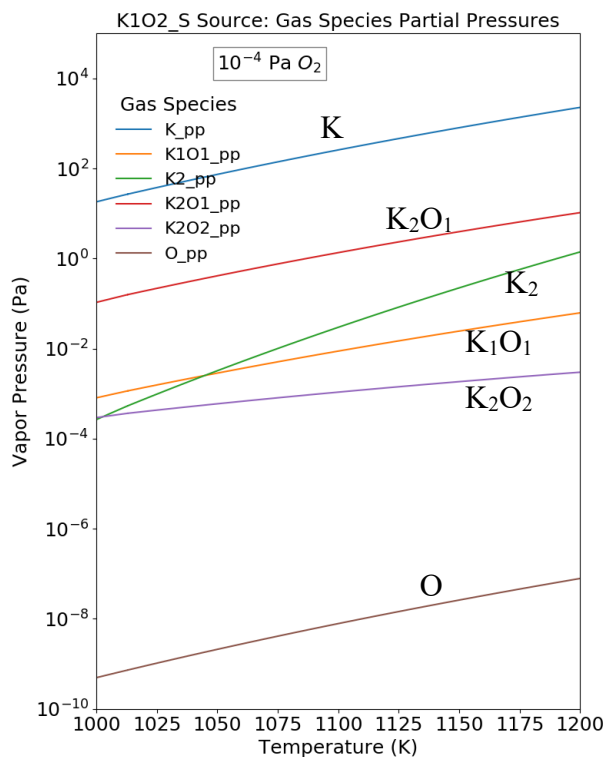
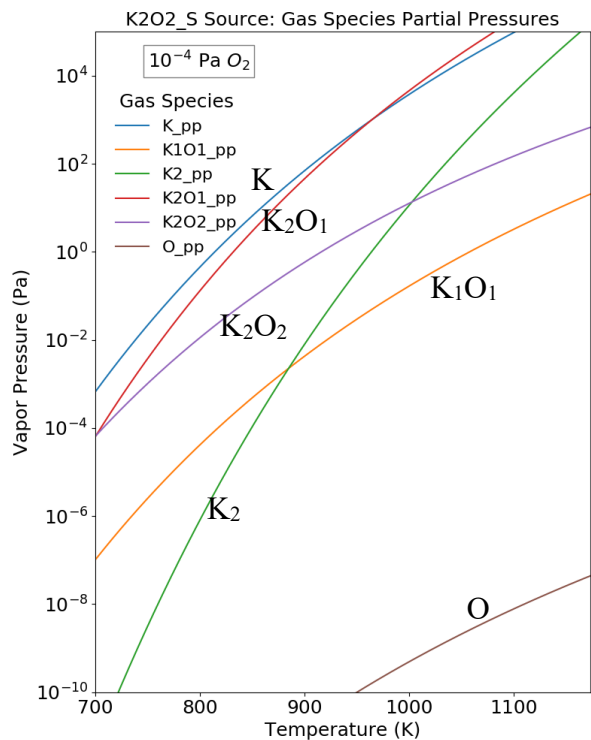
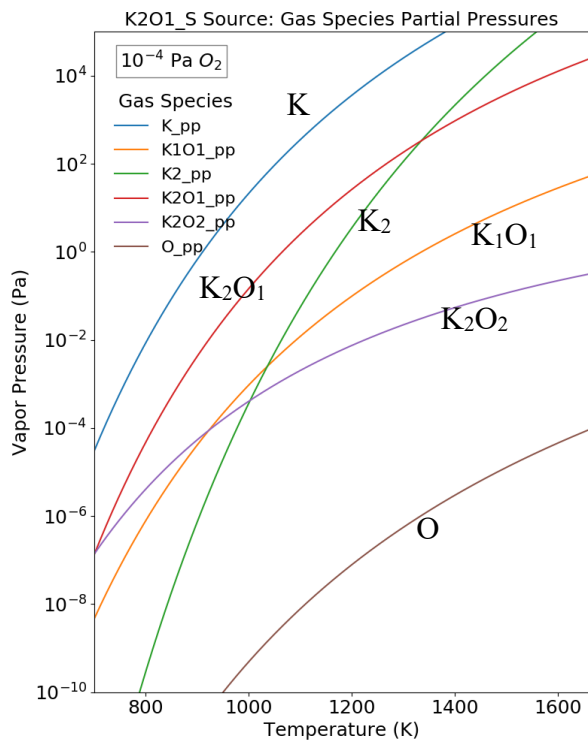


Figure S 35. Solid  $K_2O$ , solid  $K_2O_2$ , and solid  $KO_2$  (solid  $KO_2$  is the stable phase). Calculated partial pressures of the gas species over the phase(s) of interest as a function of temperature at  $P_{O_2} = 10^{-4} \text{ Pa}$ . Here, “\_pp” indicates partial pressure when available.

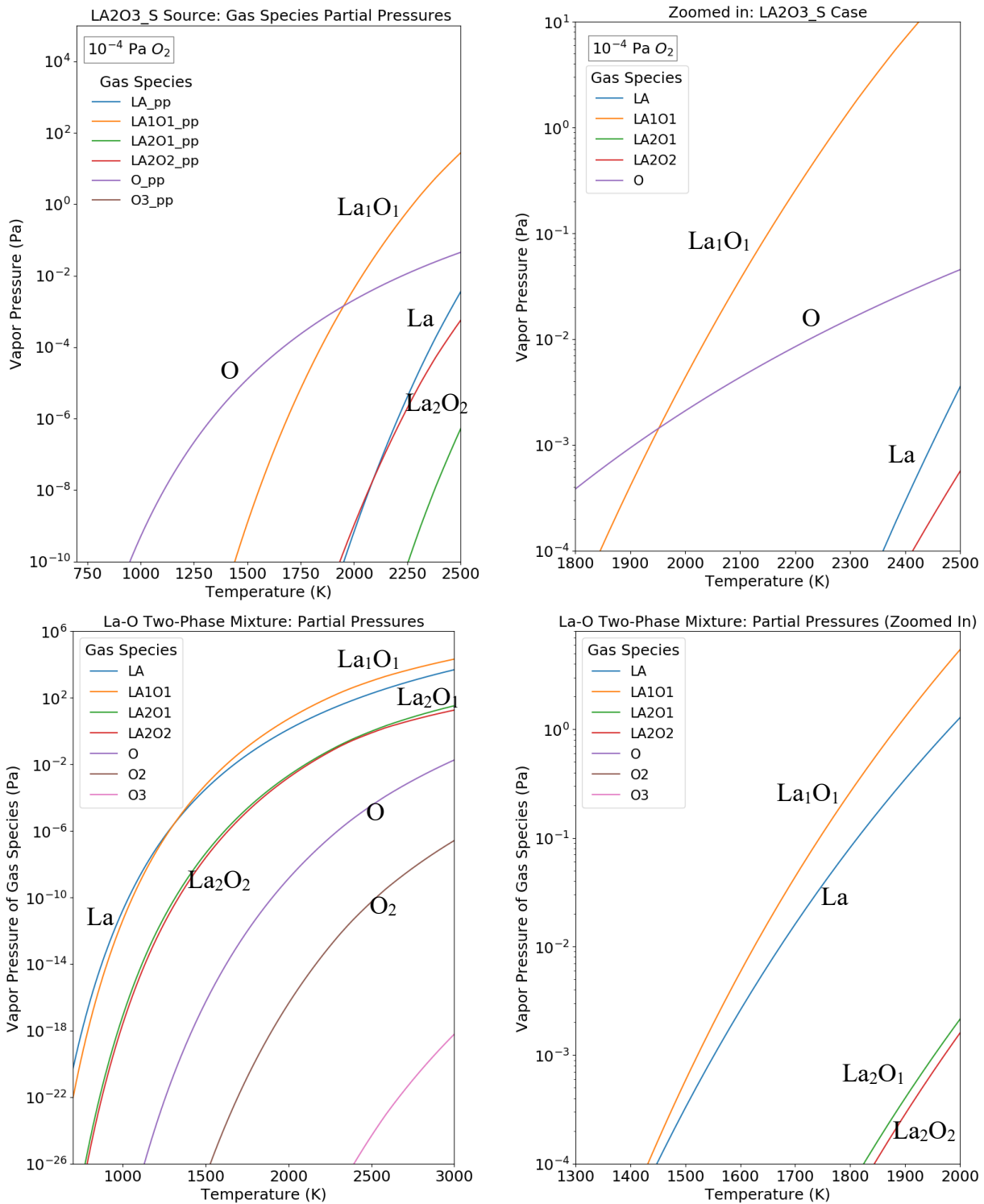


Figure S 36. Solid  $\text{La}_2\text{O}_3$  (with a zoomed-in view in the plot on the right). Calculated partial pressures of the gas species over the phase(s) of interest as a function of temperature at  $P_{\text{O}_2} = 10^{-4}$  Pa. Here, “\_pp” indicates partial pressure when available. Calculated partial pressures of the gas

species over a  $\text{La}_2\text{O}_3(\text{s},\ell) + \text{La}(\text{s},\ell)$  two-phase mixture with an overall composition of  $\text{LaO}$ . Here,  $(\text{s},\ell)$  indicate the solid phase at low temperatures and liquid phase at high temperatures.

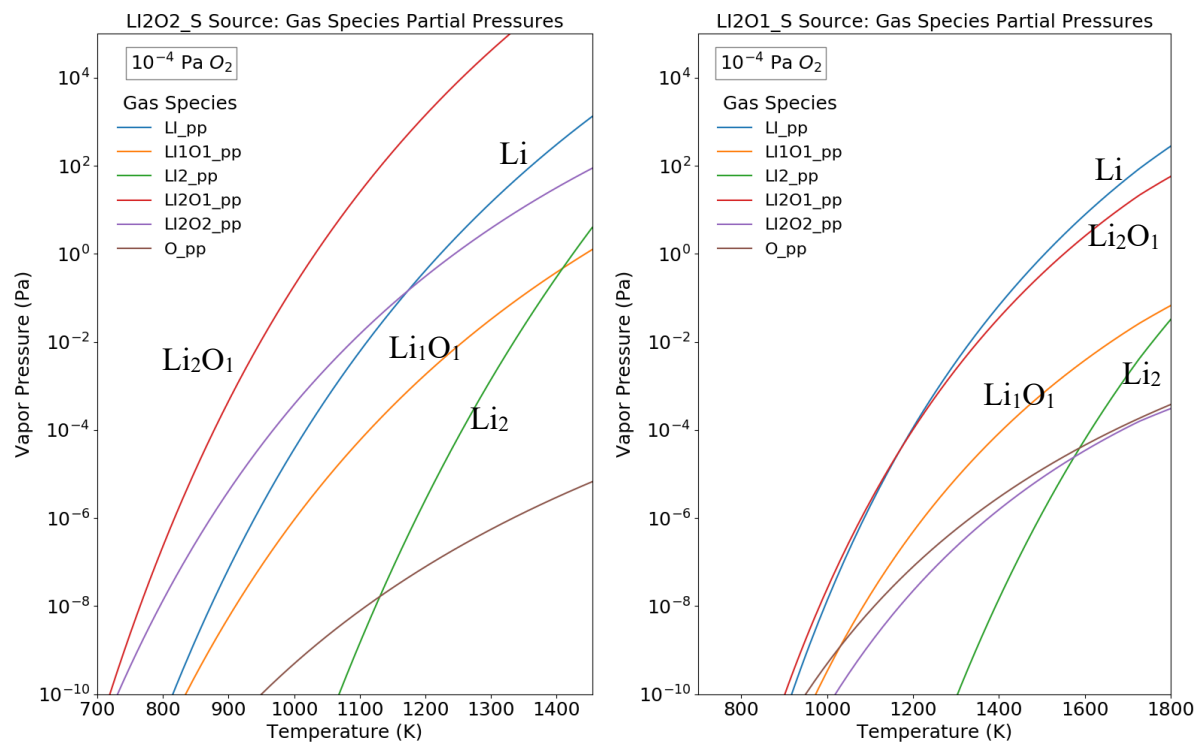


Figure S 37. Solid  $\text{Li}_2\text{O}_2$  and solid  $\text{Li}_2\text{O}$  (the stable phase). Calculated partial pressures of the gas species over the phase(s) of interest as a function of temperature at  $P_{\text{O}_2} = 10^{-4} \text{ Pa}$ . Here, “\_pp” indicates partial pressure when available.

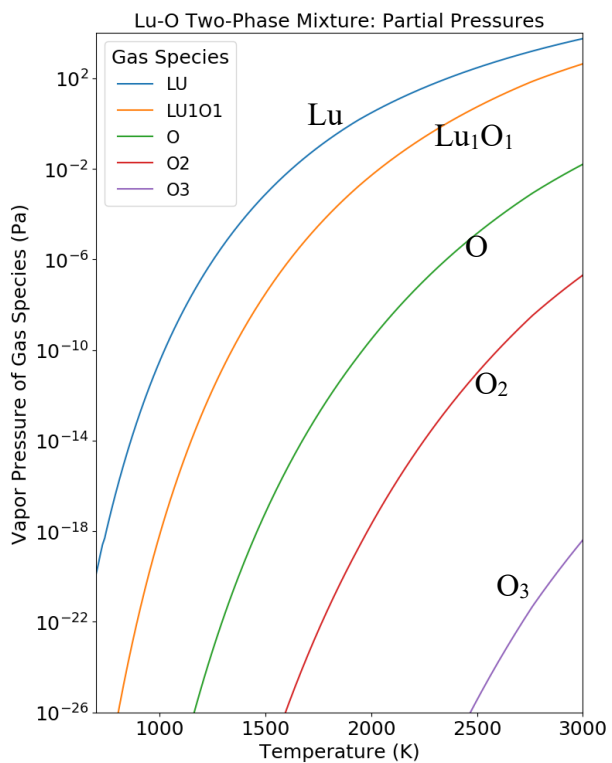
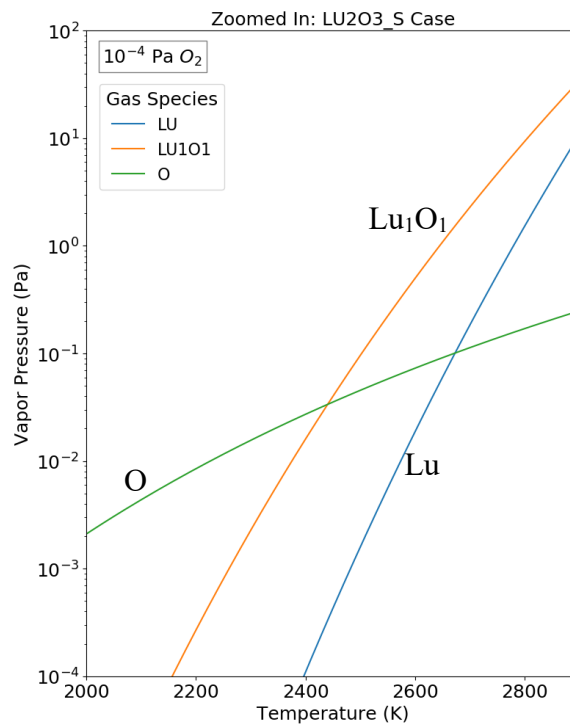
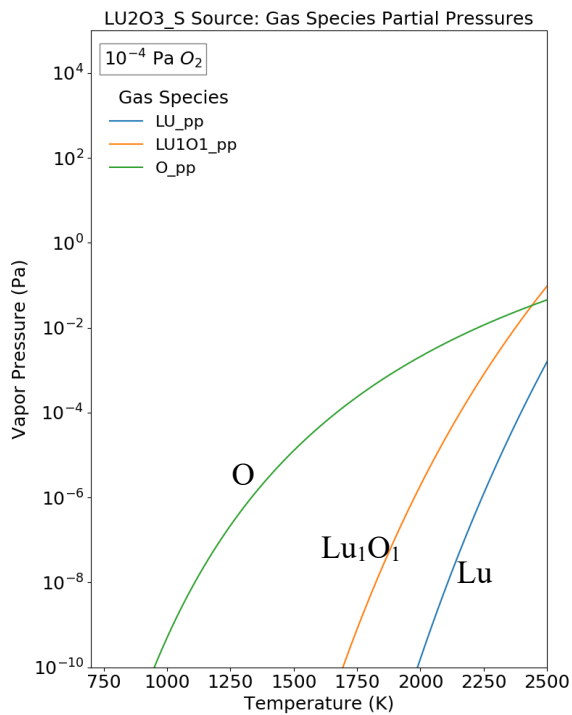


Figure S 38. Solid Lu<sub>2</sub>O<sub>3</sub> (the stable phase) with a zoomed-in view in the plot on the right. Calculated partial pressures of the gas species over the phase(s) of interest as a function of temperature at  $P_{O_2} = 10^{-4}$  Pa. Here, “pp” indicates partial pressure when available. Calculated partial pressures of the gas species over a Lu<sub>2</sub>O<sub>3</sub>(s,ℓ)+Lu(s,ℓ) two-phase mixture with an overall composition of LuO. Here, (s,ℓ) indicate the solid phase at low temperatures and liquid phase at high temperatures.

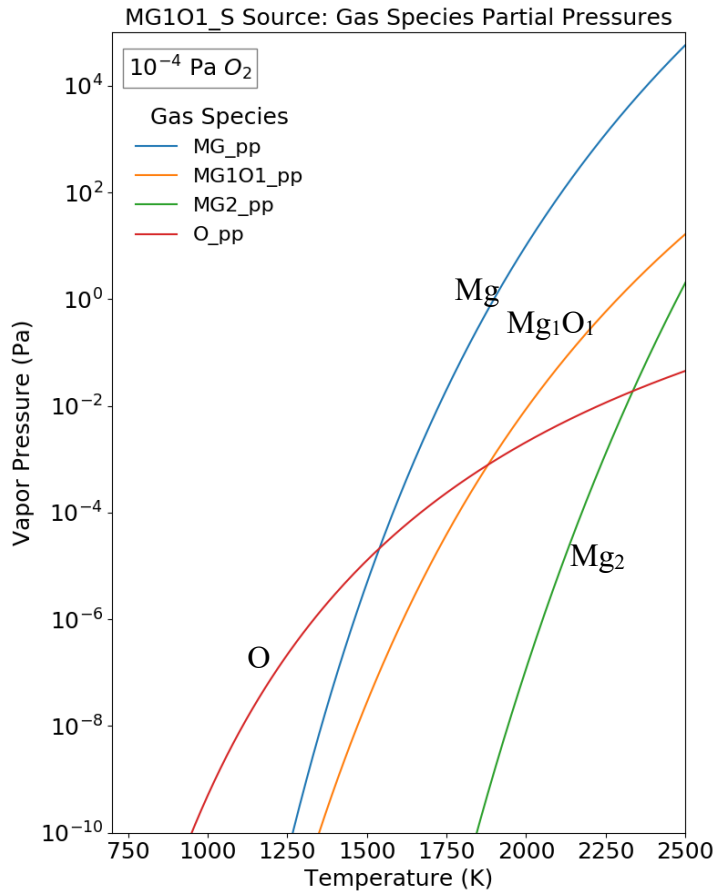


Figure S 39. Solid MgO (the stable phase). Calculated partial pressures of the gas species over the phase(s) of interest as a function of temperature at  $P_{O_2} = 10^{-4}$  Pa. Here, “\_pp” indicates partial pressure when available.

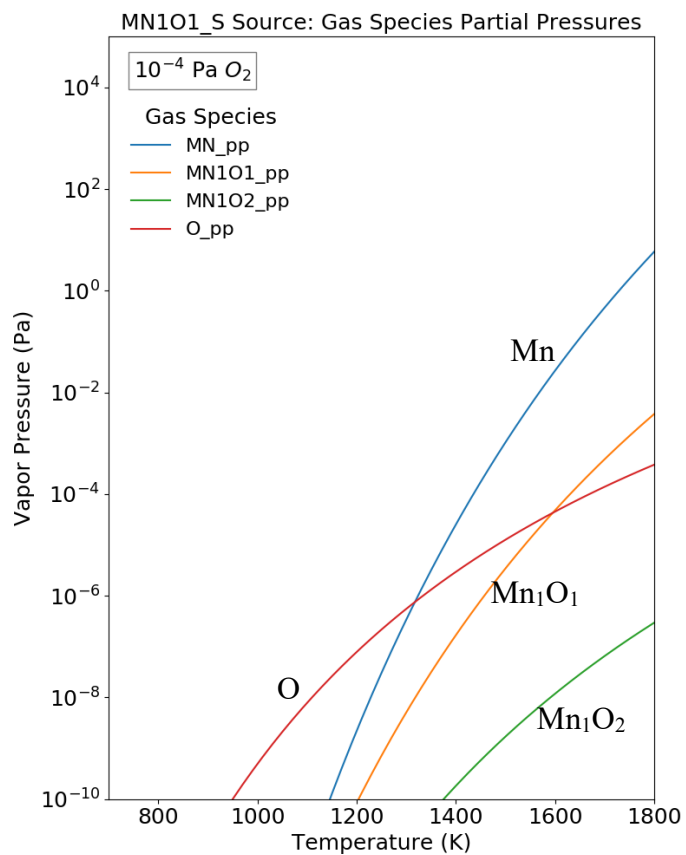


Figure S 40. Solid MnO. Calculated partial pressures of the gas species over the phase(s) of interest as a function of temperature at  $P_{O_2} = 10^{-4}$  Pa. Here, “\_pp” indicates partial pressure when available.

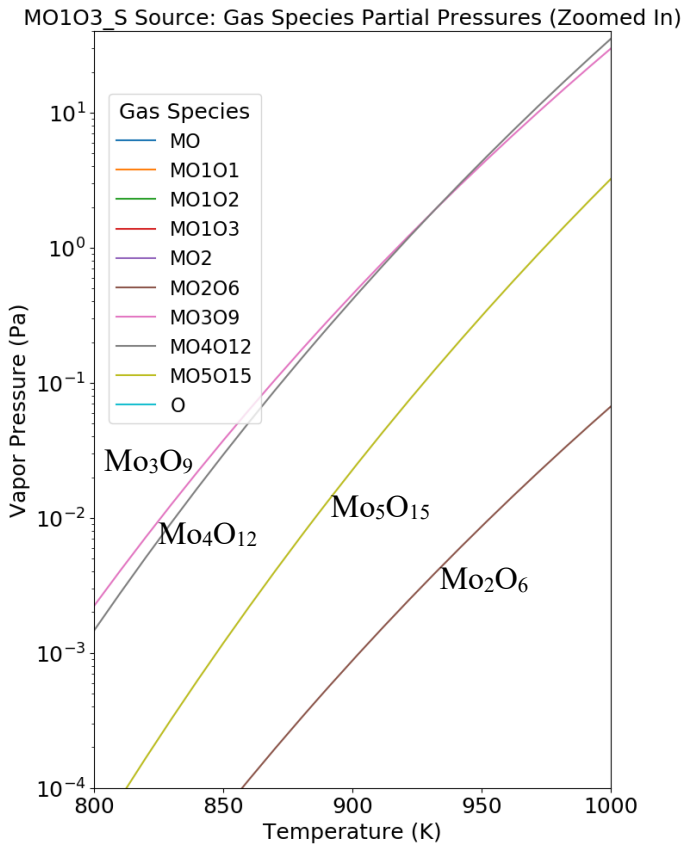
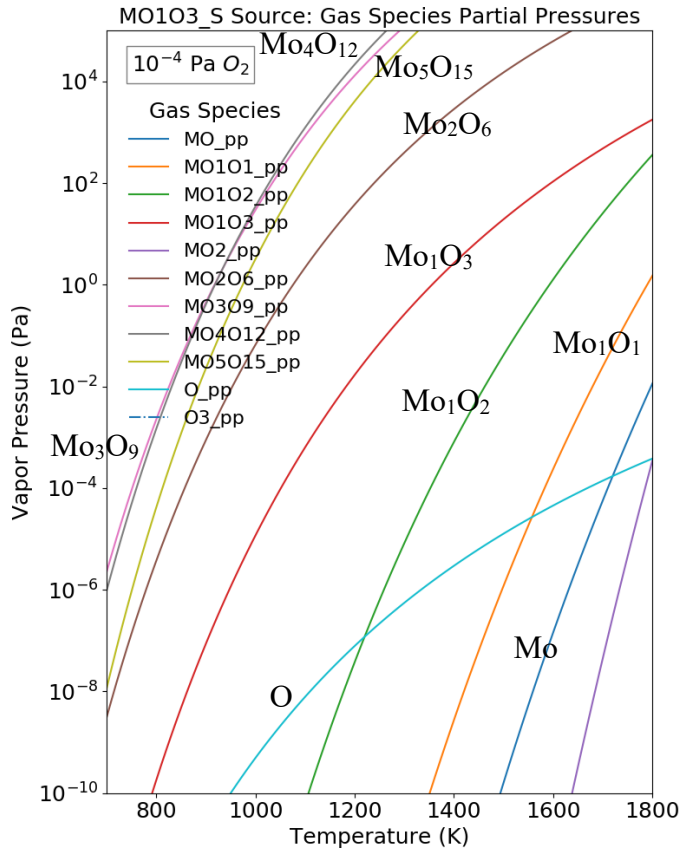


Figure S 41. Solid  $\text{MoO}_3$  (the stable phase). Calculated partial pressures of the gas species over the phase(s) of interest as a function of temperature at  $P_{\text{O}_2} = 10^{-4}$  Pa. Here, “\_pp” indicates partial pressure when available.

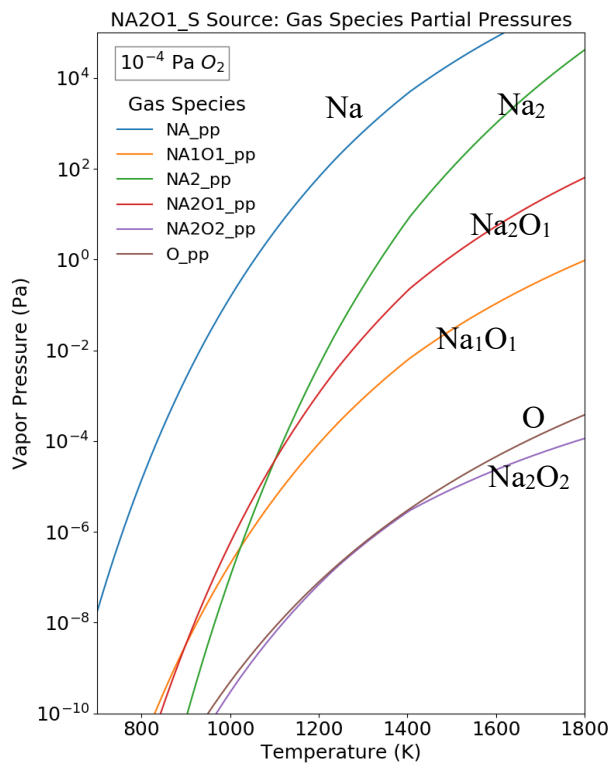
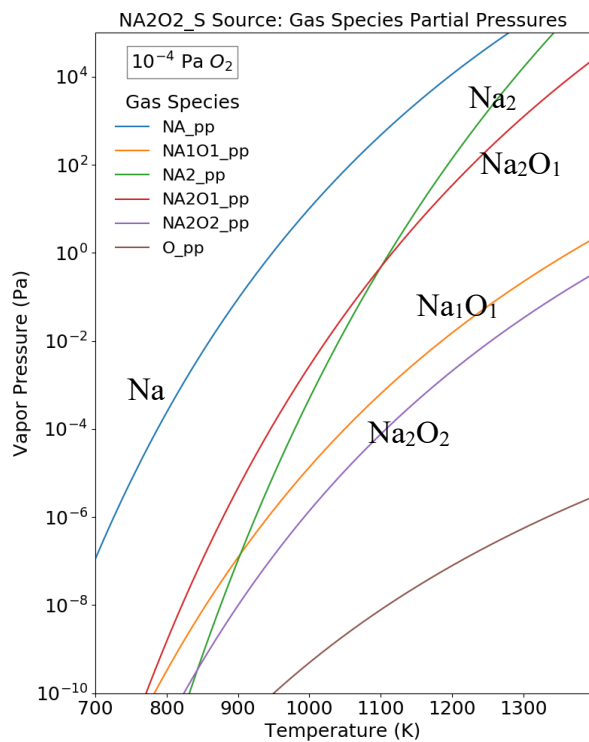
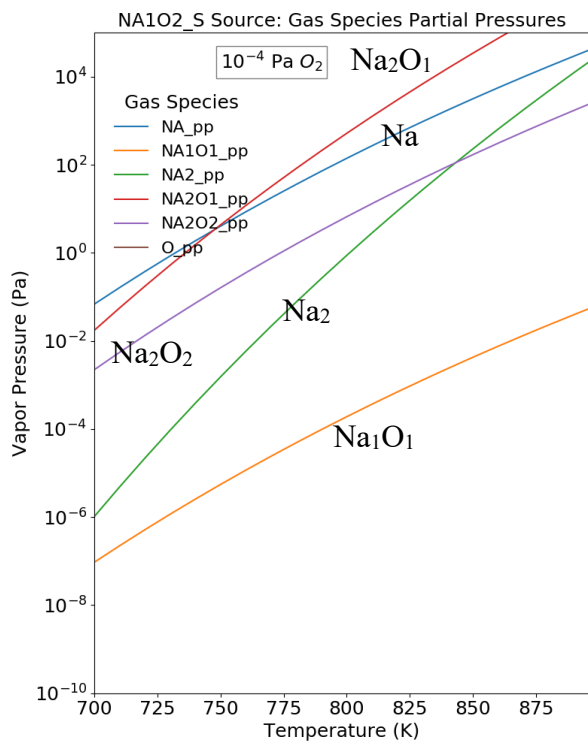


Figure S 42. Solid NaO<sub>2</sub>, solid Na<sub>2</sub>O<sub>2</sub>, and solid Na<sub>2</sub>O (the stable phase). Calculated partial pressures of the gas species over the phase(s) of interest as a function of temperature at  $P_{O_2} = 10^{-4}$  Pa. Here, “\_pp” indicates partial pressure when available.

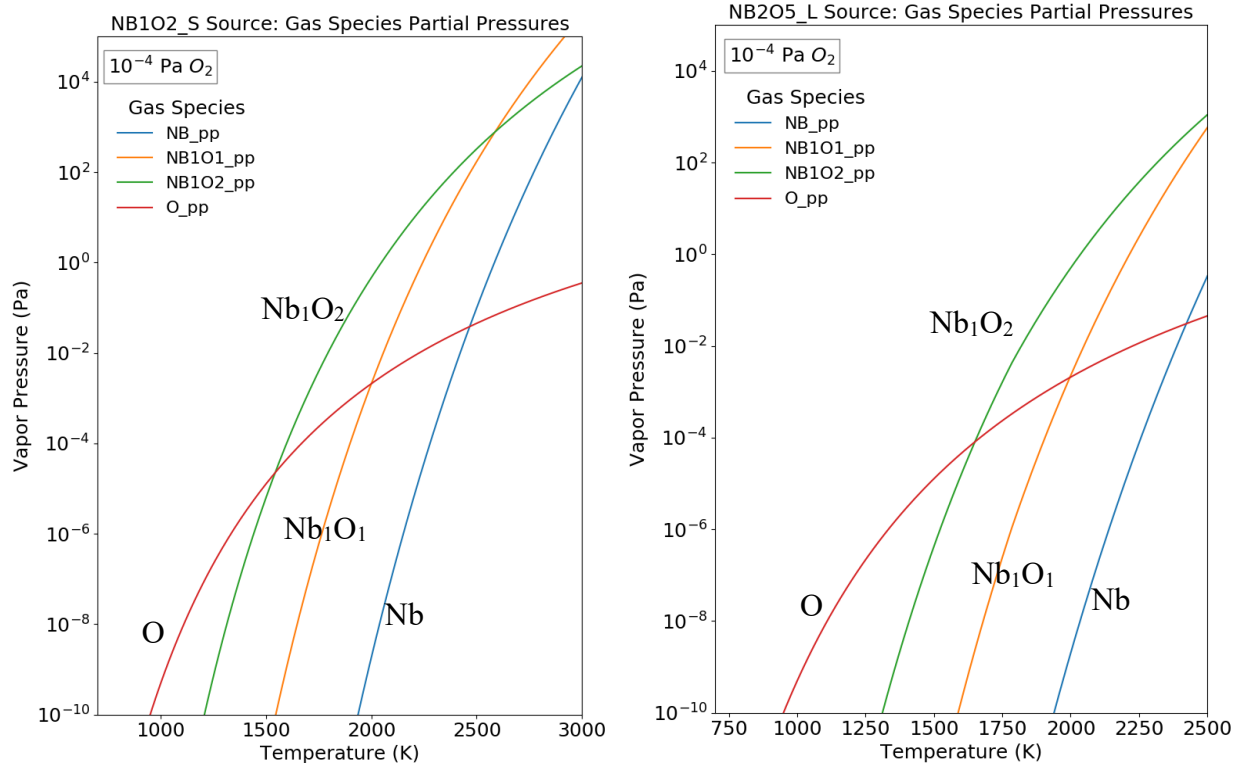


Figure S 43. Solid NbO<sub>2</sub> and liquid Nb<sub>2</sub>O<sub>5</sub> (solid Nb<sub>2</sub>O<sub>5</sub> is stable for  $T < 1785$  K and liquid Nb<sub>2</sub>O<sub>5</sub> is stable for  $T > 1785$  K). Calculated partial pressures of the gas species over the phase(s) of interest as a function of temperature at  $P_{O_2} = 10^{-4}$  Pa. Here, “\_pp” indicates partial pressure when available.

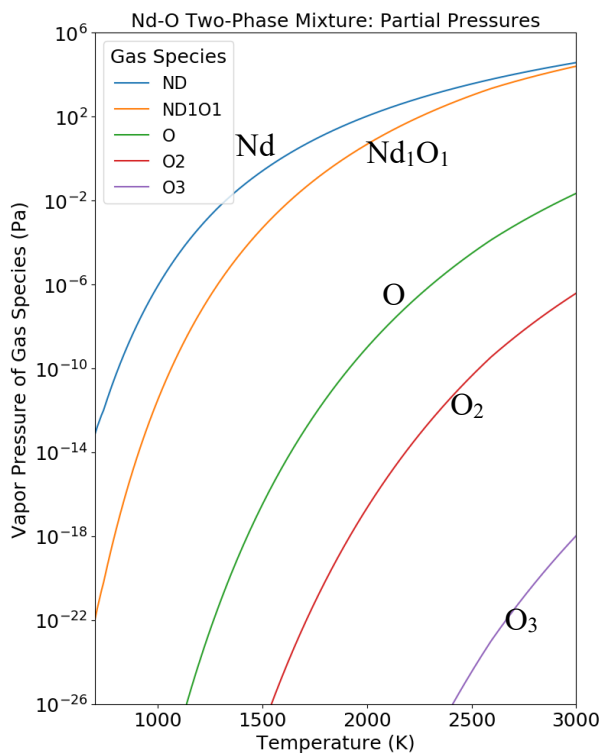
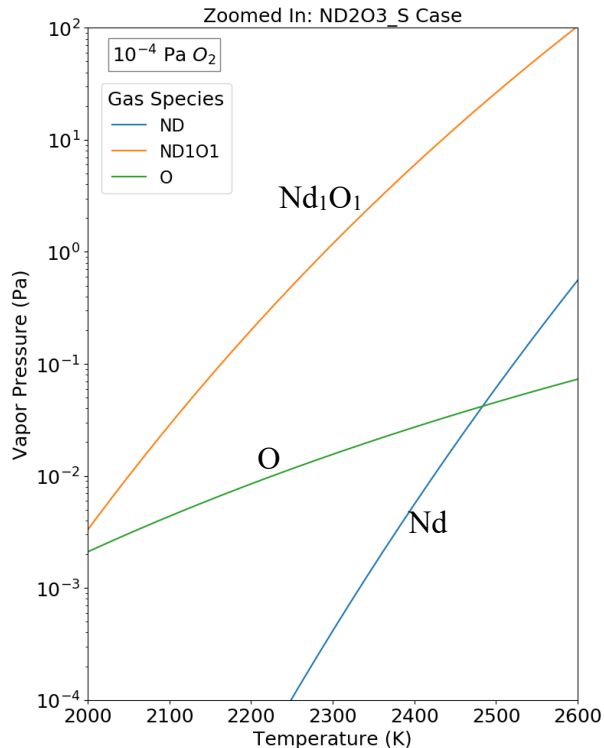
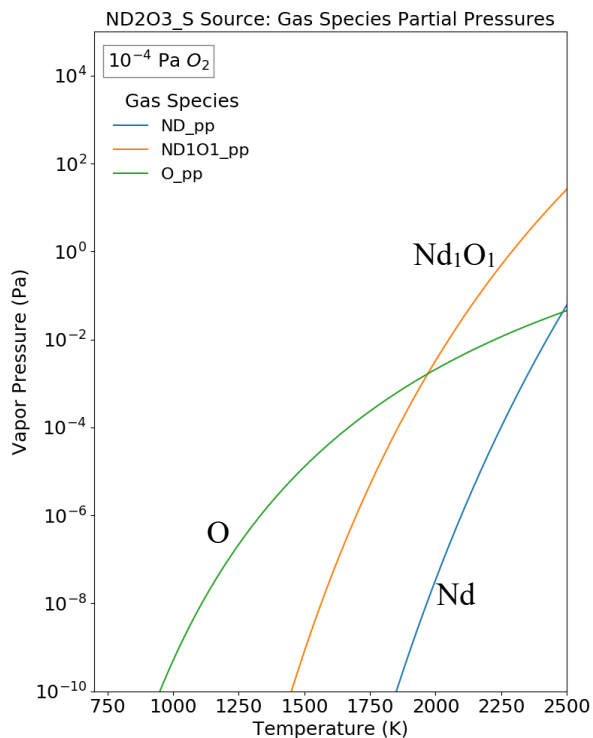


Figure S 44. Solid  $Nd_2O_3$  (the stable phase) with a zoomed-in view in the plot on the right. Calculated partial pressures of the gas species over the phase(s) of interest as a function of temperature at  $P_{O_2} = 10^{-4}$  Pa. Here, “\_pp” indicates partial pressure when available. Calculated partial pressures of the gas species over a  $Nd_2O_3(s,\ell)+Nd(s,\ell)$  two-phase mixture with an overall composition of NdO. Here, (s, $\ell$ ) indicate the solid phase at low temperatures and liquid phase at high temperatures.

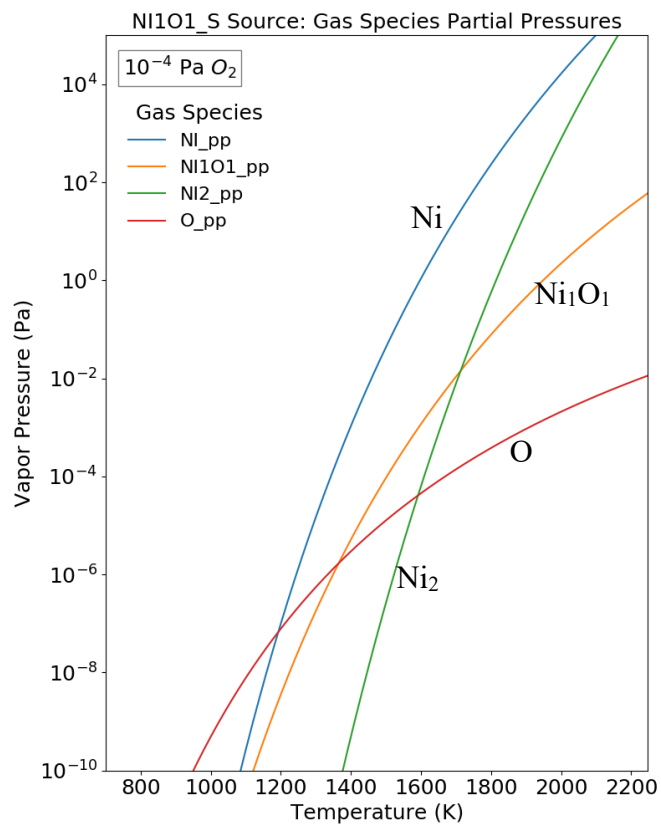


Figure S 45. Solid NiO (the stable phase). Calculated partial pressures of the gas species over the phase(s) of interest as a function of temperature at  $P_{O_2} = 10^{-4}$  Pa. Here, “\_pp” indicates partial pressure when available.

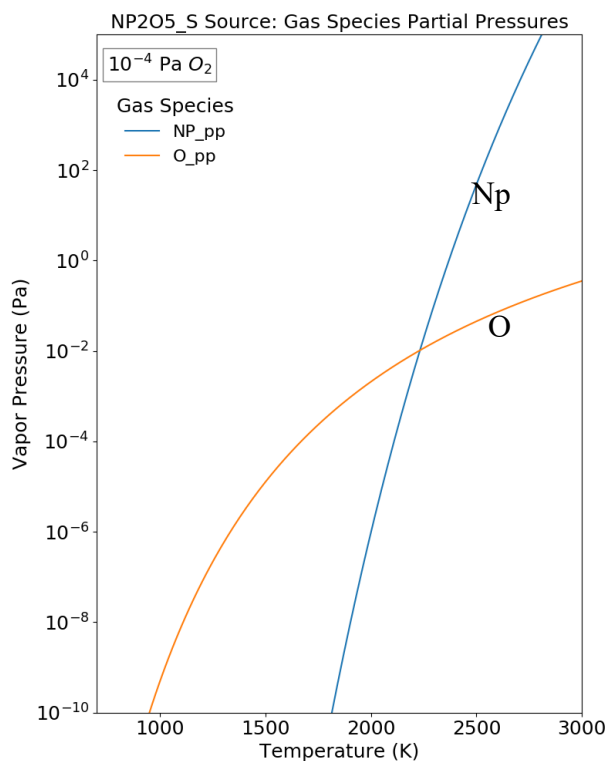
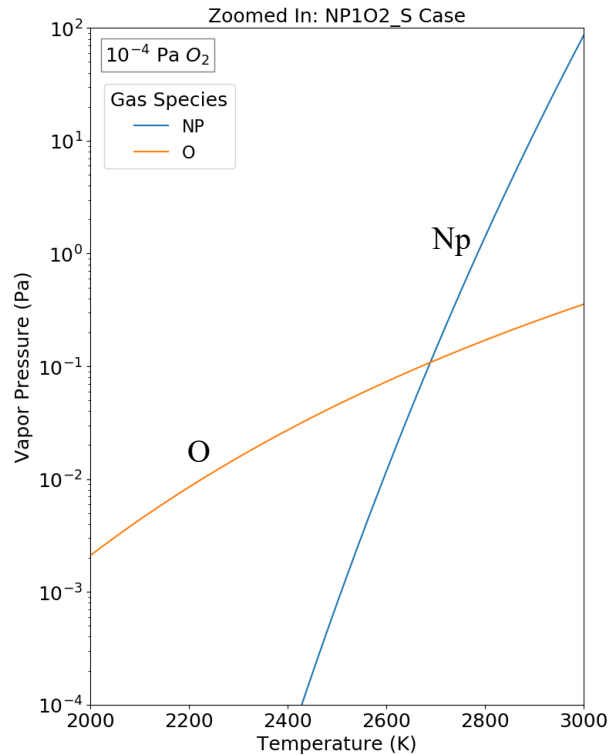
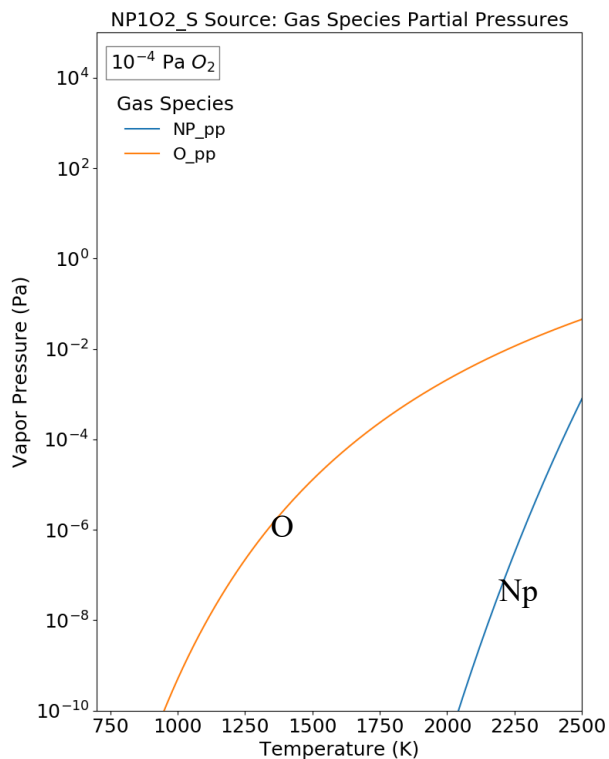


Figure S 46. Solid  $\text{Np}_2\text{O}_5$  and solid  $\text{NpO}_2$  (the stable phase, with a zoomed-in view in the plot on the right). Calculated partial pressures of the gas species over the phase(s) of interest as a function of temperature at  $P_{\text{O}_2} = 10^{-4}$  Pa. Here, “\_pp” indicates partial pressure when available.

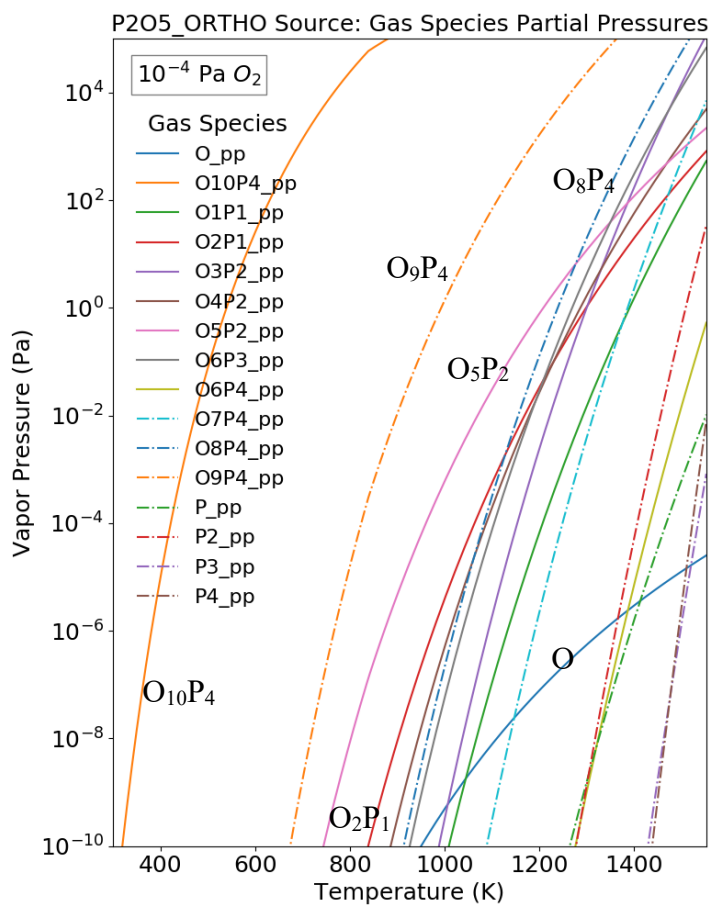
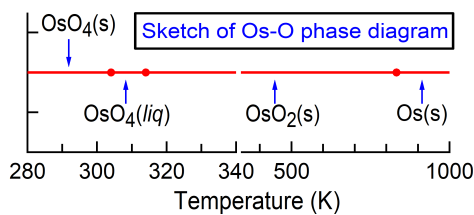
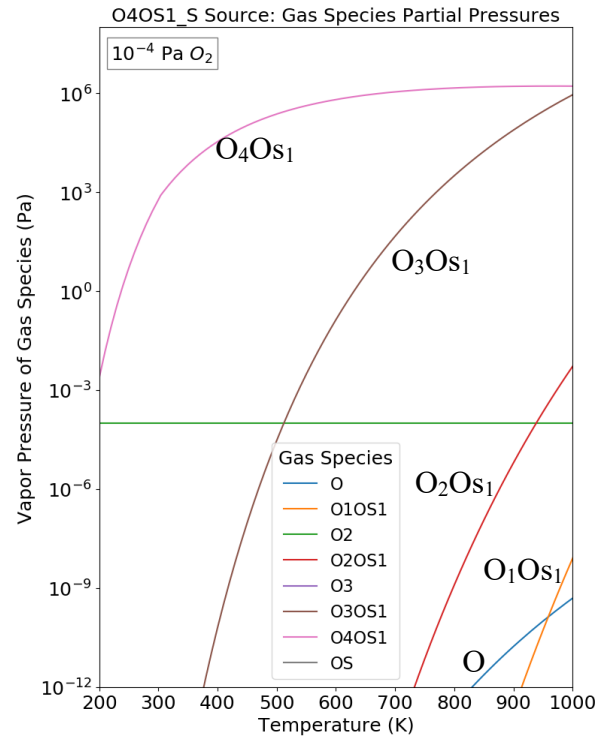
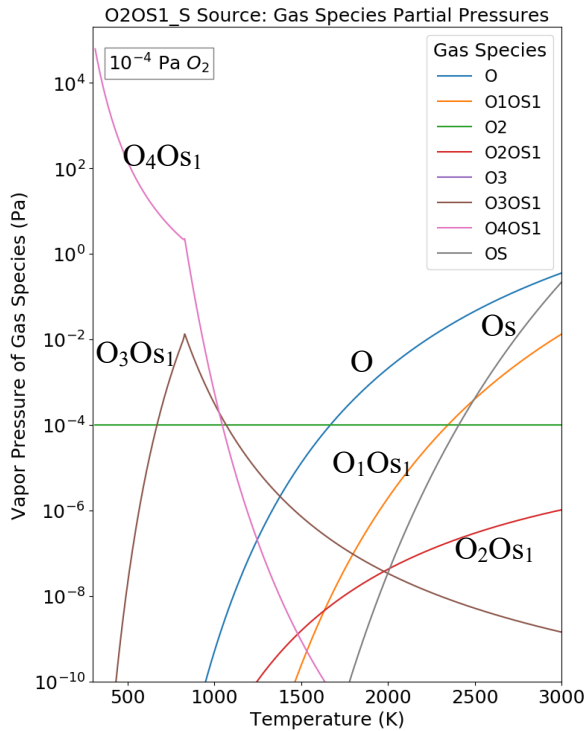


Figure S 47. Solid P<sub>2</sub>O<sub>5\_ortho</sub> (stable for  $T < 839$  K, beyond which liquid P<sub>2</sub>O<sub>5</sub> is stable). Calculated partial pressures of the gas species over the phase(s) of interest as a function of temperature at  $P_{O_2} = 10^{-4}$  Pa. Here, “\_pp” indicates partial pressure when available.



O4OS1\_S Source: Gas Species Partial Pressures (Zoomed In)

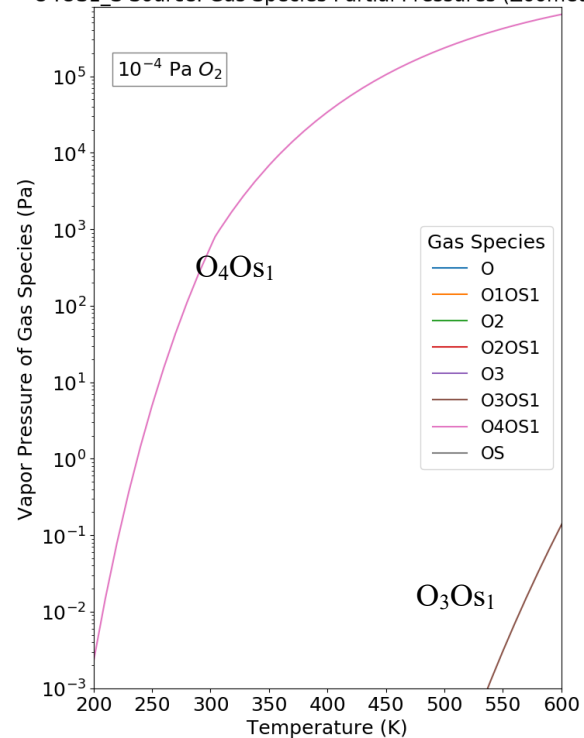


Figure S 48. Solid  $\text{OsO}_2$  and solid  $\text{OsO}_4$  (solid  $\text{OsO}_4$  is stable for  $T < 304$  K, liquid  $\text{OsO}_4$  is stable for  $304 < T < 314$  K, solid  $\text{OsO}_2$  is stable for  $314 < T < 832$  K, and solid  $\text{Os}$  is stable for  $T > 832$  K; see the sketch of the Os-O phase diagram above). Calculated partial pressures of the gas species with a zoomed-in view of the phase(s) of interest as a function of temperature at  $P_{\text{O}_2} = 10^{-4}$  Pa. Here, “\_pp” indicates partial pressure when available.

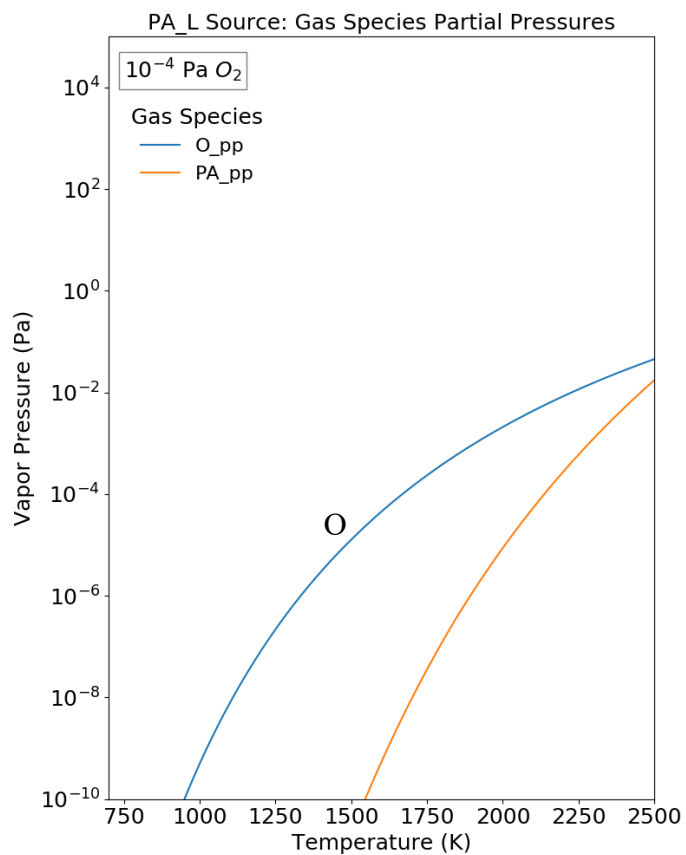
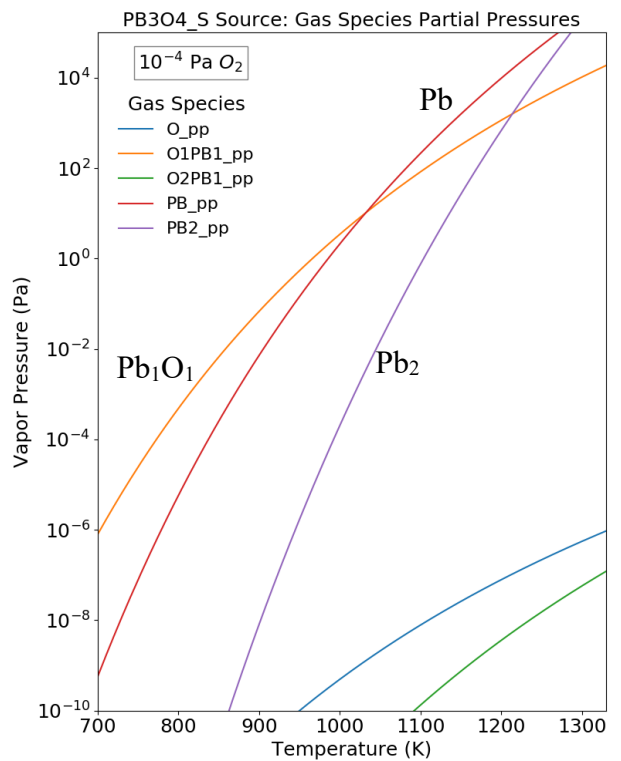
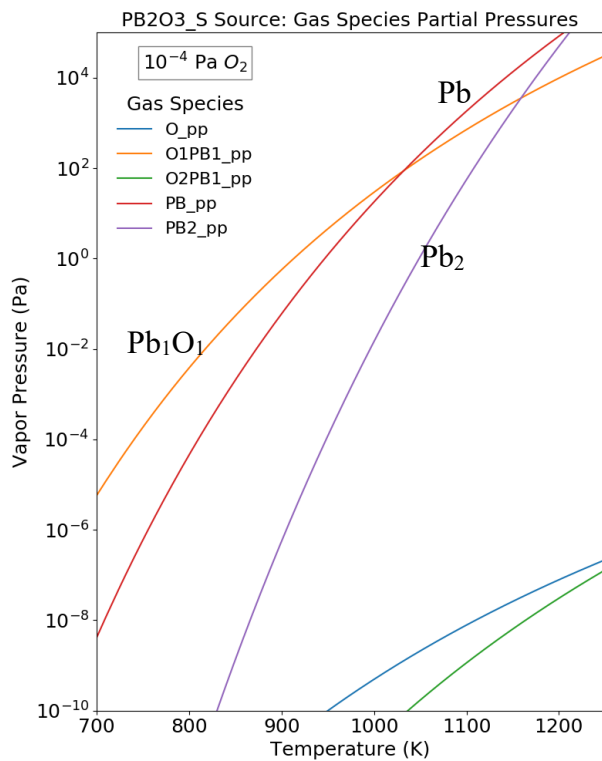
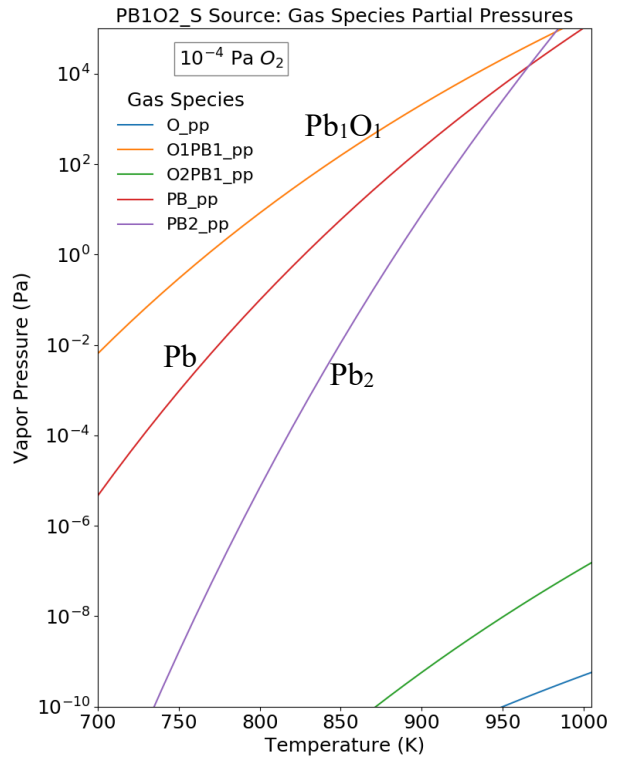
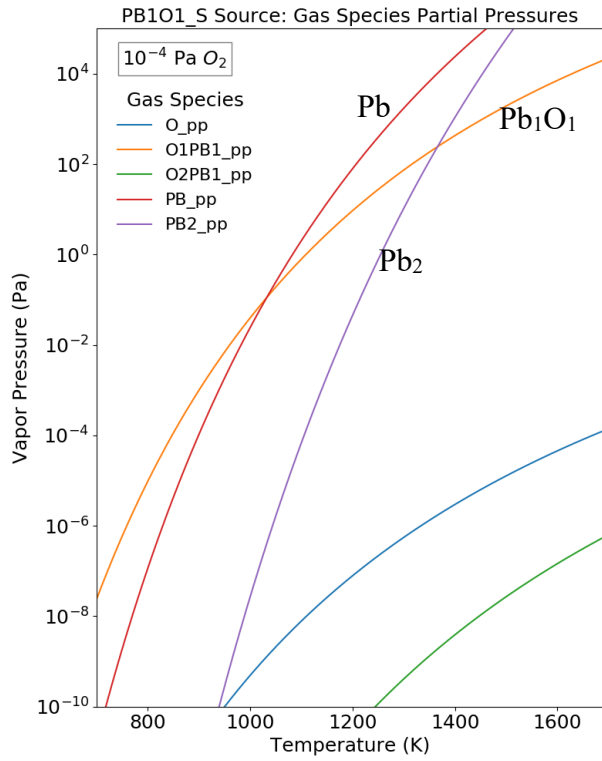


Figure S 49. Liquid Pa (metastable phase when  $T > 1845$  K). Calculated partial pressures of the gas species over the phase(s) of interest as a function of temperature at  $P_{O_2} = 10^{-4}$  Pa. Here, “\_pp” indicates partial pressure when available.



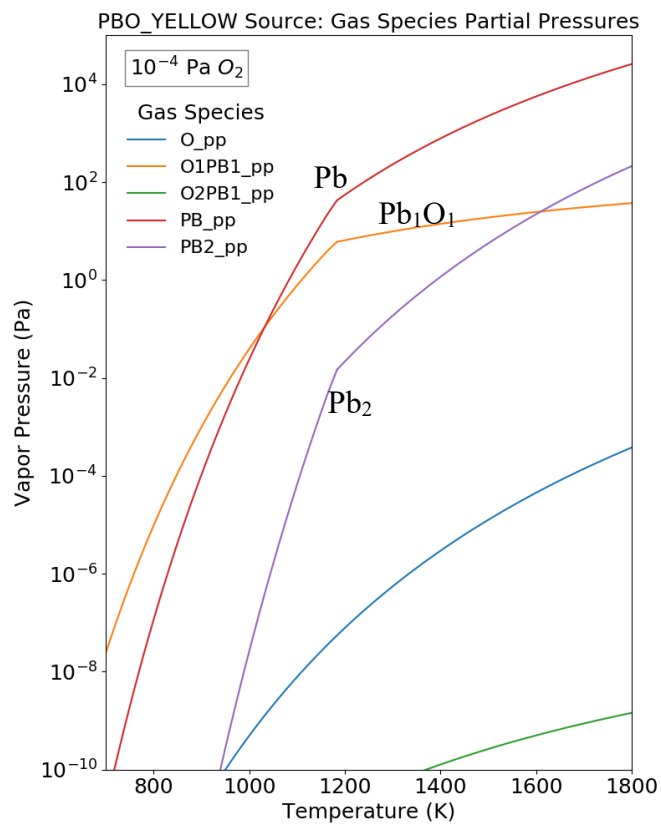


Figure S 50. Solid PbO, solid PbO<sub>2</sub>, solid Pb<sub>2</sub>O<sub>3</sub>, solid Pb<sub>3</sub>O<sub>4</sub>, and PbO<sub>yellow</sub> (the stable phase up to 1163 K). Calculated partial pressures of the gas species over the phase(s) of interest as a function of temperature at  $P_{O_2} = 10^{-4}$  Pa. Here, “\_pp” indicates partial pressure when available.

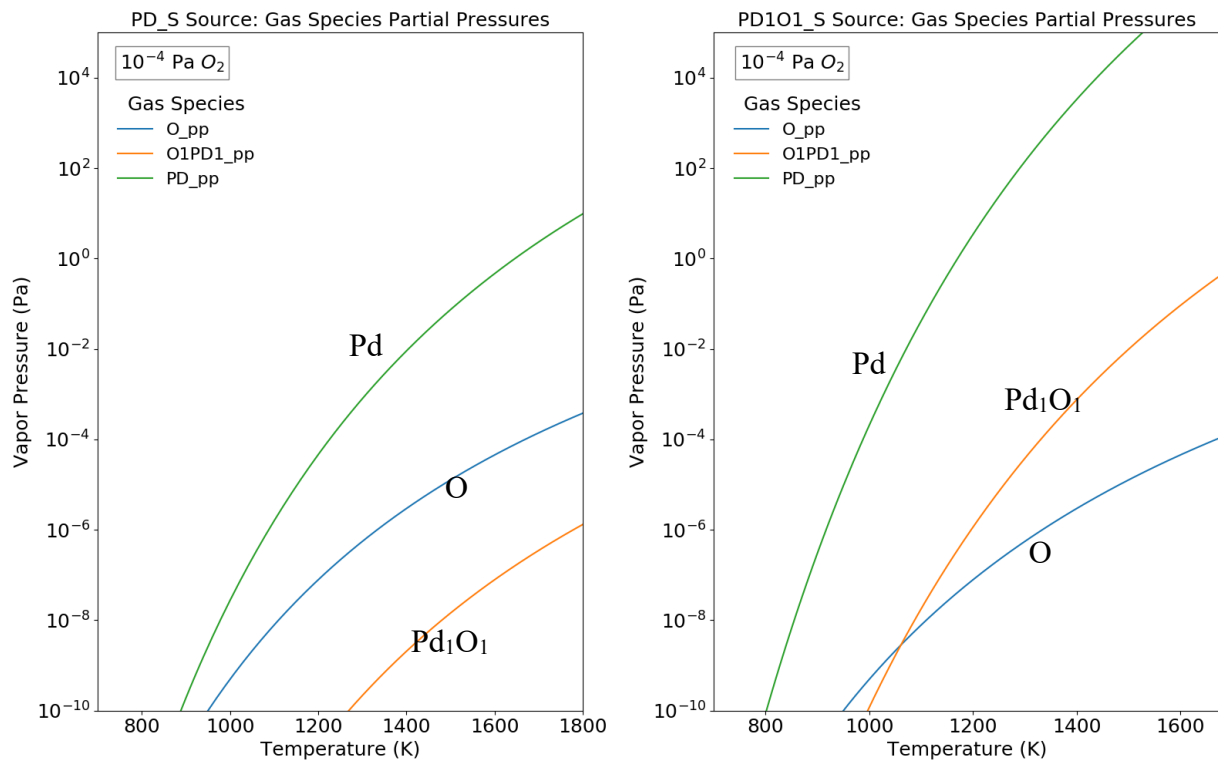


Figure S 51. Solid Pd (the stable phase) and solid PdO. Calculated partial pressures of the gas species over the phase(s) of interest as a function of temperature at  $P_{O_2} = 10^{-4}$  Pa. Here, “\_pp” indicates partial pressure when available.

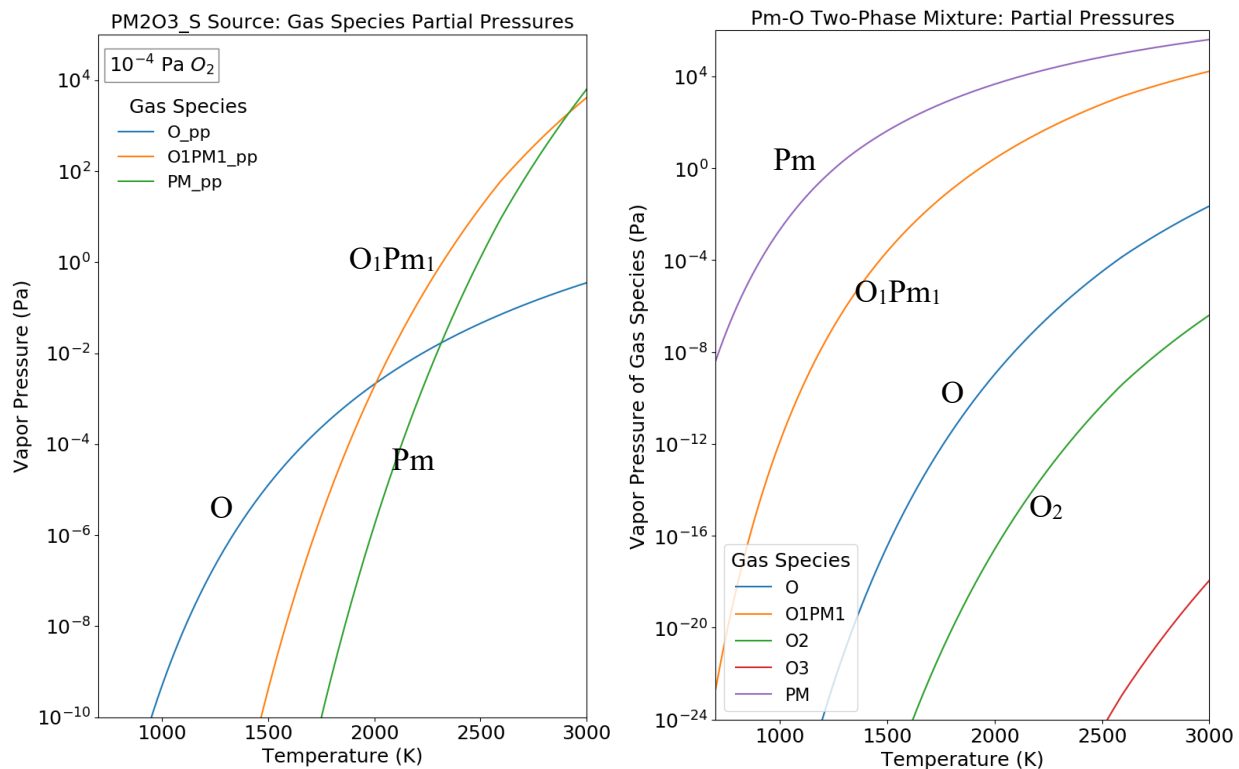
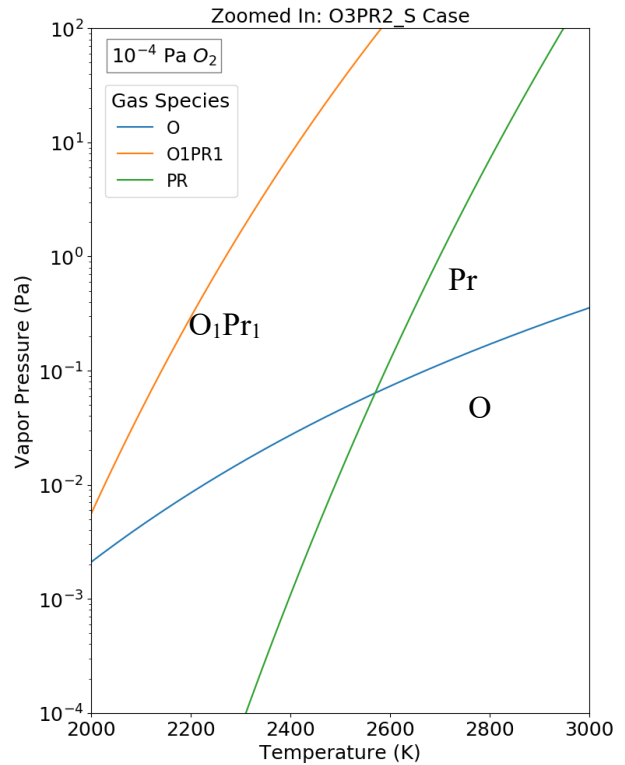
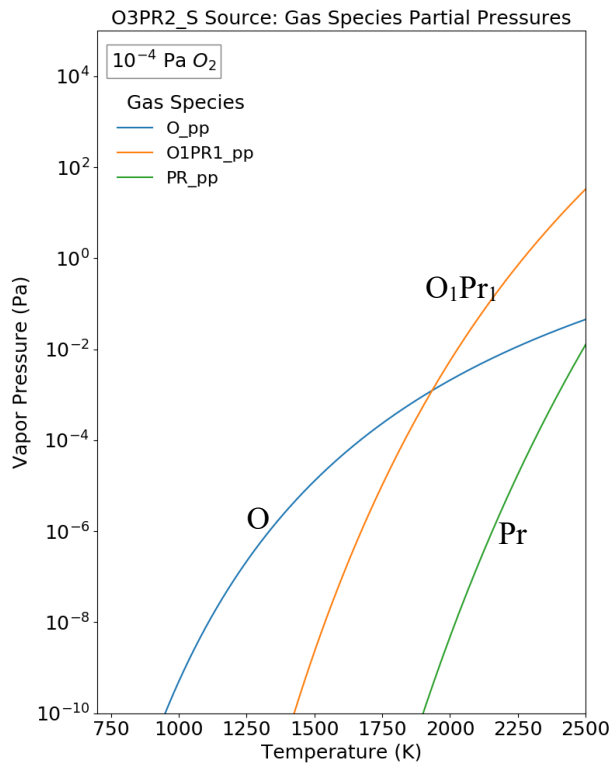
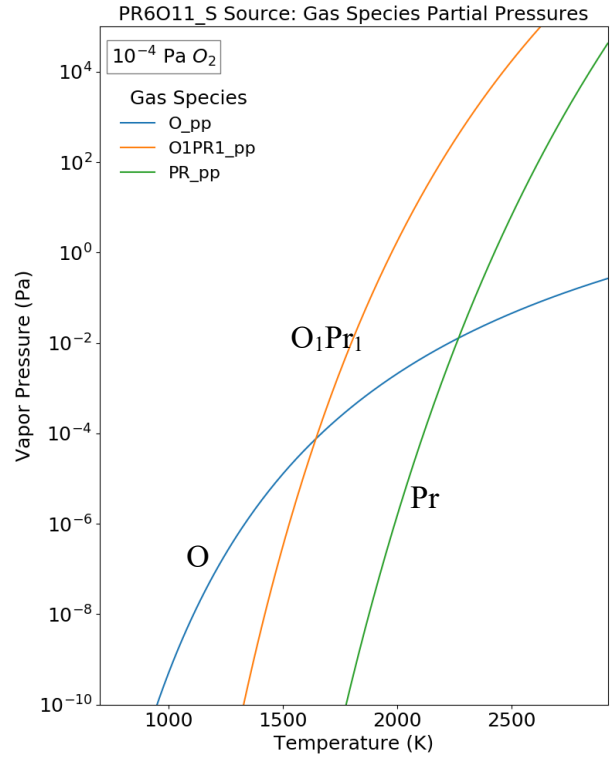
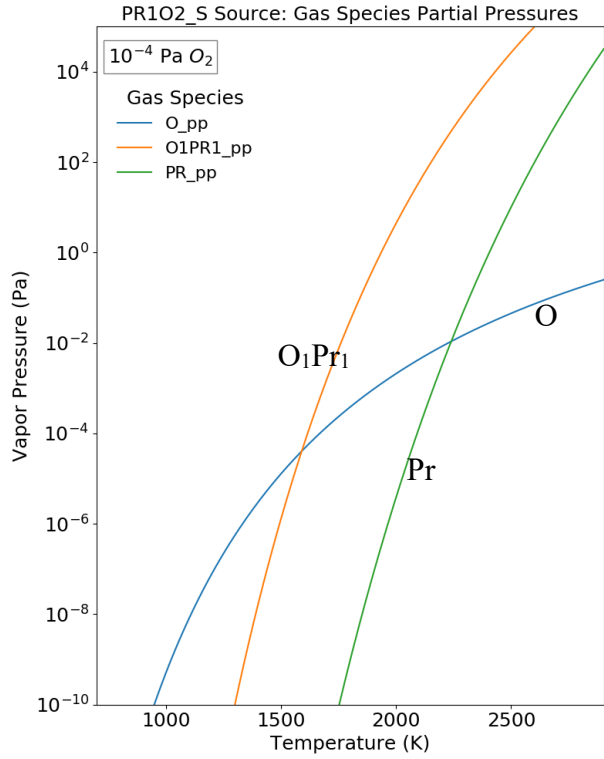


Figure S 52. Solid  $\text{Pm}_2\text{O}_3$  (stable phase up to 2593 K). Calculated partial pressures of the gas species over the phase(s) of interest as a function of temperature at  $P_{\text{O}_2} = 10^{-4}$  Pa. Here, “\_pp” indicates partial pressure when available. Calculated partial pressures of the gas species over a  $\text{Pm}_2\text{O}_3(\text{s},\ell)+\text{Pm}(\text{s},\ell)$  two-phase mixture with an overall composition of  $\text{PmO}$ . Here, (s, $\ell$ ) indicate the solid phase at low temperatures and liquid phase at high temperatures.



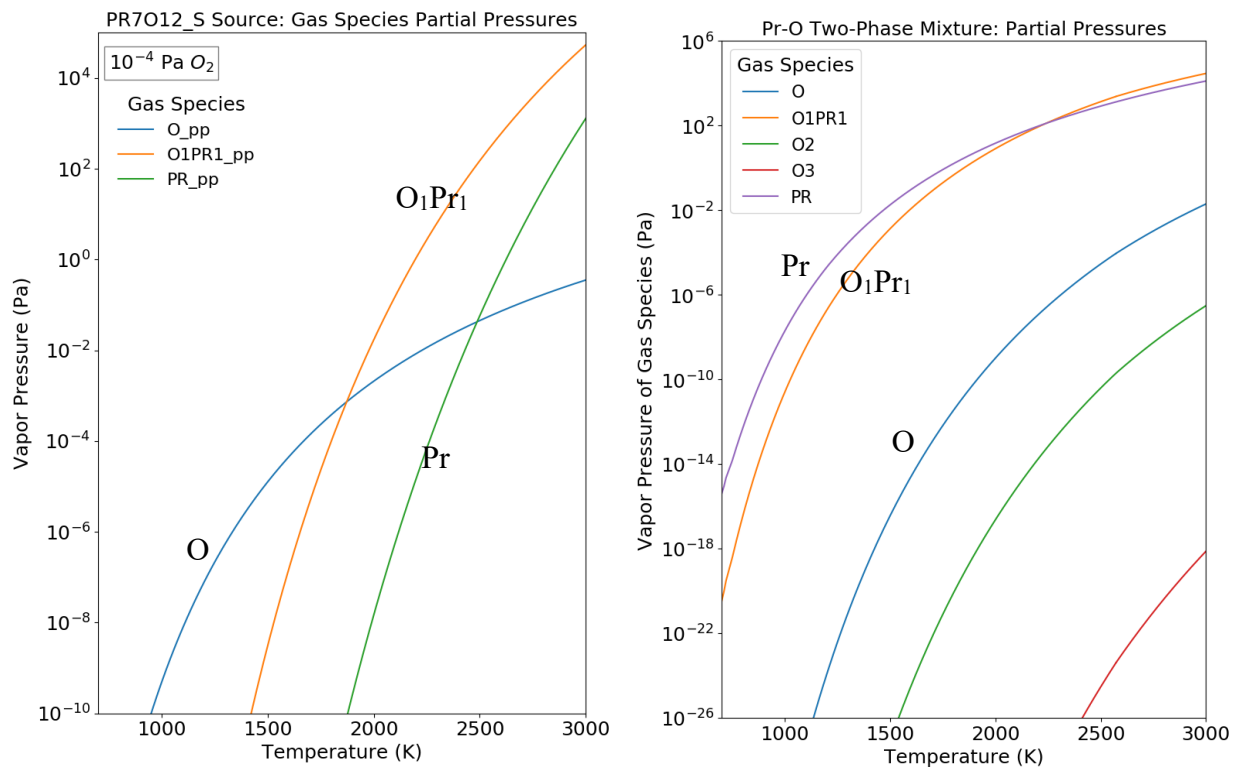


Figure S 53. Solid  $\text{PrO}_2$ , solid  $\text{Pr}_6\text{O}_{11}$ , solid  $\text{Pr}_7\text{O}_{12}$  (the stable phase up to 1361 K), and solid  $\text{Pr}_2\text{O}_3$  (stable with  $T > 1361$  K, with a zoomed-in view in the plot on the right). Calculated partial pressures of the gas species over the phase(s) of interest as a function of temperature at  $P_{\text{O}_2} = 10^{-4}$  Pa. Here, “\_pp” indicates partial pressure when available. Calculated partial pressures of the gas species over a  $\text{Pr}_2\text{O}_3(\text{s},\ell) + \text{Pr}(\text{s},\ell)$  two-phase mixture with an overall composition of  $\text{PrO}$ . Here, (s, $\ell$ ) indicate the solid phase at low temperatures and liquid phase at high temperatures.

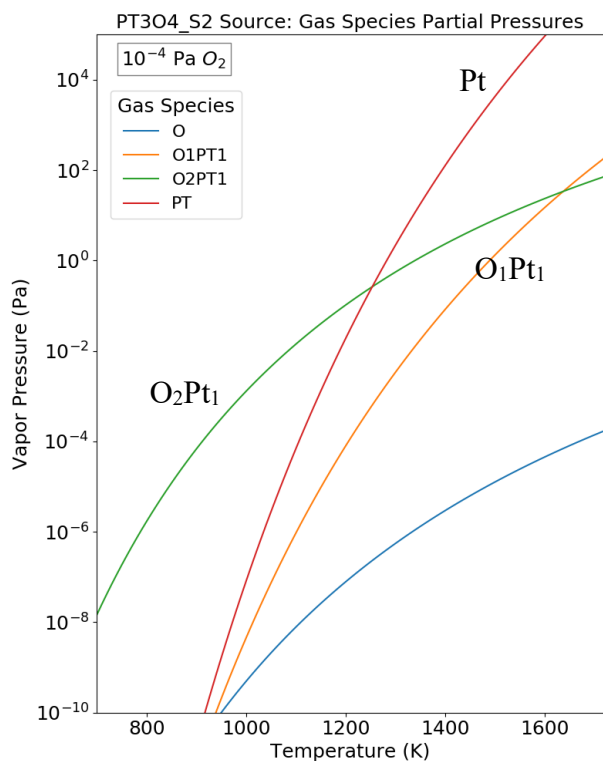
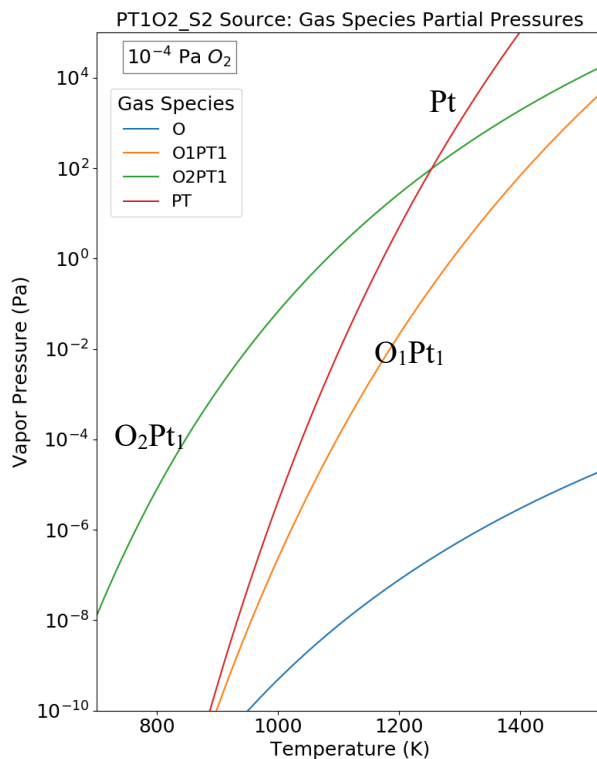
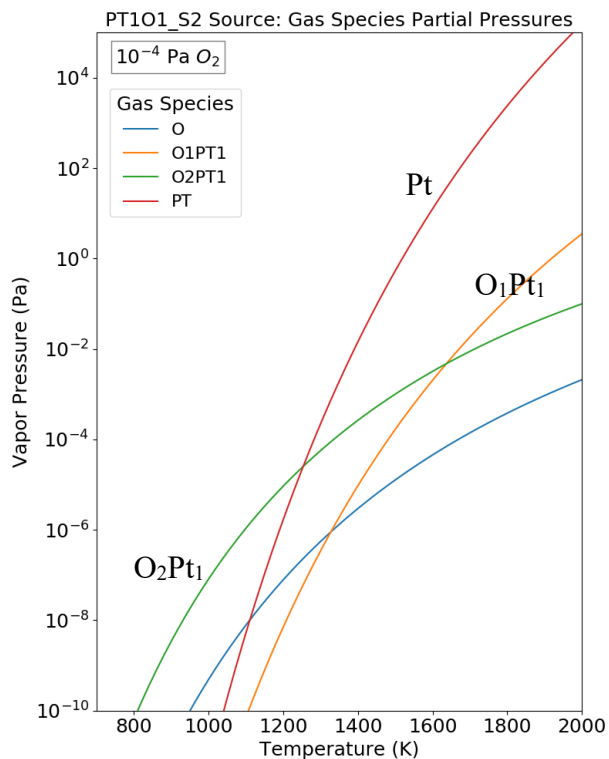


Figure S 54. Solid PtO (metastable), solid PtO<sub>2</sub> (metastable), and solid Pt<sub>3</sub>O<sub>4</sub> (metastable). Calculated partial pressures of the gas species over the phase(s) of interest as a function of temperature at  $P_{O_2} = 10^{-4}$  Pa. Here, “\_pp” indicates partial pressure when available.

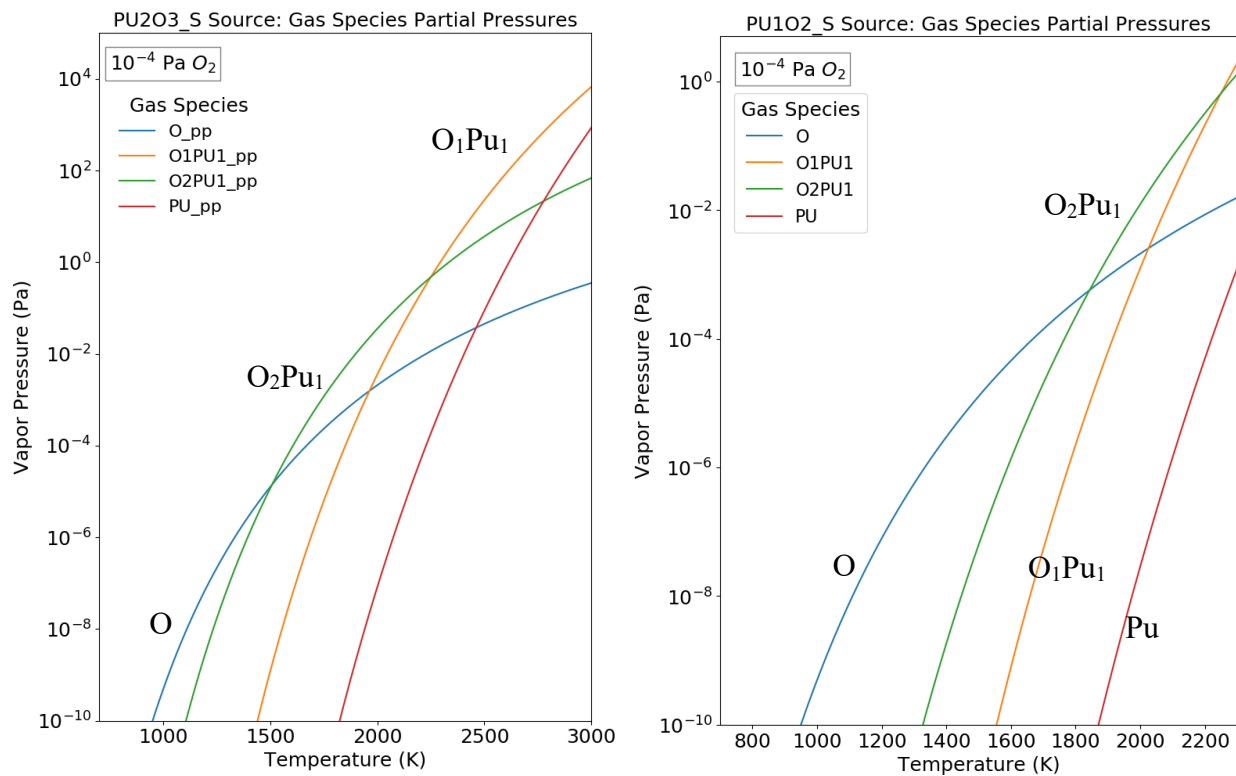
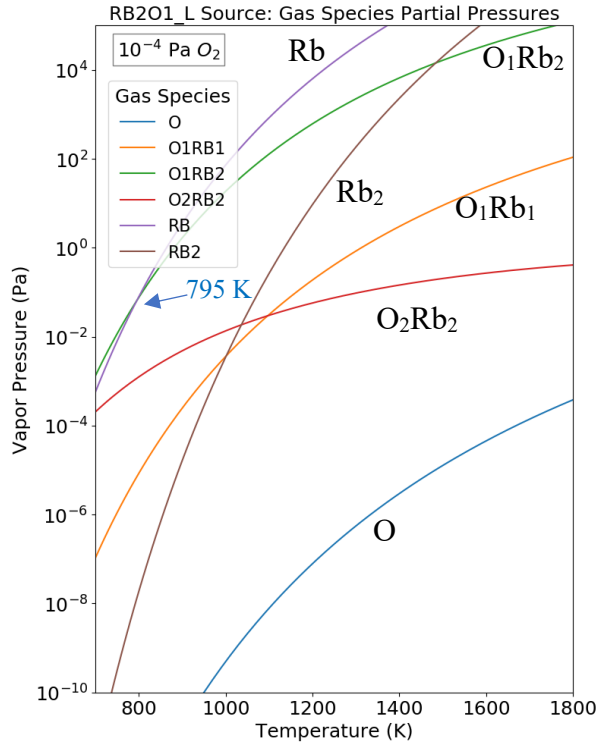
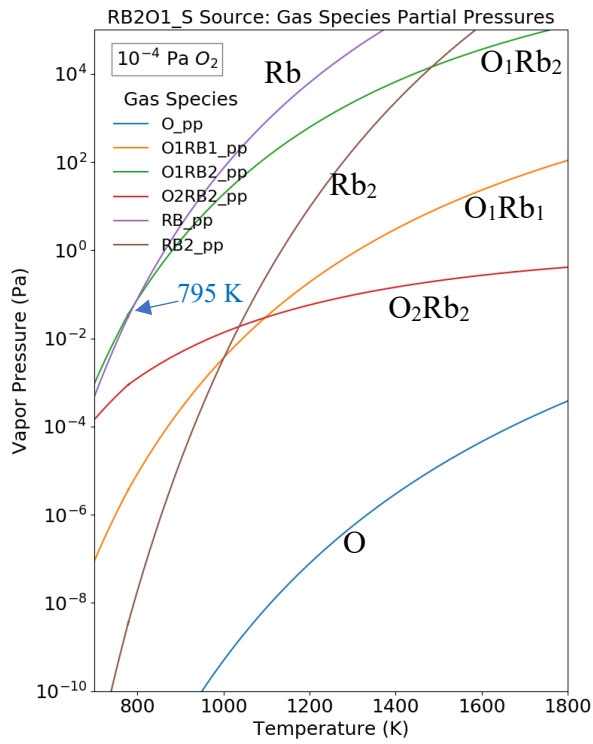
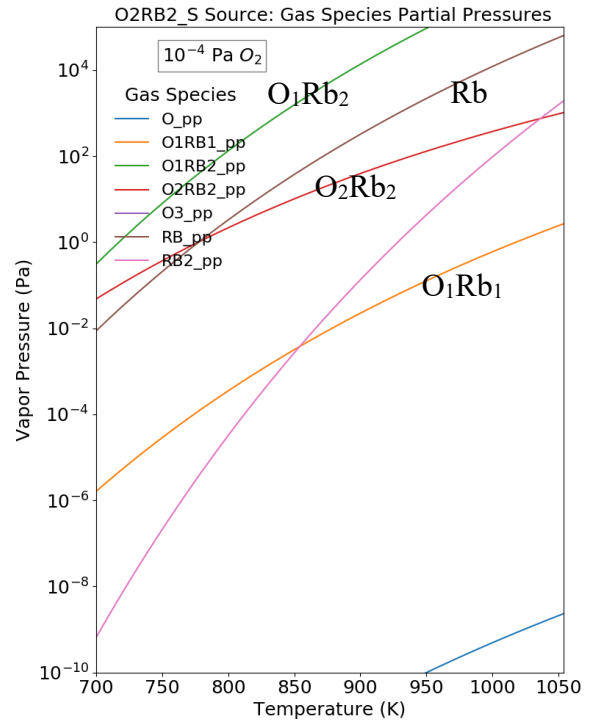
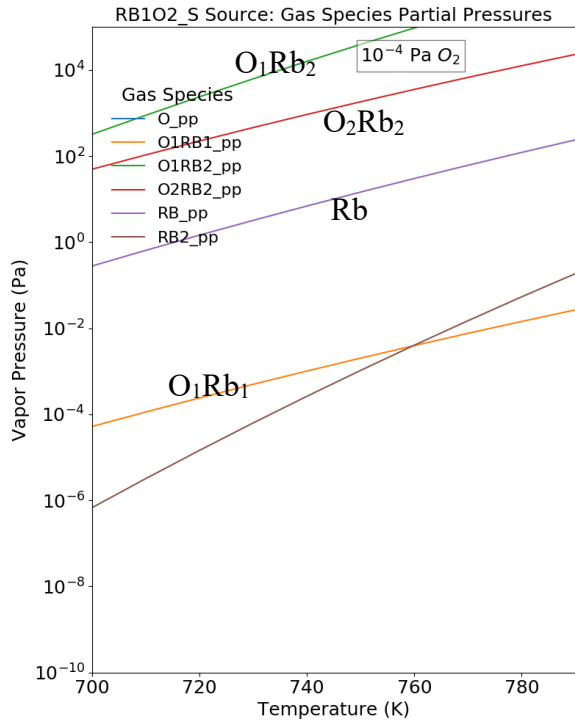


Figure S 55. Solid Pu<sub>2</sub>O<sub>3</sub> and solid PuO<sub>2</sub> (the stable phase). Calculated partial pressures of the gas species over the phase(s) of interest as a function of temperature at  $P_{O_2} = 10^{-4}$  Pa. Here, “\_pp” indicates partial pressure when available.



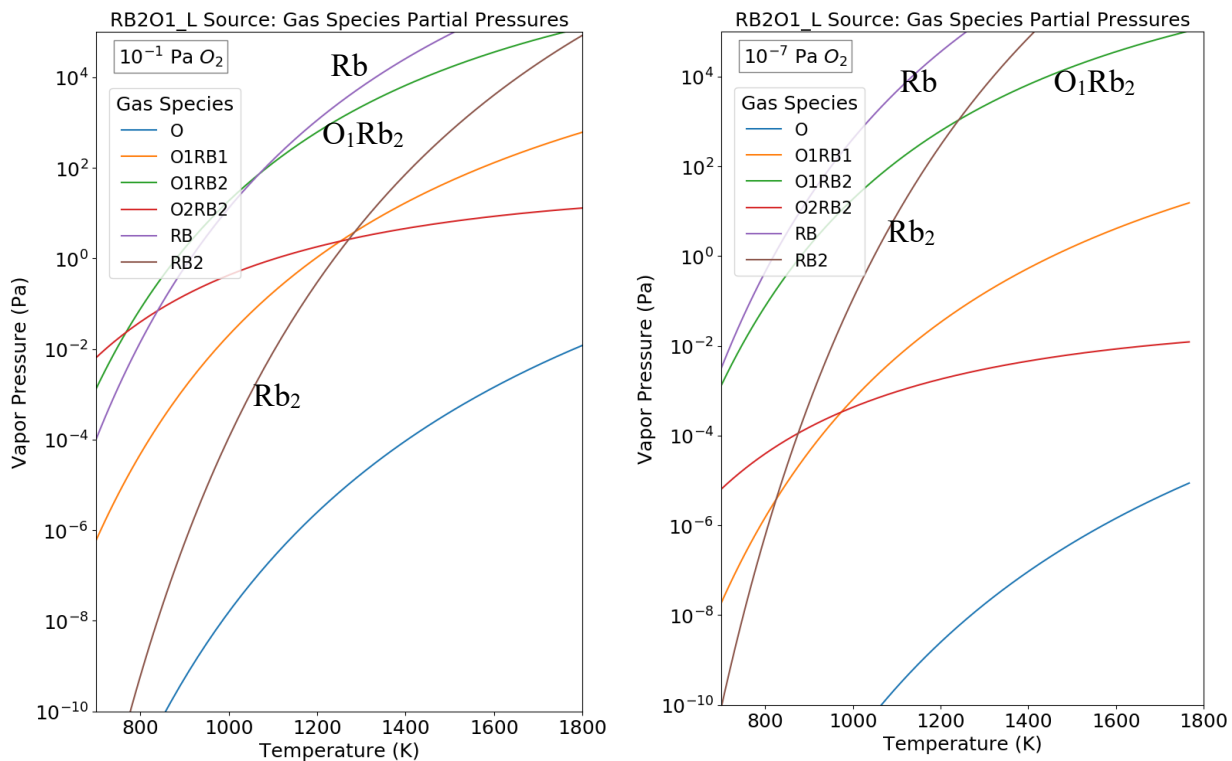


Figure S 56. Solid  $\text{RbO}_2$  (solid  $\text{RbO}_2$  is stable for  $T < 517$  K), solid  $\text{Rb}_2\text{O}_2$ , and solid/liquid  $\text{Rb}_2\text{O}$  (solid  $\text{Rb}_2\text{O}$  is the stable phase for  $T < 778$  K, beyond which liquid  $\text{Rb}_2\text{O}$  is stable). Calculated partial pressures of the gas species over the phase(s) of interest as a function of temperature at  $P_{\text{O}_2} = 10^{-4}$  Pa as well as  $10^{-1}$  Pa and  $10^{-7}$  Pa for liquid  $\text{Rb}_2\text{O}$ . Here, “\_pp” indicates partial pressure when available.

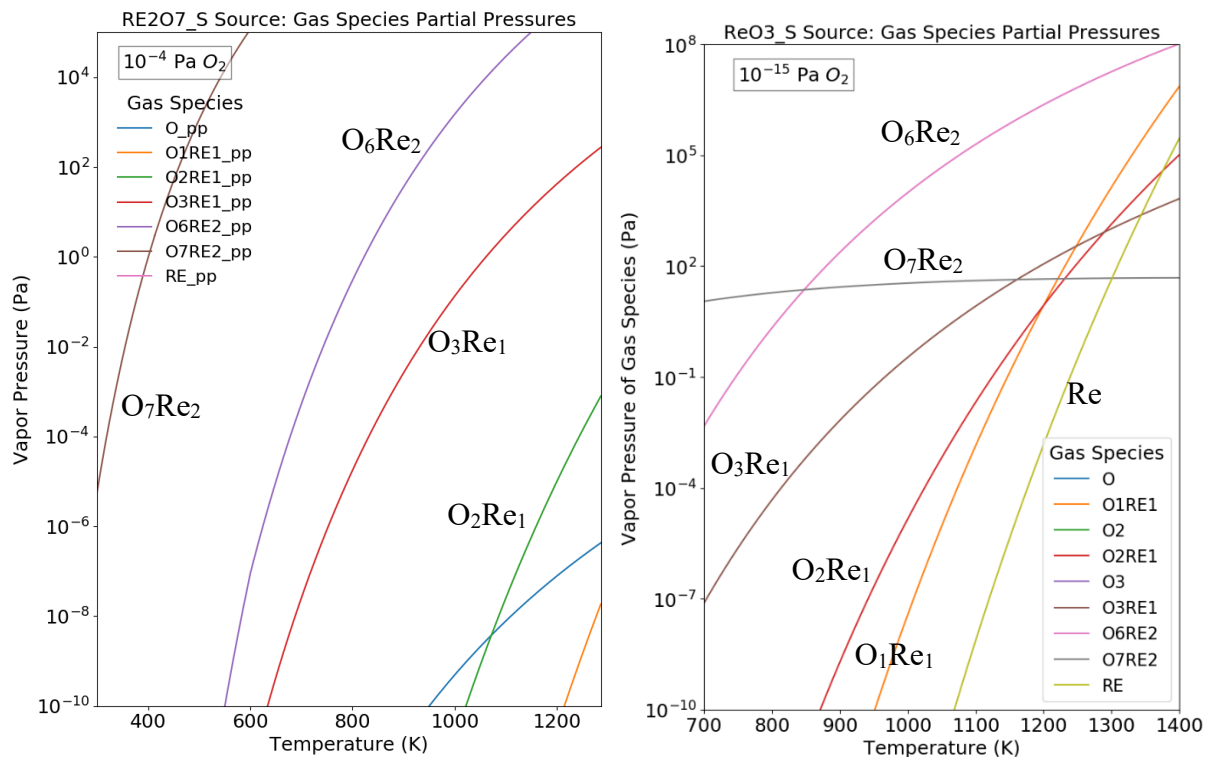


Figure S 57. Solid  $Re_2O_7$  (the stable phase for  $T < 600$  K, beyond which liquid  $Re_2O_7$  is stable) and solid  $ReO_3$ . Calculated partial pressures of the gas species over the phase(s) of interest as a function of temperature at  $P_{O_2} = 10^{-4}$  Pa for  $Re_2O_7$ ; and  $P_{O_2} = 10^{-15}$  Pa for  $ReO_3$ . Here, “\_pp” indicates partial pressure when available. Note that we cannot calculate the equilibria for the metastable  $ReO_3$  solid at  $P_{O_2} = 10^{-4}$  Pa since the gas phase is stable instead of  $ReO_3$ . Instead, we predicted the gas species over solid  $ReO_3$  at  $P_{O_2} = 10^{-15}$  Pa.

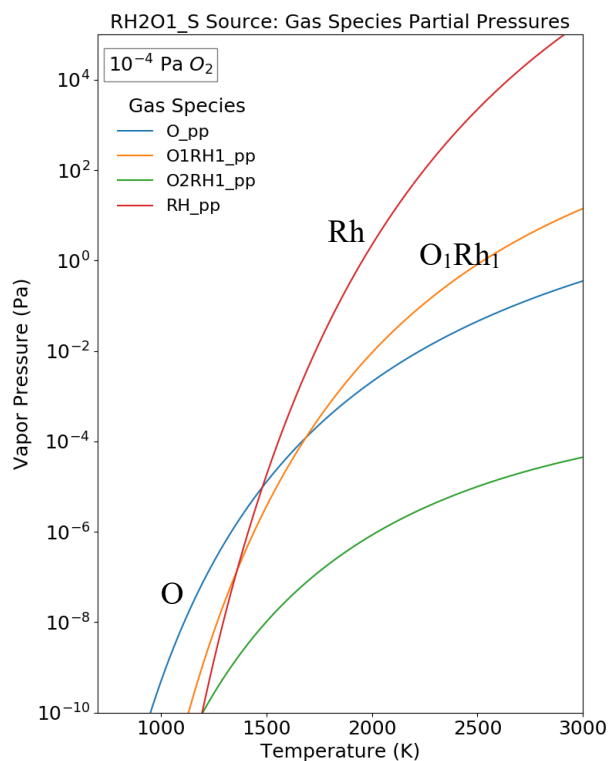
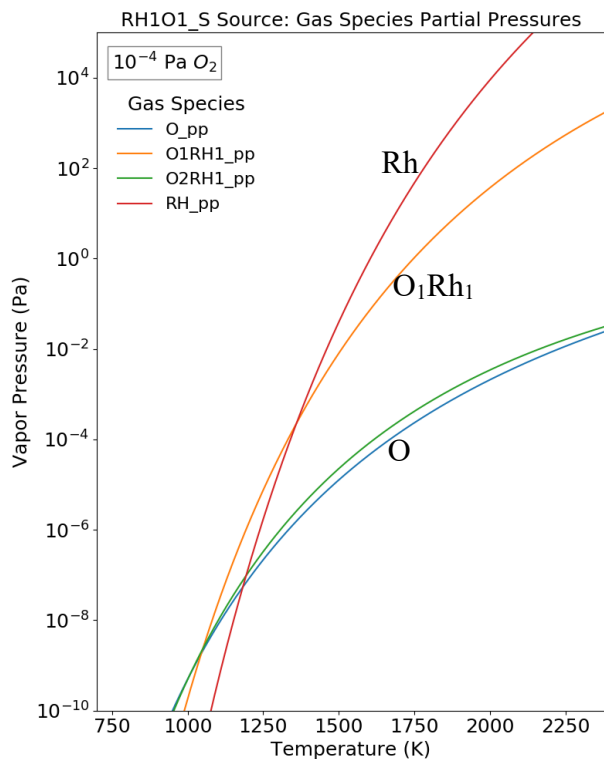
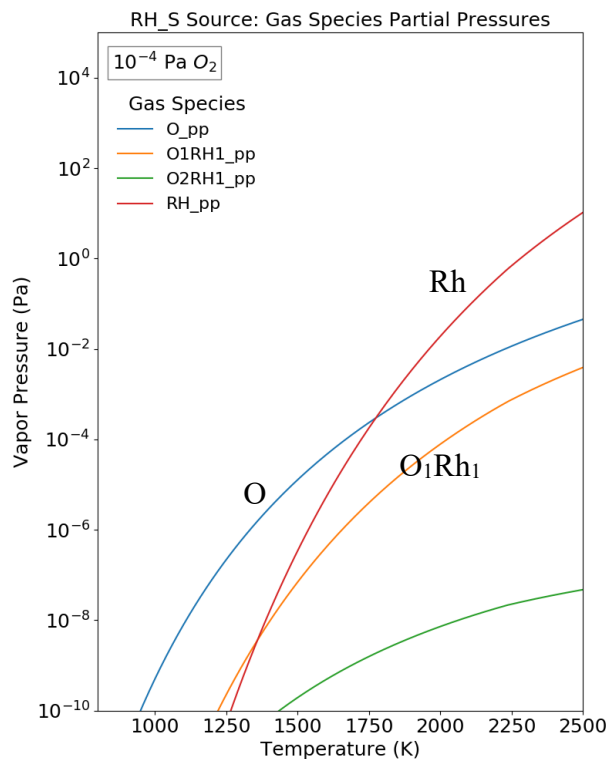


Figure S 58. Solid Rh (the stable phase for  $T < 2237$  K, beyond which liquid Rh is stable), solid RhO, and solid Rh<sub>2</sub>O. Calculated partial pressures of the gas species over the phase(s) of interest as a function of temperature at  $P_{O_2} = 10^{-4}$  Pa. Here, “\_pp” indicates partial pressure when available

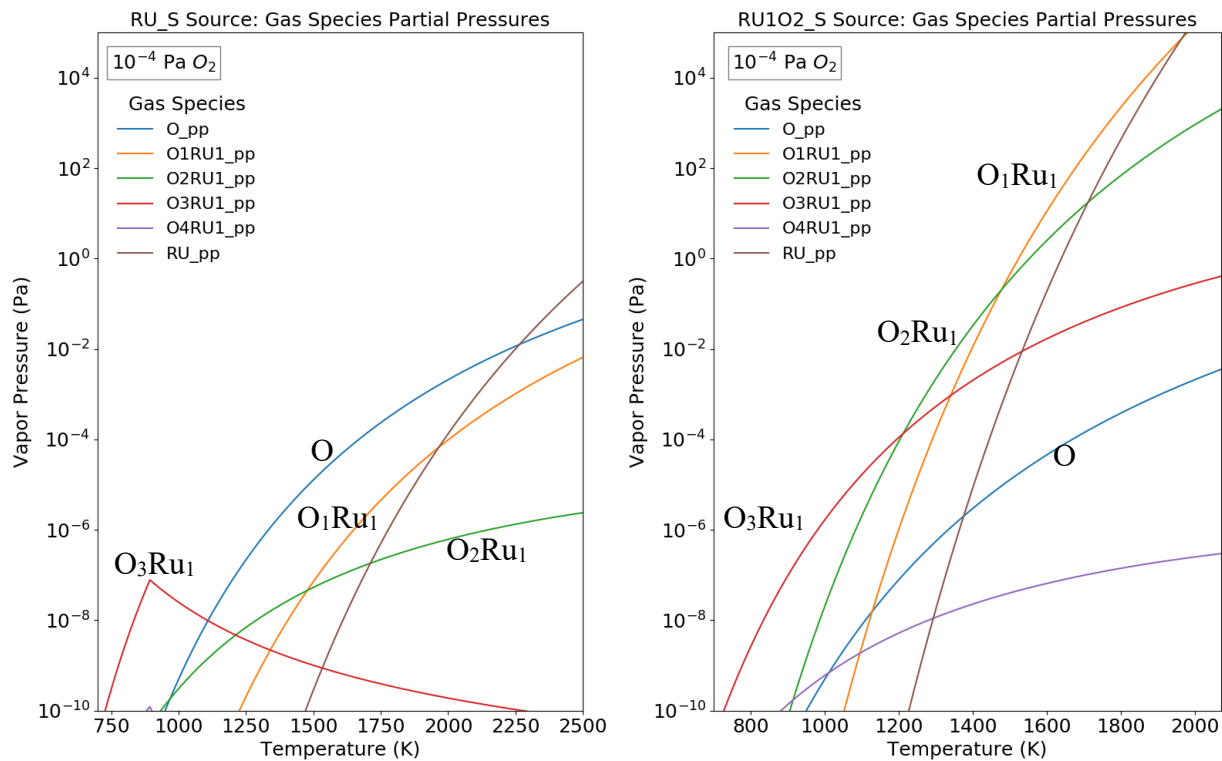


Figure S 59. Solid Ru and solid  $RuO_2$  (the stable phase for  $T < 893$  K, beyond which solid Ru is stable). Calculated partial pressures of the gas species over the phase(s) of interest as a function of temperature at  $P_{O_2} = 10^{-4}$  Pa. Here, “\_pp” indicates partial pressure when available.

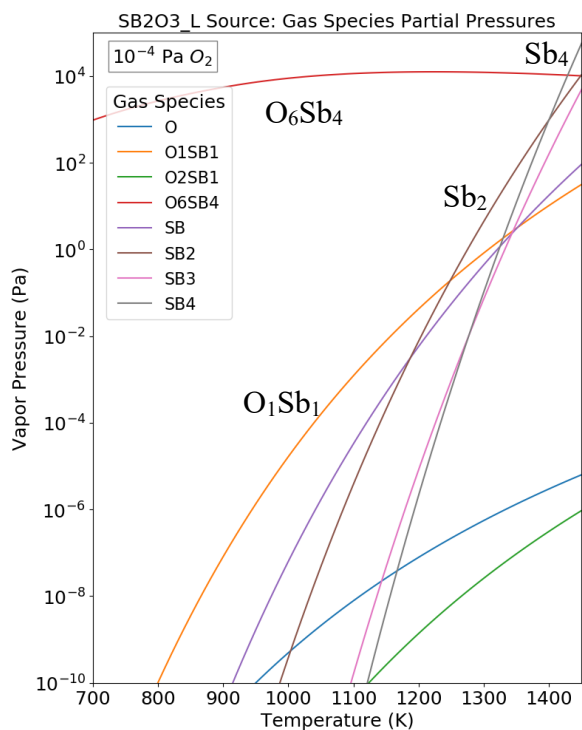
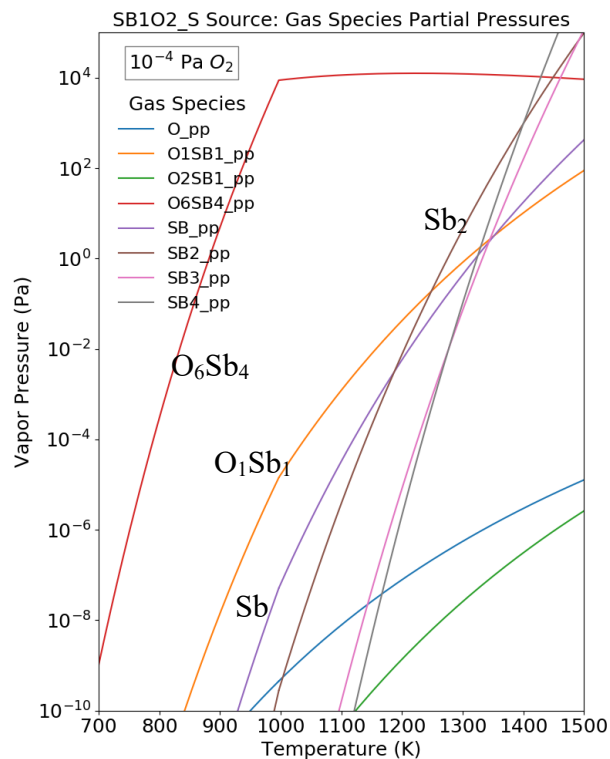
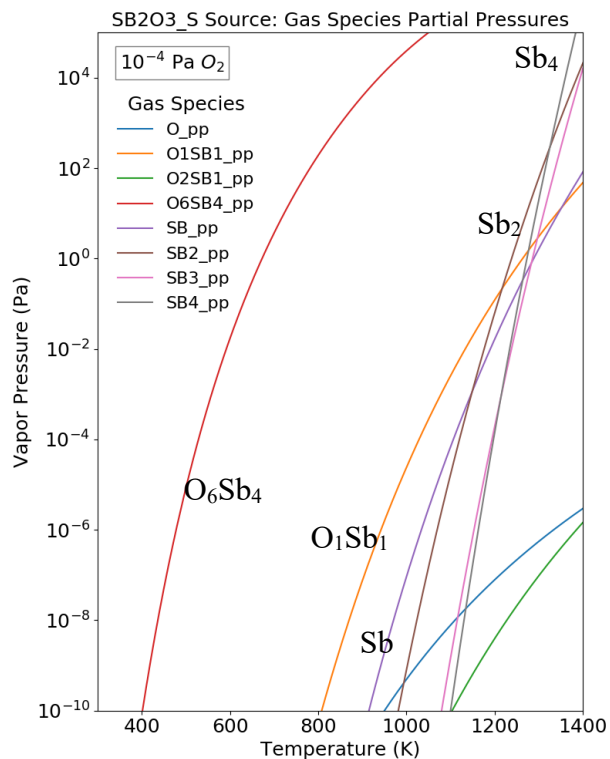


Figure S 60. Solid and liquid  $Sb_2O_3$  and solid  $SbO_2$  (solid  $SbO_2$  is the stable phase for  $T < 997$  K, beyond which liquid  $Sb_2O_3$  is stable). Calculated partial pressures of the gas species over the phase(s) of interest as a function of temperature at  $P_{O_2} = 10^{-4}$  Pa. Here, “\_pp” indicates partial pressure when available.

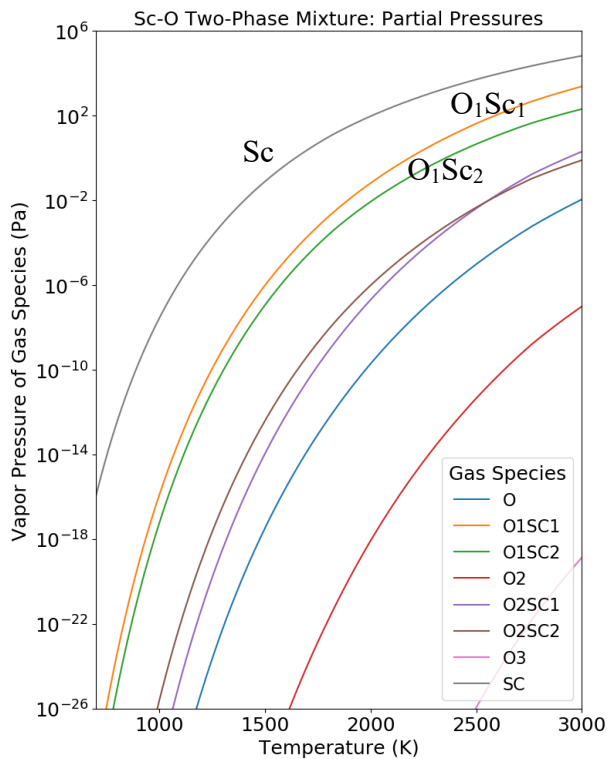
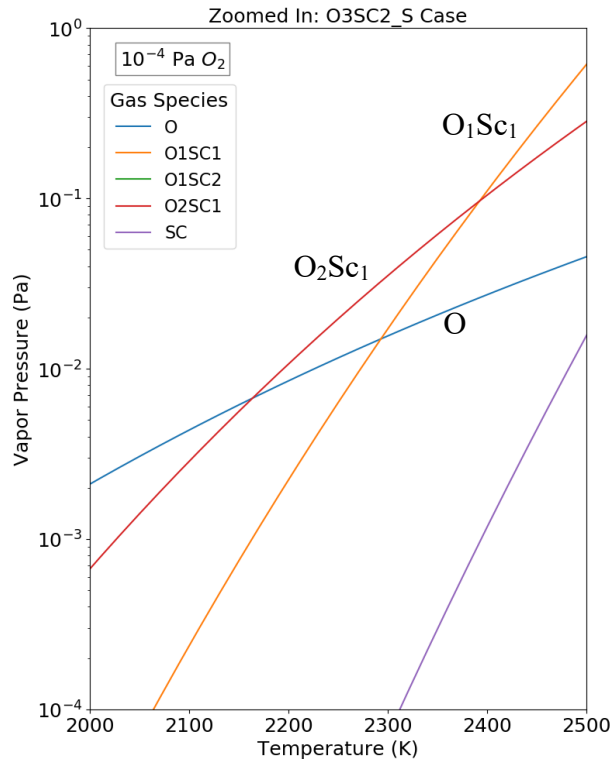
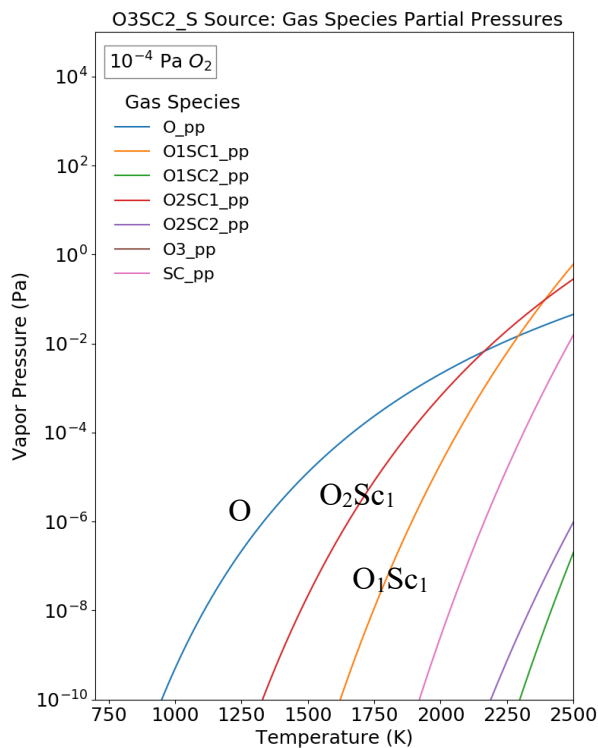


Figure S 61. Solid  $\text{Sc}_2\text{O}_3$  (with a zoomed-in view in the plot on the right). Calculated partial pressures of the gas species over the phase(s) of interest as a function of temperature at  $P_{\text{O}_2} = 10^{-4}$  Pa. Here, “\_pp” indicates partial pressure when available. Calculated partial pressures of the gas species over a  $\text{Sc}_2\text{O}_3(\text{s})+\text{Sc}(\text{s},\ell)$  two-phase mixture with an overall composition of  $\text{ScO}$ . Here, (s, $\ell$ ) indicate the solid phase at low temperatures and liquid phase at high temperatures.

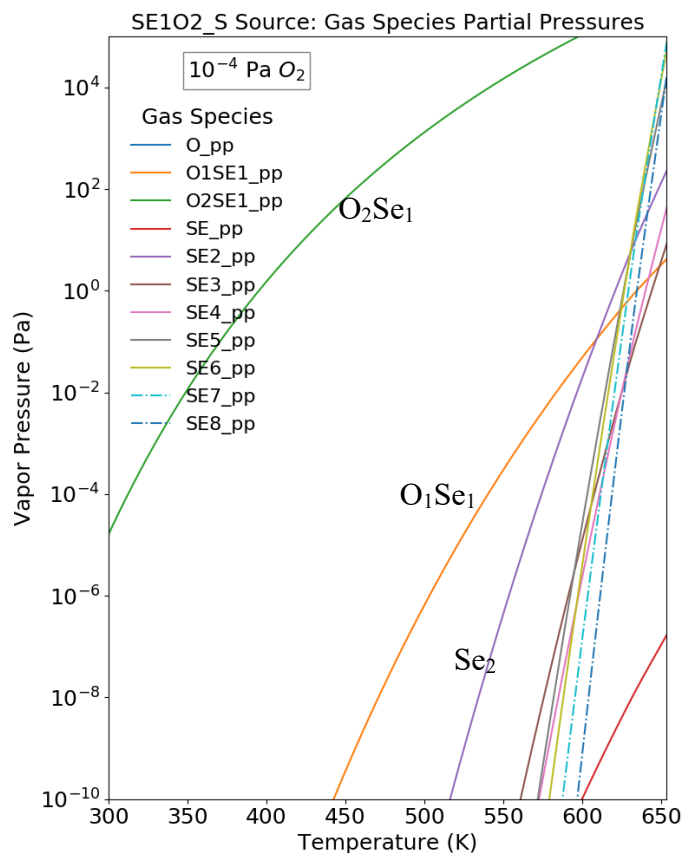
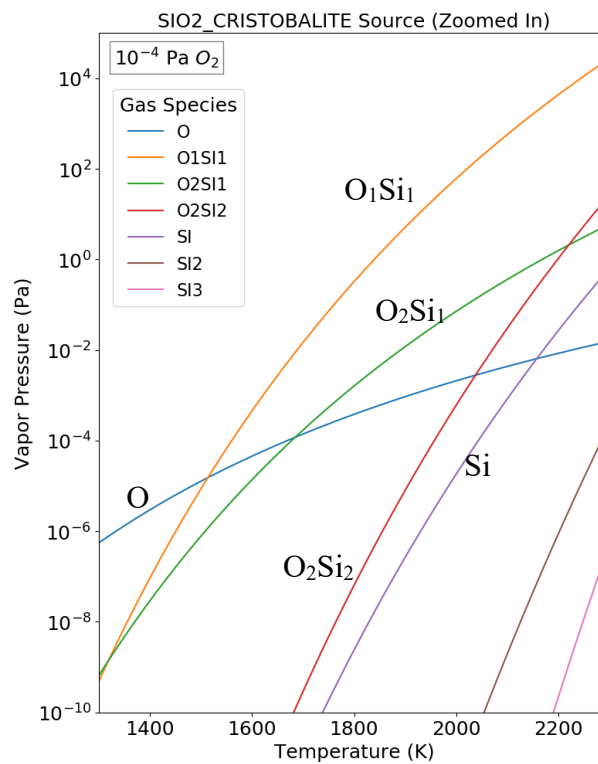
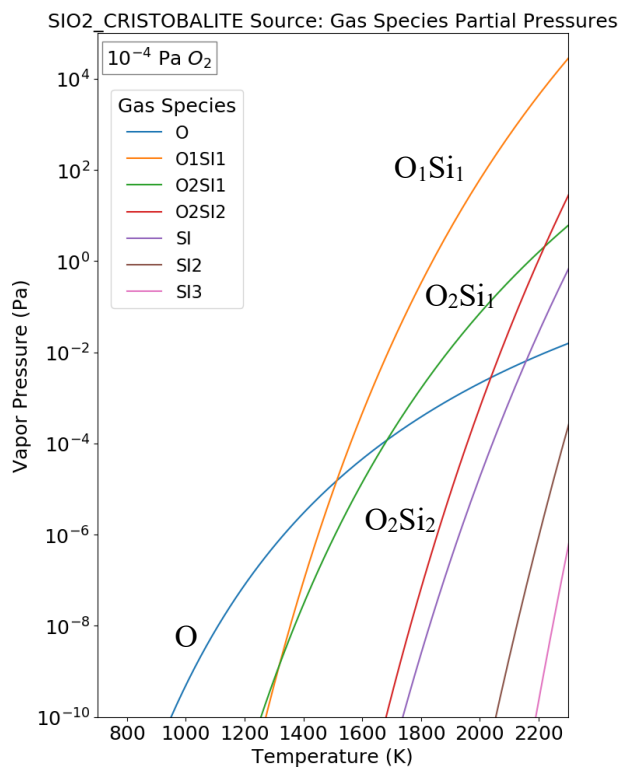
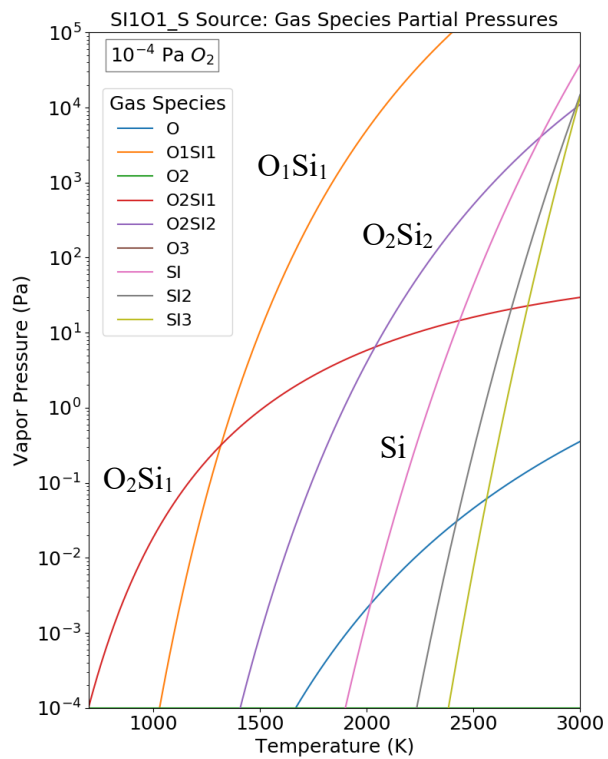


Figure S 62. Solid  $SeO_2$  (the stable phase for  $T < 633$  K, beyond which liquid  $SeO_2$  is stable). Calculated partial pressures of the gas species over the phase(s) of interest as a function of temperature at  $P_{O_2} = 10^{-4}$  Pa. Here, “\_pp” indicates partial pressure when available.



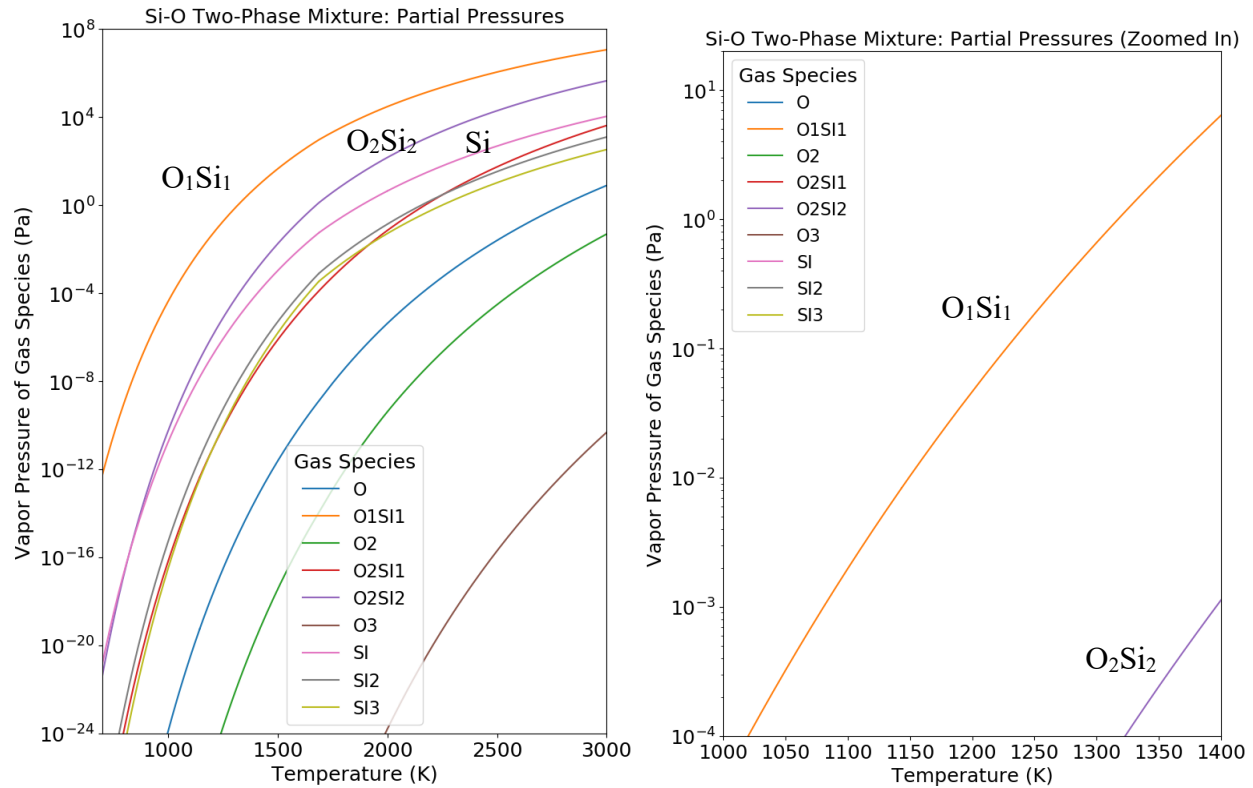


Figure S 63. Solid  $\text{SiO}_2$ \_cristobalite and  $\text{SiO}(\text{am})$ . Calculated partial pressures of the gas species over the phase(s) of interest as a function of temperature at  $P_{\text{O}_2} = 10^{-4}$  Pa. Here, “\_pp” indicates partial pressure when available. Calculated partial pressures of the gas species over a  $\text{SiO}_2(\text{s},\ell)+\text{Si}(\text{s},\ell)$  two-phase mixture with an overall composition of  $\text{SiO}$ . Here, (s, $\ell$ ) indicate the solid phase at low temperatures and liquid phase at high temperatures.

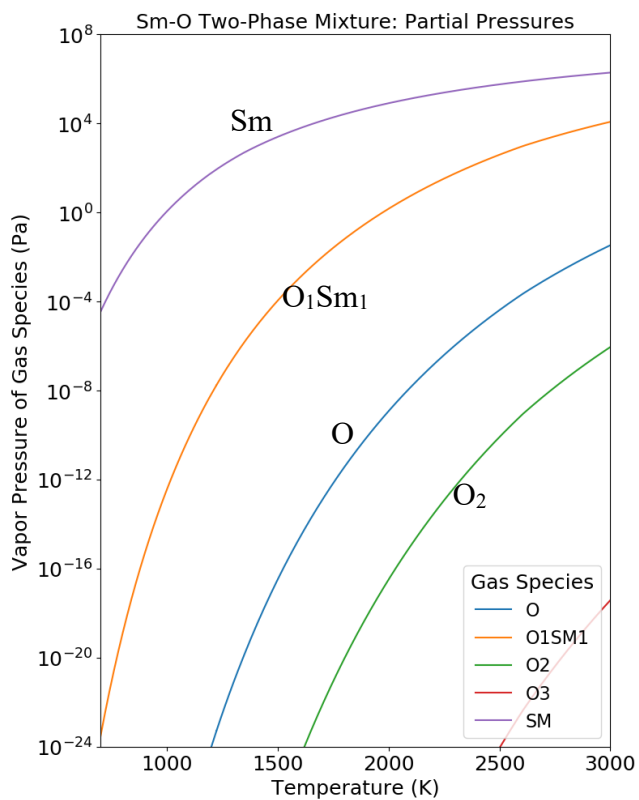
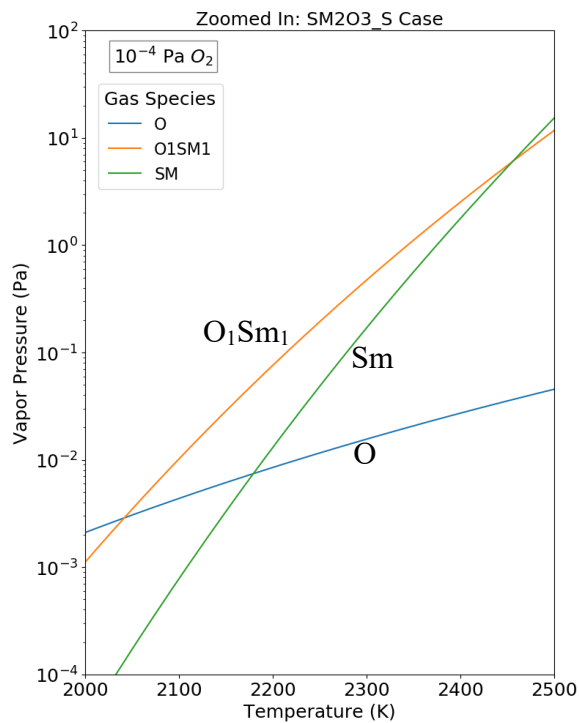
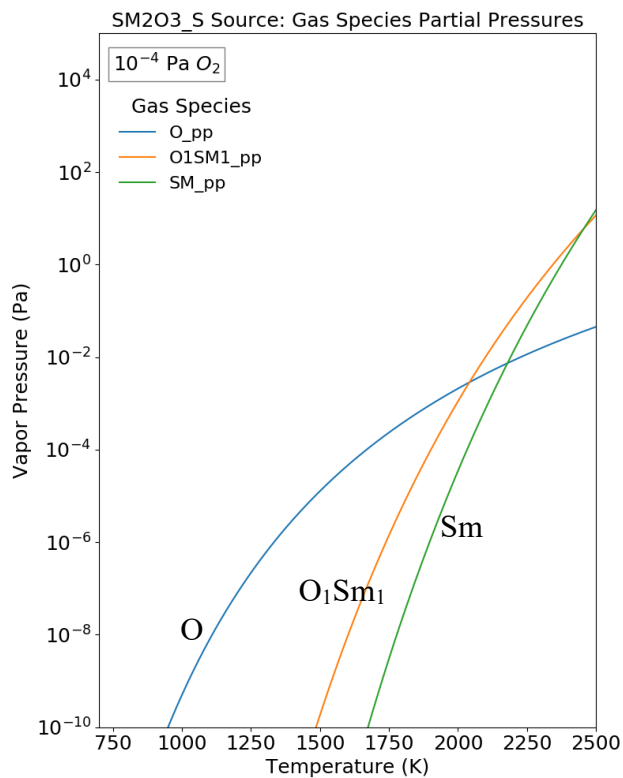


Figure S 64. Solid  $\text{Sm}_2\text{O}_3$  (the stable phase) with a zoomed-in view in the plot on the right. Calculated partial pressures of the gas species over the phase(s) of interest as a function of temperature at  $P_{\text{O}_2} = 10^{-4}$  Pa. Here, “\_pp” indicates partial pressure when available. Calculated partial pressures of the gas species over a  $\text{Sm}_2\text{O}_3(\text{s})+\text{Sm}(\text{s},\ell)$  two-phase mixture with an overall composition of  $\text{SmO}$ . Here, (s, $\ell$ ) indicate the solid phase at low temperatures and liquid phase at high temperatures.

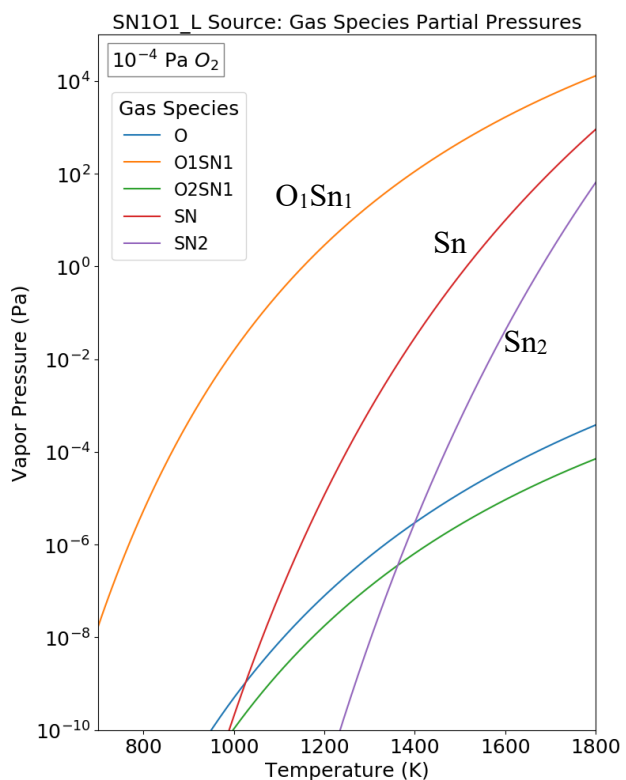
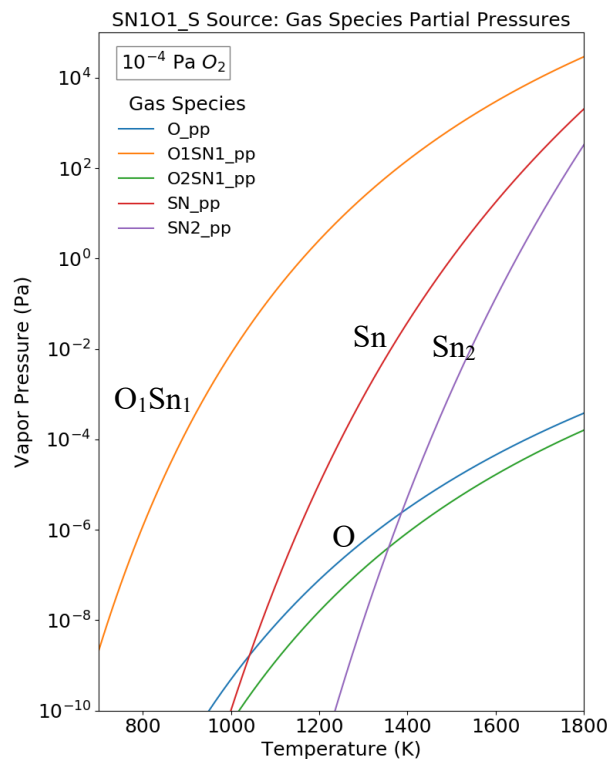
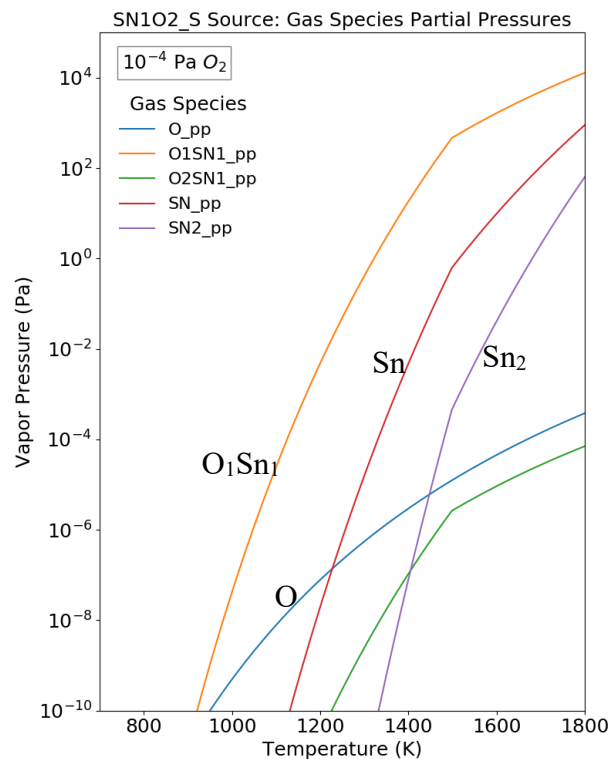


Figure S 65. Solid SnO<sub>2</sub> and solid/liquid SnO (solid SnO<sub>2</sub> is the stable phase for  $T < 1498$  K, beyond which liquid SnO is stable). Calculated partial pressures of the gas species over the phase(s) of interest as a function of temperature at  $P_{O_2} = 10^{-4}$  Pa. Here, “\_pp” indicates partial pressure when available; see also Figure 4 for the evaporation of a two-phase mixture of SnO<sub>2</sub>(s) + Sn( $\ell$ ) with an overall composition of SnO

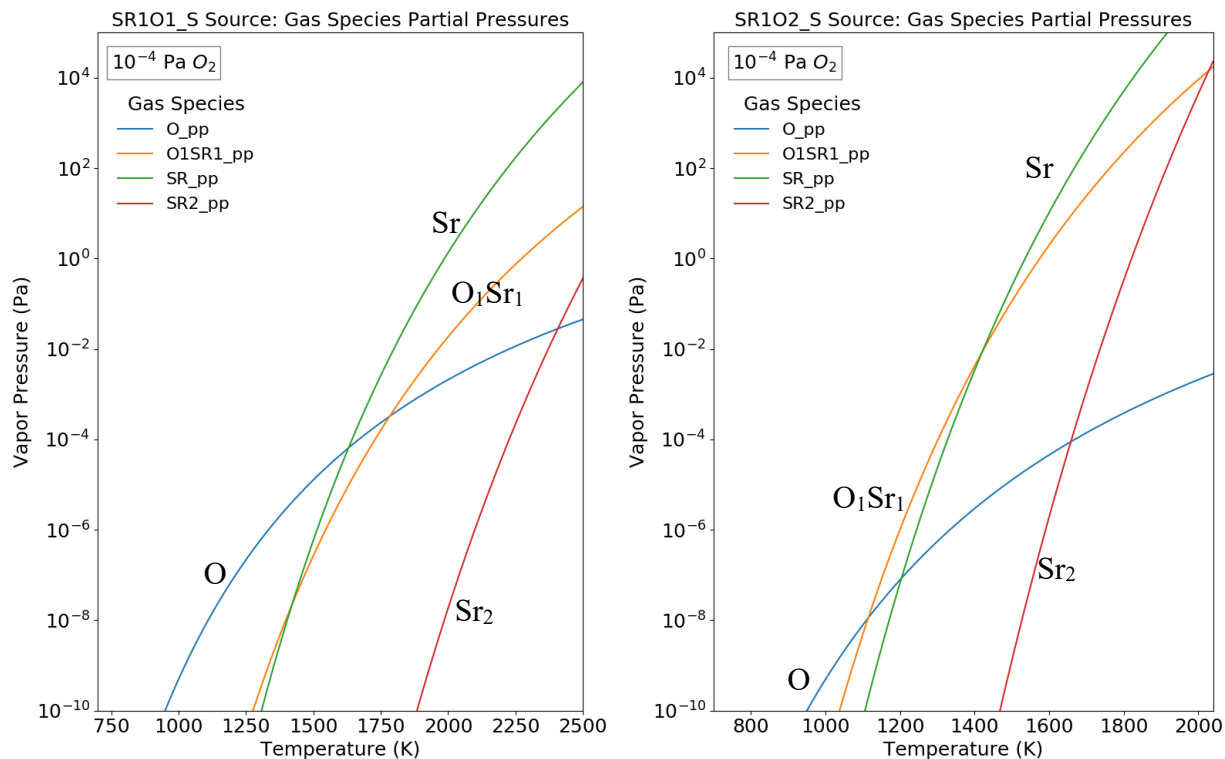


Figure S 66. Solid SrO<sub>2</sub> and solid SrO (these are the stable phases over the entire temperature range shown). Calculated partial pressures of the gas species over the phase(s) of interest as a function of temperature at  $P_{O_2} = 10^{-4}$  Pa. Here, “\_pp” indicates partial pressure when available.

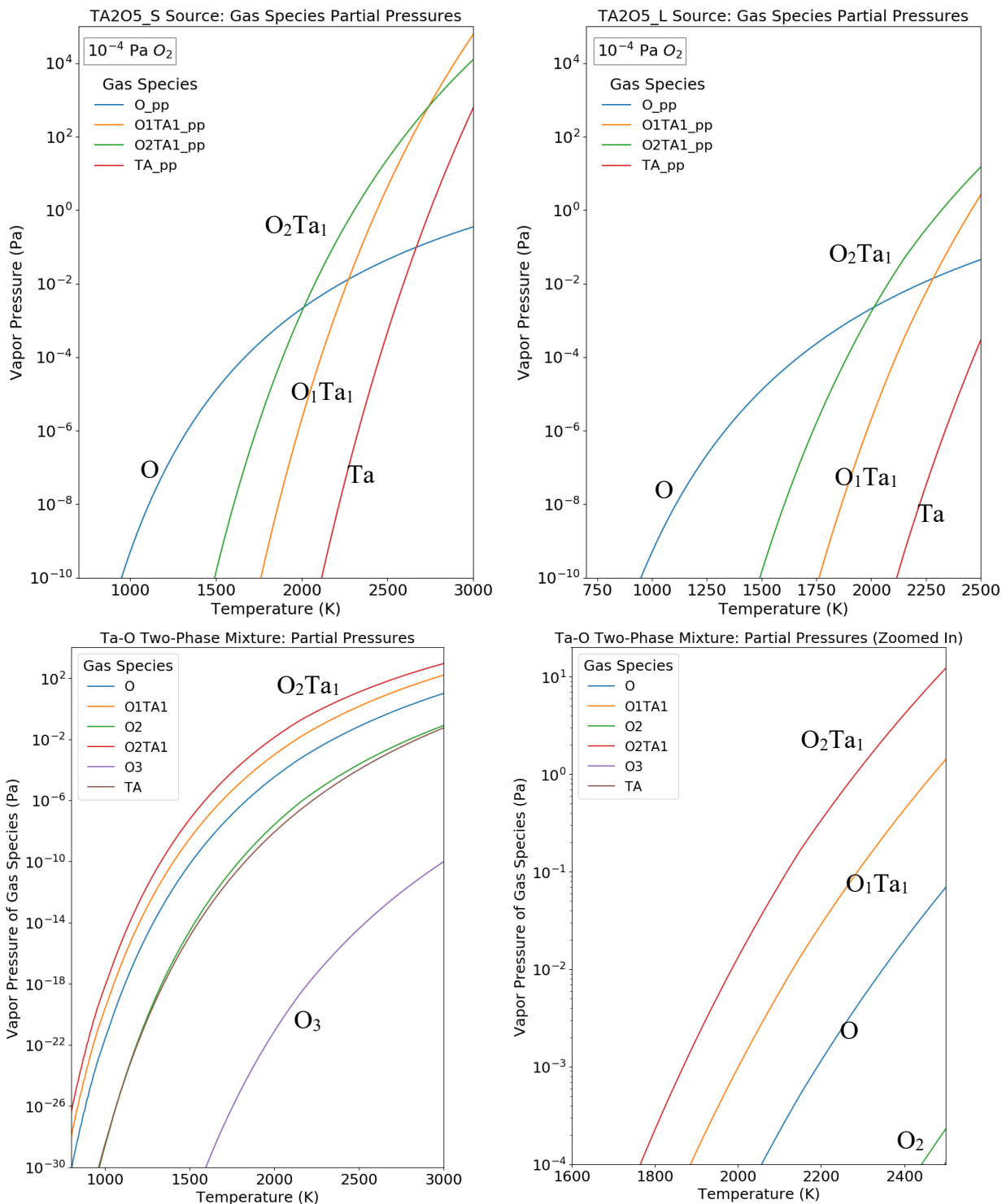


Figure S 67. Solid  $Ta_2O_5$  (stable for  $T < 2150$  K, beyond which liquid  $Ta_2O_5$  is stable) and liquid  $Ta_2O_5$ . Calculated partial pressures of the gas species over the phase(s) of interest as a function of temperature at  $P_{O_2} = 10^{-4}$  Pa. Here, “\_pp” indicates partial pressure when available. Calculated partial pressures of the gas species over a  $Ta_2O_5(s,\ell)+Ta(s)$  two-phase mixture with an overall

composition of TaO<sub>2</sub>. Here, (s,l) indicate the solid phase at low temperatures and liquid phase at high temperatures.

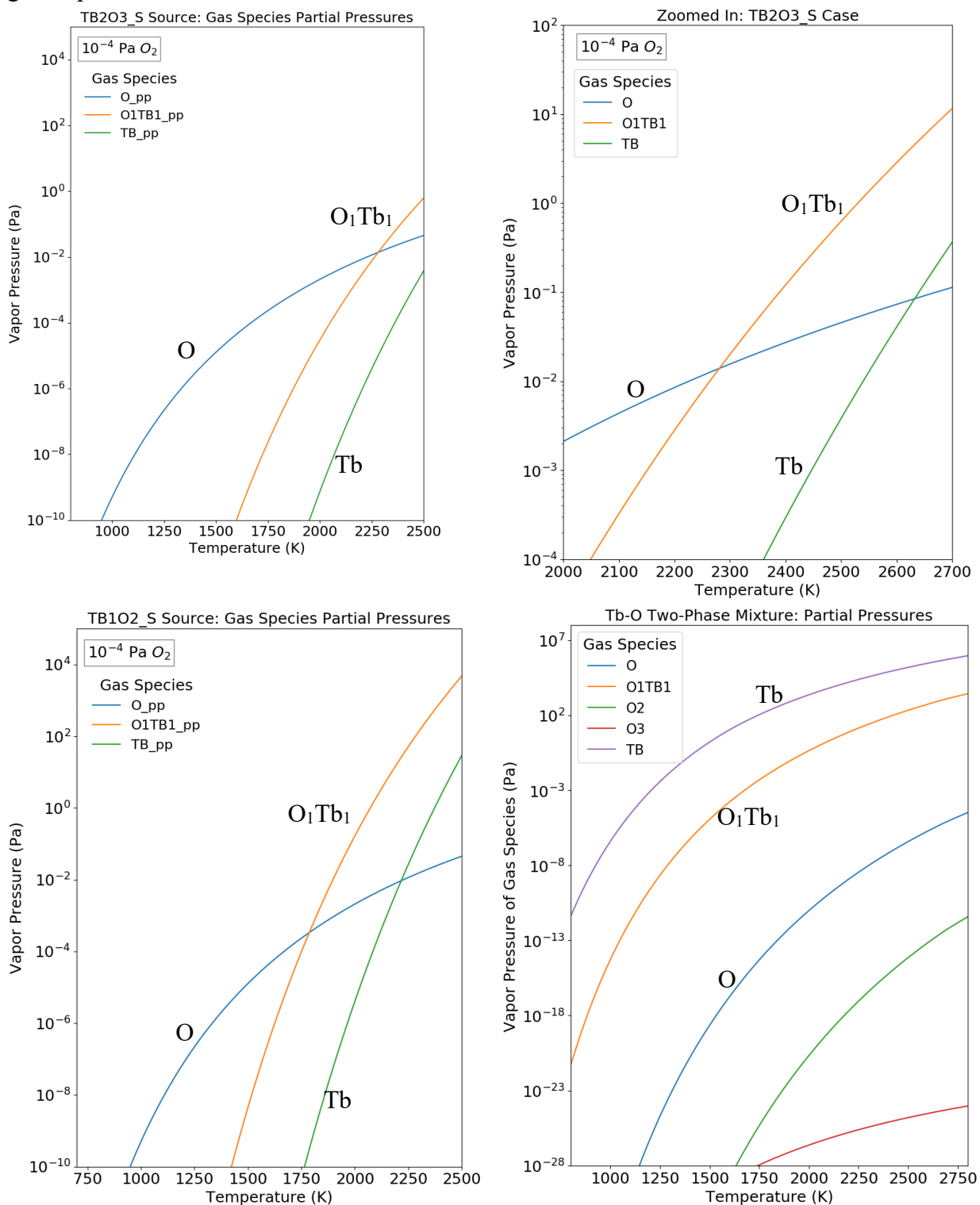


Figure S 68. Solid TbO<sub>2</sub> and solid Tb<sub>2</sub>O<sub>3</sub> (stable phase over the temperature range shown, with a zoomed-in view in the plot on the right). Calculated partial pressures of the gas species over the phase(s) of interest as a function of temperature at  $P_{O_2} = 10^{-4}$  Pa. Here, “\_pp” indicates partial

pressure when available. Calculated partial pressures of the gas species over a  $\text{Tb}_2\text{O}_3(\text{s},\ell)+\text{Tb}(\text{s},\ell)$  two-phase mixture with an overall composition of  $\text{TbO}$ . Here, (s, $\ell$ ) indicate the solid phase at low temperatures and liquid phase at high temperatures.

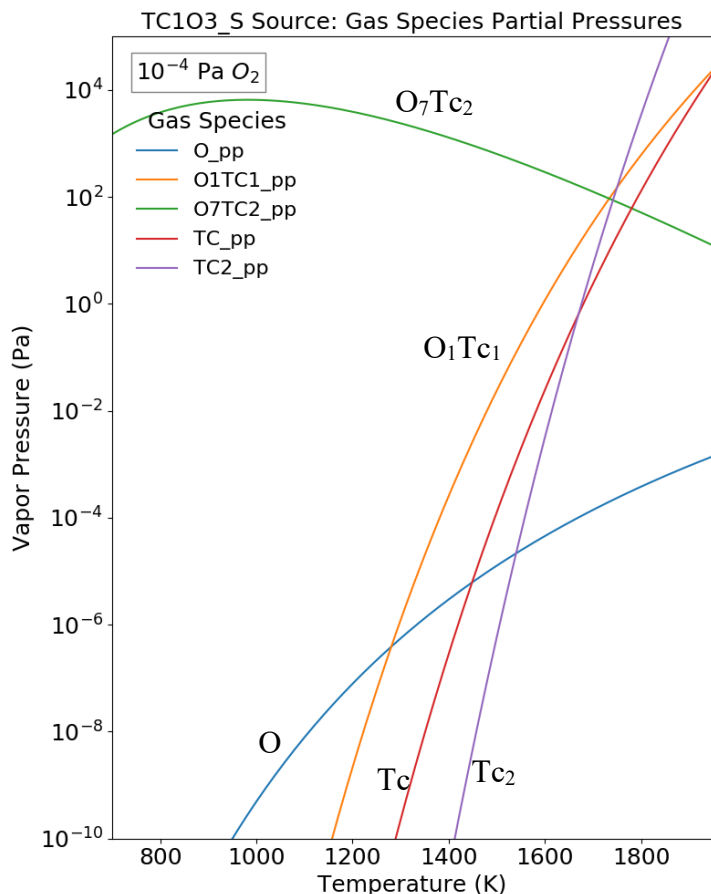


Figure S 69. Solid  $\text{TcO}_3$  (metastable phase). Calculated partial pressures of the gas species over the phase(s) of interest as a function of temperature at  $P_{\text{O}_2} = 10^{-4}$  Pa. Here, “\_pp” indicates partial pressure when available.

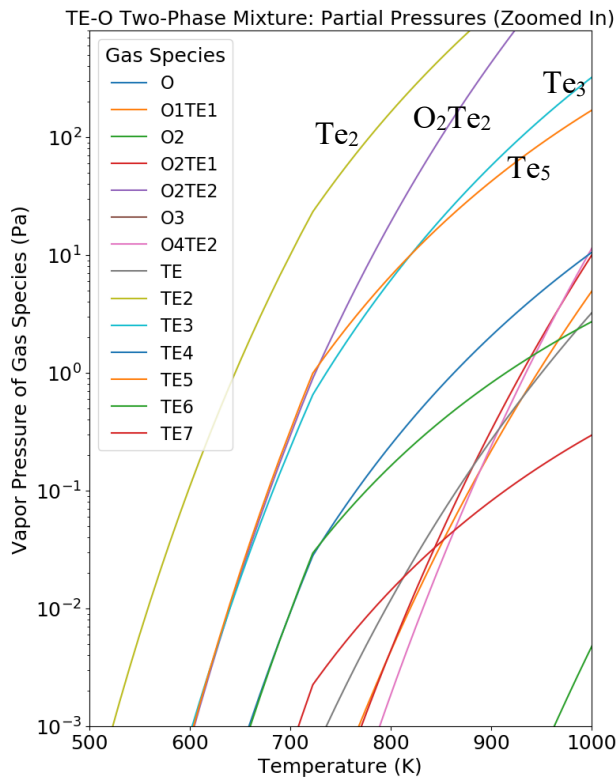
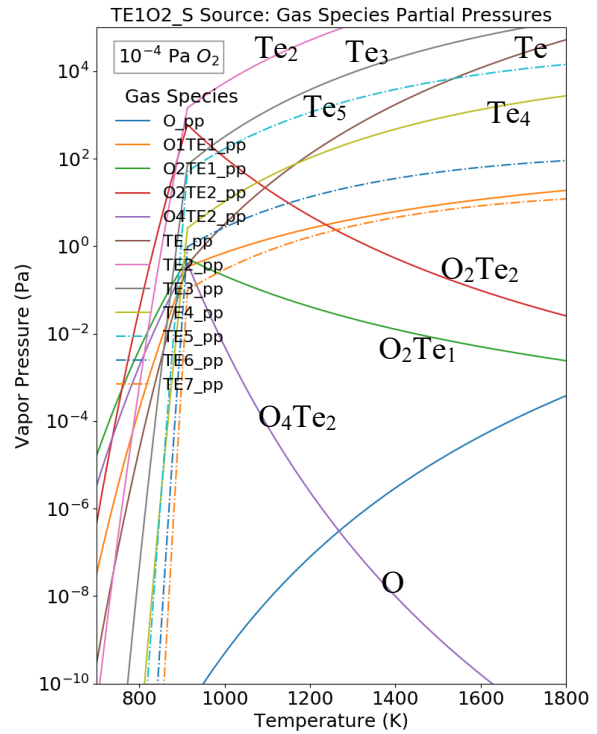
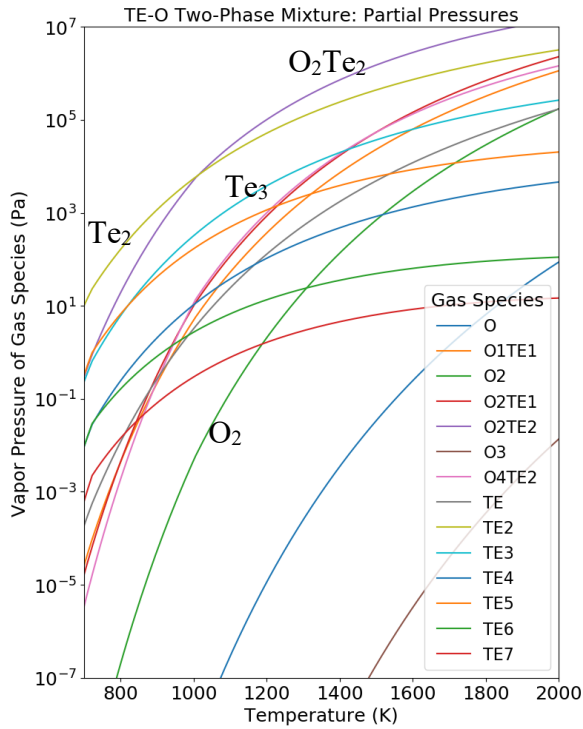


Figure S 70. Solid  $\text{TeO}_2$  (stable for  $T < 913$  K, beyond which liquid Te is stable). Calculated partial pressures of the gas species over the phase(s) of interest as a function of temperature at  $P_{\text{O}_2} = 10^{-4}$  Pa. Here, “\_pp” indicates partial pressure when available. Calculated partial pressures of the gas species over a  $\text{TeO}_2(\text{s},\ell)+\text{Te}(\text{s},\ell)$  two-phase mixture with an overall composition of TeO. Here, (s, $\ell$ ) indicate the solid phase at low temperatures and liquid phase at high temperatures.

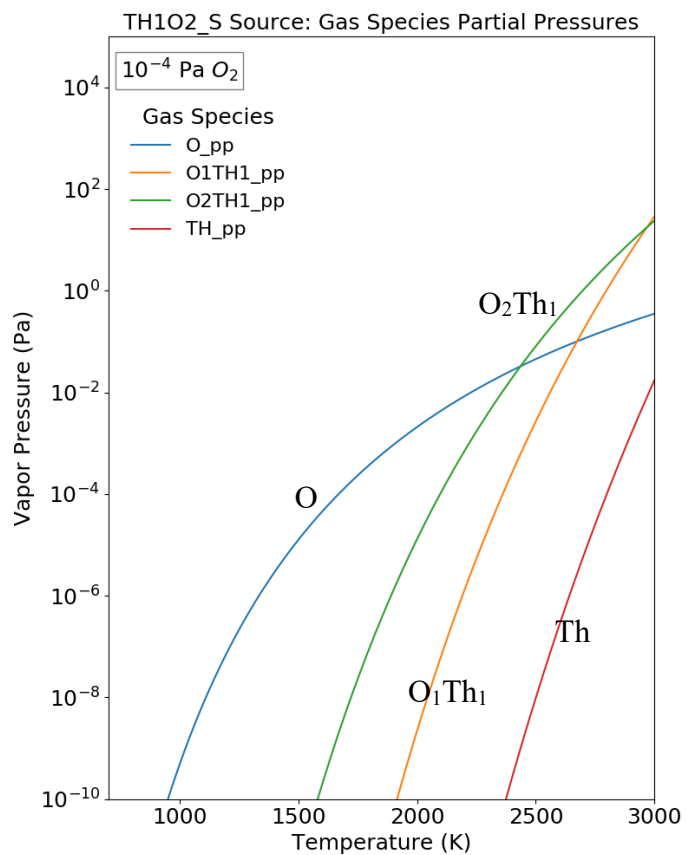
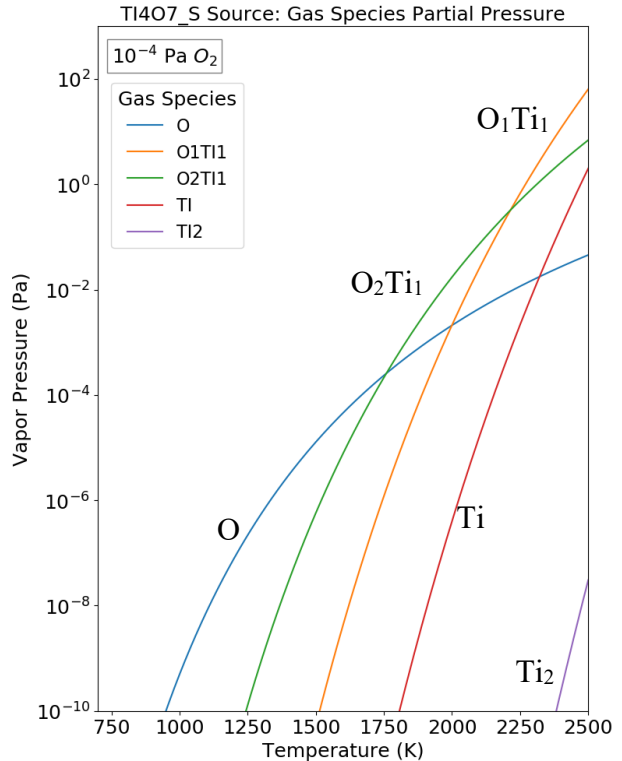
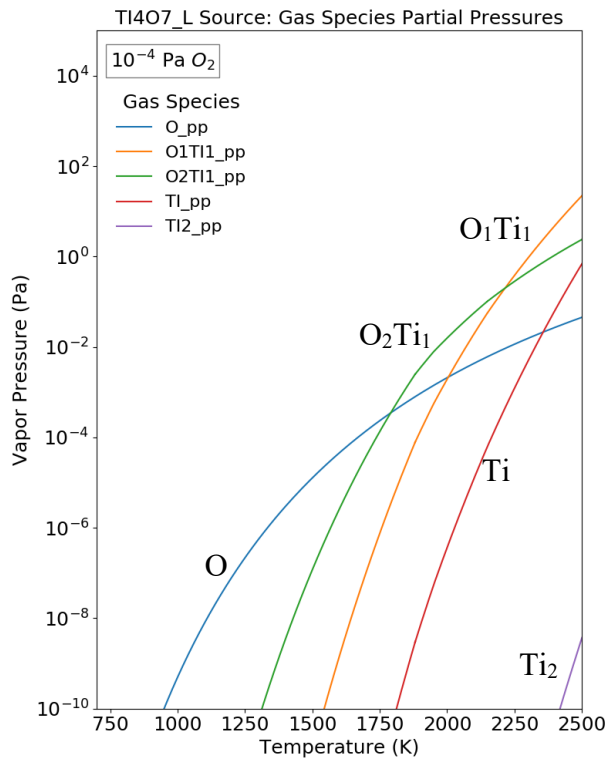
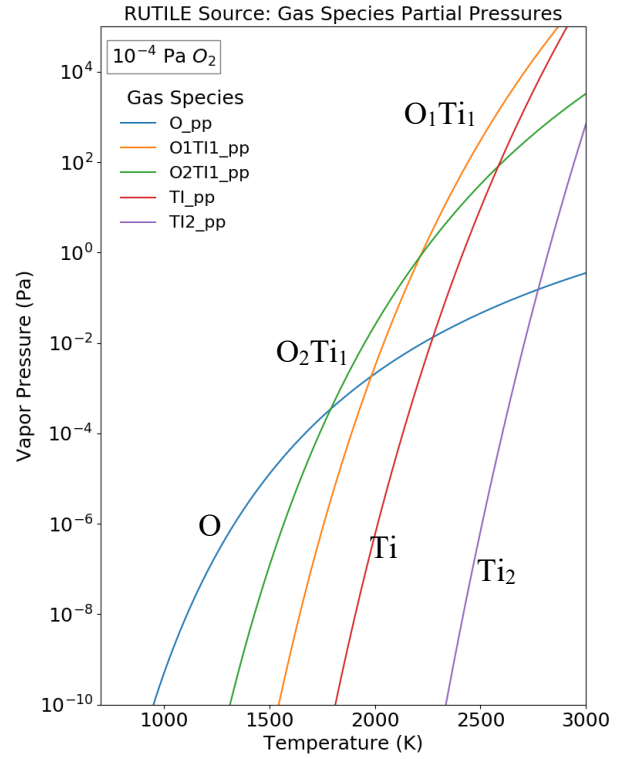
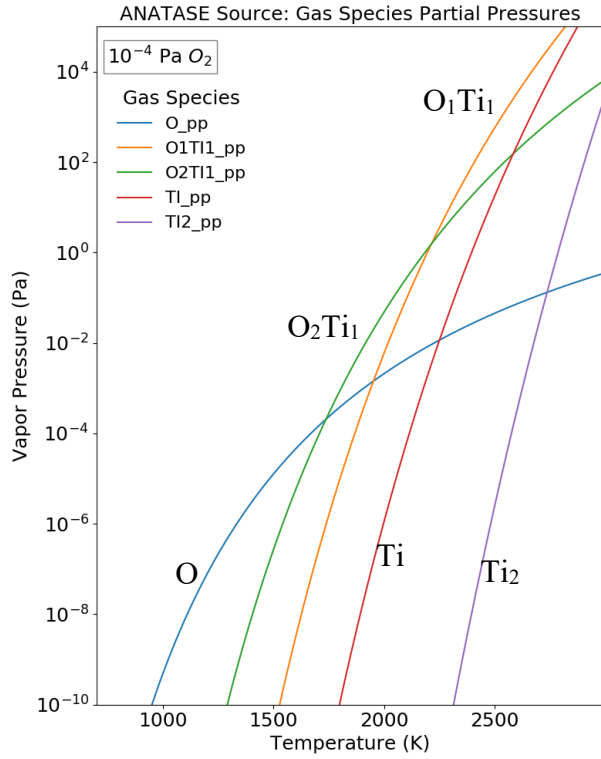


Figure S 71. Solid ThO<sub>2</sub> (stable phase over the temperature range shown). Calculated partial pressures of the gas species over the phase(s) of interest as a function of temperature at  $P_{O_2} = 10^{-4}$  Pa. Here, “\_pp” indicates partial pressure when available.



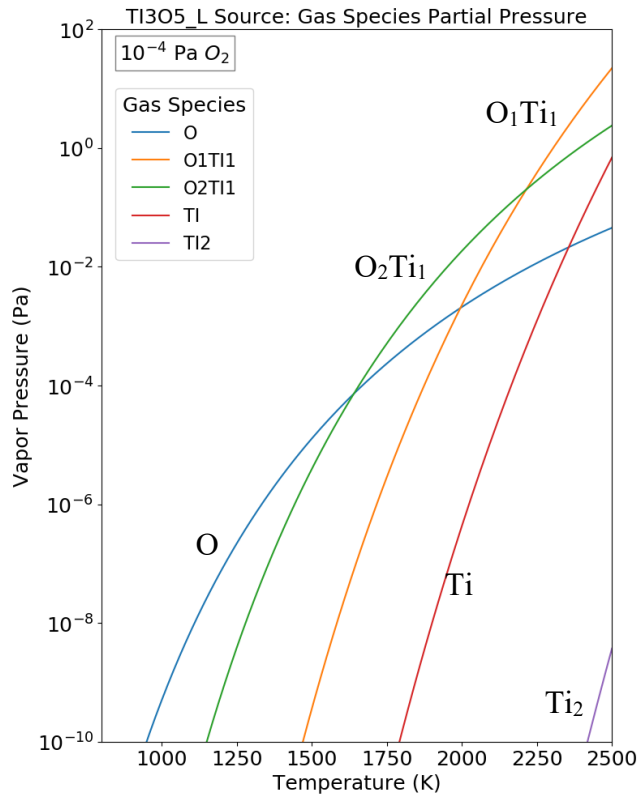


Figure S 72. Solid  $TiO_2$ \_anatase, solid  $TiO_2$ \_rutile, solid and liquid  $Ti_4O_7$ , and liquid  $Ti_3O_5$  ( $TiO_2$ \_rutile is stable for  $T < 1881$  K, followed by solid  $Ti_4O_7$  up to 1950 K, then liquid  $Ti_4O_7$  up to 2148 K, beyond which liquid  $Ti_3O_5$  is stable), and liquid  $Ti_4O_7$ . Calculated partial pressures of the gas species over the phase(s) of interest as a function of temperature at  $P_{O_2} = 10^{-4}$  Pa. Here, “\_pp” indicates partial pressure when available.

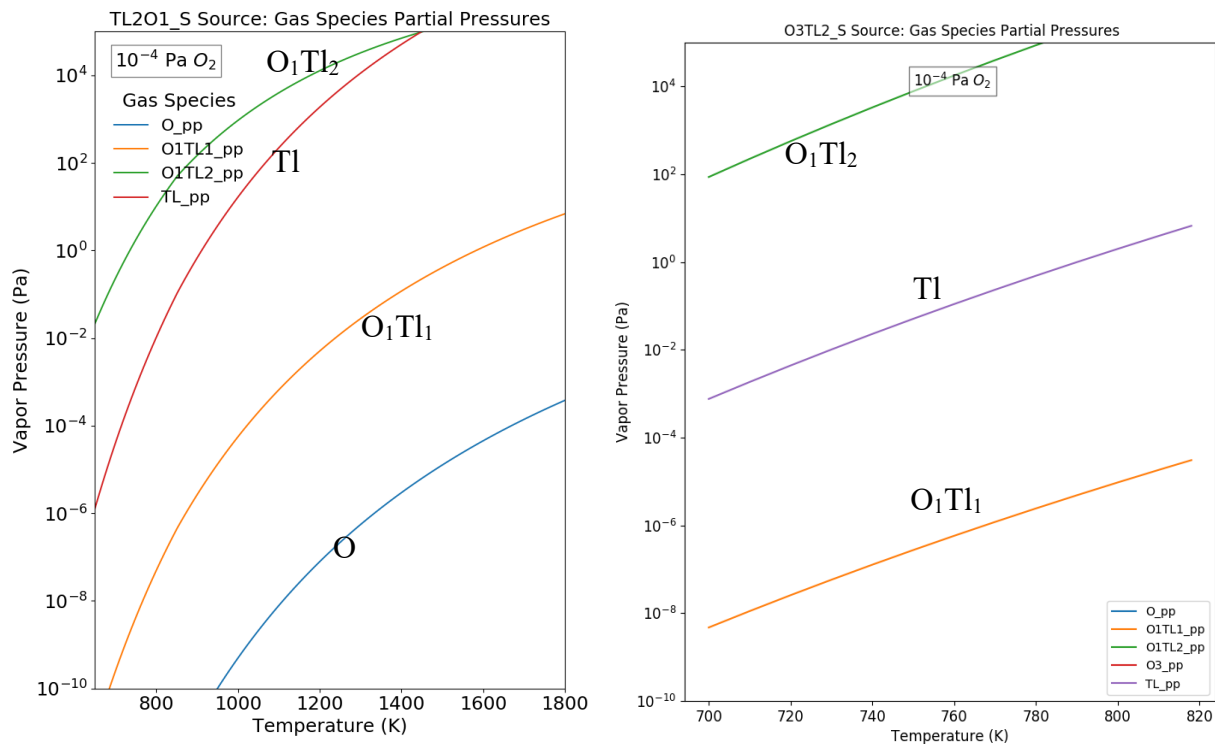


Figure S 73. Solid  $Tl_2O$  (stable for  $T < 852$  K, beyond which liquid  $Tl_2O$  is stable) and solid  $Tl_2O_3$ . Calculated partial pressures of the gas species over the phase(s) of interest as a function of temperature at  $P_{O_2} = 10^{-4}$  Pa. Here, “\_pp” indicates partial pressure when available.

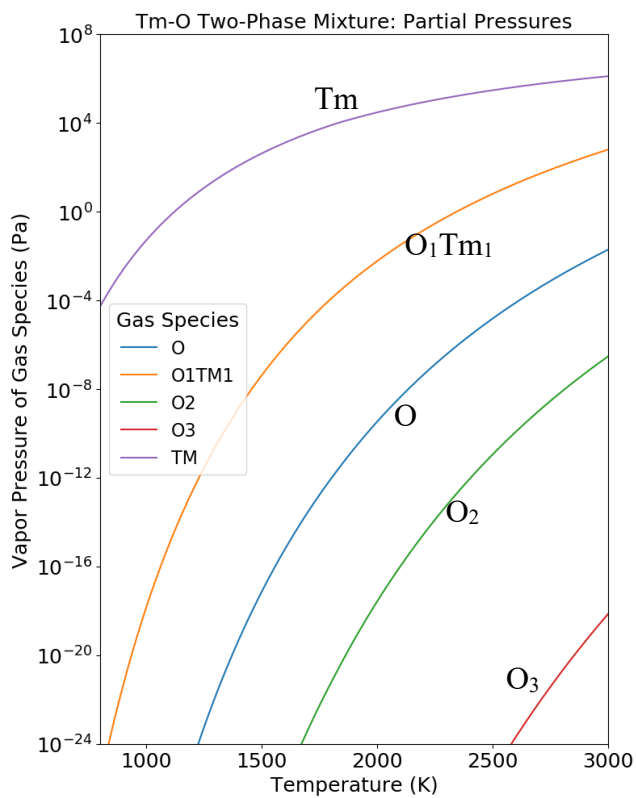
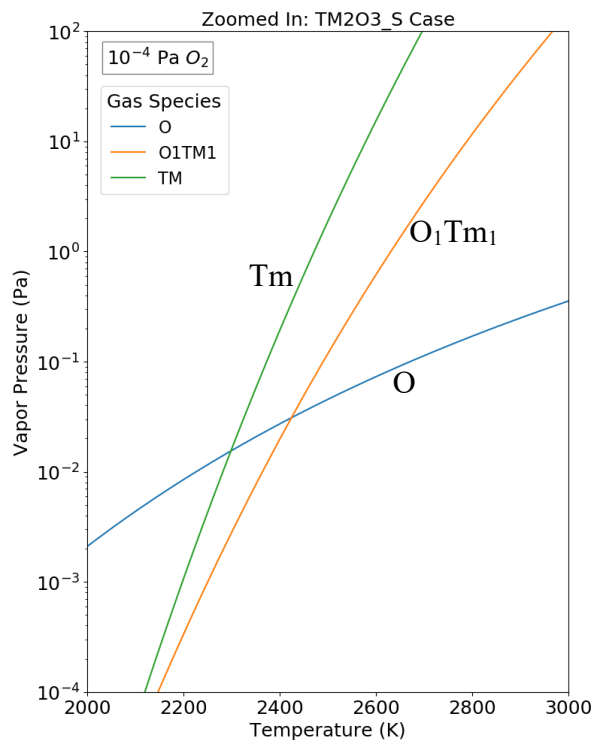
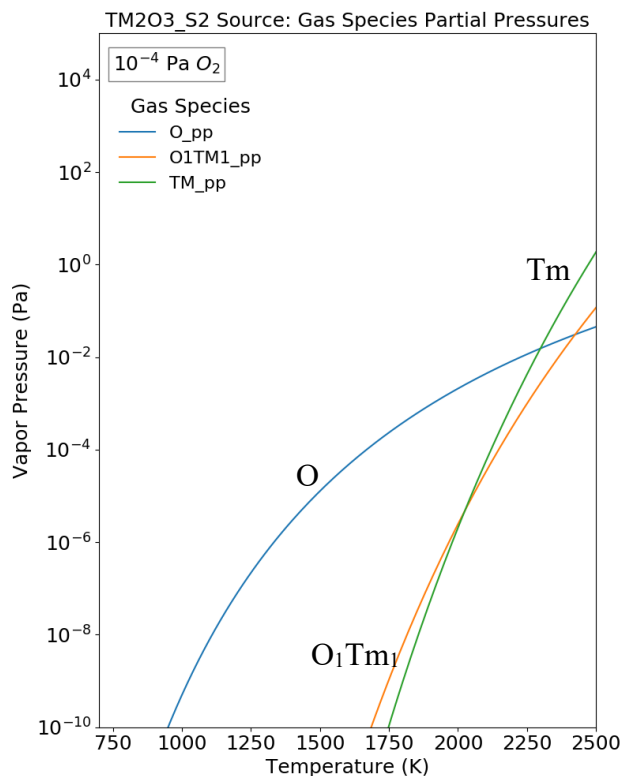


Figure S 74. Solid Tm<sub>2</sub>O<sub>3</sub> (stable phase over the temperature range shown, with a zoomed-in view in the plot on the right). Calculated partial pressures of the gas species over the phase(s) of interest as a function of temperature at  $P_{O_2} = 10^{-4}$  Pa. Here, “\_pp” indicates partial pressure when available. Calculated partial pressures of the gas species over a Tm<sub>2</sub>O<sub>3</sub>(s)+Tm(s,*l*) two-phase mixture with an overall composition of TmO. Here, (s,*l*) indicate the solid phase at low temperatures and liquid phase at high temperatures.

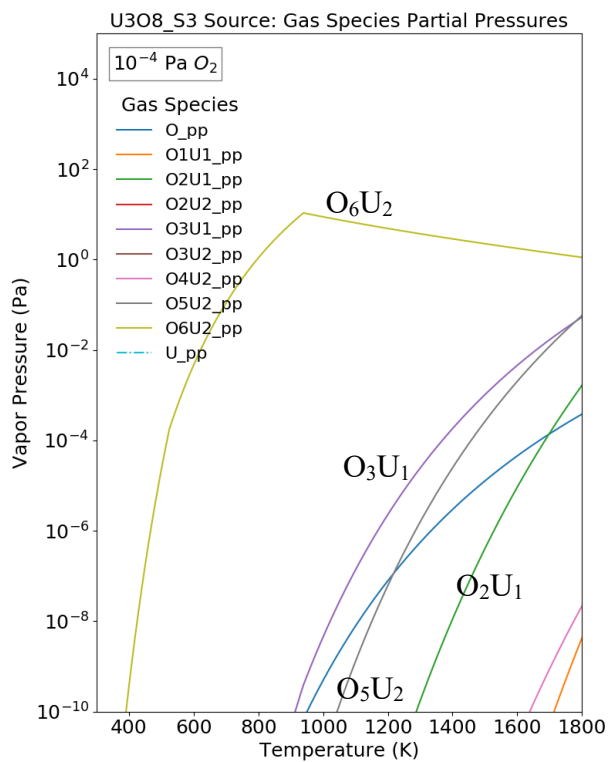
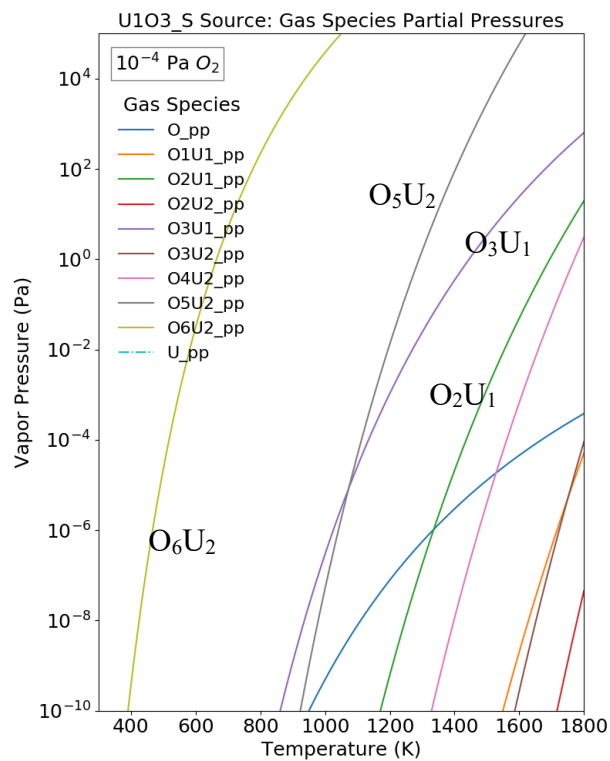
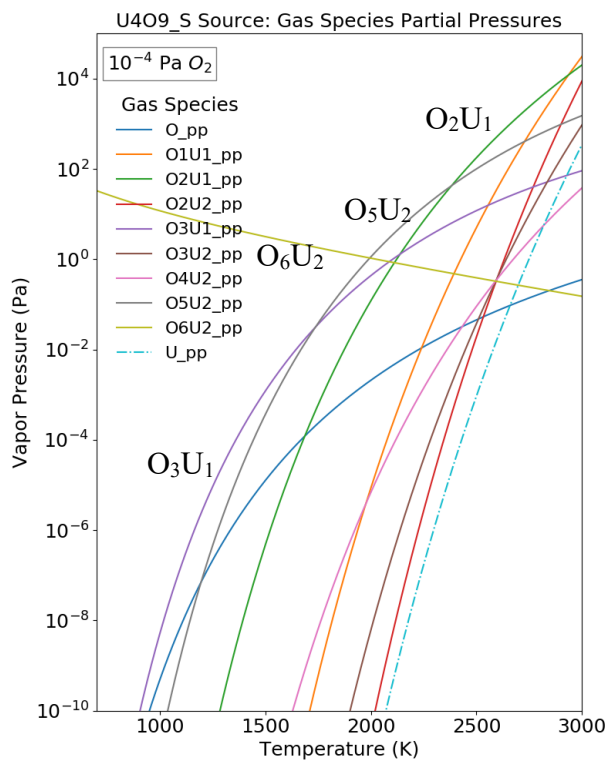


Figure S 75. Solid U<sub>4</sub>O<sub>9</sub>, solid UO<sub>3</sub> (stable for  $T < 525$  K, then solid U<sub>3</sub>O<sub>8</sub> up to 939 K, beyond which U<sub>4</sub>O<sub>9</sub> is stable), and solid U<sub>3</sub>O<sub>8</sub>. Calculated partial pressures of the gas species over the phase(s) of interest as a function of temperature at  $P_{O_2} = 10^{-4}$  Pa. Here, “\_pp” indicates partial pressure when available.

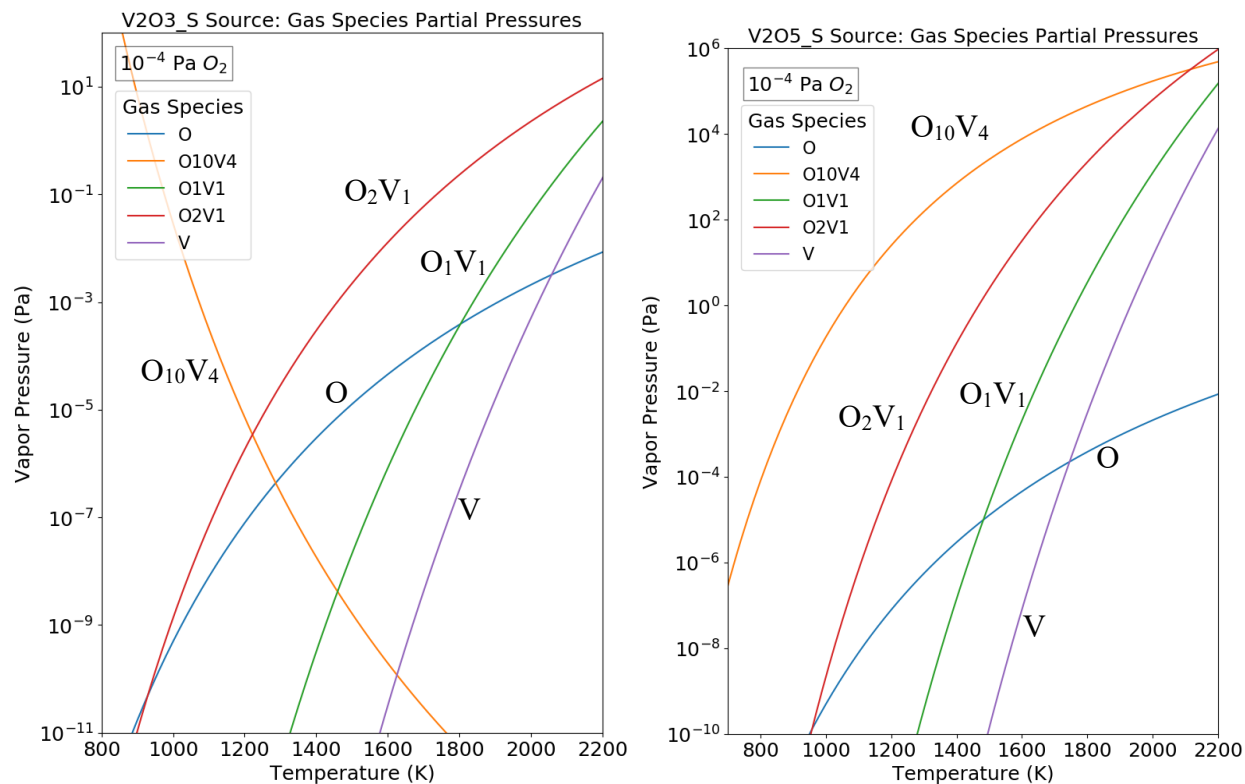


Figure S 76. Solid  $V_2O_3$  and solid  $V_2O_5$  (solid  $V_2O_5$  is a metastable phase; solid  $V_2O_3$  is stable at  $T > 1289$  K; note that solid  $V_2O_4$  is stable at low temperatures with the dominant gas species being  $O_2$ ; not shown). Calculated partial pressures of the gas species over the phase(s) of interest as a function of temperature at  $P_{O_2} = 10^{-4}$  Pa. Here, “\_pp” indicates partial pressure when available.

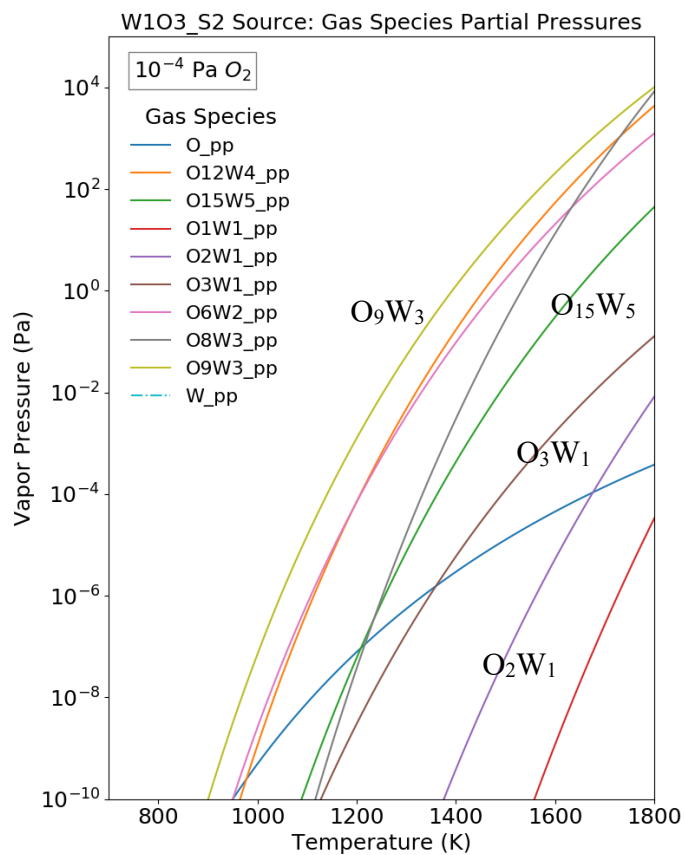


Figure S 77. Solid  $WO_3$  (stable phase over the temperature range shown). Calculated partial pressures of the gas species over the phase(s) of interest as a function of temperature at  $P_{O_2} = 10^{-4}$  Pa. Here, “\_pp” indicates partial pressure when available.

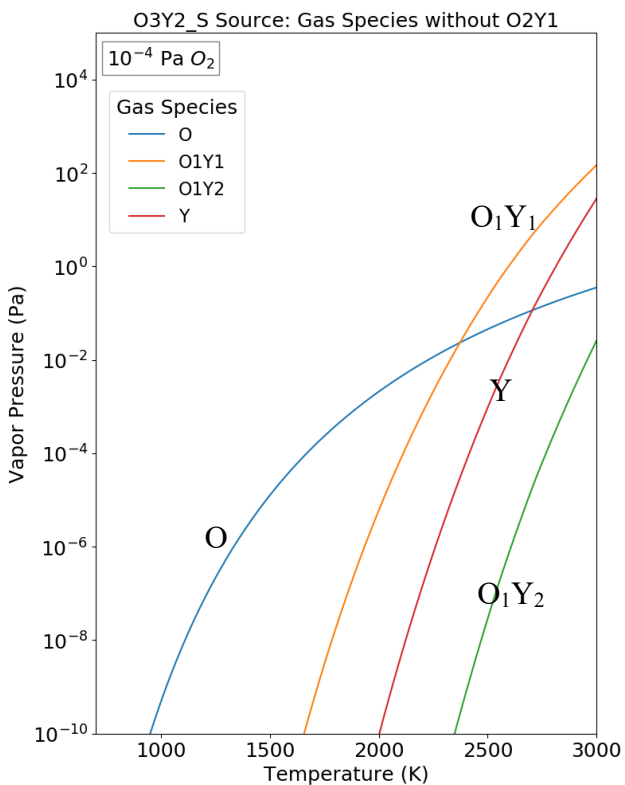
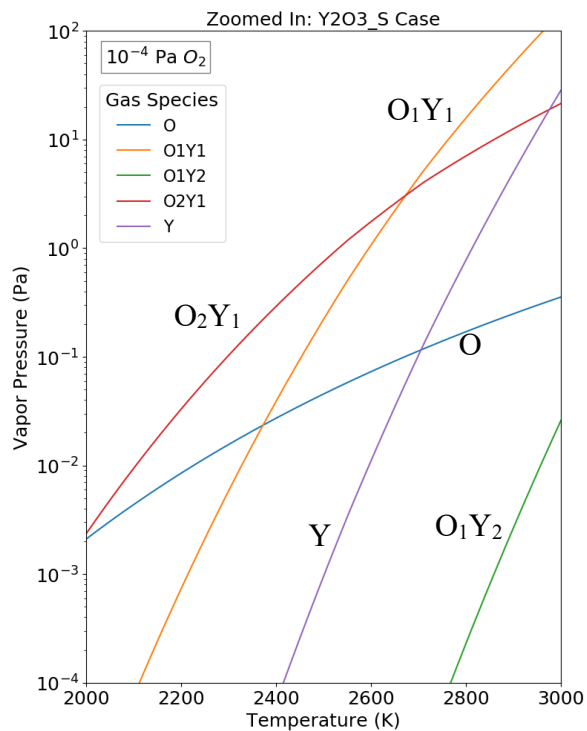
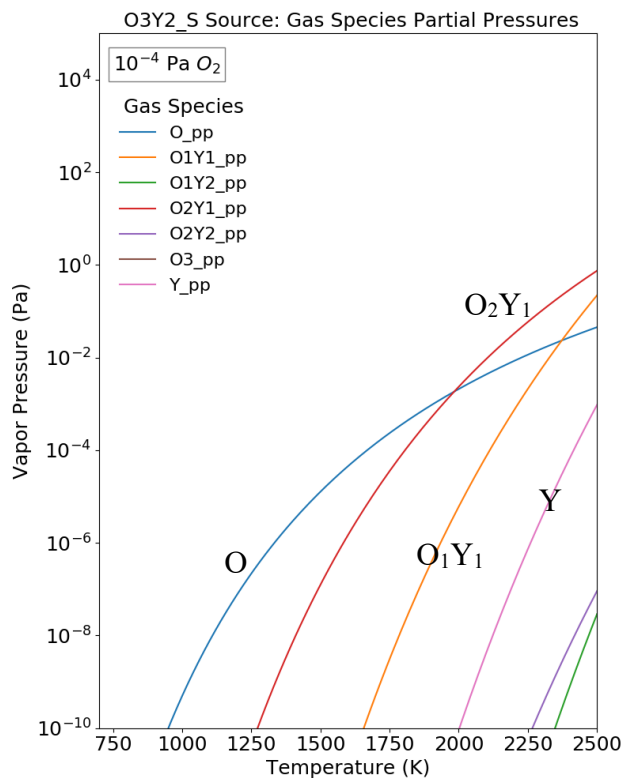


Figure S 78. Solid Y<sub>2</sub>O<sub>3</sub> (stable for  $T < 2712$  K, beyond which liquid Y<sub>2</sub>O<sub>3</sub> is stable) with a zoomed-in view in the plot on the right. Calculated partial pressures of the gas species with and without YO<sub>2</sub>(g) over the phase(s) of interest as a function of temperature at  $P_{O_2} = 10^{-4}$  Pa. Here, “\_pp” indicates partial pressure when available.

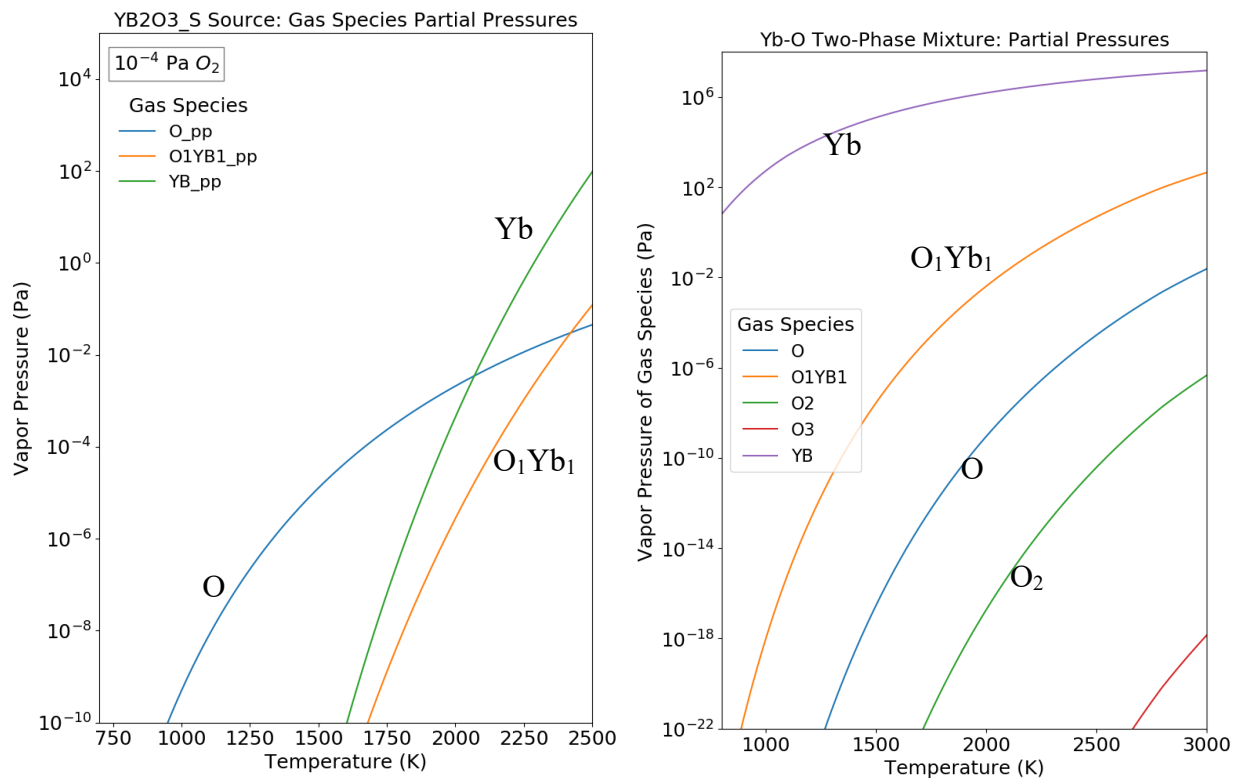


Figure S 79. Solid  $\text{Yb}_2\text{O}_3$  (stable phase over the temperature range shown). Calculated partial pressures of the gas species over the phase(s) of interest as a function of temperature at  $P_{\text{O}_2} = 10^{-4}$  Pa. Here, “\_pp” indicates partial pressure when available. Calculated partial pressures of the gas species over a  $\text{Yb}_2\text{O}_3(\text{s},\ell) + \text{Yb}(\text{s},\ell)$  two-phase mixture with an overall composition of  $\text{YbO}$ . Here, (s, $\ell$ ) indicate the solid phase at low temperatures and liquid phase at high temperatures.

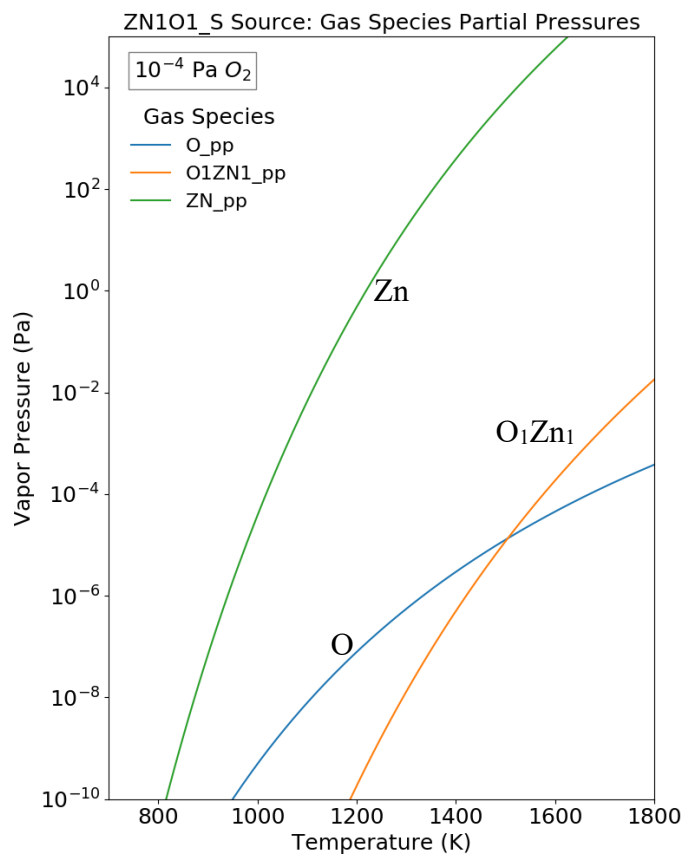


Figure S 80. Solid ZnO (stable phase over the temperature range shown). Calculated partial pressures of the gas species over the phase(s) of interest as a function of temperature at  $P_{O_2} = 10^{-4}$  Pa. Here, “\_pp” indicates partial pressure when available.

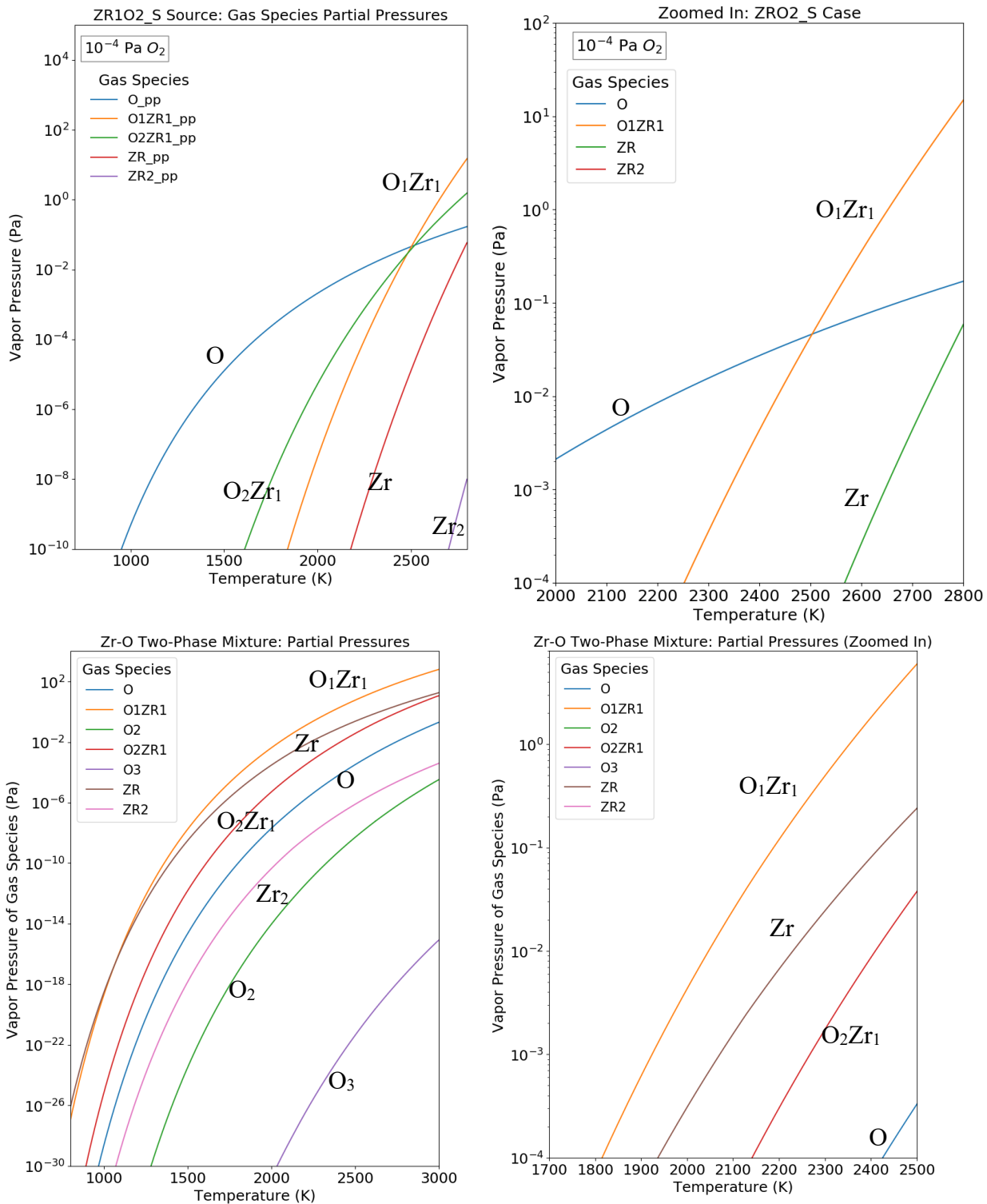


Figure S 81. Solid ZrO<sub>2</sub> (stable phase over the temperature range shown) with a zoomed-in view in the plot on the right. Calculated partial pressures of the gas species over the phase(s) of interest as a function of temperature at  $P_{O_2} = 10^{-4}$  Pa. Here, “\_pp” indicates partial pressure when available. Calculated partial pressures of the gas species over a ZrO<sub>2</sub>(s,ℓ)+Zr(s,ℓ) two-phase mixture with an

overall composition of ZrO. Here, (s, $\ell$ ) indicate the solid phase at low temperatures and liquid phase at high temperatures.